The Northern Margin of the Ferrar Large Igneous Province: Petrogenesis and Differentiation of the Tasmanian Dolerites and Kangaroo Island basalts

Paolo A. Sossi

Supervisor: John D. Foden

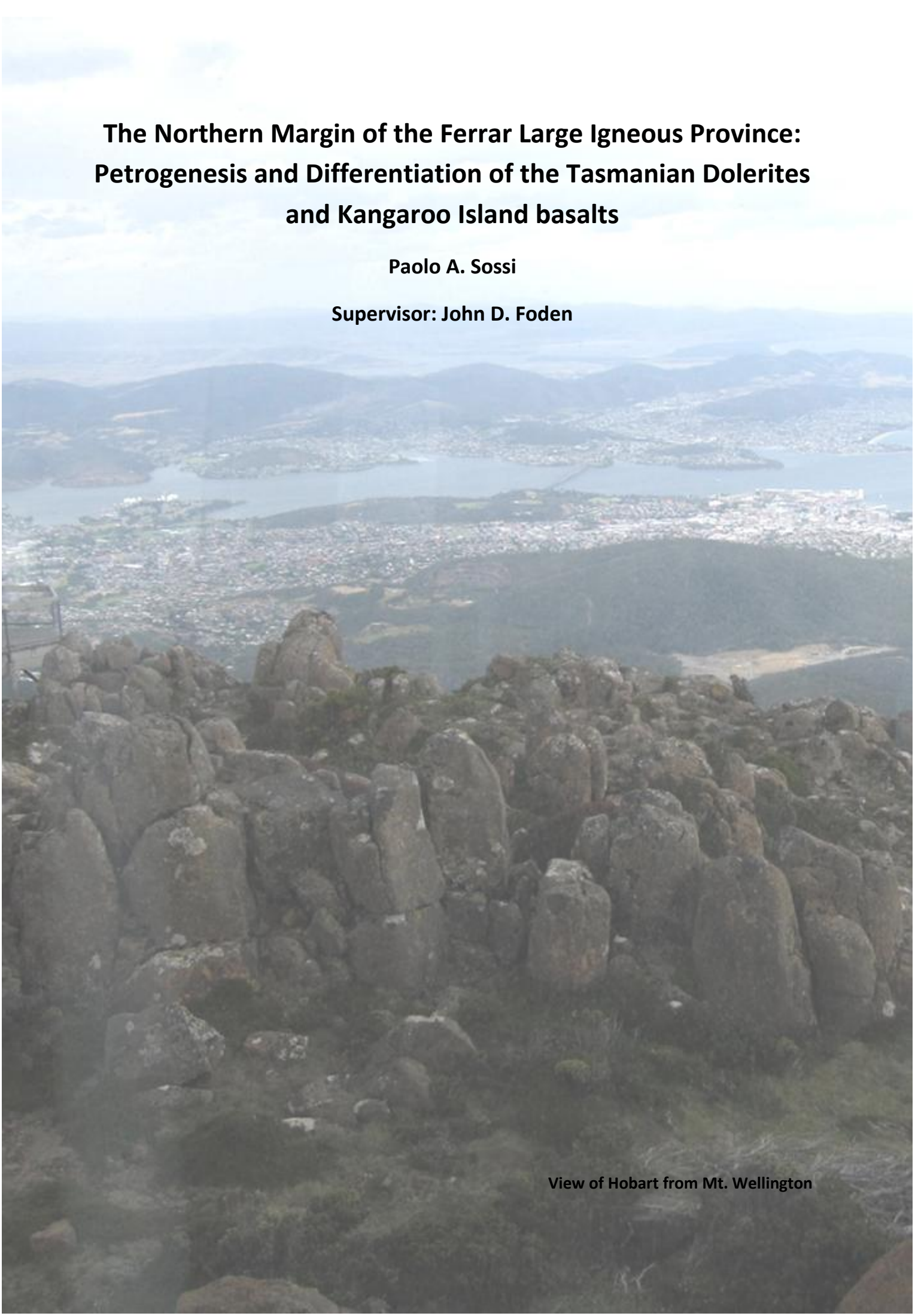

View of Hobart from Mt. Wellington

Contents

Guide to the Thesis

This thesis, entitled *"The Northern Margin of the Ferrar Large Igneous Province: Petrogenesis of the Tasmanian Dolerites and Kangaroo Island Basalts"*, investigates magmatism associated with this large igneous province on a range of scales by employing varied chemical and isotopic techniques. Owing to the length of this thesis, it has been subdivided into 5 separate sections that can be read independently, though they are best treated as composite chapters of the same story.

Section 1.0., *Analytical Methods,* is presented at the beginning of the thesis, as it details the procedures by which the data was obtained, and thus the readers may assess the uncertainties and accuracies of each of the methods employed before the data is subjected to an interpretative analysis in the later sections. Additionally, because the project has a strong emphasis on quantitative chemistry, the analytical techniques are necessarily well-refined. The methods employed here cover not only the more traditional aspects of geochemistry (such as X-Ray Fluorescence and Electron Probe Micro-Analysis) but also certain hitherto esoteric fields (particularly Iron Isotope Geochemistry). Since these more specialised techniques are not widespread in literature, it is considered beneficial to present them here.

A general overview of the field locations, and the physical and petrographic characteristics which constitute a classification scheme for the rocks, is detailed in Section 2.0. (*General*). This chapter provides a summary of the geological history of the Tasmanian Dolerites and Kangaroo Island basalts, and then proceeds to define a petrologically-based classification for the samples used in the later sections of the study. Interpretation and chemical analyses are kept to a minimum, rendering an objective view of the samples and their setting.

The discussion-based sections of the thesis are then presented as 3 discrete manuscripts, each with an abstract, introduction and conclusion. Occasionally, references will refer the readers to figures or equations from an accompanying section.

A treatment of the origin and petrogenesis of the basaltic magmas of the Tasmanian Dolerites and Kangaroo Island is eludicated upon in Section 3.0., *The Mantle Source*. This study focuses on the chemical characteristics of the least-fractionated mafic magmas of the province, using their distinctive properties to infer the timing and conditions of mantle melting. An interpretation of their petrogenesis is made in keeping with broader-scale tectonic considerations, in order to create a consistent picture for the generation of the Ferrar Large Igneous province, of which they are a part.

In edifying the chemistry of the source and its derivative magmas, the differentiation history of the magmas following their emplacement in the crust is analysed in Section 4.0., *Differentiation*. An extensive array of samples from the Red Hill intrusion, southern Tasmania are utilised for this chapter, as they record the variability shown by the differentiating magma. The large suite of rocks permits a detailed study of mineral-liquid relationships, whose systematics are interpreted in light of thermodynamic and experimental studies. The effects of various chemical parameters on the evolution of the tholeiitic trend are assessed, with a view to characterising its end-member products, and developing a model for the formation of A-Type granitoids.

Section 5.0. *Iron Isotope Variations*, represents a Nature manuscript that was submitted prior to the consignment of this work ((*In Submission)* Sossi, P.A., Foden, J.D., Halverson, G.P., 2010. Redox-controlled iron isotope fractionation during magmatic differentiation. *(Nature Geoscience)*.) For the first time this provides a quantitative determination of the fractionation factors that govern Fe isotopic fractionation in magma systems with changing saturation of ferrous and ferric iron–bearing minerals

1.0. Analytical Methods

1.1. Sample Preparation

Sample Milling
The samples collected were typically about 10-15cm^3, and were subsequently cut in half with a diamond-bladed rock saw, and were also rid of their weathered surfaces or other impurities. Rocks with considerable iron staining (as is typical for the granophyres) were rejected and left unprocessed. The resultant blocks were passed through an iron-based jaw crusher, yielding gravel-size fragments. The fragments and associated finer grains were subdivided into two halves representative of the sample, one of which was subjected to milling in a tungsten-carbide mill, which, in addition to tungsten, contains trace amounts of tantalum. The gravels were milled in a vibrating mill invariably for between 2-3 minutes to achieve a sufficiently fine powder.

Thin Sections
40µm-thick polished thin sections were provided by Pontifex and Associates in aid of in-situ mineral analytical methods (Electron Probe Microanalaysis (EPMA) for major elements, and Laser-Ablation Solution Inductively-Coupled Plasma Mass Spectrometry (LA-ICP-MS) for trace elements), in addition to petrographic work.

1.2. Major and Trace Whole Rock Geochemistry – XRF

Major Elements – Fused Discs
Approximately 5-10g of powder was desiccated by heating in an oven at 110°C for >2hours, thereby removing absorbed moisture. Following this, the dried powders were precisely weighed in a ceramic crucible on a Mettler-Toledo balance, and then ignited overnight at 960°C, yielding loss-on-ignition values, which is dominantly H_2O for the Red Hill samples. A nominal 1g of the ignited material was then weighed in conjunction with 4g of lithium borate flux (comprising 35.3% lithium tetraborate and 64.7% lithium metaborate), so as to yield a 1:4 sample:flux ratio. The resulting mixture was then fused using a propane-oxygen flame in a Pt-Au alloy crucible at ≈1150°C for 8 minutes before being cast into a mould to yield a disc suitable for analysis. The analyses were performed on a Philips PW 1480 X-ray Fluorescence Spectrometer running a dual Sc-Mo anode X-ray tube operating at 40kV and 75mA, whose analysis program is calibrated against numerous international and in-house standards. The elements analysed were: SiO_2, Al_2O_3, $Fe_2O_3^{(T)}$, MnO, MgO, CaO, Na_2O, K_2O, TiO_2, P_2O_5 and SO_3. The average total (including LOI) was 99.98% over 66 samples.

Trace Elements – Pressed Pellets
About 5-10g of powder was mixed with a notional 0.7ml of ethanol/polyvinyl binding agent and pressed to create a pellet. The pellet was permitted to dry in air before being dehydrated at 60°C in an oven before analysis on the Philips PW 1480 X-ray Fluorescence Spectrometer. Matrix corrections are made using mass absorption coefficients from major element data, which necessitates they be run first. Elements measured using this method (and their detection limits in ppm in brackets) were: Sr (1.0), Rb (1.0), Y (1.0), Zr (2.0), Nb (1.5), Pb (2.5), Th (1.5), U (1.5), Ba (3), Sc (2), Ga (2), V (2), Cr (1.5), Ce (5), Nd (3), La (2), Ni (3), Cu (4), Zn (3), Co (2).

1.3. Whole Rock Trace Element Geochemistry – S-ICP-MS

Sample Preparation Procedure for ICP-MS, devised by B. Wade, D. Bruce and P.Sossi.
About 60mg of rock powder was accurately weighed in a cleaned 8ml PFA Teflon beaker using a Mettler-Toledo AT201 balance. 2ml of single-distilled (D) 7M HNO_3 and 4ml of single-distilled 50% HF were added and the mixture was heated at 140°C overnight. The solution was dried down, and 2ml of 7M D HNO_3 was added to it periodically so as to prevent the precipitation of insoluble fluorides. This procedure was repeated twice. After the second dry-down, the solution was taken up in 6ml of 7M D HNO_3, and heated at 140°C overnight, and the solution evaporated away the next day. The residue was then dissolved in 5ml D 5% HNO_3, representing a dilution factor of ≈100x. Between 1ml and 2ml of this solution was taken to be centrifuged in order to remove any lingering insoluble components which may cause problems during analysis on the ICP-MS. The volume of solution taken is determined based on the estimated concentration of trace elements in the rock. The trace element with the highest concentration is typically Ba, which nears 700ppm in the Red Hill samples. By contrast, Lu is the least abundant, with concentrations down to 0.3 in the least differentiated rocks. This is a range of more than 3 orders of magnitude, and therefore necessitates a wide range of concentrations in the calibration solutions such that the samples remain within range of the calibration. For this reason, differentiated rocks with higher anticipated concentrations had 1ml passed through the centrifuge, running at 13,200 rpm for 10 minutes, while the most primitive samples had 2ml centrifuged. This centrifuged solution was extracted and then weighed in a clean high-density polyethylene (HDPE) tube, and diluted up to 5ml total with the complementary volume of D 5% HNO_3. Total dilution factors were typically between 200-600x. Duplicate analyses of a subset of the samples were performed, consisting of separate dissolutions and dilutions. In addition to the samples, 3 USGS international standards bracketing the range of compositions in the Red Hill suite (BHVO-2, BCR-2 and GSP-2), in addition to an in-house standard (TASBAS) were subjected to the same analytical procedure in order to quantify its reproducibility (*tables A1-A-D*). These standards were diluted to the same amount as the samples, such that matrix effects could be accounted for. The standards were normalised to their accepted values and the samples corrected by the same factor. Furthermore, total analytical blanks prepared in an identical manner to the samples, however, the concentrations of measured trace elements in these solutions were not appreciably different to those in the acid blank, which were below detection limit for all elements.

Sample Running on S-ICP-MS
The samples are run in HNO_3 rather than HCl because it preferentially retains the HFSE (particularly Nb^{5+} and Ta^{5+}) in solution. For running on the S-ICP-MS, a set of calibration solutions were also made from synthetic multielement solutions (CHOICE analytical), in the range 10-20-50-100-200-400ppb, encompassing the vast majority of element concentrations in the diluted samples. These convert the counts-per-second (cps) measured by the detector to concentration values. In addition, a dual Rhenium-Indium solution (200ppb) was formulated to account for the behaviour of the elements over time in the ICP-MS. The solution was aspirated simultaneously with the sample solution, and mirrors the time-integrated signal loss experienced over a given run due to coating of the sample and skimmer cones with positively-charged matrix ions (usually Fe) which repel incoming ions. Re was used to correct for elements with high ionisation potential (the HFSE, Mn, Co, Ni, Cu, U, Th and Pb) where Indium, because of its intermediate ionisation potential, was used in correction of the other elements analysed.

The Agilent 7500cs is fitted with an H/He reaction-collision cell which aids in the removal of spectral interferences on an analyte element. All elements are run under He (collision) tune, except for Se, which is under H (reaction) tune and Li (no gas) due to a lack of interferences on ^{7}Li owing to its low mass. In and Re are analysed under all three tune parameters to account for these elements. Collision tune functions on the premise that the polyatomic interfering molecules have larger

dimensions than the monatomic analyte element, and therefore are more susceptible to have their flight path disturbed through collision with He molecules. While collision tune effectively removes all of the spectral interferences, it also drastically reduces the counts measured on the analyte element, and hence counting time is necessarily prolonged. Typical counting times are:
Li to Rb = 0.1s
Rb to In = 0.5s
In to U = 1s
The higher mass number elements are analysed for a longer period of time due to the propensity for more isobaric interferences to coincide with the analyte mass. Each element in the cycle is analysed for 3 repetitions, and the total analysis time is of the order of 4 minutes.
Raw data was corrected against the multielement calibration solution, the Re-In solution, and finally against the internal rock standards, because of possible matrix effects.

Elements analysed during the procedure were: Li, Be, B, P, Sc, V, Cr, Mn, Co, Ni, Cu, Zn, Ga, Ge, As, Rb, Sr, Y, Zr, Nb, Mo, Ag, Cd, Sn, Sb, Cs, Ba, La, Ce, Pr, Nd, Sm, Eu, Gd, Tb, Dy, Ho, Er, Yb, Lu, Hf, Ta, Tl, Pb, Th, U.

1.4. In-Situ Major Element Mineral Chemistry – EPMA

Major element analyses of minerals were undertaken using the Cameca SX51 electron microprobe, housed at Adelaide Microscopy. The thin sections, in addition to being polished, had a thin film of carbon coating with conductive carbon tape applied in order to provide a conductive pathway to disperse any charge build-up on the surface of the slide, which would attenuate the strength of the irradiating electron beam. The beam is created by heating of tungsten filaments, yielding a 15kV beam running at 20nA, focused to 5µm in diameter, equating to an interaction volume of 0.5µm for typical silicate minerals. This is a non-destructive technique, and was performed prior to analyses by the LA-ICP-MS. The incident beam excites electrons, before they return to their ground state, triggering the emission of an X-Ray of an energy equivalent to the atomic transition, which, in wavelength-dispersive mode (WDS) is then diffracted by a crystal with known atomic spacing before being detected. Typical counting times on elements ranged from 8-20s, with the alkalis (Na, K) being measured first due to their relative volatility.
The machine was calibrated against a series of known astimex standards, and the calibration was checked or re-performed before each analytical session. The data was machine-corrected using PAP calibrations to account for changes in atomic number, absorption and fluorescence properties. The elements measured using this technique included: SiO_2, Al_2O_3, $FeO^{(T)}$, MnO, MgO, CaO, Na_2O, K_2O, TiO_2, V_2O_3, Cr_2O_3, Cl, F.

1.5. In-Situ Trace Element Mineral Chemistry – LA-ICP-MS

Individual carbon-coated thin sections were mounted in the laser-ablation cell, which is coupled to an Agilent 7500 series (quadrupole) ICP-MS. The analyses were performed using a New Wave Nd:YAG 213nm laser running in continuous mode with a 55µm spot size, a frequency of 5Hz, and at 75% intensity. Typical energy readings were 0.3mJ for sample and 12.75 J/cm^2 for fluence. The data was collected using a 40s background count prior to 60s counting time for the mineral analysis. ^{43}Ca was used as a normalising standard based on its concentration derived from a given spot from the EPMA analysis, and is suitable for pyroxenes, amphiboles and plagioclase due to their appreciable Ca contents (>2wt%). Due to the 55µm spot size and hence destructive nature of this method, the EPMA analysis must be performed first, especially in zoned minerals, such as pyroxenes and plagioclase in the Red Hill rocks. Standard corrections were based on analyses of the synthetic NIST

SRM 612 glass (Pearce et al., 1997). Internal standards of natural basaltic samples (international USGS standards, BHVO-1 and BCR-1) were also measured prior to the sample runs, as they more closely approximate the matrix effects involved with natural mineral samples. The typical analytical set-up consisted of 4 NIST SRM 612, 1 BHVO-1, 1 BCR-1, 1 NIST SRM612, ≈10 samples, 2 NIST SRM 612. Each element was set-up to be analysed in equal dwell times (20ms/element). Elements analysed were: ^{7}Li, ^{23}Na, ^{25}Mg, ^{29}Si, ^{31}P, ^{39}K, ^{43}Ca, ^{45}Sc, ^{49}Ti, ^{51}V, ^{53}Cr, ^{55}Mn, ^{57}Fe, ^{59}Co, ^{60}Ni, ^{63}Cu, ^{65}Cu, ^{66}Zn, ^{67}Zn, ^{68}Zn, ^{69}Ga, ^{71}Ga, ^{73}Ge, ^{75}As, ^{85}Rb, ^{88}Sr, ^{89}Y, ^{90}Zr, ^{91}Zr, ^{93}Nb, ^{97}Mo, ^{118}Sn, ^{137}Ba, ^{139}La, ^{140}Ce, ^{141}Pr, ^{146}Nd, ^{147}Sm, ^{153}Eu, ^{157}Gd, ^{159}Tb, ^{163}Dy, ^{165}Ho, ^{166}Er, ^{169}Tm, ^{172}Yb, ^{175}Lu, ^{178}Hf, ^{191}Ta, ^{208}Pb, ^{232}Th, ^{238}U

1.6. Radiogenic Isotope Geochemistry - TIMS

Sample Preparation Procedure (Rb/Sr, Sm/Nd, U,Th/Pb)
An amount of sample was accurately weighed out so as to yield about 2µg total of neodymium in the sample. For the Red Hill samples, which contained between 10ppm and 50ppm Nd, this necessitates 200mg to 40mg of the lowest and highest concentration samples, respectively. Samples were spiked with a mixed enriched isotope Sm-Nd spike (Sm-Nd F (1.91375 nmol/g ^{150}Nd; 3.70847 nmol/g ^{147}Sm): .2g of spike per 1µg of Nd) in order to perform isotope dilution (ID) measurements on both these elements, which provides a more accurate estimate of their concentration compared to XRF or S-ICP-MS methods. Total analytical blanks also processed with the samples had three spikes added to them to quantify the blank contribution to the sample analyses (Sm-Nd E, Sr F (56 ng/g Sr, where ^{86}Sr/^{84}Sr = 1), and Pb C (^{208}Pb = 5.61%, ^{207}Pb = 92.22%, ^{206}Pb = 2.21%, ^{204}Pb = .04%, where ^{207}Pb/^{206}Pb = 6.2)). In addition to the samples and blanks, analysis of two standards was also carried out. The standards consisted of international USGS standards BHVO-2 and BCR-2, whose isotopic compositions have been well characterised. 2ml of single-distilled (D) 7M HNO_3 and 4ml of single-distilled 50% HF were added and the mixture was heated at 140°C overnight. The solution was dried down, and 2ml of 7M D HNO_3 was added to it periodically so as to prevent the precipitation of insoluble fluorides. This procedure was repeated twice. After the second dry-down, the solution was taken up in 6ml of 6M D HCl, and heated at 140°C overnight, and the solution evaporated away the next day. The solution is then dissolved in 2ml of 2M HCl and centrifuged at 13,200rpm for 10 minutes in readiness for the anion exchange columns.

Chromatography and TIMS – Rb/Sr, Sm/Nd
Approximately a 1ml aliquot (half) of the centrifuged solution was taken for Rb/Sr and Sm/Nd purification by cation exchange chromatography. Using Bio Rad columns with 2mL AG50W X8 200-400 Bio Rad cation exchange resin, the Sr fraction is collected and passed through the columns twice, while Sm and Nd are eluted with the rest of the REE given their similar chemical behaviour, and require a pass through a second series of columns. The REE fraction was evaporated to dryness before being taken up in 0.16M HCl, and eluted through quartz glass columns impregnated with HDEHP, thereby separating the Sm from the Nd. The solutions were then evaporated to dryness.

Nd and Sm were loaded on Ta filaments, and run in double Ta-Re filament configuration. Analyses were performed on a Finnigan MAT 262 TIMS, running in dynamic mode for collection of the ^{143}Nd/^{144}Nd ratio, and in static mode for all others. The following ratios were obtained for Nd analyses:
^{143}Nd/^{144}Nd: The radiogenic isotope over the stable isotope, the ratio of interest.
^{146}Nd/^{144}Nd: This is fixed because they are both stable isotopes, thus we estimate its ratio using the natural abundance. The degree to which it diverges from the natural abundance is the machine's mass bias. We apply a Rayleigh fractionation law then to predict what the mass bias is for the ratio of interest ^{143}Nd/^{144}Nd.

$^{150}Nd/^{144}Nd$: This ratio quantifies the concentration of Nd in the sample by isotope dilution, as ^{150}Nd is the enriched spike isotope.
Similarly, for Sm:
$^{152}Sm/^{149}Sm$: This ratio also acts to correct for mass bias, assuming the Rayleigh fractionation law.
$^{147}Sm/^{149}Sm$: The enriched isotope spike (^{147}Sm) compared to a stable isotope whose abundance is unchanged (^{149}Sm) is used to calculate the Sm concentration by isotope dilution.
Corrected values are derived via the method of Wade et al., (2008).
The international Nd machine standard, JNDi-1 (Tanaka et al., 2000), yielded an $^{143}Nd/^{144}Nd$ value of 0.5120767±0.0000070 (2σ) (n=1) (accepted value = 0.512115±0.0000070 (2σ); last 10 analyses in lab = 0.5120697±0.0000061 (2σ)).
The BHVO-2 standard gave a value of 0.512993±0.0000076 (2σ) (accepted value = 0.512980±0.000012 (2σ)) while BCR-2 yielded 0.512480±0.0000300 (2σ) (accepted value = 0.512636±0.0000020 (2σ)).
The blank values returned were 113pg for Nd and 37pg for Sm, respectively.
Depleted mantle model ages used in this study were calculated from the corrected $^{143}Nd/^{144}Nd$ ratio, and the $^{147}Sm/^{144}Nd$ ratio from Workman and Hart (2005).

The Sr fraction was loaded on a Ta filament, and run in a single filament configuration. Analyses were performed on a Finnigan MAT 262 TIMS, running in dynamic mode. The following ratios were obtained during a typical analysis:
$^{87}Sr/^{86}Sr$: The radiogenic isotope over the stable isotope, the ratio of interest.
$^{88}Sr/^{86}Sr$: Two stable isotope ratios which enable correction for the mass bias of the TIMS, always following correction using the Rayleigh fractionation law.
Additionally, the $^{85}Sr/^{87}Sr$ ratio is monitored in order to ensure there is no excess Rb which may interfere with the analysis.
The strontium standard, SRM-987, (Moore et al., 1982), returned a value of 0.7102528±0.0000217 (2σ) (n=6) (accepted value = 0.71034±0.00026 (2σ)).
The BHVO-2 standard gave a value of 0.7034734±0.0000136 (2σ) (accepted value = 0.703469±0.000017 (2σ)) while BCR-2 yielded 0.7050055±0.0000143 (2σ) (accepted value = 0.70500±0.00003 (2σ)). The total analytical blank indicated that the background concentration associated with the method was 719pg.
Depleted mantle model ages used in this study were calculated from the $^{87}Sr/^{86}Sr$ ratio, and the $^{87}Rb/^{86}Sr$ ratio from Workman and Hart (2005).

Chromatography and TIMS – U,Th/Pb

The following procedure is taken from Elburg and Dougherty-Page (1997). The remaining half of the 2ml 2M HCl solution is dried down and the residue re-dissolved in 1.3ml 0.6M single-distilled HBr and left, capped, at 140°C overnight. The solutions are eluted through anion exchange columns, Dowex AG1-X8 200-400 mesh, which is re-filled for each sample. The highest partition coefficient of Pb for the resin is ≈1000 at 0.6M HBr (Manton, 1988). Since the samples contain more than 1wt% $FeO^{(T)}$, a second pass through the columns is recommended, given that iron inhibits the ionisation of lead.

The Pb fraction is dried down and loaded onto a Re filament, and run in a single Re set-up. Analyses were performed on a Finnigan MAT 262 TIMS, running in static mode. The isotopic ratios of interest collated were $^{206}Pb/^{204}Pb$, $^{207}Pb/^{204}Pb$, $^{208}Pb/^{204}Pb$, which are produced from the radioactive decay of ^{238}U, ^{235}U and ^{232}Th, respectively.
Given that Pb doesn't have enough stable isotopes to correct for fractionation, the correction is empirical, and based on analysis of the standard, NBS SRM 981 (Todt et al., 1996). Therefore, the running conditions of the samples should match those of the standard, whose isotopic composition

is characterised for running temperatures of 1150°C. The correction is linear, based on the deviation of the measured value from the accepted values of Todt et al., (1996).

$$AMU\ \%\ Mass\ Fractionation = \frac{1}{x}\left(\frac{\left(\frac{^{204+x}Pb}{^{204}Pb}\right)_{accepted} - \left(\frac{^{204+x}Pb}{^{204}Pb}\right)_{measured}}{\left(\frac{^{204+x}Pb}{^{204}Pb}\right)_{measured}}\right) \quad (1.1.)$$

Once the mass fractionation per atomic mass unit has been quantified for the standard (where x is equal to 2, 3 or 4 for ^{206}Pb, ^{207}Pb and ^{208}Pb), this fractionation factor may be used to predict the corrected isotopic composition for the samples, assuming the running conditions were identical.

$$\left(\frac{^{204+x}Pb}{^{204}Pb}\right)_{corrected} = \left(\frac{^{204+x}Pb}{^{204}Pb}\right)_{measured} \times (1 + AMU\% \times x) \quad (1.2.)$$

The average (n=2) SRM-981 ratios obtained were ^{206}Pb/^{204}Pb = 16.9040±0.0057, ^{207}Pb/^{204}Pb = 15.4477±0.0053, ^{208}Pb/^{204}Pb = 36.5604±0.0126. This compatres with the accepted values to which the data was corrected: ^{206}Pb/^{204}Pb = 16.9356, ^{207}Pb/^{204}Pb = 15.4891, ^{208}Pb/^{204}Pb = 36.7006±0.003 (Todt et al., 1996).
The procedural blank levels were moderately high at 3245pg (3.245ng), which represents ≈0.3% of the mass fraction of the analysed sample (≈1µg).

1.7. Stable Isotope Geochemisty – Fe Isotopes - MC-ICP-MS

Wet Chemical Purification

Approximately 5-10mg of finely ground rock powder representative of the sample underwent acid dissolution in a mixture of 1ml 10M HCl, 0.5ml 48% HF, and 0.2ml of 15M HNO_3, and heated at 80°C in Teflon beakers, until complete dissolution was achieved. During evaporation, aliquots of 15M HNO_3 were added to prevent the formation of insoluble fluorides. After attaining dryness, the solution was taken up in 2ml 6M HCl, before being evaporated off and dissolved in 0.5ml 6M HCl in readiness for the columns. At 6M HCl, the partition coefficient for Fe^{3+} for the resin is $D^{Fe}_{Resin-HCl}$ > 1000 (Strelow, 1980; Anbar, 2000).

The solutions were then subjected to anion exchange chromatography using columns packed with AG1-X4 200-400 mesh resin, whose lower cross-linked mesh is preferable to AG1-X8 owing to its more efficient separation of Co and Cu from Fe (Poitrasson and Freydier, 2005). Despite this, neither resin discerns between Zn and Fe effectively. However, the concentration ratio of Zn/Fe was sufficiently low (Zn/Fe <<< 2; see Schoenberg and von Blanckenburg, 2005 and Dauphas et al., 2009b) that it would not affect the analyses. Therefore, samples were eluted with 5x0.5ml 6M HCl (matrix elution), and Fe collected with 4x0.5ml 0.05M HCl. The quantitative elution of Fe must be ensured, as any remnant Fe on the columns may result in fractionation, especially at acid molarities >1M (Anbar et al., 2000). The ensuing solution was evaporated and then dissolved in 5ml 0.05M HCl and diluted to ≈4.5ppm for running with H-cones or ≈1.5ppm using the X-cones.

MC-ICP-MS

All analyses were performed on a ThermoFinnigan Neptune MC-ICP-MS housed at the CSIRO/University of Adelaide, Waite Campus. The preferred sample introduction mechanism utilised

a low-flow 50µl/min PFA nebuliser in conjunction with a coupled quartz glass spray chamber and Scott Double-Pass assembly. The set-up facilitates greater stability and fewer nitride interferences with respect to desolvating nebulisers (Weyer and Schwieters, 2003; Dauphas et al., 2009b). However, the arrangement used does not appreciably reduce ArN and ArO interferences; hence the samples were run in a 0.05M HCl medium in aid of this. Despite such safeguards, these marginally higher mass-number interferences persist, necessitating the use of the medium-resolution entrance slits (opening width = 30µm), which control the profile of the beam prior to its entrance to the electrostatic analyser, in order to resolve between the interferences and the desired Fe masses. High resolution slits were superfluous because sufficient mass resolution was obtained in MR mode, sensitivity decreases by a factor of 2, and the HR slits are more prone to degradation. In medium resolution, the resolving power, $\left(\frac{m}{m(95\%)-m(5\%)}\right)$, was approximately 7000, and the Fe masses appear as curtailed flat-topped plateaus, on the low-mass side of the ArO and ArN interferences. The plateau width, measured on the smallest plateau, ^{56}Fe, was ≥200ppm (*figure 1.1.*), where the plateau width ppm is $\frac{m_{high}-m_{low}}{m_{centre}} \times 10^6$ (Poitrasson and Freydier, 2005).

Measurements were performed in static mode (no amplifier rotation), with the simultaneous measurement of 7 masses: L4-^{53}Cr, L2-^{54}Fe, L1-^{56}Fe, C-^{57}Fe, H1-^{58}Fe, H2-^{60}Ni, H4-^{61}Ni. Before each solution (be it sample or IRMM-014 standard), an on-peak zero correction was analysed, the ion beams of which were subtracted from the sample voltage for a given isotope. Each cycle consists of a 3s idle time with an 8.389s integration time, 45 of which constitute one analysis. In accord with Schoenberg and von Blanckenburg, (2005) and Dauphas et al., (2009b), the concentration of the sample with respect to the standard, $\left(\frac{C_{sample}}{C_{standard}} - 1\right) \times 100$, were typically matched to within 10%.

In spite of the small relative mass difference between ^{61}Ni and ^{60}Ni, in addition to the inability to obtain δ^{58}Fe data, a nickel spike was added to standards and samples in order to quantify and correct for mass bias. Even though the sample and skimmer cones are manufactured from Ni, they are estimated to have a minimal contribution to the measured ^{61}Ni/^{60}Ni ratios (Dauphas et al., 2009b). These deficiencies are outweighed by obviating the need for peak-jumping (as per Cu spiking) and the greater similarity in the masses of Ni and Fe compared to Cu (i.e., $\beta^{Fe} \approx \beta^{Ni} \neq \beta^{Cu}$).
Usual beam sizes were ≈1V on ^{57}Fe and 45V on ^{56}Fe, in addition to ^{61}Ni being kept at ≈1V. Consistent with Poitrasson and Freydier (2005), improving the standard deviation for ^{61}Ni/^{60}Ni measurements by increasing the strength of the Ni signal has a marked influence on the precision of the Ni-corrected $\delta^{57(56)}$Fe ratios, exhibiting an approximately positive linear relationship. Assuming the exponential mass-bias correction law, raw $^{57(56)}$Fe/^{54}Fe data were corrected according to the relationship:

$$\left(\frac{^{57}Fe}{^{54}Fe}\right)_t = \left(\frac{^{57}Fe}{^{54}Fe}\right)_m \times \left(\frac{M^{57}Fe}{M^{54}Fe}\right)^{\beta^{Fe}} \qquad (1.3.)$$

Where β^{Fe} is the machine's fractionation factor for ^{57}Fe. For a given analysis, this is replaced with β^{Ni} (assuming $\beta^{Ni} \approx \beta^{Fe}$), giving the equation:

$$\left(\frac{^{57}Fe}{^{54}Fe}\right)_t = \left(\left(\frac{^{57}Fe}{^{54}Fe}\right)_m \times \frac{56.935396}{53.939612}\right)^{\frac{\ln\left(\frac{Ideal\ \frac{^{61}Ni}{^{60}Ni}}{\left(\frac{^{61}Ni}{^{60}Ni}\right)_m}\right)}{\ln\left(\frac{60.931059}{59.930789}\right)}} \qquad (1.4.)$$

Every sample was bracketed by the international standard, IRMM-014, which has an approximately chondritic isotopic composition. Each analysis quoted is therefore comprised of a sample measurement bracketed by two standard measurements, which are each in turn bracketed by two on-peak zero measurements, resulting in an analysis time of ≈15 minutes.

$$\delta^{57}Fe^{sample} = \left(\frac{\left(\frac{^{57}Fe}{^{54}Fe}\right)_t^{sample}}{\frac{\left(\frac{^{57}Fe}{^{54}Fe}\right)_t^{IRMM-014(1)} + \left(\frac{^{57}Fe}{^{54}Fe}\right)_t^{IRMM-014(2)}}{2}} - 1 \right) \times 1000 \quad (1.5.)$$

Each sample was run between 3-7 times, and the accuracy of the technique was assessed by running total analytical passes of the Haematite internal standard (ETH, Zürich), which was measured several times over the course of an analytical session.
The procedural and acid blanks were indistinguishable, and were 10^4 smaller than the measured sample beams, hence contributing to <.01% of the signal during a typical analysis, and subsequently considered negligible.

Uncertainties are given using the student's t-test, which takes into account the standard deviation and the number of repetitions for each sample.

$$2\sigma = Student's\ T = \frac{multiplier * standard\ deviation}{\sqrt{no.of\ repetitions}} \quad (1.6.)$$

Where the multiplier is dependent on the number of reptitions and the confidence interval specified (in this case, 2σ or 95% confidence).

Quantification of Data Accuracy
Variations in natural stable iron isotopes obey mass-dependent fractionation laws in most circumstances (e.g. Maréchal et al., 1999). The expected mass-dependent fractionation behaviour of isotopes reported with two or more isotopes, in this case, $^{57}Fe/^{54}Fe$ and $^{56}Fe/^{54}Fe$ can be predicted by numerical considerations.

The slope in *figure 1.2.* corresponds to the relative difference between the two masses as predicted by the exponential mass-dependent fractionation law:

$$Theoretical\ Slope = \frac{\ln\left(\frac{M^{56}Fe}{M^{54}Fe}\right)}{\ln\left(\frac{M^{57}Fe}{M^{54}Fe}\right)} = .67202 \quad (1.7.)$$

The fit of the linear equation obtained shows perfect agreement with that of Poitrasson and Freydier (2005), using the same wet chemical techniques, instrumentation and analytical procedure. Such a plot signals the absence of polyatomic interferences, though it does not preclude a systematic mass bias shift parallel to the slope of the line (different intercept).

When corrected for instrumental mass bias and interferences, the retention of a slope similar to that delineated by the uncorrected ratios, and an intercept of 0 suggests the robust correction of raw $^{57,56}Fe/^{54}Fe$ ratios for mass bias using the $^{61}Ni/^{60}Ni$ correction technique outlined (*figure 1.3.*).

2.0. General

2. 1. Geological Setting

2.1.1. KI Basalts

The basalts of Kangaroo Island are preserved as near 20m-thick flows which are characterised by columnar jointed bases, and capped with pillow-like tops. The basalts occur near the Kingscote area (*figure 2.1*.), and appear to be eroded remnants of formerly more extensive extrusive flows, based on the uniform structural and topographic elevation of the flows. The basalt invariably unconformably overlies pale, metre-scale cross-bedded clay and gravel-rich conglomeritic sands of fluviatile origin. These sediments are highly leached and kaolinitised, and also contain ferruginous concretions near Beatrice Point (*figure 2.1*.). This sedimentary package is a part of the more widespread glacigene sediments of the Permo-Carboniferous Cape Jervis Formation, which is up to ≈300m thick on Kangaroo Island (Bourman and Alley, 1999). McDougall and Wellman (1976), conducted K-Ar dating of the basalts, which yielded a Jurassic age for their emplacement (170±5Ma). In a survey of Kangaroo Island (Wisanger) Basalts, Milnes et al., (1982), also noted the occurrence of similar mafic composition of purported Mesozoic age along the southern contintental margin of Australia, in the Polda and Otway basins. This suggests that Jurassic magmatism associated with the Ferrar large igneous province may be more voluminous than recorded by the Kangaroo Island Basalts and the Tasmanian Dolerites.

2.1.2. Tasmanian Dolerites

Red Hill is a rare region of the extensive Tasmanian Dolerites which exhibits a continuum of compositions ranging from mafic dolerites to alkali-enriched granophyres, and is located near the settlement of Snug, 25km SSW of Hobart (*figure 2.2.*). The Tasmanian Dolerites comprise a relatively minor component of the Jurassic Ferrar large igneous province which stretches across the Transantarctic Mountains, and has a magmatic volume of ≈$0.5x10^6$ km^3 (Condie, 2001). The Tasmanian portion, by contrast, with an estimated volume of 15,000km^3, covers an area of 30,000km^2; much of eastern Tasmania. Its large areal extent is a product of uplift penecontemporaneous with emplacement and subsequent resistance to erosion.

The magmas were emplaced almost entirely within the confines of the Carboniferous-Triassic Parmeener Supergroup, with little in the underlying basement rocks. The structure of western Tasmania is comprised of two Precambrian basement blocks, which largely consist of metamorphosed sedimentary sequences with minor amphibolites (Hergt et al., 1989a). The Precambrian basement is overlain by Ordovician-Devonian sediments, and the entire block is intruded by granitic rocks which are largely Palaeozoic in age (Precambrian intrusions are restricted to King Island). The two separate basement provinces may also be subdivided geochemically on the basis of the chemistry of their constituent granites, which has been used to infer that the blocks were subjected to differing geological histories.

If Tasmania does indeed comprise two microplates, then they must have been conjoined by the Late Carboniferous, perhaps along the Tamar Fracture System, a major tectonic lineament between western and eastern Tasmania. The evidence for this is the continuity of the Parmeener Supergroup across both terranes, the deposition of which commenced in the Late Carboniferous (Clarke and Banks, 1975). The main depocentre was situated along the axis of this postulated Tamar Fracture

System (Seymour and Calver, 2001). The Lower Parmeener Supergroup consists of dominantly glaciogenic and shallow water periglacial rocks unconformably overlying the aforementioned basement, and extending with a vertical relief of near 1000m. By contrast, the Upper Parmeener Supergroup is a non-marine succession, reflective of relative regression and/or eustatic sea level drop. Sedimentary sequences are initially quartzofeldspathic, but prograde into conglomeritic units before giving way to sandstone-coal associations. The Upper Parmeener Supergroup is between 450 and 600m thick, and its deposition took place between the Late Permian and Late Triassic, with the youngest succession being constrained by K-Ar dating on biotite in a tuff layer with an age of 214±1Ma (Seymour and Calver, 2001).

2.2. The Red Hill Intrusion

2.2.1. Structure

The Red Hill intrusion is sheet-like in form, with vertical columnar jointing indicating cooling perpendicular to the contacts with the largely flat-lying Carboniferous-Triassic sediments of the Parmeener Supergroup, although the base or top of the sequence are unexposed. In general, the sheet is transgressive through the sedimentary sequence from east to west, and the dolerite in the area comprises part of a single body (McDougall, 1962). The sheet is a total of 400m thick, and to the south, is characterised by protruding cupola structure (*figure 2.2.*), which hosts a considerable portion of differentiated granophyre (almost 200m; McDougall (1962)). The cupola structure is about 1.5km wide, reaches an elevation of ≈420m above sea level, whose north-south striking products are preserved on a number of hills, from north to south; Hickman's Hill, Red Hill and O'Brien's Hill, each containing domains of differentiated granophyres (*figure 2.2.*).
The sedimentary rocks are concordant around the margins of the intrusion, evidencing that the magma was emplaced by uplift of the roof rather than by horizontal dilation and stoping of the sediments, which have subsequently been removed by erosion (McDougall, 1962).

2.2.2. Contacts

The contacts on the margins of the intrusion are extremely abrupt and invariably juxtapose fine-grained dolerite against Parmeener Supergroup sedimentary rocks which, in the Red Hill region, range from mudstones and sandstones to calcareous limestone. The dolerite composition is fine-grained owing to quenching against the cool sediments, and therefore approximates the initial composition of the intruded liquid. The sediments themselves show little evidence of assimilation into the melt, but are hornfelsed a few metres from the contact of the sheet. The limited extent of the metamorphic aureoles as well as the absence of any interaction between catalysing fluids derived from the crystallising magma suggest relatively cool wall rocks and therefore high structural levels. Given that chilled margins line the walls of the intrusion, it is likely that the remaining volume of liquid was effectively shielded from any interaction with the surrounding sedimentary rocks. Therefore, the system remained closed to any external fluctuations in oxygen fugacity, in addition to chemical input from other batches of magma or crustal assimilation. Such a history is supported by the coherent chemical trends delineated by the chilled dolerite (which is homogeneous over much of Tasmania; Hergt et al., 1989a; Hergt and Brauns, 2001) and its differentiates (*section 4.0.*).

2.2.3. Stratigraphy

Rocks preserved at Red Hill generally become more differentiated moving up through the stratigraphy. At low elevations (e.g. where the Snug River has cut into the surrounding dolerite), the compositions are more mafic, consisting of augite-pigeonite-plagioclase, with some degree of pyroxene accumulation present. The medium-grained dolerites are gradationally ceded by dolerites also containing quartz, and whose feldspars are tinged with green indicating an increasing alkalic character. The dolerite becomes coarser-grained and attains a spotty texture upon the crystallisation of fayalite, which is surrounded by iron oxides in a quartz-feldspar groundmass. The most differentiated granophyres, invariably present at the highest stratigraphic levels of the intrusion, defining hills in the area, are typified by coarse-grained elongate, dendritic pyroxenes set in granophyric quartz-alkali feldspar intergrowths. The succession lacks any modal layering, which precludes any preferential crystal settling over the time scale of crystallisation. This is probably due to the relatively small size of the intrusion (≈400m), such that convection currents were unable to establish themselves, and that the initial magma did not carry appreciable phenocrysts (Marsh, 2007).
Pegmatitic segregations, which sometimes coalesce to form veins, are associated with typical fine-medium grained dolerite, and are present throughout the intrusion. These regions represent coarse-grained, volatile and alkali-enriched regions of magma that, owing to viscosity differences, have mixed incompletely with the bulk magma. The fact that they are chemically similar to their host dolerites (*section 4.0.*) suggests that they crystallised *in-situ* and did not migrate to areas of low pressure such as a fracture in the crystal mush. The formation of pegmatites within the intrusion highlights the inability for these patches of melt to escape the crystallising body, as may have been possible had the intrusion not been protected from the sedimentary wall rocks by a carapace of chilled dolerite.

2.3. Petrography

The Red Hill sequence consists of a well-preserved succession of two pyroxenes and plagioclase-dominated, medium-grained doleritic rocks which occupy the lower portion of the sill (*figure 2.8.*). Pyroxenes in these rocks are distinctly normally zoned (Fe-Mg), as is the plagioclase (Ca-Na), which is relatively calcic in character. However, a broad gradational divide exists between the lower and upper parts of the intrusion, as demarcated by the appearance of fayalite and magnetite in the fayalite granophyres (*table 2.1., figure 2.8.*). These rocks, and the more differentiated granophyres, lack zoned feldspar or pyroxene, and rather tend to smaller proportions of a single, iron-enriched pyroxene of the augite series (hedenbergite). Quartz and alkali feldspar are the most volumetrically significant phases, whilst iron oxides (largely magnetite) are also quite abundant.

2.3.1. Chilled Dolerites and KI Basalts

This rock occurs at the contacts of the intrusion, and may extend for several to tens of metres inboard of them. The groundmass consists of An-rich plagioclase microlites, with interstitial ilmenite, and three pyroxenes. Orthopyroxene occurs as microphenocrysts (up to 0.6mm), unzoned En_{83} (*figure 2.3.*), while augite (Di_{83}) and plagioclase are also rare phenocryst phases, with pigeonite occurring exclusively in the groundmass. Plagioclase phenocrysts are lath-shaped to swallow-tailed reflecting rapid cooling, and mildly zoned, ranging from An_{86}-An_{60}, while groundmass plagioclase may be as sodic as An_{42}. Interstitial granophyric intergrowths of alkali-feldspar and quartz are present, but constitute <1% of the rock. This is representative of a highly differentiated liquid, which trends towards the Albite-Orthoclase-Quartz eutectic at low temperatures (e.g. Tuttle and Bowen, 1958; Carmichael et al., 1974).

Kangaroo Island basalts share the same characteristics, but rather than granophyric intergrowths, preserve trapped interstitial melt of an iron-rich composition (cf. Milnes et al., 1982). The crystalline phases tend to show less variation to Fe-rich compositions, while the preservation of glass attests to their slightly quicker cooling regime. Plagioclase phenocrysts extend to slightly higher values, An_{89}, and are relatively homogeneous, trending down to An_{80} for the phenocrysts, and An_{65} in the groundmass.

Orthopyroxene phenocrysts are rimmed by Fe-rich augite (Di_{60}) in both the chilled dolerites and KI Basalts. Phenocryst phases comprise about 5% of the rock and are euhedral in habit, showing no evidence of resorption.

2.3.2. Dolerites and Quartz Dolerites

Progressively further from the margins, grain size increases and the dolerites assume a more mottled texture characterised by pyroxene agglomerates and a blue-grey plagioclase-rich groundmass. The dolerites, and subsequently, dolerites containing cumulus quartz (as opposed to granophyrically intergrown quartz-alkali feldspar), exhibit a sub-ophitic to ophitic texture in which the pyroxenes partially, and sometimes completely, envelop smaller plagioclase laths.
These intermediate dolerites lack orthopyroxene, which has been replaced by pigeonite. Pigeonite and augite are typically found in cumulophyric clusters, with pigeonite coring the augite at times (*figure 2.4b*). The truncation of crystal zones at the core of these clusters insinuates a coupled growth history, perhaps due to synneusis of nascent nuclei, owing to the lower free energy of the shared crystal face (e.g. Vernon, 2004). Both clinopyroxenes exhibit an elongate habit, which trends to feathery in some examples, sometimes reaching 1cm in length. Plagioclase is considerably smaller, reaching about 5mm in length.

The pyroxene:plagioclase ratio increases with increasing differentiation, beginning at ≈1:1 and reaching 2:1 by the disappearance of pigeonite. As a result of the slow cooling experienced by intrusive rocks, both pigeonite and augite show exsolution along their [001] axis, which, in the case of pigeonite, may occur perpendicular to a simple twin along [100] (*figure 2.4b*). Exsolution along this plane is indicative of both the host and the lamellae being monoclinic pyroxenes, such that augite exsolves pigeonite, and vice-versa. The clinopyroxenes are heavily zoned, with individual grains showing considerable variation, with Mg/(Fe+Mg) ranging from .75 to .30 from core to rim (*figure 2.4b*). Such extreme zonation is also mirrored in plagioclase compositions, the bulk of which is labradorite ($An_{70\text{-}60}$), however a bytownite core (An_{83}) extensively zoned to an oligoclase rim (An_{25}) is not uncommon.

Titanomagnetite joins ilmenite as the oxide phases, but ilmenite is volumetrically more significant. Titanomagnetite appears to be of secondary origin, being an unmixing product of ilmenite during sub-solidus cooling and exsolution-oxidation.

The proportion of granophyrically intergrown alkali feldspar and quartz increases in proportion from the chilled dolerites to the granophyres, and is therefore intermediate in these main sequence rocks, comprising ≈15% of the rock.

Accessory minerals include, but are not limited to, apatite, pyrite and titanite. Apatite occurs as needles forming around pyroxenes, as a response to their rejection of phosphorus during growth. Since P diffuses particularly slowly in silicate liquids due to its tendency to form $PO_4^{3-}M^{3+}$ complexes in the melt (Toplis et al., 1994), apatite crystallisation is enforced through its supersaturation at the crystal-liquid interface (Vernon, 2004; Mallmann et al., 2009).

2.3.3. Fayalite Granophyres

Quartz dolerite, which assumes a distinctly green-grey groundmass, grades into the fayalite granophyres, and delineates a convenient boundary between 'dolerites' and 'granophyres'. The appearance of fayalitic olivine typifies the eponymous fayalite granophyres, which are also marked by increasing proportions of granophyric quartz-alkali feldspar intergrowths, the prevalence of individual cumulus quartz and alkali feldspar, and the disappearance of pigeonite. Clinopyroxene occurs as unzoned brown ferroaugite (Di_{30-20}) (very rarely ferriferous pigeonite), commonly rimmed by vermicular hedenbergite (Di_{15-10}) (*figure 2.5a*). Pyroxenes are small (<2mm) and constitute diminishing proportions of the assemblage, nearing 15-10%, reflecting the considerably larger proportion of iron being incorporated into fayalite and magnetite. Amphibole, whose green-brown pleochroism is suggestive of low Fe^{3+}, is ferroedenite, and tends towards more Fe-rich ferropargasite with differentiation. It also occurs as rims around both ferroaugite and hedenbergite, indicating increasing $X_{H_2O}^{liquid}$, likely in response to its relative incompatibility in earlier phases. The fayalite granophyres also herald the appearance of magnetite, which occurs commensurate with the rising (ferric) iron contents of the magma, and is present as dispersed anhedral grains throughout the rock. Plagioclase, now distinctly more sodic (An_{60-35}) constitutes a much smaller percentage of the rock (20%), with much of the aluminium being taken up in potassium feldspar. Potassium feldspar is present both as discrete, tabular grains (≈3mm) and as acicular, rod-like granophyric intergrowths with quartz, together accounting for 20% of the rock, whereas quartz is nearer to 30%. Fayalite (<5% modal abundance), in its unaltered state, forms large (up to 5mm) yellow euhedral crystals of a homogeneous Fa_{95} composition, however it has become pervaded along fractures by iron-rich alteration phases (laihunite and iron oxides).
Accessory phases also consist of chalcopyrite, as well as pyrite, apatite and zircon.

2.3.4. Granophyres

Alkali feldspar and quartz become more volumetrically signifcant, whereas the only ferromagnesian phases is green hedenbergite (Di_{20-10}), comprising ≈10% of the rock, and forming elongate, feathery crystals (0.1-1cm) reflective of sluggish diffusion kinetics caused by high degrees of undercooling (low temperatures). Another contributing factor is the polymerised nature of the melt, which is highly siliceous, and stifles the diffusion of cations and therefore crystal growth. The pyroxenes are are unzoned, and commonly altered by magnetite which inherits their plumose habit (*figure 2.6a*). Granophyric integrowths, possessing an increasingly higher aspect ratio, are abundant (>50%), while the proportion of plagioclase, now oligoclase-albite (An_{18-2}) continues to decrease (<15%), and both prismatic plagioclase and alkali feldspar become corroded by fine-grained alteration phases.

Notably, the granophyre at Red Hill is distinct from that on O'Brien's Hill. The latter contains pyroxenes, which, while being compositionally similar to those at Red Hill, have a more skeletal habit and do not display any green pleochroism, rather exhibiting a cream colour.

2.3.5. Pegmatitic Dolerites

Pegmatitic dolerites chemically span the entire sequence of differentiated rocks in the intrusion, and exhibit similar bulk and crystal chemistry to their surrounding dolerites. Despite this ostensible similarity, crystal dimensions are enlarged (consistent with the effect of volatiles increasing growth rate whilst inhibiting nucleation), the percentage of granophyric intergrowths dramatically increases regardless of the state of differentiation, and hydrous phases, including primary biotite, are extant. The increased proportion of granophyric intergrowths may reflect the solidus depression induced by

additional water, resulting in relatively more liquid being present at a given temperature. Pyroxenes, even in the more mafic pegmatites, are feathery in habit and may locally exceed 3cm in length, while the plagioclase is of a comparable size (*figure 2.7a*). These characteristics point to the volatile- and K-enriched nature of the pegmatitic dolerites. These dolerites typically form as coarse, initially vein-like segregations, but coalesce to create bands.

3.0. The Mantle Source

Abstract

The Tasmanian Dolerites and Kangaroo Island basalts represent the northernmost expression of the Ferrar Large Igneous Province (LIP), which was emplaced in a short period along a linear-trending belt across the Transantarctic Mountains in the Middle Jurassic (≈180Ma). This widespread tholeiitic magmatism, along with the chemically similar Karoo LIP, marked the first stage of Gondwana continental break-up. The Ferrar magmas are enriched in SiO_2, and depleted in $Fe_2O_3^{(T)}$, Na_2O, TiO_2 and P_2O_5 with respect to oceanic basalts and other Mesozoic continental tholeiites. These major element compositions are indicative of their derivation from a mantle source that has experienced greater degrees of prior melt-extraction than the source of mid-ocean ridge basalts (MORB). The trace element signature of these basaltic rocks is typical of the upper continental crust, whilst their radiogenic isotope systematics point to long time-integrated Rb/Sr, Nd/Sm and U/Pb enrichment in the source. It is demonstrated that the major, trace, and radiogenic isotope characteristics may be reconciled by contaminating a depleted harzburgite source with a small fraction of upper continental crustal sediment. Refertilisation of the source mantle may have conceivably taken place during Cambrian west-directed subduction along the Gondwanan margin, or as a result of lithospheric delamination which marked the termination the Cambro-Ordovician Delamerian-Ross Orogeny. The enriched concentrations of radioactive elements (U, Th, K) in the sediment-affected mantle, along with the incubating effect of a stable continental lid between the Cambrian and the Jurassic, acted to increase subcontinental lithospheric mantle temperatures, and trigger melt production. The melt was subsequently channelled into a linear zone of thin lithosphere, defined by the Delamerian-Ross orogeny which facilitated adiabatic decompression.

3.1. Introduction

The Tasmanian Dolerites and Kangaroo Island Basalts comprise a minor portion of the extensive tholeiitic magmatism associated with the Ferrar Large Igneous Province on Australia and Antarctica. These regions mark the most northerly expression of Jurassic magmatism in Gondwana, and are distinguished from oceanic basalts by their extreme major, trace and isotopic characteristics. This distinctive signature endures from Kangaroo Island, to Tasmania and across the Transantarctic Mountains in the Kirkpatrick Basalts (Elliott et al., 1999) and the Portal Peak Basalts (Hergt et al., 1989b), a distance of more than 4000km, attesting to the homogeneity of the province as a whole (*figure 3.1.*).

Specifically, the Northern Ferrar magmas are depleted in Fe, Ti, Na, K and P; and enriched in Si with respect to other Mesozoic continental tholeiites and oceanic basalts (Hergt et al., 1989a; Hergt et al., 1991; Turner and Hawkesworth; 1995). Despite these refractory major element compositions, the magmas exhibit upper continental crust-like trace element properties. Certain trace element ratios such as Ce/Pb and Nb/U diverge from the canonical estimate expected for mantle-derived basalts (Hofmann, 1997), contrasting with their relatively high Mg#s (58-67) (*table 3.1.*). A crustal input is also corroborated by enriched Sr, Nd, and Pb isotope systematics (Allegre et al., 1982; Hergt et al., 1989a).

To a first order, the major element compositions have become decoupled from their incompatible element signatures, suggesting at least a two-stage evolution for the source of these magmas. Evidently, the seemingly disparate elemental and isotopic traits of the magmas point to crust-mantle interaction during their generation. While the location of this interaction is a matter of debate, the prevailing view is that it occurred via contamination of the mantle source with upper crustal material, due to the following considerations (Hergt et al., 1989a; Hergt et al., 1991; Hergt and Brauns, 2001):

1. The low trace element abundances dictate that the crustal signature be imposed on a source which has already been stripped of its incompatible elements. Contamination of a basaltic melt which already has elevated trace element abundances is inconsistent with the high Mg#s observed, as it would require extensive interaction between surrounding sediments (25-30%) and the magma accompanied with little or no crystal fractionation (Hergt et al., 1991; Molzahn et al., 1996). Furthermore, the parental magma would have to be picritic (49% SiO_2) with 0.35% TiO_2 and have trace element abundances more akin to depleted peridotite.
2. The remarkable homogeneity of the magmas, not only in Tasmania and Kangaroo Island, but across Antarctica is hard to reconcile with crustal-level contamination, given the disparate compositions of crustal rocks in each of these locations.
3. The abrupt magma-country rock contacts and absence of crustal xenoliths in the magmas further argues against any significant interaction with rocks in the crust.
4. Oxygen, a major element in terrestrial magmas, should be sensitive only to wholesale modification of the melt or source. The mantle-like $\delta^{18}O$ ratios of +6‰ (MORB = +5.7‰) preclude any mixing of crustal material, which have compositions between 15-25‰ (Eiler et al., 1997), at the high percentages needed to explain the assimilation-fractional crystallisation model (DePaolo, 1981).
5. Unradiogenic $^{187}Os/^{188}Os$, equivalent to mantle values at the time (≈0.125 at 175Ma) also prohibit any significant assimilation of continental material to the degree required by trace and major element considerations (Brauns et al., 2000; Hergt and Brauns, 2001).

The incumbent model that invokes contamination of the mantle source is much more favourable, as it requires only ≈3% of a sedimentary contaminant (Hergt et al., 1989a; Hergt et al., 1991; Molzahn et al., 1996; Foden et al., 2002) to account for the trace element abundances of the magmas. Additionally, such a scenario is also consistent with their isotopic characteristics, where it may be shown that the continental material must be relatively old; possessing long time-integrated Rb, LREE and U/Pb,Th/Pb enrichment for such a small portion of sediment to confer the evolved isotopic signatures on the mantle source.

While such a scenario is readily acceptable for the petrogenesis of the Tasmanian Dolerites and Kangaroo Island Basalts, specific parameters remain unconstrained:

1. The nature of the mantle source.
   Previous studies invoke a refractory mantle source that was subsequently refertilised (perhaps during subduction processes) with a minor fraction of sediment. However, depleted mantle is expected to be more difficult to melt due to the removal of alkalis and water, both of which act to depress the solidus (Hirschmann et al., 1999a,b), and its bimodal

mineral assemblage (olivine and orthopyroxene). The Ferrar Magmas, and Large Igneous Provinces in general, however, are characterised by high eruption rates (0.1-8 km^3/yr) (Ferrar = 0.4 km^3/yr; Hawkesworth et al., 1999) and voluminous outpourings of magma over a few million years (Coffin and Eldholm, 1994; Elliott et al., 1999). Therefore, an enriched component, such as additional water or mafic eclogite is often cited to reconcile the high production rates of LIPs (Gallagher and Hawkesworth, 1992; Anderson, 1994; Leitch and Davies, 2001; Sobolev et al., 2005) with their major element chemistry. This possibility may be elucidated through the comparison of experimental melts from hydrated, depleted peridotite, eclogite, pyroxenite, as well as thermodynamic models for melting under different conditions using the MELTS formulation (Ghiorso and Sack, 1995; Smith and Asimow,2007).

Additionally, parameters such as temperature and depth of melting, residual mineralogy and oxygen fugacity are poorly known. Such questions are investigated through the assessment of the major and trace element characteristics of the least fractionated magmas (chilled margins and KI Basalts).

2. The mechanism for sediment addition.
   Sediment addition to the source of the Ferrar magmas has typically been modelled assuming bulk sediment-mantle admixture, where the sediment contribution is estimated by Post-Archaean Terrestrial Shale (Hergt et al., 1989a; Molzahn et al., 1996; Foden et al., 2002). However, recent experimental data indicate that sediment melting is widespread in the mantle, even under anhydrous conditions (Rapp et al., 2008; Wu et al., 2009; Spandler et al., 2010). Therefore, it may be more pertinent to investigate the effect of a sediment-derived melt rather than bulk sediment addition.
   Furthermore, there is an increasing inventory of information to support the view that much of the sedimentary package escapes geochemical modification at subduction zones. Such conclusions are substantiated by the chemistry of high pressure and ultra-high pressure metasediments in eclogite terranes (e.g. the Dora Maira), which are analogous to their unmetamorphosed equivalents (Schertl and Schreyer, 2008), as well as evidence for highly channelised flow of fluids in these environments (Bebout, 2007). The fluids themselves are very dilute, as shown in experimental studies (Hermann and Spandler, 2008), and hence only affect the mobility of the large ion lithophile elements (LILE) and U, Th, Pb, B, however only in localised zones. The net result is that sedimentary components should retain their chemical and isotopic signatures into the mantle, and their low solidus temperatures make them a viable metasomatising agent in the mantle (Spandler et al., 2010).

3.2 Major Element Chemistry

The relative abundance of major elements in basalts is controlled by the melting regime of the source mantle (temperature, pressure, fo_2, volatile content) and by the mineralogy of that source (spinel-bearing, garnet-bearing, clinopyroxene-absent, olivine-absent). Notwithstanding the variable conditions conceivable in planetary mantles, major element compositions typically vary within ±30%

between two extremes of typical basalts – alkali and tholeiitic. Variations are usually even more subdued when considering only tholeiitic basalts, such as those found in continental flood basalt provinces, mid-ocean ridges, and some ocean islands. Despite these subtle variations, certain elements behave differently depending on the melting parameters outlined above, and as evidenced through melting experiments on likely source compositions. Potential melt compositions parental to the Ferrar province are assessed in light of such experiments and thermodynamic considerations. Eclogite/pyroxenite-derived experimental melts were taken from (Johnston, 1986; Takahashi et al., 1998; Pertermann and Hirschmann, 2003; Spandler et al., 2008; Lambart et al., 2009) and filtered such that only compositions with similar MgO contents (largely between 5 and 9 wt%) to the Tasmanian chilled dolerites and Kangaroo Island basalts were plotted.

3.2.1 SiO_2

SiO_2 contents of the Northern Ferrar Magmas, at 54±1wt%, are consistently higher than those observed in OIB and N-MORB (*figure 3.2., figure 3.3.*). This Si-enrichment is also a feature of the fractionation-corrected magmas, where SiO_2 = 53±1wt% (see section 3.2.5). $MORB_{8.0.}$ (Workman and Hart, 2005) plots towards lower SiO_2, lower Mg# and higher $Fe_2O_3^{(T)}$. Fractional crystallisation of a gabbroic assemblage (plagioclase, clinopyroxene ± olivine) is expected to produce the opposing effect – that is, it creates melts with lower Mg#, higher $Fe_2O_3^{(T)}$, but higher SiO_2 (*figure 3.2.*). Also plotted is the field of pyroxenite/eclogite melts, which roughly demarcate a trend in Mg#-SiO_2 space perpendicular to that shown by the Ferrar magmas. This is due to the extended stability of garnet, such that low percentage melts are high in SiO_2 (e.g. Yaxley and Green, 1998; Pertermann and Hirschmann, 2003; Spandler et al., 2008) High percentage pyroxenite/eclogite melts have similar Mg# but are lower in SiO_2 than the Ferrar rocks, a product of their protolith's SiO_2 content (≈50wt%).

There are numerous parameters which may influence the SiO_2 contents of derivative magmas.

Pressure and Extent of Melting: Due to the expansion of the pyroxene phase-field at the expense of olivine with increasing pressure owing to its steep Clapeyron slope, the contribution of olivine to the melt increases with pressure. Thus, melts that segregate from their source at a deeper level tend to be silica-poor in comparison to ones from low pressure melting regimes.

Quantitatively, the increase in orthopyroxene stability with pressure can be understood because reaction *3.1.* has a large molar volume change (ΔV_{rxn} = -5.7 cm^3/mol) (Carmichael, 1970, Nicholls et al., 1971). This indicates that the volume of orthopyroxene is smaller than that of olivine and quartz, hence its formation is favoured at higher pressures, and consequently contributes less to melt production. The net result is an increase in $a_{SiO_2}^{liquid}$ with decreasing pressure.

When olivine and orthopyroxene are in equilibrium, as expected in a typical peridotite, the silica activity of the resulting melt will be controlled through the reaction:

$$Mg_2SiO_4 + SiO_2 \rightleftharpoons Mg_2Si_2O_6 \qquad (3.1.)$$

The corresponding equilibrium constant is:

$$K = \frac{(aMg_2Si_2O_6)}{(aMg_2SiO_4)(aSiO_2)} \quad (3.2.)$$

During small-moderate degrees of melting, changes in $a_{Mg_2Si_2O_6}^{orthopyroxene}$ and $a_{Mg_2SiO_4}^{olivine}$ are small, as are the effects of temperature on this equilibrium, and $a_{SiO_2}^{liquid}$ scales inversely with K. Thus, $a_{SiO_2}^{liquid}$ is constant at a given pressure and temperature even though the liquid composition may vary considerably. Since activity is fixed, any changes in liquid silica concentration ($X_{SiO_2}^{liquid}$) must be accompanied by changes in the activity coefficient ($\gamma_{SiO_2}^{liquid}$) and vice-versa, given that:

$$aSiO_2 = \gamma SiO_2 \times XSiO_2 \quad (3.3.)$$

Changing $\gamma_{SiO_2}^{liquid}$ occurs because of increased alkali concentrations in the melt, which is most pronounced near the solidus. Alkalis promote non-ideal mixing of Si-O groups, thereby lowering its activity coefficient, and causing increases in $X_{SiO_2}^{liquid}$ (Hirschmann et al., 1999a). This explains the high SiO_2 contents of very small melt fractions.

Volatile Content: Owing to its low molar mass, even minor amounts of H_2O (wt%) may have a profound impact on melting systematics on a molar basis. During low pressure melting of the mantle, orthopyroxene melts incongruently, producing a melt more siliceous than itself and a solid phase that is less siliceous (olivine). However, due to the increasing stability of orthopyroxene with pressure, this melting behaviour disappears at ≈5 kbars in anhydrous systems (Kushiro et al., 1968). Water, however, acts as a network modifier by depolymerising the melt:

$$H_2O + O^{2-} = 2OH^- \quad (3.4.)$$

The stability of a depolymerised phase, such as olivine, thereby increases at the expense of a more polymerised one, such as orthopyroxene. Therefore, orthopyroxene contributes more to the melt in high-H_2O systems (Kushiro, 1972), and the incongruent melting behaviour of enstatite is prolonged to at least 3 GPa. The greater contribution of orthopyroxene to the melt, which has higher silica contents with respect to olivine (≈55 wt% and ≈40 wt%, respectively (Workman and Hart, 2005)), results in an increase in $X_{SiO_2}^{liquid}$. Water solubility, however, increases with increasing pressure, thus the effectiveness of this change is opposite to that of the pressure effect alone.
Experimental melts from H_2O-undersaturated peridotites show higher SiO_2/(MgO+FeO) than melts at the same conditions for an anhydrous peridotite (Hirose, 1997; Gaetani and Grove, 1998; Parman and Grove, 2004). The suppression of MgO and FeO in hydrous melts derives from the lower average melting temperatures for hydrated peridotites.
Noteworthy is the CO_2 budget, as it tends to decrease SiO_2 contents of mantle-derived melts (e.g. Dasgupta et al., 2007).

Modal Mineralogy: The fertility of mantle peridotite is roughly approximated by the relative abundances of incompatible/compatible elements, for example (Al_2O_3, CaO, Na_2O)/(Cr_2O_3, MgO) (Canil, 2004; Carlson et al., 2005; Lee, 2006). The dominant host for incompatible elements in

peridotite is clinopyroxene, therefore it follows that depleted peridotites are also empoverished in this phase. Melting of anhydrous spinel lherzolites at moderate pressure (1-1.7 GPa) occurs through a peritectic reaction in which clinopyroxene, orthopyroxene and spinel are consumed to produce melt + olivine (e.g. Kinzler and Grove, 1992; Baker and Stolper, 1994; Kinzler, 1997; Wasylenki et al., 2003). At the point of clinopyroxene exhaustion, this reaction changes to OPX ± spinel = Ol + Melt. Typical mantle clinopyroxenes have SiO_2 contents ≈50wt%, while orthopyroxenes are closer to 55wt% (Workman and Hart, 2005). Qualitatively then it can be seen that melts of depleted peridotite, whose contribution is dominated by OPX, will tend to have higher SiO_2 contents (Wasylenki et al., 2003; Parman and Grove, 2004).

In eclogitic or pyroxenitic compositions, however, $a_{SiO_2}^{liquid}$ is not buffered, as olivine is typically absent. The dependence of the SiO_2 content of the melt at consant melt fraction is therefore more sensitive to the starting composition of the eclogite/pyroxenite. In contrast to peridotite, the two dominant minerals in eclogites/pyroxenites above ≈2 GPa are clinopyroxene and garnet (e.g., Kogiso et al., 2004; Downes, 2007). Despite the compositional diversity of high pressure mafic rocks, they may be subdivided into two classes; silica-excess and and silica-deficient. This classification is based on a join that connects the compositions of Calcium-Tschermak's Pyroxene ($CaAl_2SiO_6$) and Enstatite ($Mg_2Si_2O_6$), on a normative CMAS projection (O'Hara, 1968, *figure 3.4.*). Stoichiometric pyroxenes and garnet lie directly on this line, which is in fact a high temperature thermal divide – compositions with lower normative SiO_2 contents plot to the Fo-side (first melt at P), while those with higher SiO_2 plot to the Qtz-side (first melt at E). Subsequent melts are controlled by low temperature eutectics on either side, such that the derivative melts attenuate the variability seen in pyroxenite sources (e.g. Yaxley and Green, 1998; Yaxley, 2000).

The effect of pressure in determining the SiO_2 content of eclogite/pyroxenite melts is deemed to play a subordinate role to the extent of melting (Pertermann and Hirschmann, 2003; Spandler et al., 2008). The behavioural difference as compared to peridotites is attributed to the fact that garnet and clinopyroxene both respond similarly to changes in pressure, unlike olivine and pyroxenes in a peridotitic assemblage. As in peridotite, the SiO_2 contents of eclogitic melts correlate positively to the alkali content of the melt (Pertermann and Hirschmann, 2003). Mass balance dictates that the creation of a silica-rich melt from a basaltic composition must be compensated by a silica-poor residue. Recognising that $X_{SiO_2}^{clinopyroxene}$ is similar in basalts and eclogites, (48-52 wt%), garnet (or amphibole in hydrous systems) is necessarily stabilised in the residue to account for the silica deficit. Thus a high silica melt of eclogitic affinity should possess strong HREE and Y depletion. This is the opposite of peridotitic melts, where siliceous melts are characterised by the absence of a garnet signature due to their segregation from the source at low pressure.

3.2.2 $Fe_2O_3^{(T)}$ -Na_2O-TiO_2

$Fe_2O_3^{(T)}$-Na_2O systematics for the Northern Ferrar Magmas show a relatively constant $X_{Na_2O}^{liquid}$ for variable $X_{Fe_2O_3^{(T)}}^{liquid}$ (*figure 3.5.*). Secondly, the NFMs are displaced towards lower Fe and Na compared to $MORB_{8.0}$. Klein and Langmuir (1987) noted a strong negative correlation between these two elements, and attributed it to depth and extent of melting. Deeper melts are depleted in Na due to

its increasing compatibility in jadeite component ($NaAlSi_2O_6$) of clinopyroxene with pressure (e.g. Blundy et al., 1995). Contrastingly, the predominant host of $Fe^{(2+)}$ in the mantle, olivine, is increasingly stable at lower pressures, hence the X_{FeO}^{liquid} is also function of the Mg# of the source, where high Mg#s would cause resultant melts to be depleted in FeO. Furthermore, because sodium is incompatible during melting, its concentration in the liquid decreases with increasing melt fraction. Therefore, during melting of Depleted MORB Mantle (DMM), one would expect that shallow melts produce low Fe-high Na, and melts that are derived from higher pressures should have high Fe-low Na (Klein and Langmuir, 1987). The fact that the Ferrar melts delineate a trend of low Fe and low Na points to melting regime which is not typical of asthenospheric (DMM) melts such as N-MORB.

Peridotites that are residual from melting are typically lacking in Na_2O (and other incompatibles) in addition to having lower $FeO^{(T)}$ and hence high Mg#s (>90). Hirschmann et al., (1999a) illustrated that large percentage melts of peridotite will have Na_2O contents that reflect their source composition. Similarly, iron content is relatively insensitive to the degree of melting at a given pressure. Melting of highly depleted mantle (moreso than DMM) to moderate-large extents at low pressure may therefore represent a plausible method for generating the Fe, Na depletions observed (e.g. Parman and Grove, 2004).

The low concentration of TiO_2 in the Ferrar magmas is one of their most distinctive characteristics. Like Na_2O, TiO_2 is incompatible during mantle melting, and its major host is clinopyroxene. Considering Ti^{4+} is accommodated in the clinopyroxene structure in charge couplets involving Na^+, Fe^{3+} and Al^{3+}, whose compatibility increases with pressure, it is to be expected that $D_{CPX-Melt}^{Ti^{4+}}$ also increases. Indeed, $Fe_2O_3^{(T)}$-TiO_2 relations are synonymous with $Fe_2O_3^{(T)}$-Na_2O, pointing to similar behaviour during melting. As with Na_2O, melts of peridotite with little clinopyroxene in the source offer a reasonable explanation for depletions in Fe, Na and Ti with respect to MORB and pyroxenite melts.

Pyroxenite melts show a trend towards increasing $Fe_2O_3^{(T)}$ with decreasing TiO_2, as expected when TiO_2 becomes more compatible with pressure, while Fe^{2+} becomes less compatible, as discussed. Rutile may also play a significant role in the TiO_2 budget of the melt, however, its stabilisation is positively dependent on $X_{TiO_2}^{source}$ (Klemme et al., 2002), and therefore is expected to be exhausted quickly in low TiO_2 compositions, as would be anticipated for sources parental to the Ferrar Magmas.

3.2.3 Al_2O_3-CaO

Apparent from the CaO/Al_2O_3-Na_2O array (*figure 3.7.*) is the trend of increasing Na_2O with decreasing CaO/Al_2O_3 defined by all melt compositions. Particularly poignant is the fact that all pyroxenite melts are offset towards higher Na_2O and much lower CaO/Al_2O_3 than the Ferrar magmas or even MORB. Calcium is partitioned strongly into clinopyroxene in the mantle, whereas Al is typically found in an aluminous phase – spinel at low pressure (<2.5 GPa) and garnet at high pressure. X_{CaO}^{liquid} maxima in peridotite-derived melts coincide with the point of clinopyroxene exhaustion (Hirschmann et al., 1999a), after which it is diluted by the contributions of orthopyroxene and olivine to the melt, both of which contain minimal CaO or Al_2O_3.

In contrast to CaO, $X_{Al_2O_3}^{liquid}$ decreases monotonically with rising melt fraction for a given bulk composition. Near solidus, Na_2O is enriched due to its incompatibility, and since Na^+ bonds preferentially with $^{IV}Al^{3+}$ to charge-balance tetrahedral sites, $\gamma_{Al_2O_3}^{liquid}$ is reduced, and hence $X_{Al_2O_3}^{liquid}$ is enriched. In addition, $X_{Al_2O_3}^{liquid}$ is greatest when the spinels are aluminous. This relationship may be quantitatively understood from the following equilibrium:

$$MgAl_2O_4 + \frac{1}{2}Mg_2Si_2O_6 \rightleftharpoons Al_2O_3 + Mg_2SiO_4 \qquad (3.5.)$$

Because depleted mantle has lower Na_2O, and since the spinels are Al-depleted (low Al/(Al+Cr)), their partial melts are depleted in Al_2O_3 and enriched in CaO, leading to high CaO/Al_2O_3 at the same melt fraction. The fact that the Ferrar magmas exhibit greater CaO/Al_2O_3 than MORB at a similar MgO (and melt fraction) insinuates that the former were derived from a more depleted source.

The constituent eclogite/pyroxenite minerals, garnet and clinopyroxene, can be considered rough proxies for Al_2O_3 and CaO respectively. These high pressure mafic rocks are therefore enriched, in absolute terms, in both oxides. The ratio, however, is sensitive to the relative proportions of garnet/ clinopyroxene in the residue of melting. Experiments on natural pyroxenites portray increasing CaO/Al_2O_3 with increasing pressure (Pertermann and Hirschmann, 2003; Kogiso et al., 2004; Spandler et al., 2008; Lambert et al., 2009). This can be accounted for due to the expansion of the garnet phase volume with pressure, and thereby suppressing any $X_{Al_2O_3}^{liquid}$ enrichment. Correspondingly, CaO becomes more enriched at high pressure, as clinopyroxene contributes more to the melt than garnet.
However, owing to the enduring stability of clinopyroxene at most pressures, CaO behaves compatibly throughout the pyroxenite/eclogite melting interval. Given that melts of peridotite (such as MORB) invariably have ≈10wt% CaO (Herzberg, 2006), melts of MORB-like eclogite are characterised by CaO < 10wt% (Pertermann and Hirschmann, 2003; Spandler, 2008; Gao et al., 2008; Herzberg and Asimow, 2008). The Ferrar Magmas have high CaO/Al_2O_3 ratios, more consistent with melts from a depleted peridotite source.

3.2.4 Pyroxenite vs. Peridotite – Element Ratios

Certain pairs of trace elements are often used to search for a specific feature of the source that can be explained by a given component, for example, fractionation of Nb/Ta ratios by rutile, Fe/Mn ratios affected by pyroxenite sources, and P/Nd by nesosilicates.

Fe/Mn, Zn/Fe
The premise for using such ratios is that they are light transition metals with a nominally divalent charge and comparable ionic radii (≈0.8Å), and thus behave similarly during mantle melting (Humayun et al., 2004). The efficacy of Fe/Mn for probing the mineralogy of the source lies in its variable $K_D{}^{Fe/Mn}_{Min-Liq}$ between different mantle phases. The relative compatibility of Fe and Mn are broadly described below:

$$K_{D\,Ol-Liq}^{Fe/Mn} > K_{D\,Bulk-Liq}^{Fe/Mn} \approx 1 > K_{D\,OPX-Liq}^{Fe/Mn} > K_{D\,CPX-Liq}^{Fe/Mn} > K_{D\,Gt-Liq}^{Fe/Mn}$$

While these characteristics aid in identification of the character of the source mantle, the Fe/Mn ratio of a melt may be changed through crystal fractionation. Generally, olivine fractionation will decrease Fe/Mn and $FeO^{(T)}$, whilst clino- and orthopyroxene will impart the opposite effect. Following the considerations section 3.2.5, the Fe/Mn of the Ferrar magmas is taken to be representative of the magma when last in equilibrium with its mantle source.

Upon inspection of the Fe/Mn ratios (*table 3.2.*), the Ferrar magmas, show distinctly lower values relative to MORB, OIB, and depleted mantle. Likely mechanisms for fractionating Fe/Mn may include:

1. Pyroxenite-rich lithologies (e.g. Sobolev et al., 2007) or olivine-rich lithologies. Melting residua dominated by one or two constituent phases may impose a distinctive Fe/Mn ratio on the derivative melts. Realising that $K_{D\,CPX-Liq}^{Fe/Mn}$ and $K_{D\,Gt-Liq}^{Fe/Mn}$ are both <1, residual clinopyroxene and garnet in the source requires elevated Fe/Mn in the melt, by mass-balance. Such is the prevailing view on the elevated Fe/Mn of OIB lavas. Conversely, if the source retains olivine in the residuum, then, because it partitions Fe preferentially to Mn, the melts should have lower Fe/Mn ratios.
2. Higher oxidation state or deeper melting. According to studies on the oxygen fugacity of peridotite xenoliths (Frost and McCammon, 2008, and references therein) most record fo_2s between QFM and QFM-1, constrained by the activity of Fe^{3+} in mantle phases. This is equivalent to a typical $Fe^{3+}/\Sigma Fe_{melt} \approx 0.1$, consistent with the observation of the constant $Fe^{3+}/\Sigma Fe$ in MORB at 0.12 (QFM-0.41±.43) (Bezos and Humler, 2005). Given that Fe^{3+} is more incompatible than Fe^{2+} as its ionic radius is too small for the VI-fold M1 and M2 sites of olivine and pyroxene, the Fe/Mn ratios of melts from high fo_2 sources may be expected to be higher, since Mn is invariably divalent at mantle fo_2s. This is not borne out, however, because OIBs display higher Fe/Mn despite having lower (but variable) $Fe^{3+}/\Sigma Fe$ (Qin and Humayun, 2008). Deeper melting in the garnet stability-field may also fractionate Fe/Mn owing to the lower compatibility of Fe^{3+} relative to spinel. This effect may be small, because OIBs also display elevated Zn/Fe ratios (*table 3.2.*).

While Fe/Mn may be informative, coupling this data with Zn/Fe ratios renders possible a more complete treatment of the conditions of melting. Because olivine and orthopyroxene dominate the Zn and Fe budgets of peridotite (>95%, Le Roux et al., 2010), clinopyroxene contributes very little, and hence Zn/Fe is not an effective tracer of lherzolite vs. harzburgite lithologies. However, it is particularly powerful for discerning between peridotite and pyroxenite, based on the variance in $K_{D\,Min-Liq}^{Zn/Fe}$ for CPX and garnet compared to olivine and orthopyroxene. Additionally, Zn/Fe is insensitive to olivine or orthopyroxene fractionation, since their $K_{D\,Min-Liq}^{Zn/Fe}$ is ≈1.

With knowledge of $K_{D\,Min-Liq}^{Zn/Fe}$ and $K_{D\,Min-Liq}^{Fe/Mn}$, we can model melting of heterogeneous source lithologies and calculate the Zn/Fe and Fe/Mn of the melts created. This does however assume that $K_{D\,Source-Liq}$ stays constant throughout the melting history, which of course it does not. However,

in a typical peridotite-melting case, clinopyroxene is removed preferentially, thus $K_{D\,Source-Liq}$ would be expected to increase for both Zn/Fe and Fe/Mn, thereby decreasing those ratios in the melt. Thus, the estimates here place an upper bound on the expected ratios derived.
Zn/Fe of pyroxenites is highly variable (6-11, up to 17) (Le Roux et al., 2010). However, if their melting is controlled by garnet-clinopyroxene, then the Zn/Fe and Fe/Mn will be much higher than their source ratios. Since garnet is the typical liquidus phase for all pyroxenites (Pertermann and Hirschmann; Kogiso et al., 2004), the removal of clinopyroxene will further decrease $K_{D\,Source-Liq}$ as melting proceeds. Thus, unlike peridotite models, the estimates are minimum bounds.

Upper crustal contamination shouldn't have much of an effect on the ratios, given its very small proportion in the source region of magmas (<5%) and the comparable concentrations of Zn and Fe with depleted mantle. The general form of the calculation is:

$$\left(\frac{Zn}{Fe}\right)_{melt} = \frac{\left(\frac{Zn}{Fe}\right)_{peridotite}}{K^{Zn/Fe}_{D(\frac{peridotite}{melt})}} \qquad (3.6.)$$

In addition to the $K_{D\,Min-Liq}$ values from *table 3.2.*, the parameters and results for various types of source lithologies are presented in *table 3.3.* and in *figure 3.8.*

The Ferrar melts show Zn/Fe and Fe/Mn systematic clearly distinct from those of pyroxenite melts, and are even lower than those of typical MORB-source depleted mantle (DMM Gt-Peridotite). Only OIB lavas show Zn/Fe and Fe/Mn ratios similar to those of pyroxenite melts (e.g. the Cape Verde Islands with Zn/Fe up to 16 and Hawaii and Reunion with Fe/Mn > 65), consistent with the possibility of involvement of recycled oceanic crust (eclogite) in their source.
The Ferrar melts delineate a trend to decreasing Fe/Mn with decreasing Zn/Fe, with the KI Basalts being slightly more primitive (*figure 3.8.*). This tendency is expected for fractionation of pyroxene, which have $K_{D\,Min-Liq}$ < 1 for both ratios. Most ratios are clustered between depleted, cratonic mantle and DMM, perhaps implying a depleted composition intermediate between these two, as approximated by the OPX-enriched peridotite.

3.2.5 Primary Magma Calculation

Having established that it is unlikely that the Northern Ferrar magmas are products of high degree melts of silica-excess eclogite/pyroxenite, whose primary liquids may be expected to have low Mg#s (<70), and since they display Mg#s lower than that expected for melts in equilibrium with mantle olivine, some degree of crystal fractionation must have occurred to propel the compositions to more evolved values. The ubiquitous presence of plagioclase, low-Al pyroxenes (+/- olivine) as the dominant phenocryst phases bears out this widely accepted notion that CFBs undergo low pressure fractionation (Cox, 1980).

The composition of olivine in equilibrium with a melt with a given Mg# may be calculated using known exchange coefficients for Fe and Mg between the two phases. The relationship can be written as:

$$K_{D}{}^{Mg-Fe}_{Ol-Liq} = \frac{X^{Mg}_{Liq}/X^{Mg}_{Ol}}{X^{Fe^{2+}}_{Liq}/X^{Fe^{2+}}_{Ol}} \quad (3.7.)$$

Roeder and Emslie (1970) contended that the equation is independent of temperature, resulting in a constant value of $K_{D}{}^{Mg-Fe}_{Ol-Liq} \approx 0.3$. Subsequently, however the value was shown to vary with temperature, pressure, and the compositions of olivine and liquid, ranging between 0.17 and 0.45 (Toplis, 2005). Silica and alkali content appear to exert the strongest influence on the parameter, while increasing pressure increases the K_D, and temperature has the opposite effect. For simplicity, however, an average value of 0.3 is assumed in the calculations.

This correction cannot be applied *ab initio* to the average NFM, because olivine is not on the liquidus, as attested to by petrographic studies. The widespread presence of orthopyroxene and plagioclase as phenocryst phases in the chilled margins of Tasmania (Edwards, 1942; McDougall, 1962; Hergt, 1989a; *section 2.3.1.*) and the Wisanger Basalts of Kangaroo Island (Milnes et al., 1982; *section 2.3.1*), along with Antarctic Ferrar Magmas such as the McMurdo Dry Valleys (Marsh, 2004) and the Dufek Intrusion (Himmelberg and Ford, 1976) underline their ubiquity as early fractionating phases in the Ferrar province as a whole. In order to quantify the extent of plagioclase and orthopyroxene fractionation prior to the saturation of olivine, average electron microprobe analyses of the two phases were used and then added to the mean Tasmanian Dolerite magma in a 1:1 ratio (approximately mirroring their relative abundance in the chilled margins).

The approximate point at which olivine is found on the liquidus using PELE (Boudreau, 1999) at ≈3kbars coincides with an $Mg\#_{melt}$ = 68.5, which is close to that expected of melts in equilibrium with mantle olivine (Mg# = 69-75; $Fo_{88\text{-}91}$). This melt composition (CM + 25% OPX-Plag) very closely resembles an olivine-bearing Ferrar Dolerite from Antarctica (*table 3.4., column 8*) (Hergt et al., 1989a) aside from the slightly higher Al_2O_3 content of the latter. At this point, only olivine was deemed to occur on the liquidus, and the magma in equilibrium with mantle olivine fertile mantle, Fo_{88}. The X^{Mg}_{Ol}, and therefore $Fo_{olivine}$ was derived using the following expression:

$$X^{Mg}_{Ol} = \frac{2}{(K_{D}{}^{Mg-Fe}_{Ol-Liq} \times \left(\frac{X^{Fe^{2+}}_{Liq}}{X^{Mg}_{Liq}}\right) + 1)} \quad (3.8.)$$

Olivine addition was calculated until the melt was shown to be in equilibrium with DMM (Fo_{89}), represented by melt CM + 25% OPX-Plag +3% Ol. Even at this point, SiO_2 wt% (≈53) is in excess of that of primitive N-MORB (≈49.5), reflecting derivation from an anomalously silicic source. However, because major element systematics outlined above indicate that the mantle source may have been more refractory than DMM, a melt composition was calculated for equilibrium with Fo_{92} (CM + 25% OPX-Plag +12% Ol), which is representative of highly melt-depleted cratonic mantle (e.g. Kelemen et al., 1998; Carlson et al., 2005; Lee, 2006). This composition still retains the characteristic major element concentrations that typify the Ferrar tholeiites, providing evidence that their disparity compared to MORB is a function of varying mantle source composition. The back-calculation also renders comparison between experimental peridotite (lherzolite and harzburgite) melts possible. In an attempt to assess the feasibility of such melts being parental to the Ferrar tholeiites, an inventory

of liquid compositions was compiled. Experimental melts applicable to comparison with the Ferrar magmas were taken from the following: Wasylenki et al., (2003); Jaques and Green (1980); Falloon and Danyushevsky (2000) and Kushiro (1996).

The data was filtered to include only melt compositions that had similar MgO contents to the calculated primary Ferrar tholeiite (≈14wt±2.5%, *table 3.4., column 7*). Concordant with a small range of X_{MgO}^{liquid}, the experimental temperatures spanned were limited between 1325-1400°C, at 1-1.5 GPa. These experimental data were further supplemented by melt compositions produced from depleted peridotite (*table 3.6., column 4*) using the pMELTS algorithm via adiabat_1ph (Smith and Asimow, 2005).

3.2.6. Lherzolite vs Harzburgite Melting

Central to the composition of peridotite melts is the modal mineralogy of the source. Seeing as it is the minerals themselves that melt, not the bulk composition of the rock, the relative contributions of these phases are what control the liquid's characteristics. During shallow melting of the mantle, the two predominant melt-producing phases are clinopyroxene and orthopyroxene. Furthermore, when both are present in the residue of melting, the former contributes more to the melting, such that fertile lherzolites create melts dominated by the clinopyroxene component. As noted by several workers (e.g. Baker and Stolper, 1994; Pickering-Witter and Johnston, 2000; Wasylenki et al., 2003), clinopyroxene reaction coefficients exhibit minimal variation over a range of multicomponent lherzolite compositions, and dominates the melting assemblage in each case. A typical lherzolite melting reaction may be (MM3; Baker and Stolper, 1994):

$$0.38OPX + 0.77CPX + 0.06Sp = 0.21Ol + 1Liq \quad (3.9.)$$

During melting of a harzburgitic residue, orthopyroxene is the prevailing contributor to melt composition. Wasylenki et al., (2003), during melting of the depleted mantle compositon, DMM-1 (Mg# = 90) at 1GPa, characterised the melting relationship to be:

$$1.24OPX = 0.24Ol + 1Liq \quad (3.10.)$$

Similarly, the calculated melting relations for a cratonic harzburgite (*table 3.6.*) at 1GPa used in the pMELTS (adiabat_1ph) calculations yielded the reaction:

$$1.07OPX + 0.05Sp = 0.12Ol + 1Liq \quad (3.11.)$$

Qualitatively, analysing the chemistry of typical mantle phases (*table 3.5.*), we would expect that a lherzolitic melt would be enriched in CaO, Al_2O_3, TiO_2, Na_2O, and K_2O and depleted in MgO and SiO_2 relative to a harzburgitic melt. Indeed, upon inspection of the experimental melts, we observe a similar relationship.

Liquids derived from the melting of a lherzolitic assemblage (*equation 3.9.*) are characterised by low SiO_2 concentrations at low Mg#, as would be expected for a melt whose composition is controlled by

the clinopyroxene component (*figure 3.9.*). Because MgO behaves compatibly, and the proportion of orthopyroxene entering the melt increases near clinopyroxene -out (compare the melting equations for increasingly depleted peridotite compositions in Wasylenki et al., 2003), SiO_2 increases concomitantly with Mg# (MgO). Note that this relationship doesn't hold near the lherzolite solidus, where abundant alkalis lower $\gamma_{SiO_2}^{liquid}$ producing highly siliceous melts (Hirschmann et al., 1999a). However, these melts have very low Mg# (<70) and high concentrations of incompatible elements, at odds with what is observed.
The high SiO_2 at high Mg# is characteristic of harzburgite melts (*equations 3.10., 3.11.*), and both these descriptors increase until the exhaustion of orthopyroxene.

Al_2O_3 is generally enriched in fertile lherzolite melts (*figure 3.10*), as the greater abundance of alkalis and clinopyroxene would predict (section 3.2.3.). Absolute Al_2O_3 contents in depleted peridotites are also diminished, as it is hosted largely in clinopyroxene (*table 3.5.*), whose modal abundance is reduced. The Ferrar parent magma plots within the field for typical harzburgite melts. The trend for harzburgite melts is that of increasing $FeO^{(T)}$ with increasing melt fraction, as the majority is held in olivine, which is produced through the incongruent melting of OPX (*equations 3.10., 3.11.*).

The vast majority of CaO in peridotites is hosted in clinopyroxene. It therefore behaves as a compatible element prior to clinopyroxene exhaustion, but incompatibly thereafter as a general feature of peridotite melting. Consequently, the low CaO contents observed in harzburgite melts and the Ferrar primary magma substantiate this behaviour (*figure 3.11.*). Na_2O is incompatible throughout the melting duration, and displays a uniform decrease. Na_2O is also intrinsically lower in harzburgitic compositions, given that they have experienced (greater degrees of) melt extraction relative to lherzolites, producing Na-poor liquids.

3.2.7. Pressure – Temperature Estimates

Forward Model - pMELTS

The pMELTS algorithm permits a thermodynamically quantitative treatment of variable parameters during mantle melting, such as temperature, pressure, fo_2, entropy, etc. The starting composition used was that of a low-temperature peridotite, averaged from Carlson, 2005 (from McDonough, 1990). Low- temperature peridotites have low equilibration pressures, and are thought to be representative of highly depleted cratonic mantle that have undergone 30-50% melt extraction, largely between 1-4 GPa (Walter, 1998; Kelemen et al., 1998; Lee, 2006). A feature of some cratonic peridotites (e.g. from Kapvaal and Siberian cratons) is that their silica content is higher than expected by melt extraction alone, and is manifest by the presence of excess orthopyroxene. The working hypothesis is, based on the fact that it is not a ubiquitous feature of the cratonic mantle, and a correlation between Ni in olivine and the proportion of modal orthopyroxene (Kelemen et al., 1998), that the silica enrichment was instigated by the infiltration and subsequent reaction of a siliceous melt with already-depleted peridotite. The ensuing reaction may be qualitatively expressed as:

$$\underset{olivine}{Mg_2SiO_4} + \underset{liquid_1}{SiO_2} = \underset{orthopyroxene}{Mg_2Si_2O_6}\ (+liquid_2) \qquad (3.12.)$$

Where $X_{SiO_2}^{liquid}$ of liquid 1 is greater than that of liquid 2.

Given that the reaction consumes olivine (the liquid is silica-saturated) and precipitates orthopyroxene, and since, at equilibrium, $K_{D_{Ni}}^{ol-opx}$>1, the decrease in olivine proportion forces Ni abundance in olivine to increase. Reactions of this description are more likely to occur in the shallow mantle, potentially where the melts percolate through the conductive boundary layer, dissolving olivine in an effort to equilibrate with ambient peridotite. Such a melt may be sourced from sedimentary material from a downgoing slab, whose partial melts are anticipated to be siliceous (e.g. Spandler et al., 2010), or from eclogite (e.g. Pertermann and Hirschmann, 2003). Since even anhydrous sediment has a solidus temperature 50-150°C lower than MORB-like eclogite (Spandler et al., 2010), melts of sedimentary protoliths are expected to be high degree (>50%), leaving only quartz in the residue. Conversely, in order for eclogitic melts to exhibit an SiO_2-rich character, they must be of a small degree, with garnet remaining in the restite (Pertermann and Hirschmann, 2003). Therefore, sediment melts are expected to preserve the trace element signature of their source, whilst siliceous eclogitic melts should impart a strong garnet signature to their host peridotite. The LREE-enriched composition of the upper continental crust (Rudnick and Gao, 2003) is consistent with the LREE-enriched character of many cratonic peridotites (Kelemen et al., 1998). To simulate this interaction, a cratonic peridotite was reacted with a small percentage (3%) of melt with an upper-crustal composition to create a hybridised peridotite (*table 3.6.*). This scenario is likely an oversimplification, considering that small melt fractions migrate through channels in the upper mantle, rather than through porous flow. Reactive porous flow would result in a more homogeneous hybrid peridotite (modelled here) whereas in actuality, the intermediate, OPX-rich composition may be present as discrete veins (e.g. Arai et al., 2003).

Owing to the much lower concentration of FeO+MgO in the sediment as compared to the peridotite, the Mg# remains relatively unchanged with even large fractions of sediment addition (>50%) (*figure 3.12a*). This evolution mirrors that seen in natural samples, which show a broad, linear increase in SiO_2 and a decrease in FeO and MgO, at near-constant Mg#s (Lee, 2006). The end-product is an OPX-enriched (≈30vol%) harzburgite with a high Mg# and a crustal trace element signature.

At subsolidus conditions and 1 GPa, pMELTS calculates a phase assemblage which consists of 65% olivine, 29% orthopyroxene, 5% clinopyroxene and 1% spinel (*table 3.7.*).

The melt fraction and temperature of the melt may be roughly estimated using the oxide-melt fraction relations (*figure 3.13.*). A linear equation was fit to each of the 4 predominating oxides (CaO, MgO, Al_2O_3, $FeO^{(T)}$) that are sensitive to the extent of melting, and aren't markedly affected by pressure (SiO_2 is strongly P-dependent and was therefore omitted). The set of equations give a melt fraction and temperature of 8.86±.33% and 1367±3°C not including $FeO^{(T)}$, and 9.71±1.65% and 1377±19°C including $FeO^{(T)}$. Pressure can be crudely estimated through the silica content of the melt, such that it is clear the melts are derived from an average pressure slightly greater than 1 GPa, given the lower SiO_2 content of the Ferrar parent magma compared to the experimental compositions.

Inverse Model – Geothermobarometry

Both pressure and temperature estimates may be sought from inverse modelling for a specific melt composition using the geothermobarometer of Lee et al., (2009), which is based upon silica activity. Silica provides a more favourable monitor of pressure and temperature because it is buffered in the mantle at a given P, T by olivine and orthopyroxene (*equation 3.1.*), and is much less prone to resetting compared to minor or trace elements, which can vary greatly between tectonic settings. The caveats include that the melt must be primary, and in equilibrium with olivine and orthopyroxene, and that the mantle source Mg# and fo_2 are set. Underestimating the Mg# or the $Fe^{3+}/\sum Fe$ of the source results in an underestimation of the temperature and pressure. To that end, the Mg# of the source was set to 91.5, and the fo_2 to QFM-0.5 ($Fe^{3+}/\sum Fe \approx 0.1$).

The resulting calculation for the Ferrar Primary Magma (which had 25% OPX-Plag and then 12% olivine added to it to finally be in equilibrium with a mantle with $Fo_{91.5}$) yields a temperature of 1378°C at a pressure of 1.08 GPa, figures which are in fantastic agreement with the forward model derived from pMELTS, despite being calculated via vastly disparate methods *(figure 3.14.*). Using a less depleted peridotite (e.g. fertile lherzolite with Mg# = 89) produces temperatures and pressures that are abundantly too shallow to form beneath continental crust (1274°C, 0.5 GPa), even using the composition purportedly in equilibrium with Fo_{89} mantle. Conversely, changing the Mg# to 93 creates an increase in temperature and pressure to ≈1470°C at 1.75 GPa, conditions which are more akin to melting in a hot plume head. The chemistry of the magmas do not support such a scenario, as their resemblance to tholeiitic OIB such as Hawaii or Iceland is remote. Fe, for example, is higher (≈12wt%, Jackson and Dasgupta, 2008) due to higher pressures of melting (olivine contribution to the melt is increased).

3.2.8. The Role of Water?

Some workers have invoked the melting of hydrated and depleted peridotite to explain the high silica content of CFB melts (e.g. Gallagher and Hawkesworth, 1992; Turner and Hawkesworth, 1995; Puffer, 2001; Ivanov et al., 2008). On the contrary, water cannot exert a controlling influence on the Ferrar melt compositions or indeed continental flood basalt provinces in general, given that they are dry (<0.3 wt% H_2O), and subsequently follow a tholeiitic differentiation trend typified by low fo_2 and $a_{H_2O}^{liquid}$ (*section 4.0.*). Taking the partition coefficients for H_2O from Hauri et al., (2006) for each mineral and their modal abundances (*table 3.7.*) or a bulk D from Hirschmann (2006), it is readily demonstrated that during 10% melting of peridotite composed of nominally anhydrous minerals only, the maximum water content of the source must be below 500ppm (0.05 wt%), similar to that of MORB and OIB (<1000ppm) (*figure 3.15.*). However, due to water's low molecular weight, its influence on a molar basis may still result in the expansion of incongruent melting of OPX. Despite this, it is evident that the high silica contents of the Northern Ferrar magmas derive from the consumption of orthopyroxene due to melting at low pressure rather than appreciable amounts of water in the source (though this would have the same net effect), which could facilitate the creation of melts with similar characteristics at higher pressure.

Water is also appealed to in order to explain the high melt productivities of continental flood basalts (Gallagher and Hawkesworth, 1992; Ivanov et al., 2008). Thermodynamic predictions, on the other

hand, suggest that, while water acts as a flux to lower the solidus by an amount approximated through the cryogenic equation (Hirschmann, 1999b), the melt productivity of the peridotite before it reaches its nominally dry solidus is very low (Gaetani and Grove, 1998; Hirschmann et al., 1999b). The isobaric melt production, dF/dT, which is shown to exert a controlling influence on polybaric melt production (Asimow et al., 1997), is of the order of 0.02%/°C. Only when it passes the dry solidus does it increase to higher values (dF/dT= 0.5%/°C). This reflects a convergence of the melt and solid compositions by dilution of the incompatible elements (*equation 3.20.*).

3.2.9. Oxygen Fugacity

The oxygen fugacity of a magma is defined by the partial pressure of oxygen in the melt (not necessarily a free gas phase), and is controlled by the relative activities of Fe^{3+} and Fe^{2+} as these are the dominant polyvalent molecular species in terrestrial magmas, whose range of redox states bracket the equilibrium:

$$Fe^{2+}O + \frac{1}{4}O_2 = Fe^{3+}O_{1.5} \qquad (3.13.)$$

The generalised thermodynamic expression is:

$$\frac{-\Delta G^{\circ}_{(T,P)}}{RT} = \ln\left(\frac{X^{melt}_{Fe^{3+}O_{1.5}}}{X^{melt}_{Fe^{2+}O}}\right) + \ln\left(\frac{\gamma^{melt}_{Fe^{3+}O_{1.5}}}{\gamma^{melt}_{Fe^{2+}O}}\right) - \frac{1}{4}\ln f_{O_2} \qquad (3.14.)$$

The $Fe^{3+}/\Sigma Fe$ decreases as a function of pressure due to the smaller partial molar volume of $^{VI}Fe^{2+}$ as compared with $^{IV}Fe^{3+}$ (e.g. O'Neill et al., 2006). This effect is accounted for in the thermodynamic equation of O'Neill et al., (2006), enabling calculation of fo_2 at different pressures for a given liquid composition. Additionally, the activity of Fe^{3+} and Fe^{2+} vary as a function of composition and each others' concentration, owing to non-ideal interactions between them in the melt structure. Alkalis, for example, increase the proportion of $^{IV}Fe^{3+}$ in the melt owing to the sterically-assisted charge-balance capability via a substitution of the form $(A^{+IV}Fe^{3+})(^{IV}Si^{4+})^{-1}$. With decreasing iron concentration, Fe behaves according to Henry's Law, where the activity coefficient is independent of concentration, however, with greater [Fe], Fe^{2+} and Fe^{3+} interact non-ideally, and therefore necessitate a mixing function to correct for this (Jayasuriya et al., 2004).

Because absolute fo_2 varies predictably with temperature, it is preferable to report fo_2 values with respect to a buffer curve that mirrors this temperature dependence to enable comparison between magmas at different temperatures, even if the melt itself is not buffered. Henceforth, the fo_2 has the fo_2 of the Fayalite-Magnetite-Quartz (FMQ) buffer (O'Neill, 1987; Ballhaus, 1991) subtracted from it:

$$3Fe_2SiO_4 + O_2 \rightleftharpoons 2Fe_3O_4 + 3SiO_2 \qquad (3.15.)$$

In order to perform these calculations, both $[Fe^{3+}]$ and $[Fe^{2+}]$ must be known. A subset of the samples had wet chemical analyses performed on them using the Wilson method (Wilson, 1960), in

order to quantify FeO. Fe_2O_3 could then be derived by subtraction from the $Fe_2O_3^{(T)}$ derived from XRF.

$$\log f_{O_2} = 4\log\left(\frac{X_{Fe^{3+}O_{1.5}}}{X_{Fe^{2+}O_{1.5}}}\right) - \frac{28144}{T} + 13.95 + 3905\frac{X_{MgO}}{T} - 13359\frac{X_{CaO}}{T} - 14858\frac{X_{NaO_{0.5}}}{T} - 9805\frac{X_{KO_{0.5}}}{T} + 10906\frac{X_{AlO_{1.5}}}{T} + 110971\frac{X_{PO_{2.5}}}{T} - 11952\frac{\left(X_{Fe^{2+}O_{1.5}} - X_{Fe^{3+}O_{1.5}}\right)}{T} + \left(\frac{33122}{T} - 5.24\right)\left[(1+0.241P)^{\left(\frac{3}{4}\right)} - 1\right] - \left(\frac{39156}{T} - 6.17\right)\left[(1+0.132P)^{\left(\frac{3}{4}\right)} - 1\right] \quad (3.16.)$$

The calculated fo_2 values (*equation 3.16.,* O'Neill et al., 2006) suggest that the melts, on average (ΔFMQ=-0.30±0.5, n=3), equilibrated at about half a log-unit below the FMQ buffer (*figure 3.16.*). Such a value is typical of N-MORB (Bézos and Humler, 2005), which has $Fe^{3+}/\Sigma Fe \approx 0.12$ (FMQ-0.41±.43). This estimate is also compatible with oxygen fugacities derived from barometric methods from mantle peridotites from cratonic areas, which show a relatively narrow range of redox conditions, FMQ-0.5±0.5 (e.g. Ionov and Wood, 1992; Frost and McCammon, 2008, their figure 1). Typical spinel peridotites contain .1-.3 wt% Fe_2O_3, ($Fe^{3+}/\sum Fe$ = 1-3%) distributed equally amongst its constituent phases except olivine, which contains negligible amounts (Canil and O'Neill, 1996). Spinels have $Fe^{3+}/\sum Fe$ = 15-34%, which can fall to 5-15% in peridotites that have experienced extensive melt extraction. Although spinels have high Fe_2O_3 contents, they generally make up less than 3% of the rock, and their contribution to the rock's total Fe_2O_3 is subequal to ortho- and clinopyroxene. Lithospheric mantle is expected to be even more depleted than fertile asthenospheric (depleted-MORB-mantle), owing to melt extraction. Since MORB has a $Fe^{3+}/\sum Fe$ > $Fe^{3+}/\sum Fe$ of its peridotite source, one might expect fo_2 in the source to decrease. This depletion of $Fe^{3+}/\sum Fe$ is indeed borne out in the redox-sensitive stable isotope systematics of iron, which illustrate that peridotites exhibit continually lighter $\delta^{57,}$Fe values concomitant with melt extraction (Weyer and Ionov, 2007). However, the constancy of the fo_2 in MORB and mantle peridotites appears to argue for a buffered redox state. This may be understood due to the role of spinel, as the principal host of Fe^{3+}, in buffering the oxygen fugacity of the resultant melts. As melting proceeds, spinel is removed from the peridotitic assemblage (*section 3.2.6., equation 3.9.*), but it also becomes more refractory (i.e., its $Cr/(Cr+Al+Fe^{3+})$ ratio increases). Since Fe^{3+}-Cr substitutions are more favourable than Fe^{3+}-Al substitutions in spinel (e.g. Papike et al., 2005), the activity of Fe^{3+} in spinel increases. Therefore, although its modal proportion decreases, this change is offset by an increased $a_{Fe_2O_3}^{spinel}$ and oxygen fugacity is buffered, resulting in the constancy seen in the Ferrar magmas, N-MORB, and the lithospheric mantle.

Barometric methods in peridotite rely upon calibration of oxygen buffers using the activity of Fe^{3+} distributed amongst the constituent phases. Fortunately, it is also feasible to apply such methods to the Ferrar magmas through the use of the magnetite-ilmenite thermobarometer (Buddington and Lindsley, 1964).

$$\underset{\text{Ülvospinel}}{XFe_2TiO_4} + \underset{\text{Magnetite}}{(1-X)Fe_3O_4} + \frac{1}{4}O_2 = \underset{\text{Ilmenite}}{XFeTiO_3} + \underset{\text{Haematite}}{\left(\frac{3}{2}-X\right)Fe_2O_3} \quad (3.17.)$$

To exploit this equilibrium, the activities of Fe^{3+} and Fe^{2+} must be known in the magnetite- ülvospinel solid solution and the ilmenite-haematite solid solution. The concentration of Fe was measured via electron microprobe (*section 1.4.)* and the Fe^{3+}/Fe^{2+} was recalculated stoichiometrically using the method of Carmichael (1967). An added bonus of the geothermometer is its independence of pressure and the ability to obtain rough temperature estimates (e.g. Carmichael et al., 1974). However, in intrusive bodies, where cooling is relatively slow, the oxides are prone to resetting during subsolidus oxidation-exsolution (*section 4.0.*). Exchange of this type is evident upon backscattered electron imaging, and testifies to their low-temperature resetting. Despite this, given the temperature-dependence of absolute fo_2, the magnetites will never have $a_{Fe_2O_3}$ higher than their original value, and similarly that ilmenites never exceed their initial a_{TiO_2}, the fo_2 estimates may be considered as maximum values (i.e., the fo_2 cannot be any more oxidised) (Lindsley and Frost, 1992; Frost et al., 1988). The derived values for barometric fo_2 on a mafic dolerite with a whole rock bulk composition similar to those of the Tasmanian dolerite chilled margins and KI basalts (which have only ilmenite; *section 2.3.1.*) yields equilibration conditions of 843°C and QFM-0.45, in fine agreement with thermodynamically-calculated values.

Yet another method of fo_2 calculation is at our disposal if we know the abundances of V, Ga and/or Sc in the bulk magma. Vanadium is a polyvalent element that may exist in four (4) valence states; V^{2+}, V^{3+}, V^{4+} and V^{5+}, whose relative abundance is controlled by the prevailing $fo_2$of the system. At terrestrial redox conditions, V^{3+}, V^{4+} and V^{5+} predominate, with their compatibility in minerals generally being an inverse function of their valence (Toplis and Corgne, 2002; Balan et al., 2006; Karner et al., 2008; Mallmann and O'Neill, 2009). Normalising the concentration of V by a similarly incompatible yet homovalent element, such as Sc or Ga therefore provides a measure of the fo_2, as long as the compatibility of these elements during melting of mantle peridotite can be parameterised. Lee et al., (2003) and Lee et al., (2005) modelled the evolution of V/Sc_{melt} during isobaric, isothermal melting of a spinel lherzolite with uniform V/Sc at 1.5GPa using the pMELTS algorithm (Ghiorso et al., 2002) to calibrate the oxybarometer, and used it to argue that the depletion of the continental lithosphere occurred between 1-4 GPa at FMQ to FMQ-1, and that arc peridotites were not significantly more oxidised than cratonic or oceanic peridotites. Subsequent work in the application of V/Sc to magmas confirmed the similarities in the redox state of arc lavas and MORB, discrepant with barometric results. Therefore, the V/Sc ratio offers several advantages over barometric fo_2 estimations:

- Early fractional crystallisation of reduced phases in a system closed to oxygen exchange enriches the residual melt in O_2, shifting equilibrium *3.13.* to the right, resulting in the increase of $Fe^{3+}/\Sigma Fe_{melt}$
- Interaction with fluids and/or wall rocks from the continental crust may impose a change in fO_2 depending on the oxidation state of the assimilating phase
- Degassing of reduced species, C, H, S (Mathez, 1984) enforce an increase in fO_2 as the magma ascends
- Reaction of H_2O with reduced species (Fe^{2+}) in conjunction with preferential loss of H_2 to the atmosphere can result in auto-oxidation of the magma without any open-system exchange other than H_2 loss via the reaction below (Holloway, 2004):

$$Fe^{2+}O + H_2O = {Fe^{3+}}_2O_3 + H_2 \qquad (3.18.)$$

Of these considerations, only the possibility of fractional crystallisation appears to be pertinent to the Ferrar magmas, given their low H_2O contents and minimal crustal-level contamination. V/Sc are an ideal pairing because they are geochemically similar, refractory lithophile elements (not partitioned into gases) that have similar enrichments in the continental crust, arc magmas and MORB with respect to primitive mantle (McDonough and Sun, 1995). Additionally beneficial during mantle melting of spinel lherzolite is that between FMQ and FMQ-1, $D^{V}_{Mantle-Melt} \approx D^{Sc}_{Mantle-Melt}$ and is therefore independent of the degree of melting. A deficiency of the V/Sc ratio is that it can be perturbed by fractional crystallisation of pyroxene. The magnitude and direction of the change are dependent on the oxygen fugacity of the system, but typically, above FMQ-1, V is less compatible than Sc, and segregation of pyroxenes from the melt will cause an increase in the V/Sc ratio. Therefore, the fo_2s derived from V/Sc from the Ferrar magmas represent maximum estimates. Given the similarities in the melting behaviour for the model calibration (melting of a spinel peridotite at 1.5GPa) and the Ferrar magmas, the V/Sc systematics are applicable. Additionally, Mallmann and O'Neill (2009), with partitioning data for V and other homovalent elements between mantle phases and melt, were able to parameterise the V/Ga-fo_2 relationship in the same way. Using V/Ga may be slightly more advantageous because Ga, like V, is compatible in spinel, and so variations of spinel mode in the source shouldn't affect the V/Ga-fo_2 correlation.

V/Sc-fO_2 relationships appear to be more internally coherent (*figure 3.17a*), perhaps due to the relative ease of measuring Sc via Solution ICP-MS as compared to Ga, given its high 1st ionisation potential and spectral interferences (*section 1.3.*). Both datasets show that the melts record oxygen fugacities between FMQ and FMQ-1, with a tendency to be below FMQ-0.5. V/Sc ratios exhibit fo_2 near FMQ-0.8, while the average is slightly higher for V/Ga, at FMQ-0.7. From the V/Sc systematics, it appears as though the Kangaroo Island basalts have been less affected by pyroxene crystallisation and record a slightly lower fo_2. Concordant with the Kangaroo Island basalts more primitive Zn/Fe and Fe/Mn ratios, their redox state is taken to most closely approximate that of the mantle source.

Consolidating the results garnered from the diverse methods used to calculate oxygen fugacity, the relatively convergent view is that the Ferrar liquids were in equilibrium with a mantle source buffered near FMQ-0.5. This is considerably lower than arc lavas, which may have V/Sc up to 11 (Lee et al., 2005) and oxygen fugacities between FMQ and FMQ+2 (Carmichael and Ghiorso, 1990; Carmichael, 1991). The low fo_2 recorded by the magmas are in line with those from MORB and other continental tholeiites which subsequently follow a tholeiitic differentiation trend (e.g. Berndt et al., 2005; Botcharnikov et al., 2008; *section 4.0.*). The reduced redox state of the melt is also compatible with a subcontinental lithospheric mantle source (Ionov and Wood, 1992).

3.2.10. Summary

In general, at low melt fractions, a fertile peridotite that still has CPX in the residue produces a melt that has high Al_2O_3, alkalis, CaO, and an Mg# too low to be a likely source for the Ferrar melts. This does not preclude initial melting with small fractions of CPX, however, modelling considerations suggest that the Ferrar magmas left behind a dry (<.05 wt% H_2O) depleted (Mg# ≈ 91.5) residue consisting of olivine and orthopyroxene, formed from extraction of a medium-degree (10±2%) melt

at low pressures (1.25±.25GPa) at near typical mantle potential temperatures (≈1370°C) and buffered near FMQ-0.5.

3.3. Element Ratios and Trace Elements

The distinctive feature the Tasmanian Dolerites and Kangaroo Island Basalts exhibit is the striking resemblance of their trace element signature to the upper continental crust. The difference in abundances of trace elements between the mantle and crust may provide a first order inference as to their compatibility in the mantle.

Trace element ratios of elements that behave geochemically similarly during partial melting of typical depleted upper mantle may provide clues into the petrogenesis of a given magma. When two elements had the same, $D_{Mineral-Melt}$, their ratio is independent of the extent of partial melting. A departure of the ratio from their canonical values (e.g. Sun and McDonough, 1989) implies additional variables that cannot be attributed solely to melting of depleted mantle in an oceanic setting. Such perturbations may arise from melting of a heterogeneous source, the mineralogy of the mantle, contamination by a foreign component, and other variables such as fo_2 and aH_2O.

Hofmann et al., (1986) noted that some element ratios that are constant in oceanic basalts are fractionated in the average continental crust. The continental crust is, in a broad sense, the complement to the depleted mantle, a hypothesis inferred through mass balance arguments (Hofmann, 1997 and references therein). Trace element budgets between the mantle and crust are modified through melting and crystallisation processes, which are influenced by the mode of melting and conditions incumbent during crystallisation (e.g. aH_2O, fo_2). Hawkesworth and Kemp (2006) contended that the continental crust was formed from accretion of arc-like basaltic material as well as OIB, based on trace element ratios that behave differently in these melting settings. The La/Nb ratio is oft-used to discriminate between arc-like and tholeiitic magmas, because Nb^{5+} is preferentially retained in the slab in rutile during slab melting (e.g. Bromiley and Redfern, 2008), whereas, owing to the lower $X_{TiO_2}^{peridotite}$, rutile is absent, and because $D_{Nb} \approx D_{La} << 1$ in the remaining phases, La/Nb remains unfractionated and near 1.

As evidenced (*figure 3.19.*), the Ferrar magmas have trace element ratios exactly akin to those of the upper continental crust, or are intermediate between the UCC and N-MORB. The degree to which the ratios reflect the upper continental crust is dependent on the concentration ratio of a given element in the sedimentary contaminant and the MORB source (DMM), i.e., C_X^{UCC}/C_X^{DMM}. Ratios such as Ce/Pb, wherein $\frac{C_{Pb}^{UCC}}{C_{Pb}^{DMM}} \gg 1$ are therefore highly sensitive to the proportion of the upper-crustal contaminant. Of particular note is the Eu/Eu* ratio of the Ferrar magmas. Even though this ratio is calculated for the chilled margin/KI Basalt composition, using trace element partition coefficients from Aigner-Torres et al. (2007) for Eu^{2+} at QFM-0.5, 12.5% plagioclase addition (as calculated in section 3.2.5.) is only sufficient to shift the observed Eu/Eu* ratio by +0.05, meaning that the primary magma still exhibited a negative Eu anomaly of the order of 0.86. This ratio discerns between the relative contribution of the lower and upper continental crust, which have Eu/Eu* ratios of 1.13 and 0.69, respectively. Eu is preferentially incorporated into plagioclase as Eu^{2+},

especially at low fo_2 where Eu^{2+}/Eu^{3+} increases. The lower continental crust is broadly basaltic to basalt-andesitic in composition (e.g. Hawkesworth and Kemp, 2006), and is generally at pressures low enough (<1.5 GPa) to retain plagioclase as its aluminous phase. Partial melting of the lower crust in the presence of residual plagioclase is inferred to create the (-) Eu anomaly of the upper crust, whilst maintaining a (+) Eu anomaly in the lower crust. Immediately apparent is that the Eu/Eu* of the Ferrar magmas may have been imposed through contamination by the upper continental crust. A similarly diagnostic ratio is their low Ti/Zr, where it is evident that interaction with the upper continental crust must have occurred. Another poignant feature of the Ferrar magmas is the degree of LREE enrichment relative to MORB (as expressed by the La_N/Sm_N ratio). The source of MORB possesses a LREE depletion, due to their incompatibility relative to the HREE during melting. However, the LREE-enriched signature is typical of the upper continental crust (*figure 3.18.*) and orthopyroxene-enriched cratonic peridotites (Kelemen et al., 1998), lending support to the hypothesis that the metasomatising melt is derived from subducted upper crustal material.

To assess the suitability of the contaminant for each of these ratios visually, the data for the UCC, LCC and the Ferrar Magmas was normalised to N-MORB, which is estimated to represent an unmodified melt from depleted MORB mantle (DMM) (*figure 3.19.*).

For values that are >1, it indicates that the Ferrar magmas have a higher ratio of these elements than N-MORB. The contaminant must therefore have a higher element ratio than the Ferrar Magmas (blue line) in order for it to act as the enriching agent. For example, only the upper, not lower, continental crust is a feasible contaminant to explain the Rb/Sr and Ba/Nb ratios of the Ferrar melt, whereas, theoretically, it may be possible for the LCC to cause the increase in Sr/Y observed with respect to N-MORB. More LCC than UCC would be required to enact this change, as the closer the lines are together, the more the mass fraction of the contaminant that is needed (i.e., $Sr/Y_{UCC} > Sr/Y_{LCC} > Sr/Y_{Ferrar} > Sr/Y_{MORB}$). Similarly, below 1, the ratio of the prospective contaminant must be below that of Ferrar. Plainly visible is the more agreeable correlation with the trend of the Ferrar melts shown by the UCC. The LCC appears to be unsuitable as a contaminant for most of the ratios, particularly Rb/Sr, Eu/Eu*, Ba/Rb and Nb/U.

Having established the UCC as a likely contaminant, the trace element budget of the continental crust was incorporated into the pMELTS model, and, consistent with the major element modelling, 3% by mass was added to a highly depleted upper mantle composition (DMM; Workman and Hart, 2005) with major element characteristics as detailed in section *3.2.7*.

The salient features of the Ferrar magmas are reproduced by the source contamination of a highly depleted residue with 3% upper crust. If less than 3% sediment is added, then the modelled trace element abundances would be lower than those observed for the magmas for the calculated degree of partial melting. This difficulty could be alleviated by assuming a source less depleted than used in the model, however, this would be contrary to the major element studies which necessitate a refractory source (*section 3.2.6.*). Conversely, if the proportion of sediment is increased, then additional extents of partial melting would be required to dilute their concentration. The melt fractions would be in excess of those dictated by the melts' major element composition. For example, at higher degrees of melting (15-20%), the liquids tend towards more magnesian picrites

with ≈20% MgO, 6% CaO, and 9% Al_2O_3, quite incompatible with actual melt compositions (*table 3.7.*).

The largest discrepancy between the modelled melt and the actual magmas are the more compatible elements, such as Hf, Y, and the HREE, which appear to have been overestimated in the model. This difficulty is also present in the modelling of Hergt et al., (1989a), and may be attributed to preferential stabilisation of these elements in the residue of the sedimentary melt, meaning their budget in the sedimentary contaminant was overestimated. Another possibility may be that the source was metasomatised not by a sedimentary melt, but by a siliceous, supercritical fluid which contained elevated concentrations of the fluid mobile elements such as Rb, Pb and Ba, and a more dilute amount of elements that are typically only transported in melts (HFSE, REE). A miscalculation of partition coefficients used in the pMELTS algorithm for these more compatible elements may also play a role.

An additional consideration to bear in mind is that the trace element abundances reflect those of the erupted basalts and chilled margins. As demonstrated in the previous section, these magmas may have undergone as much as 37% by mass fractional crystallisation, having the effect of lowering the trace element concentrations, but not appreciably changing their ratios. This may also explain the slightly elevated concentrations for the melt-mobile elements, as they are more compatible in OPX and plagioclase than the fluid-mobile elements (*table A16, table A17*). Therefore, the 3% sediment estimate is a maximum bound, and could conceivably become smaller if the sedimentary component was incorporated as a partial melt.

Rare earth element abundances, especially the HREE, are not drastically affected by sediment contamination of the source peridotite as long as the mass fraction of the contaminant remains small. The abundances of the HREE may only be modified if residual garnet or amphibole (e.g. Tiepolo et al., 2000) is present in the residue of melting, owing to their strong affinity for these elements. The Northern Ferrar magmas exhibit conspicuously flat REE patterns, precluding the presence of residual garnet or amphibole in the mantle source. Such an interpretation is consistent with the major element characteristics of the magmas, which dictate melting of depleted peridotite at shallow depths (<1.5 GPa), which is too shallow to stabilise garnet in peridotite (>2.5 GPa). Additionally, an anomalously H_2O-rich source may also be ruled out, given the low water content of the melts and the absence of an amphibole signature, which may have been imparted on the magmas had the metasomatising fluid or melt been enriched in H_2O. Water would also promote deeper melting through solidus depression. Furthermore, the absence of an HREE-depletion trend obviates the involvement of pyroxenites or eclogites in the source. Given their higher $FeO^{(T)}$ contents, high pressure mafic lithologies stabilise garnet at lower pressures (near 1.5 GPa) (O'Neill, 1981; Kogiso et al., 2004), and garnet forms a more volumetric constituent of the assemblage, and hence more likely to be a residual phase following melt extraction.

On the whole, however, it appears that a small (3%) incursion of upper crustal material into a harzburgitic source which was melted at medium degrees (≈10%) is sufficient to explain the trace element properties of the Ferrar magmas.

3.4. Radiogenic Isotopes

Whilst trace element abundances and ratios appear to be relatively well modelled by the addition of 3% sedimentary material to the source, such a model must also be reconcilable with the isotopic signature of the magmas. Consistent with the trace element concentrations used for modelling in pMELTS, their abundances can be considered fixed, and hence, the ratios controlling the isotopic evolution of the source are constrained. The variables are therefore the isotopic composition of the peridotite and contaminant. For this exercise, the peridotite component is assumed to have a constant isotopic ratio, and the isotopic composition of the contaminant was allowed to vary. Since the upper crustal component must have a fixed parent/daughter element ratio (that is, that of the upper continental crust, *table 3.9.*), the controlling factor in its composition is its age. Thus, such a calculation may provide a broad age constraint for the contaminant. A caveat one must be mindful of is the behaviour of the sediment-peridotite mixture during melting. It is unclear whether the source approximates a homogeneous mixture (as might be the case for diffuse veining of peridotite interstices by a liquid) or a carapace present in distinct channels. Whatever the distribution, the following calculations assume:

- Isotopes are not fractionated from each other during melting
- The upper-crustal contaminant is derived from MORB mantle, but evolves with parent/daughter ratios equivalent to UCC (*table 3.9.*, Rudnick and Gao, 2003) upon extraction and thereafter.
- The isotope ratios are corrected to their initial ratios ($t_0 \approx 180$Ma) such that the calculations consider only the parent/daughter ratios of the source components (peridotite, upper crust) and not that of the Ferrar melt.

For the calculations, the hyperbolic mixing equation between two components possessing variable isotope ratios and concentrations was utilised (Albarède, 1996):

$$\left(\frac{^rE}{^sE}\right)_{mix} = \frac{f_b[E]_b\left(\frac{^rE}{^sE}\right)_b + (1-f_b)[E]_a\left(\frac{^rE}{^sE}\right)_a}{f_b[E]_b + (1-f_b)[E]_a} \qquad (3.19.)$$

Where ^rE is the radiogenic isotope of element, E, whereas ^sE is the reference stable isotope. f is the fraction of either component, *a* or *b*, and $[E]$ is the concentration of the radiogenic element in *a* or *b*. It can be seen therefore that $[E]$ is fixed for peridotite and contaminant, $\left(\frac{^rE}{^sE}\right)_{peridotite}$ is fixed, whilst $\left(\frac{^rE}{^sE}\right)_{sediment}$ is allowed to vary by changing its depleted mantle model age.

Based on simple binary mixtures for $[E]_{peridotite}$ and $[E]_{sediment}$, it is evident that, for 3% addition of the sedimentary component, it accounts for 62%, 61% and 97% of the total Nd, Sr, and Pb in the source. The depleted mantle model ages for the bulk magma composition are not overly instructive for Sr and Nd isotopic compositions of the contaminant because it represents a mixture of 60/40 UCC/mantle, not the depleted mantle on its lonesome. At the same time, it can provide an upper bound for the age at which the Rb/Sr or Sm/Nd of the source became the same as for that in the Ferrar magmas, and hence the age of the enrichment event. Using this method, the depleted mantle

model ages for the most primitive composition (PS65, a chilled dolerite) are 1.16 Ga for the Sm-Nd system and 0.95 Ga for the Rb-Sr system (*table 3.10.*). This is in reasonable agreement with the 0.9 Ga±0.2 Ga derived by Hergt et al., (1989a).
However, to edify the properties and age of the sediment itself, the crustal end-member must be isolated for Nd and Sr, whilst the Pb isotope composition of the Ferrar magmas directly reflects that of the continental crustal contaminant, and consequently its age.

The relative concordance of the depleted mantle model ages for the sedimentary component using both the Sm-Nd and Rb-Sr systems (1.45 Ga and 1.43 Ga, respectively), point to a rather ancient, Middle Proterzoic source for the sediments. This is not unexpected, given the extreme radiogenic isotope systematics observed in the magmas consistent with long time-integrated low Sm/Nd and high Rb/Sr ratios. Such characteristics are typical of the upper continental crust, as, in broad terms, $D^{Sm}_{Mantle-Melt} > D^{Nd}_{Mantle-Melt}$ and $D^{Sr}_{Mantle-Melt} > D^{Rb}_{Mantle-Melt}$. The Lower crust is typically displaced to much lower εNd values and does not extend to such high $^{87}Sr/^{86}Sr$ ratios (e.g. Jahn et al., 1999). The Sm-Nd characteristics of the Cambrian Kanmantoo Group (Turner et al., 1993) yield model ages between 1.48 Ga and 1.64 Ga, similar to those derived from the model (*table 3.10.*), suggesting this may be a viable sedimentary contaminant in the source of the Ferrar magmas (*section 3.5*.). The Kanmantoo Group is characterised by anomalously low $^{87}Sr/^{86}Sr$ ratios as compared to Adelaidean or Archaean rocks of the South Australian Craton (Turner et al., 1993), and subsequently represents a more likely contaminant.

3.4.1 Pb Isotopes

Pb isotopes, because of lead's strong affinity to partition into the continental crustal reservoir, are a sensitive tracer of crustal input, and have been used to elucidate the possible sources of EM-type OIB (e.g. Hart et al., 1992; Hofmann, 1997; Willbold and Stracke, 2010). For example, Willbold and Stracke (2010) identified that time-integrated Th/U ratios (expressed as $^{208}Pb^*/^{206}Pb^*$) in EM basalts are higher in those with Eu/Eu* ≥ 1 compared to those with Eu/Eu* <1. Such a trend is consistent with the complementary elevated and depleted Th/U ratios in the lower and upper continental crust, respectively. Therefore, it can be expected that either the $^{206}Pb/^{204}Pb$ or $^{207}Pb/^{204}Pb$ of the upper crust is higher at a given $^{208}Pb/^{204}Pb$ than the lower crust.

When compared to the MORB array, $^{207}Pb/^{204}Pb$ is indeed enriched at a given $^{206}Pb/^{204}Pb$, whereas the $^{208}Pb/^{204}Pb$ value shows no significant enrichment with respect to MORB (*figure 3.22.*). This feature reflects long time-integrated U-enrichment, as would occur in an upper crustal reservoir. The MORB-like $^{208}Pb/^{204}Pb$ ratios of the Ferrar magmas suggests that the enriched component that contributed to the Ferrar magmas evolved with time-integrated Th/Pb ratios akin to that of MORB. The Ferrar magmas show enriched $^{207}Pb/^{204}Pb$ and $^{206}Pb/^{204}Pb$ similar to OIBs Gough and Samoa, whose incompatible element and radiogenic isotope characteristics have been influenced by an ancient recycled upper crustal component (Jackson et al., 2007).

3.4.2. Age of the Intrusion

Age constraints may be derived by applying an isochron to the sequence of rocks in the Red Hill intrusion, assuming they were derived purely from fractional crystallisation of a common parent magma. The Red Hill sequence is particularly amenable to such a treatment, given the presence of chilled dolerites and a continuum of differentiates which approximate the composition of the liquid at a given stage of its evolution (*section 4.2.*). Previous age constraints have come from a U-Pb zircon age in a Red Hill granophyre, 185.6±1.5Ma (Williams and Hergt, 2000) and K-Ar whole rock age of 177±6.2Ma (Schmidt and McDougall, 1977).

Figure *3.23* illustrates a tight isochron with an initial $^{87}Sr/^{86}Sr$ value of 0.7107±0.00023 (2σ) and an age of 174±10Ma (2σ), in fine agreement with previously published ages, confirming its Middle Jurassic age.

3.5. A Tectonic Appraisal

Considerations explored here imply that the source of the Ferrar magmas was a refractory but refertilised harzburgitic source situated within the lithospheric mantle, which subsequently underwent partial fusion at low pressures. The tectonic feasibility of such a scenario hinges upon:

1. The likelihood for mantle of this composition to be present at shallow depths
2. The propensity for such a mantle to produce the large volumes of magma in short periods of time that characterise flood basalt provinces
3. A viable method for mantle refertilisation

The first point may be addressed through the assessment of peridotite xenolith data from continental areas. Melt-depleted peridotite, due to the efficient removal of iron and water, becomes not only compositionally buoyant but also quite viscous and strong with respect to convecting asthenospheric mantle. Peridotite xenoliths that have equilibrated at low temperatures on the conductive continental geotherm (Low-T peridotites) such as those in the Kaapvaal and Siberian cratons (Carlson et al., 2005), tend to be more highly depleted than xenoliths that record high temperatures offset from the cratonic geotherm. This dichotomy insinuates a degree of compositional stratification, at least in some continental regions, wherein the upper part of the lithospheric mantle is volumetrically dominated by highly melt-depleted spinel harzburgites (Song, 1994).

The isentropic productivity, that is, the change in the extent of melting per unit pressure drop during adiabatic upwelling, $(dF/dP)_S$, is controlled by the isobaric melt productivity $(dF/dT)_P$. The isobaric melt productivity during batch melting is quantified by the following equaton (Asimow et al., 1997):

$$\left(\frac{\partial F}{\partial T}\right)_P = -\left(\frac{\partial X_b^s}{\partial T}\right)_P \left(\frac{1}{(X_b^l - X_b^s)}\right) - \frac{(X_b - X_b^s)\left(\frac{\partial (X_b^l - X_b^s)}{\partial T}\right)_P}{(X_b^l - X_b^s)^2} \qquad (3.20.)$$

It illustrates that isobaric melt productivity is, in turn, strongly dependent on two dominant factors:

1. The compositional difference between the solid and melt ($X_b^l - X_b^s$)
2. The rate of change of compositional difference $\frac{\partial X_b^s}{\partial T}$

During peridotite melting, these two controls can be thought of as representing the degree of melting and phase exhaustion, respectively. Because melts near-solidus are rich in alkalis and diverge from the composition of the source, melting near the solidus is rather unproductive, but consequently melt productivity increases in a concave-up fashion as the liquid and solid compositions converge. Alternatively, when a phase is exhausted from the assemblage, there is a discontinuous drop in productivity owing to less variation in the source composition (∂X_b^s). These factors are important because melting of harzburgite, as suggested here, with a nominal absence of clinopyroxene, is expected to exhibit reduced productivity as compared to lherzolite melting. Wasylenki et al. (2003) derive melting rates equal to 0.3±0.2%/°C prior to CPX exhaustion, and 0.08±0.01%/°C during harzburgite melting. Baker and Stolper (1994) report similar values of 0.21±0.02%/°C and 0.12±0.01%/°C, respectively. In agreement with these studies, the average productivity above CPX-out for the peridotite composition used in the pMELTS calculation is 0.085±0.02%/°C (all uncertainties 1σ).

This represents a conundrum for the formation of large igneous provinces, which have eruption rates of the order of 0.1-8km^3/yr, assuming emplacement times of 1-3My and volumes in the range of 0.1-10 x 10^6 km^3 (Coffin and Eldholm, 1994). Leitch and Davies (2001), on the basis of numerical modelling, were able to reproduce LIP-like eruption rates by mixing 15% eclogite into a plume, and, given its lower solidus temperature and shorter melting interval, increase the rate of (volumetric) melt production by an order of magnitude. However, their scenarios require that the excess temperature of the mantle plume be ≥200°C, and that eclogite has a solidus temperature at least 200°C lower than peridotite. Since solidus temperature is a strong inverse function of alkali content (Herzberg et al., 2000; Pertermann and Hirschmann, 2003; Kogiso et al., 2004), these eclogites would necessarily be alkali-enriched, a trait which is not at all observed in tholeiitic flood basalt provinces. Additionally, with the exception of the Deccan (e.g. Turner and Hawkesworth, 1995), a plume component is inconsistent with the major, trace or radiogenic isotope chemistry of Mesozoic flood basalt provinces (Hawkesworth et al., 1999), which tend to exhibit characteristics typical of lithospheric mantle, as suggested here. Furthermore, the emplacement of the Ferrar magmas in a linear belt along the footprint of the Cambro-Ordovician Delamerian-Ross Orogeny rather than a radial plume head (e.g. Ernst, 2009), points to a genetic link between the two, rather than a plume whose position would not be so intimately linked to the crustal architecture.

The models presented hitherto assume that melt productivity during mantle melting is directly proportional to eruption rate. On the contrary, it has been evidenced here that continental flood basalts undergo a protracted period of fractional crystallisation before being emplaced as sills in the upper crust or extruding as lavas. Furthermore, the mantle potential temperature and the temperature of the erupted lavas differ by some 150°C, implicating a period of dormancy in which fractional crystallisation was permitted. A generic calculation based on the characteristic length scale of the intrusion (taken arbitrarily to be 10km), gives an equilibration time of 2My at moho temperatures.

These considerations imply that the rate of melt production from peridotite and the emplacement rate need not necessarily be coupled, indeed, the period of fractional crystallisation suggests they are not. Further support for this argument is lent by the fact that picrites are confined to early stages of LIP eruptions (Campbell, 1998). If melt was produced and erupted simultaneously, then with continued thermal weakening and thinning of the lithosphere, the extent of partial melting would increase, favouring the production of picritic melts later in the eruptive cycle. These characteristics are suggestive of a time-component to the emplacement of flood basalts.

The voluminous outpourings of mantle-derived magma during flood basalt eruptions are evidence for very high continental heat flows. The thermal state of the lithosphere is therefore of paramount importance when considering the volume of melt that can be produced from peridotitic mantle upwelling adiabatically at a given potential temperature.
Estimating the thickness of melt that would form from melting at a minimum depth of 45km with a mantle potential temperature of 1370°C equates to about 4.5km kilometres of magma, and 10% melting of the source, in agreement with calculations (McKenzie and Bickle, 1988). The calculated temperature of ≈1370°C at 1-1.5 GPa is excessively elevated to typify that of a stable continental region, which may have a lithospheric thickness of 150km and a continental geotherm of 40mW/m^2, intersecting the adiabat at ≈6GPa (Carlson, et al., 2005). For the adiabat to reach such temperatures at 45km depth necessitates extension of the continental lithosphere and an absence of thick continental lithosphere. Such a scenario is likely to be realised during rifting, where β-factors are greater than ≈2. McKenzie and Bickle (1988), for a fertile asthenospheric composition, estimated that a mantle potential temperature of 1380°C may produce 4km of melt for a β-factor of ≈ 2.7 and initial lithospheric thickness of 100km. Current extension in the basin and range province is likely to exceed 2 and locally reaches 3, which may be considered a rough analog for the tectonic state of the Ferrar province.

The very high temperatures near the base of the crust and the absence of any discernible crustal-level contamination demand that the lower crust be composed of refractory granulitic rocks that are resistant to melting. High pressure two pyroxene-garnet eclogite xenoliths in late Jurassic lamprophyre dykes are reflective of Tasmania's Precambrian lower crust, attesting to the presence of these litholigies in the Jurassic (Seymour and Calver, 2001). If the lower crust is indeed composed of cumulate high-pressure gabbroic-eclogitic lithologies which consist of garnet and clinopyroxene±plagioclase (Rudnick and Fountain, 1995; Hawkesworth and Kemp, 2006), then they would also be expected to be low in alkalis (Rudnick and Gao, 2003), and therefore their solidus temperature should be relatively high. Furthermore, garnet-clinopyroxene compositions may lie on the high temperature thermal divide (*figure 3.4.*), which requires high temperatures in order to produce melt, especially in the absence of appreciable alkalis. Experimentally-determined phase relations show that solidus temperatures of alkali-depleted pyroxenites and eclogites, regardless of whether they have a silica excess or silica depletion, are comparable to, or even higher than, those of peridotites with similar alkali contents (Kogiso et al., 2004). Therefore, it is feasible that the lower crust remained relatively unaffected during melt generation, and did not contribute significantly to the major or trace element characteristics of the Ferrar magmas. This does not preclude small degrees of contamination, however, it was not extensive enough to modify their properties.

Data for eclogite samples from the Jurassic (≈180Ma) Angaston Kimberlite (Segui, unpublished Honours thesis, 2010), whose emplacement precedes that of the Ferrar magmas, and whose location is on the peripheries of the northern margin of the Ferrar province, record temperatures of ≈800°C-≈1000°C. Furthermore, the equilibration (Sm-Nd closure) ages yield 247±62Ma, attesting to the presence of a typical continental geotherm during the Jurassic, and a lithospheric thickness between 150-200km. The change from 800°C at 1GPa to ≥1300°C between ≈250Ma and ≈180Ma lends support to an extensional setting which induced thinning of the continental lithosphere prior to continental break-up.

Magnetic dating of the earliest oceanic crust that marked the separation of East and West Gondwana yields an age of ≈150Ma in the Mozambique Ocean (Simpson et al., 1979). However, the region of Ferrar magmatism is sufficiently far-removed from that region such that it is feasible oceanic crust formation in the area began significantly earlier (170-180My; Encarnaciòn et al., 1996). The age of rifting between Australia and Antarctica is even more ambiguous, owing to the lack of a clear boundary between oceanic and continental crust, although oceanic spreading may have initiated by 140Ma (Whittaker et al., 2008). The creation of oceanic crust soon after the emplacement of the Ferrar magmas lends plausibility to the model whereby the Ferrar magmas were formed from melting of thinned subcontinental lithospheric mantle at shallow depths.

Given the absence of a plume component deduced from the chemical characteristics of the Ferrar magmas, rifting in this region may be induced by internal heating (Hawkesworth et al., 1999). A period of ≈300My in which subduction was not able to cool the underlying mantle may contribute to elevated temperatures (up to 50°C for temperature-dependent viscosity models) under a stable continental lid (Coltice et al., 2007; O'Neill et al., 2009). Another mechanism that could contribute to rising temperatures under large continental areas is through radioactive decay of U, Th and K. These elements are highly incompatible during mantle melting, and enriched in the continental crust by ≈10^3 with respect to DMM (Hofmann, 2003). As proposed, a sedimentary component that enriches the SCLM through metasomatism of the otherwise refractory and barren depleted mantle may therefore have implications for the thermal state of the lithosphere. 3% of the enriching agent increases the budget of U by up to 50x, and that of Th by up to 100x compared with the depleted mantle composition. K is less affected, being enriched by a factor of 5-10x, but this depends on the original concentration of K in the peridotite, which is less well constrained.
We may then take the concentrations of U, Th, and K in the metasomatised peridotite (*table 3.9.*), and calculate the temperature difference caused by decay of their radioactive isotopes.

$$dT = \frac{S}{c_p \rho}(dt) \qquad (3.21.)$$

Where S is the volumetric heat production in W/m^3, c_p is the specific heat capacity of peridotite (1150 J/kg°K) and ρ is the density of peridotite (3300 kg/m^3).
S for the enriched peridotite is ≈6x10^{-7} W/m^3, while that for depleted mantle is ≈2x10^{-8}. This equates to a temperature change over a million years of ≈5°C and 0.2°C, respectively. This of course is calculated in the absence of conduction, which, depending on the length scale of the heterogeneity, may be significant. Regardless, the calculations demonstrate that the capacity of sediment-affected peridotite to produce heat in the lithospheric mantle is in excess of that of typical convecting

asthenosphere. Considering that the maximum age for this enrichment event is ≈1Ga (*section 3.4.*), the incubation time for this process may be in excess of 800My. Tectonic considerations suggest however that this enrichment likely occurred during the Cambrian. However, it is feasible that the thermal pulse was in fact created within the lithosphere itself instigating thermal buoyancy and obviating the need for a plume from the core-mantle boundary (*figure 3.26.*).

The sedimentary component may be incorporated into the source region of the Ferrar magmas in one of two ways:

1. Partial melts from downgoing sediments on the upper plate of subducting oceanic crust (Plank and Langmuir, 1998)
2. Delamination of lithospheric mantle and concomitant lower crust due to convective or gravitative instability (Kay and Kay, 1993; Lustrino, 2005; Elkins-Tanton, 2007).

In Southern South Australia, the initiation of subduction is punctuated by the inversion of the juvenile Kanmantoo basin (a thick, turbiditic sequence) and I-type granitic magmatism at ca. 520Ma (Foden et al., 2006), marking the onset of the Delamerian Orogeny (*figure 3.25a*). Given that subduction-induced magmatism was occurring at this time, it is conceivable that melts of sedimentary material did not traverse the crust, and were trapped in the lithosphere, owing to their high reactivity with olivine (*figure 3.25b, section 3.2.7.*).

However, within a span of 30My, the period of tectonic convergence abruptly ceased, and the mode of the magmatism changed from I- and S-Type (subduction-influenced) to an A-Type (anorogenic, tholeiitic) regime. Expressions of the terminal magmatism associated with orogenic collapse are observed in the Black Hill Mafic intrusive body, the Padthaway A-Type granites, and the Truro Lamprophyres (Turner et al., 1992; Turner, 1996), which have emplacement ages near 490Ma (Foden et al., 2002). The rapid cessation is also attested to by Ar-Ar cooling ages for all I-, S- and A-type magmatic bodies near 490Ma, regardless of their crystallisation age (Turner et al., 1996). Sediments of the Lachlan Fold Belt also record exhumation ages which are indistinguishable from their depositional ages**.**

The termination of the orogen in such a short time-span is consistent with lithospheric delamination. Lee et al., (2006) tabulated that instabilities may require 10-30My to develop in overthickened lithosphere, depending on the viscosity and density of the lithospheric keel. Prior to orogenesis, the Kanmantoo sediments were filling-in a newly opened segment of oceanic crust (evidenced by the ≈520Ma pillow basalts at Red Creek), which, upon structural thickening during the Delamerian Orogeny, would be composed of mafic eclogite. Thus, during delamination, a portion of sediments may have also been transported into the asthenospheric mantle along with subcontinetal lithospheric mantle and an eclogitic root. Since these were juvenile sediments that had not experienced any prior dehydration; upon entrance to the mantle they were able to melt relatively easily, and may have metasomatised any remaining lithosphere at 490Ma (*figure 3.25c*). The eclogites must have been refractory and could not have contributed appreciably to the melting regime in this case. This is due to the absence of any garnet signatures in the Ferrar magmas, and their disparate major element compositions compared to experimental eclogite melts.

Because the signature of unaltered upper continental crust is so well preserved in the Ferrar magmas, it suggests that the sediment component underwent very little geochemical modification before it metasomatised the mantle lithosphere.

In the case of a subduction scenario, the unfractionated upper crustal geochemical signature would argue for a fast and cold subduction zone where sediments remained unaffected by melting during subduction, and may have only been subjected to dehydration or melting in discrete zones. It is also a possibility that the subduction zone was hot, resulting in the creation of significant amounts of melt, some of which was trapped within the subcontinental lithospheric mantle to metasomatise cratonic mantle. This interpretation is not favoured, because it may also promote melting of the eclogitic slab, which, in accord with prior considerations, cannot have a significant influence on the chemical signature of the Ferrar magmas.

These scenarios are not mutually exclusive, however, the homogeneous trace element signatures over a large areal extent in the Ferrar province necessitate a well-mixed sedimentary contaminant. Since bulk admixture of sediments and depleted mantle is unlikely to produce such a homogeneous mixture, sediment melting is required. If both delamination and subduction processes were operative in the Cambrian, then two possibilies exist. It is possible that either only one set of sediments contributed to the source of the Ferrar magmas, or that both sediment types were mixed via melt-melt interaction, homogenising the two sources, and then metasomatised the source peridotite.

Conclusion

The high SiO_2 contents of the Northern Ferrar magmas cannot be explained through melting of high pressure mafic lithologies in the mantle, due to the disparity between their partial melts and other major element compositions, especially alkali and CaO contents. Since the magmas exhibit Mg#s that are too low ($Mg\#_{melt} \approx 61$) to be in equilibrium with typical mantle olivine ($Mg\#_{melt} = 69\text{-}75$), they are deemed to have undergone low-pressure fractionation, a hypothesis consistent with the presence of orthopyroxene and plagioclase in the chilled dolerites. After correction for orthopyroxene, plagioclase and olivine fractionation, their depleted major element compositions resemble experimental harzburgite melts, which are characterised by high SiO_2, high Mg# and low Fe_2O_3 and incompatible elements. Peridotite with such a composition is present in the shallow areas of cratonic lithospheric mantle due to its positive buoyancy resulting from iron loss during melt extraction. The source of the Ferrar magmas has been refertilised by a small (≈3%) proportion of upper crustal sediment, conferring incompatible element and LREE enrichment on the source, in addition to the creation of excess orthopyroxene through reaction between peridotite and the siliceous sedimentary melt. This scenario is analogous to that hypothesised for the creation of LREE-enriched, OPX-enriched cratonic peridotites (Kelemen et al., 1998). Consolidation of these characteristics with the radiogenic isotope signatures of the magmas indicate that the proposed contaminant has properties similar to the Kanmantoo Group ($T_{DM} \approx 1.5Ga$), a turbiditic sequence deposited across Southern South Australia immediately prior to the Delamerian Orogeny. This may have been introduced into the mantle through Cambrian delamination or subduction. The contaminated source, due to its relatively higher concentrations of radioactive elements compared

to typical depleted mantle, is capable of producing significant amounts of volumetric heat, and triggering the wholesale melting of the lithospheric mantle.

4.0. Differentiation

Abstract

The composition of the melt, during differentiation of a tholeiitic magma, is defined by an early enrichment in $Fe_2O_3^{(T)}$ at near-constant SiO_2 contents, before the trend is reversed, and iron is depleted in the evolving liquid, with a concomitant enrichment in alkalis and SiO_2. The Red Hill intrusion, southern Tasmania, represents a rare portion of the tholeiitic Tasmanian Dolerites which preserves a continuum of magma compositions, ranging from mafic dolerite to alkali-enriched granophyre. The magmas are typified by a complex pyroxene assemblage, consisting of early orthopyroxene, succeeded by extensively zoned pigeonites and augites. Magnetite saturation, which is delayed until the later stages of crystallisation in the magmas due to their low prevailing oxygen fugacity, exerts a strong control on the point of iron depletion in the liquid. This event also marks a significant petrological change in the mineralogy of the magma, where pigeonite is succeeded by fayalite, and pyroxene zonation ceases. Crystallisation of the Red Hill magma occurred at low fo_2, low $X_{H_2O}^{liquid}$ and at low to moderate pressures, similar to other tholeiitic magmas such as the Skaergaard intrusion. The oxygen fugacity and H_2O content of the magma reflects that of its source mantle, such that melts of a tholeiitic affinity are found only in anorogenic tectonic settings where melting is induced by thermal-compositional anomalies or adiabatic decompression, and not by hydrous fluid flux as in subduction zones. The entire range of differentiates, through numerical modelling considerations, is shown to have been produced solely by *in-situ* fractional crystallisation from a single parental liquid, which is preserved in the chilled dolerites that line the intrusion. The chemical and petrological similarities of the Red Hill granophyres to Delamerian-aged A-type granites of the Padthaway ridge indicate that A-type granites are produced by protracted fractional crystallisation of mafic magma. These systematics are corroborated by the iron isotopic characteristics of the evolving melt, which are sensitive to the redox state of the magma.

4.1. Introduction

Basaltic magmas change their composition upon cooling through a range of processes; however, the most widespread of these is fractional crystallisation. The type of minerals that crystallise depends strongly on the chemical composition of the magma, which is a function of its mantle source region, but also on the temperature and pressure at which crystallisation occurs. In particular, the two parameters which exert most control over the liquid line of descent of a basaltic magma are the oxygen fugacity, fo_2, and water content, $X_{H_2O}^{liquid}$ (e.g. Grove and Juster, 1989; Toplis and Carroll, 1995; Feig et al., 2010). Like the chemistry of the magma, these variables are dependent on the melting regime and composition of the mantle source, which, in turn, is influenced by the tectonic setting.

The tholeiitic trend is characterised by an evolving residual melt which shows an increase in FeO^T and TiO_2 at near-constant SiO_2 as crystallisation proceeds, before undergoing a sharp drop in FeO^T and TiO_2 and a concomitant enrichment in SiO_2 and alkalis (Fenner, 1929). This change is enacted by the onset of titanomagnetite crystallisation, whose saturation conditions are strongly dependent on the oxygen fugacity of the system (e.g. Toplis and Carroll, 1995). Such a trend typifies Mid-Ocean Ridge Basalts (MORB), continental basaltic rocks, and some Ocean Island Basalts (OIB), but rarely arc magmas. Tholeiitic magmas represent relatively large extents of melting of the mantle, and are

subsequently enriched in SiO_2, FeO, MgO and depleted in incompatible elements, such as alkalis and water (Jaques and Green, 1980; *section 3.0.*). This tectonic affiliation with tholeiitic magmatism suggests that the chemical characteristics and oxygen fugacities of terrestrial mafic magmas are representative of their mantle sources (Carmichael, 1991).

H_2O is excluded from early-crystallising phases such as pyroxene and plagioclase during differentiation, and is therefore enriched in the remaining melt. Water may act as an oxidising agent in magmas, and has been cited to explain the elevated fo_2 of arc lavas with respect to tholeiitic magmas (Holloway, 2004). However, water bonds with non-bridging oxygens in the melt polymer to form OH^- groups thereby attenuating the activity of free water and its capacity to oxidise iron (Carmichael, 1991; Botcharnikov et al., 2005). While water may have a marginal effect on oxidation state, its impact on the stability of crystalline phases in mafic systems has been studied extensively (e.g. Sisson and Grove, 1993; Berndt et al., 2005; Botcharnikov et al., 2008; Feig et al., 2010), and is shown to act as a flux to decrease liquidus temperatures, as well as the proportions, temperature interval and order of crystallising phases.

The differentiation sequence of Red Hill has been described in detail by McDougall (1962), and represents a classic example of tholeiitic evolution. The composition of the parental liquid to the Red Hill intrusion is given by the homogeneous chilled margins which case its walls. This offers a convenient starting point from which to assess the differentiation trend. Unlike the majority of sills which comprise the Tasmanian Dolerites, Red Hill exhibits a continuum of compositions ranging from mafic dolerite to alkali-enriched granophyres. The sill is typically 400m thick, and a cupola-structure protrudes from the centre of the body, hosting up to 200m of differentiated granophyre.
McDougall (ibid.), based on the knife-sharp contacts of the intrusion, suggested that the magma had been subjected to minimal interaction with surrounding wall rocks, and that the entire range of differentiates in the intrusion could be explained through fractional crystallisation of a single liquid alone.

While the general form of the intrusion and the crystallisation sequence are well-characterised, many details remain unconstrained with regards to the effect of fo_2 and H_2O on the evolving melt, how the minerals' chemistry changes with differentiation, as well as the trace element compositions of the evolved rocks. This study therefore has two primary aims:

1. Elucidate the impact of fo_2, H_2O and pressure on the stability of mineral phases and therefore the liquid line of descent. Oxygen fugacity, in particular, is important because it regulates the ratio of ferric to ferrous iron in the melt. In a system closed to oxygen, such as a plutonic body, the $Fe^{3+}/\Sigma Fe$ ratio is fixed for the bulk composition, and hence the distribution of $Fe^{3+}/\Sigma Fe$ may change as a function of the crystallising phases (Carmichael, 1991; Toplis and Carroll, 1995; Toplis and Carroll, 1996). Specifically, ferromagnesian silicates (pyroxene, olivine) have a greater affinity for ferrous iron, while ferric iron is readily partitioned into magnetite. The oxygen fugacity, and therefore, the relative stability of these phases have a critical bearing on the chemical characteristics of the evolving liquid.

2. Investigate the change in mineral chemistry – both major and trace – and how it relates to the evolution of the melt. While major element chemistry of the constituent minerals is

dependent upon intensive properties such as P, T, fo_2, and $a_{H_2O}^{liquid}$ for a given chemical composition, the trace element budgets are in turn reliant upon the mineral chemistry and the ideality of the sites that are present. A-type granites commonly occur in bimodal association with mafic rocks, typically in extensional settings where the magma is able to rise to high crustal levels (Foden, 2010). Characteristic of A-type granites are their low aH_2O, presence of anhydrous mafic phases (fayalite, hedenbergite); high Fe# (Fe/(Fe+Mg)), and enrichment in elements that are incompatible in gabbroic minerals and oxides (Turner et al., 1992). The Red Hill sequence offers the ideal opportunity to elucidate the conditions that amount to the production of granitic rocks through fractional crystallisation of a mafic, tholeiitic parent magma.

4.2. The Liquid Line of Descent

The factors that influence the liquid line of descent (LLOD) of a given magma are imposed upon it by the melting conditions experienced by its mantle source. Such chemical traits are its major element chemistry, oxygen fugacity, and water content. However, variables such as pressure and temperature of differentiation also exert strong controls over the compositions of the derivative liquids by influencing the stability of different mineral phases, and tend to be a function of their level of crustal emplacement, as dictated by lithospheric stresses (e.g. compressional vs. extensional). The major element composition of the continuum of magmas preserved at Red Hill is compared to known experimental trends in order to constrain the conditions of crystallisation.

The Red Hill magmas exhibit well-defined trends in major element space suggesting that the differentiates are consanguineous with a single parental liquid, of chilled-margin composition (*figure 4.1.*), where each rock approximates the liquid composition at a given stage of its evolution. The behaviour of the major elements is consistent with that anticipated from crystallisation experiments of ferrobasaltic liquids (e.g. Snyder et al., 1993; Toplis and Carroll, 1995; Berndt et al., 2005; Botcharnikov et al., 2008). Furthermore, the succession of mineral phases observed in the intrusion attest to a continually evolving liquid that is the complement of crystallised minerals preserved (*section 2.3.*). This consistency argues for fractional crystallisation as the primary process giving rise to the variations observed in the Red Hill sequence.

4.2.1. SiO_2

As corroborated by the SiO_2-MgO plot (*figure 4.1a.*), MgO is a much better discriminant over the early interval of differentiation, given the relative constancy of SiO_2 during gabbroic fractionation of plagioclase-pyroxene. Over the same interval, MgO drops by ≈4wt%.
The SiO_2 content of the evolving liquid reflects a competition between Si-poor phases (oxides, olivine) and Si-rich phases (pyroxenes, plagioclase). Therefore, conditions which control the relative stability of these phases exert a primary influence on the SiO_2 of the liquid. Given the high $X_{SiO_2}^{liquid}$, and hence high $a_{SiO_2}^{liquid}$ of the chilled dolerites, it lies to the high $a_{SiO_2}^{liquid}$-side of the Ol-OPX curve, and therefore precipitates orthopyroxene rather than olivine (*figure 4.8.*). The orthopyroxene present in the chilled margins contains 55 wt% SiO_2 (*table A9*), slightly in excess of the liquid (≈54 wt%) and

much higher than typical magnesian olivine (≈40 wt%). In the dolerites and quartz dolerites, however, plagioclase becomes increasingly significant, and it is also joined by augite and pigeonite. Clinopyroxenes have ≈52 wt% SiO_2 which decreases with Mg#, due to the higher molar mass of Fe. Contrastingly the SiO_2 content of plagioclase increase from ≈48 wt% in the chilled dolerites up to ≈60 wt% in the most albitic compositions, representative of the exchange reaction $Ca^{2+}Al^{3+}(Na^{+}Si^{4+})^{-1}$. Importantly, these compositional changes balance, and the SiO_2 content of the liquid remains constant during this gabbroic fractionation phase.

In addition, the effect of water activity, $a_{H_2O}^{liquid}$, may also play a significant role in modulating the silica content of the melt. Due to its network modifying role (*section 3.2.1.*), H_2O depolymerises the melt, thereby increasing the stability of depolymerised phases (olivine, clinopyroxene) at the expense of more polymerised ones (plagioclase). In general, water acts to depress the liquidus temperature of silicate phases, whereas the stability of magnetite is unaffected, and hence tend to crystallise earlier in the sequence (Botcharnikov et al., 2008). Orthopyroxene and ilmenite also appear to favour low $a_{H_2O}^{liquid}$ conditions (Berndt et al., 2005). Given this, it may be expected that volatile-rich liquids follow more rapid silica-enrichment trends. The fact that the Red Hill magmas do not bear out this trend suggests a fairly dry magma. However, upon inspection of the pegmatite trend, it clearly delineates a tendency towards more SiO_2-rich compositions at a given MgO content. To a first order, this would suggest higher $a_{H_2O}^{liquid}$, consistent with the presence of hydrous phases in these rocks.

Oxygen fugacity also affects the degree of silica enrichment in crystallising systems due to the steep T-fo_2 slope of the titanomagnetite liquidus. Ilmenite stability and mode is also influenced strongly by $X_{TiO_2}^{liquid}$ (Toplis and Carroll, 1995). Therefore, at high fo_2 where titanomagnetite crystallisation occurs earlier, greater silica enrichment should be evident, with concomitant iron depletion. The fact that neither the pegmatites nor the main sequence reflect such an evolution suggests low fo_2 conditions. Furthermore, ilmenite is commonly the earlier-crystallising Fe-Ti oxide at conditions below the FMQ buffer (Snyder et al., 1993; Toplis and Carroll, 1995), consistent with its presence in the chilled dolerites.
However, magnetite saturation is accompanied by a dramatic increase in SiO_2 over a small MgO interval; almost 10 wt% over 1.5 wt% MgO. SiO_2 enrichment is enhanced when magnetite and ilmenite co-crystallise (Toplis and Carroll, 1995), as is the case in the Red Hill granophyres.

4.2.2. Al_2O_3-CaO-CaO/Al_2O_3

The predominant host of Al in igneous minerals is plagioclase, and therefore the evolution of Al_2O_3 in the liquid should be highly sensitive to plagioclase crystallisation. The main Red Hill sequence evolves with a slight Al-enrichment trend, before falling at ≈1.5 wt% MgO (*figure 4.1c*). Conversely, the pegmatites show immediate displacement to much lower Al_2O_3 contents at a given MgO. This suggests plagioclase crystallisation was more pronounced in the pegmatites, which is seemingly at odds with their elevated volatile contents. Additional plagioclase fractionation in the pegmatites is substantiated by their systematically lower CaO contents than the main series (*figure 4.1e*). The fact that the pegmatites lie on the same trend as the main series in CaO/Al_2O_3-MgO space implies that

varying proportions of plagioclase crystallisation do not cause a departure from the prevailing trend (*figure 4.1h*). CaO also decreases gradually before tailing off considerably after ≈1.5 wt% MgO. The decrease in CaO illustrates its compatibility in both plagioclase, augite, and, to a lesser degree, pigeonite.

4.2.3. FeO-TiO_2

Iron and titanium illustrate concordant trends with declining MgO due to their mutual compatibility in Fe-Ti oxides (*figures 4.1b,d*). Experimental studies indicate that iron enrichment is most pronounced at low pressures (plagioclase stability increases with respect to clinopyroxene), at low fo_2 (where magnetite saturation is delayed) and at low water contents. Low $a_{H_2O}^{liquid}$ facilitates the early crystallisation of silicate minerals, and also hinders the oxidation of iron by H_2O. Decreasing $a_{H_2O}^{liquid}$ also aids in increasing the plagioclase/pyroxenes ratio, further stifling Fe-enrichment. Despite the fact that ilmenite is present in the chilled dolerites (and its derivative liquids), its modal abundance is low such that $D_{Solid-Melt}^{Ti^{4+}} < 1$, and is enriched in the remaining melt.

The salient feature of Fe, Ti evolution in the remaining liquid is that it reaches a maximum at ≈1.5wt% MgO before falling abruptly thereafter. While the increase in Ti is a product of its incompatibility in the bulk crystallising assemblage, the existence of Fe in two oxidation states (Fe^{2+}, Fe^{3+}) in the magma means that they must be considered separately, given their disparate chemical properties and bonding environments (e.g. Wilke, 2005; *section 4.4.*). In spite of this duality, the ΣFe and TiO_2 contents of the melt both experience a drop owing to the crystallisation of titanomagnetite. As aforementioned, the stability of magnetite is greatly reduced in reducing systems such that it crystallises much later in the differentiation sequence, enabling early iron enrichment. However, when magnetite does crystallise, it induces a significant decrease in both Fe and Ti, given that the abundance of ferromagnesian phases is greatly diminished at the end of the differentiation sequence (*table 2.1.*).

4.2.4. K_2O-Na_2O

Sodium and potassium are broadly incompatible in gabbroic minerals, however, the former displays a relatively linear increase, perhaps due to the gradual uptake of Na in plagioclase (*figure 4.1f*). This effect is most pronounced at high percentage of crystallisation, owing to the increasing amount of Na in plagioclase. K_2O, by contrast, exhibits a curvilinear increase, which is consistent with experimental trends (e.g. Toplis and Carroll, 1995; *figure 4.1g*). This behaviour shadows that of an incompatible element with roughly constant $D_{Solid-Melt}^{K}$ undergoing fractional crystallisation (Allégre and Minster, 1978). Despite the fact that potassium feldspar becomes a prevalent crystallising phase in the fayalite granophyres onwards, it doesn't appear to affect the concentration of K_2O in the remaining liquid. This may be due to the fact that the K-feldspar crystallises later and hence residual liquid is negligible. Alternatively, the K-feldspar is too buoyant to gravitationally segregate from the remaining liquid, and its elevated abundance is a function of its in-situ crystallisation from a K-rich liquid. These possibilities also apply to quartz, because SiO_2 shows broadly the same evolution as K_2O.

The stability of amphibole in the main sequence rocks and amphibole and biotite in pegmatites suggests that Na and K (in addition to H_2O) reach relatively high concentrations. The presence of biotite, even in mafic pegmatites is attributed to their elevated K contents.

4.2.5. The Crystallising Assemblage

While binary Harker diagrams are illustrative for determining the relative contributions of the crystallising phases at a given level of differentiation, these relationships may be more effectively visualised in ternary diagrams. Projecting the melt compositions into normative mineralogies also provide some quantification as to the expected phase proportions.

The AFM diagram, (*figure 4.2c*) is an instructive diagram for detailing the extent and magnitude of the iron enrichment trend, as controlled by the timing of magnetite saturation. The rocks show a systematic increase in $Fe_2O_3^{(T)}$ with decreasing MgO, owing to the co-precipitation of plagioclase and pyroxenes. Alkali enrichment is modest until the crystallisation of magnetite, at which point the MgO stays relatively constant with respect to changes in $Fe_2O_3^{(T)}$ and alkalis.

In contrast to simple chemical discrimination diagrams, normative projections account for all oxide components in the bulk rock and formulate compositions and modal abundances of mineral phases according to set guidelines (*figure 4.2a*). The normative projection (Kelsey, 1965) from plagioclase differentiates between the KI Basalts and the chilled dolerites of Red Hill; where the latter lie on an orthopyroxene control line from the former, consistent with its presence as a phenocryst phase in both localities. This indicates the magma began in the orthopyroxene phase field before becoming saturated in both augite and pigeonite in subequal proportions, delineating a trend towards the quartz apex. The final stage of crystallisation in the granophyres is typified by augite-quartz, again in agreement with petrographic observations.

The mineral recalculation shown in (*figure 4.2b*), projected from olivine according to Grove (1993), after Tormey et al. (1987) highlights the difference between the pegmatites and the main series rocks. As expected from analysis of binary plots, the pegmatites are clearly saturated with greater proportions of plagioclase and comparatively less clinopyroxene. The main sequence shows an initial control by clinopyroxene (augite+pigeonite), moving towards the plagioclase apex before it, too, joins the crystallising assemblage. Subsequent liquid evolution shows cotectic precipitation of plagioclase and pyroxene, with plagioclase predominating. Both the pegmatitic liquid and the main liquid evolution terminate at the granophyres, which show the greatest enrichment in normative quartz, as indicated through petrographic studies.

Figure *4.2d* details a point-counting study (McDougall, 1962), which summarises the trends delineated in the preceding ternary projections. It edifies the early predominance of pyroxene, which is slowly superseded by plagioclase and finally trending towards alkali feldspar-quartz compositions. The presence of two feldspars throughout the crystallisation history suggests the pressures of crystallisation are high enough such that the compositions lie on a Ab-Or-Qtz eutectic minimum, rather than the alkali feldspar-quartz cotectic found at pressures lower than .2GPa (Ebadi and Johannes, 1991, *section 4.3.3*.).

4.2.6. Summary

The major element chemical trends and the crystallising mineral assemblage provide qualitative estimates for the conditions of differentiation. The Red Hill intrusion preserves a succession of liquids produced from fractional crystallisation of low pressure gabbroic minerals, initially orthopyroxene, which was quickly replaced by a three-phase assemblage of augite-pigeonite-plagioclase. These three minerals characterise the bulk of the rocks which comprise the Red Hill intrusion, and result in iron enrichment without a significant increase in SiO_2 (*figure 4.1a*). CaO and Al_2O_3 become impoverished with continued fractional crystallisation, whilst TiO_2, Na_2O, and K_2O all behave incompatibly (*figure 4.1.*). TiO_2, however, is coupled with $Fe_2O_3^{(T)}$, and is depleted by the crystallisation of magnetite late in the sequence; while at the same time it induces significant silica and relative alkali enrichment. This delayed saturation of magnetite indicates that the liquid was quite reduced, typical of other tholeiitic intrusions (e.g. the Skaergaard; McBirney and Naslund, 1990; Jang et al., 2001). Additionally, the high plagioclase/pyroxenes ratio is suggestive of low water activity, a conclusion supported by the general dearth of hydrous phases preserved throughout the sequence. Major element evidence points to a high volatile, high K and higher modal plagioclase crystallisation path followed by the pegmatitic rocks with respect to the main sequence of rocks at Red Hill.

Qualitatively, it appears that the Red Hill magma evolved at conditions of relatively low pressure, low oxygen fugacity and low water activity. This overview concludes that both low fo_2 and low $a_{H_2O}^{liquid}$ are pre-requisites for evolution along a tholeiitic differentiation trend (Fenner, 1929). Low fo_2 acts to delay magnetite saturation, while low $a_{H_2O}^{liquid}$ increases the crystallising plagioclase/pyroxenes ratio, promoting the enrichment of iron in the residual melt.

4.2.7. Temperature Estimates

Grove and Juster (1989) and Sisson and Grove (1993) have demonstrated that the bulk composition of a liquid can be used to derive temperature estimates via purely empirical equations as long as the necessary boundary conditions are enforced with regards to the fractionating phases and bulk composition of the rock. The formulation of Grove and Juster (1989) is calibrated for assemblages which include olivine, low-Ca pyroxene, high-Ca pyroxene and plagioclase at 1atm, the 4 phases (+liquid) constitute a low variance assemblage, ensuring temperatures changes may be expressed by changes in Mg#, NaK# (Na+K/(Na+K+Ca)) and TiO_2 content. Conversely, the calibration of Sisson and Grove (1993), is tailored towards assemblages which contain augite and plagioclase, but not low-Ca pyroxene or olivine. Their equation however accounts for the presence of water, which significantly depresses solidus temperatures of ferromagnesian silicates in equilibrium with a silicate melt (e.g. Hirschmann, 1999b; Feig et al., 2010). Additionally, the calibration is viable between 1atm and 12kbars, and uses Al# (Al/(Al+Si)) rather than TiO_2 content to predict temperatures. This is pertinent in tholeiitic systems where TiO_2 does not show a monotonic trend with differentiation. Furthermore, the granophyres are in equilibrium with only augite and plagioclase, and although the dolerites contain low-Ca pyroxene, they do not contain olivine. Additionally, a pressure term (in kbars) is included, which is also beneficial for plutonic rocks. As a result, the formulation of Sisson and Grove (1993) is preferred, and was applied to the entire dataset (*figure 4.3.*):

$$T(°C) = 969.33 - 33.1(H_2O) + 0.0052(P-1) + 742.7\left(Al^{\#}\right) - 138\left(NaK^{\#}\right) + 125.3(Mg^{\#}) \quad (4.1.)$$

The samples which delineate a trend to lower temperatures at a given Mg# are the pegmatitic rocks, owing to their higher concentration of K and lower concentration of Al.

4.3. Mineral Chemistry and Mineral-Liquid Equilibria

The chemistry of the mineral phases that precipitate to control the liquid line of descent depends upon the relationships between a crystallising phase and the chemical properties of the melt. Quantitative parameterisation of such relationships, and those between the minerals themselves, may garner important evidence as to the evolutionary conditions the magma body was subjected to.

4.3.1. Pyroxenes

Pyroxenes of the augite, orthopyroxene and pigeonite series are important phases in the crystallisation of the Red Hill intrusion, and, together, are present throughout the entire crystallisation sequence (*figure 2.8.*), making them invaluable records of the state of the coexisting liquid.

The pyroxenes present in the Red Hill intrusion are dominated by quadrilateral components, that is, they consist of solid solutions between Ca, Mg and Fe^{2+} (En+Wo+Fs ≥ 90%), with minimal participation of other elements (Al, Na, Fe^{3+}). This makes them amenable to comparison with pyroxenes from other tholeiitic intrusions, as well as to temperature determinations using the graphical geothermometer (Lindsley, 1983).

4.3.1a. Pyroxene Thermometry

Thermometric estimates based on pyroxene compositions are founded upon the parameterisation of calcium exchange between co-crystallising augite and low-calcium pyroxene. Specifically, the Ca-content of augite decreases with increasing temperature, while that of the low Ca phase (orthopyroxene or pigeonite) increases. The dodecahedral (VIII-fold) M2 site in augite is an ideal size for Ca^{2+}, but both M1 and M2 in low Ca pyroxene are octahedral, and therefore slightly too small for Ca^{2+} (Papike et al., 2005). Calcium becomes less discerning between low and high-Ca pyroxene at high temperatures due to the relative ease of distortion of the crystal lattice.
Increasing pressure widens the solvus between augite and low Ca-PX, and the three-pyroxene tie triangles become more iron-rich. Furthermore, the 'forbidden zone' of pyroxenes, which lies to the Fe-side of the consolute point becomes smaller; eventually disappearing near 11.5 kbars (Lindlsey, 1983).

While the pyroxenes at Red Hill exhibit exsolution, the scale of these lamellae are too small to appreciably affect the microprobe analyses, and hence the recombination of the host pyroxene and its lamellae is superfluous. However, given the extensive zoning exhibited by both pigeonite and

augite, a graphical geothermometer such as that of Lindlsey (1983) and Sack and Ghiorso (1994) is more instructive; rather than attempting to assess equilibrium between each pyroxene zone.

Taking these considerations into account, figure *4.4.* was formulated at 0 kbars. The homogeneous orthopyroxene phenocrysts of the chilled dolerites and KI basalts (En_{83}), which are purportedly in equilibrium with the rare augite phenocrysts in the same rocks, yield temperatures touching on 1200°C. The spread of the main-sequence samples record temperatures between 1150°C and 1000°C; with the resolution of the Wo content in the pyroxenes a limiting factor in improving the precision for these temperatures. The slight tendency for the pyroxenes to record increasing temperature with decreasing Di content suggests crystallisation at a pressure greater than 0 kbars. Most pyroxenes plot to the stable side of the forbidden zone at 5 kbars, insinuating pressures close to or less than this value. Temperature estimates are limited to those rocks containing coexisting pigeonite and augite; rendering the granophyres, which only contain ferroan augite and later, hedenbergite, inappropriate for temperature determinations through this method. The point at which pigeonite precipitation ceases, the augite compositions are allowed to become more Ca-enriched and temperatures are not constrained by Ca-exchange with pigeonite (*section 4.3.1c*).

4.3.1b. Pigeonite thermometry

An additional cross-check may be performed using temperatures derived from single pigeonites. The method was developed by Singletary and Grove (2003) in view of applications towards pigeonites in urelites (igneous rocks quenched from superliquidus conditions). The parameterisation is calibrated against crystallisation experiments wherein only pigeonite and olivine are the two mineral phases, and their CaO and MgO content is found to be a strong function of temperature. The expression used in the calculation is:

$$T(°C) = 812.6 + 11.1 \times MgO(mol\%) + 4 \times CaO(mol\%) \quad (4.2.)$$

Pigeonite-derived temperature estimates are largely in agreement with those from two-pyroxene thermometry. The chilled dolerites record temperatures of 1215±35°C and 1174±35°C, while the main-phase dolerites record temperatures down to 1030±13°C. Plotted against Mg#, the samples show the expected decrease in temperature with decreasing Mg# (*figure 4.5.*). One sample, PS63, a pegmatitic dolerite, plots to much lower temperatures for its Mg#. The reason for the discrepancy is not apparent, but may be related to that fact that the pegmatites follow a different fractionation trend in major element space (*section 4.2.*). This lower temperature estimate is consistent with the lower temperature estimated by the Sisson and Grove (1993) thermometer for the bulk rock.

Comparisons between temperature estimates from pigeonite thermometry are in agreement within error at higher temperatures between the pigeonite thermometer of Singletary and Grove (2003) and the liquid thermometer of Sisson and Grove (1993). The temperature estimates diverge at lower temperatures, with the pigeonite thermometer consistently underestimating the temperatures (*figure 4.6.*). This is likely due to the fact that the pigeonites in the more differentiated rocks lie outside the range of the Singletary and Grove (2003) calibration, which was based on anhydrous,

high Mg# (>46.7) glass compositions between 1150-1220°C, the temperature range over which the thermometric estimates are most agreeable.

4.3.1c. Pyroxene Trends and the Origin of the Pyroxene Minimum

The pseudo-ternary pyroxene quadrilateral, which plots the molar Ca, Mg and Fe components of pyroxenes, is not only a convenient method by which to differentiate between pyroxene types, but also to track their chemical evolution through Fe-Mg exchange. Studies of tholeiitic intrusions illustrate their well-established behavioural traits; namely (Campbell and Nolan, 1974):

1. Early crystallisation of magnesian orthopyroxene in concert with magnesian augite
2. Replacement of orthopyroxene with pigeonite, and continued co-precipitation of these two phases
3. Cessation of pigeonite crystallisation, which is accompanied by a minimum in Ca-content of augite and the appearance of fayalite
4. Disappearance of fayalite, leaving the precipitation of augite alone, which becomes more calcic

The two important transitions in this sequence are controlled by the chemical properties of the liquid; the commencement and disappearance of pigeonite.
The appearance of pigeonite can be described by a reaction of the form:

$$orthopyroxene + melt = pigeonite + augite \qquad (4.3.)$$

This reaction is shown to be sensitive to temperature at a given Mg# (Huebner and Turnock, 1980; Lindlsey, 1983), with pigeonite being favoured by higher temperatures, and, similarly, by a lower Mg# at a certain temperature. Tholeiitic liquids evolve along T-Mg# slopes in which both decrease during differentiation, due to the quick depletion in MgO, and concomitant Fe enrichment (*section 4.2*.). Grove and Juster (1989), recognised that the effect of increasing fo_2 promotes precipitation of ferromagnesian phases with higher Mg# (where Mg# = Mg/(Mg+Fe^{2+})). This is a result of reducing a_{FeO}^{liquid} by increasing the Fe^{3+}/ΣFe ratio of the melt. Since orthopyroxene is the stable low-Ca pyroxene at higher Mg#s, increasing the fo_2 of the liquid will induce its crystallisation in preference to pigeonite. However, in tholeiitic liquids, the Mg# decreases monotonically owing to the delay of magnetite precipitation. Thus, due to the tendency for greater iron enrichment to occur in more reduced intrusions (e.g. Rutherford et al., 2006); their orthopyroxene-pigeonite transition should occur relatively early. Such an interpretation is consistent with the high Mg# of the pigeonite in the Tasmanian Dolerites (up to 80; *figure 4.10.*); and its presence in the chilled dolerites.

Using the calibration of Grove and Juster (1989), it can be seen that the chilled dolerites plot on the transition of orthopyroxene and pigeonite stability (*figure 4.7.*). This is in agreement with the observed assemblage - orthopyroxene phenocrysts in the chilled dolerites are indicative of their early stability, while pigeonite's presence in the groundmass suggests differentiation towards the pigeonite-stable side of the equilibrium. Calc-alkaline liquids, whose high fo_2 triggers the early precipitation of magnetite, follow a trend of near-constant Mg# with decreasing temperature owing to the depletion of $Fe_2O_3^{(T)}$.

Following the replacement of orthopyroxene by pigeonite in the Red Hill sequence, its co-precipitation with augite, in addition to plagioclase, defines the mineralogy of the bulk of the doleritic rocks in the intrusion. The Ca-content of both pyroxenes is defined by the temperature of pyroxene crystallisation (Lindsley, 1983, *section 4.3.1a*). However, a conspicuous feature of pyroxene crystallisation in tholeiitic intrusions is the coincidence of the minimum Wo content of high-calcium clinopyroxene (augite) with the cessation of pigeonite crystallisation (*figure 4.4.*). This pyroxene 'minimum' occurs at varying pyroxene Mg# in different tholeiitic intrusions (Campbell and Nolan, 1974), after which point the augite is permitted to fractionate towards the hedenbergite apex. This minimum point is controlled by the thermodynamic properties of the liquid with which the pyroxene is in equilibrium.

At Red Hill, and in other tholeiitic intrusions, the disappearance of pigeonite is accompanied by the arrival of fayalite, implying a reaction that limits the stability of pigeonite of the form (Lindsley and Munoz, 1969; Campbell and Nolan, 1974):

$$Fe_2Si_2O_6 = Fe_2SiO_4 + SiO_2 \qquad (4.4.)$$

Evidently, an increase in the silica activity of the melt will force the equilibrium to the left and prolong the stability of pigeonite. At equilibrium, the $a\mathrm{SiO_2}$ of the liquid may be calculated:

$$\ln a_{SiO_2}^{liquid} = \frac{\Delta G}{RT} + \ln a_{Fe_2Si_2O_6}^{pigeonite} - \ln a_{Fe_2SiO_4}^{olivine} \qquad (4.5.)$$

The activity of the ferrosilite and fayalite components in pigeonite and olivine, respectively, may be derived through EPMA analyses of the mineral phases (*section 1.4., table A9, table A13*), and, assuming ideal mixing (the activity coefficient, γ = 1) that $a_{Fe_2Si_2O_6}^{pigeonite}$ and $a_{Fe_2SiO_4}^{olivine}$ are equivalent to $X_{Fe_2Si_2O_6}^{pigeonite}$ and $X_{Fe_2SiO_4}^{olivine}$.

For the components in their standard states (pure solids of unit activity and silica glass) at the temperature and pressure of interest, the variation of $\log a_{SiO_2}^{liquid}$ with temperature can be represented by a purely empirical equation of the form (Carmichael 1970; Nicholls et al., 1971; Campbell and Nolan, 1974):

$$-log\ K = \frac{A}{T} + B + C\frac{(P-1)}{T} \qquad (4.6.)$$

Where A, B, and C are constants given by linear regression of experimental datasets. Having calculated the silica activity of the liquid at a given state, these may then be compared to Low Ca-PX/Olivine and quartz equilibria. Since the equilibrium constants of these equilibria, and hence their position in En-$a_{SiO_2}^{liquid}$ space, are pressure and temperature dependent, a broad estimate for both these parameters may be obtained.

The $a_{SiO_2}^{liquid}$, even when the liquid is at its most magnesian, is still well above the OPX-Ol equilibrium curve (*figure 4.8.*). This is manifest in the absence of olivine in any of the chilled dolerites (cf. McDougall, 1962; Hergt et al., 1989a), and is typical of tholeiitic liquids owing to their derivation

from low-pressure, incongruent melting of orthopyroxene in the mantle, producing siliceous liquids (*section 3.2.1*).

The silica activity of the liquid intersects the quartz curve at ≈En_{38}, indicating quartz precipitated before fayalite, as observed in the dolerites which have cumulus quartz. The liquid crosses the OPX-Ol curve at slightly lower En contents, indicative of the delayed crystallisation of fayalite as a result of high $a_{SiO_2}^{liquid}$ (*equation 4.4.*). If $a_{SiO_2}^{liquid}$ were lower, then the Fe/(Fe+Mg) of the last pigeonite to crystallise would be more magnesian. Increasing the temperature of crystallisation could produce a similar effect, however, this is well constrained independently through thermometric analyses (*section 4.2.7., 4.3.1.*). The pressure of crystallisation, which is less well known, has a similar effect, since the volume change of the reaction (ΔV_{rxn}) is positive (Carmichael, 1970; Nicholls et al., 1971), in that the low-calcium pyroxene is favoured at higher pressures. The presence of granophyric intergrowths, fine exsolution features, and abundant plagioclase qualitatively suggest relatively low pressures of crystallisation, within several kilometres of the surface. Commensurate with these observations, the estimate of 3 kbars roughly fits the succession of quartz and fayalite for the liquid's calculated silica activity.

The other component common to both minerals, iron, may also play a limiting role in pigeonite stability:

$$\frac{1}{2}Fe_2Si_2O_6 + FeO = Fe_2SiO_4 \qquad (4.7.)$$

This equilibrium may explain the protracted stability of pigeonite in tholeiitic systems. Since magnetite crystallisation is delayed, Fe^{2+} is depleted through its incorporation into ferromagnesian silicates during the early fractionation stage. This decreases a_{FeO}^{liquid}, forcing the equilibrium to the left, thereby stabilising pigeonite. However, upon magnetite precipitation, $a_{Fe_2O_3}^{liquid}$ drastically decreases because of its compatibility in magnetite. Therefore, a_{FeO}^{liquid} increases passively (i.e., through removal of Fe^{3+}), perhaps instigating fayalite precipitation. Such a mechanism would be consistent with the co-precipitation of magnetite and fayalite (+augite) as the two primary iron-bearing phases in the fayalite granophyres, rather than pigeonite and augite in the quartz dolerites (*section 2.3.*). Since this relationship hinges upon the crystallisation of magnetite, which is fo_2-dependent, it follows that the pyroxene minimum is also a function of oxygen fugacity. In experimental modelling of a tholeiitic magma closed to oxygen exchange, Toplis and Carroll (1996), also observed an extension of the Fe/(Fe+Mg) of the augite at the pyroxene minimum with decreasing fo_2. The low fo_2 prolongs Fe^{3+} enrichment with corresponding Fe^{2+} depletion. The precipitation of magnetite should not affect $a_{SiO_2}^{liquid}$ in the Red Hill intrusion because it is already at quartz saturation, but in other, less siliceous tholeiitic intrusions, this may help prolong pigeonite's existence (*equation 4.4.*).

Minor elements that have a disproportionately large effect on mineral-liquid equilibria, such as phosphorus (e.g. Mallmann et al., 2009), could also influence the order and timing of crystallisation. Dissolved phosphorus, which occurs as PO_4^{3-}, preferentially bonds with network modifying cations (M^{3+}) over Si^{4+}, owing to the greater electronegativity of P^{5+}. Thus, Si-O-M networks are disrupted, and P-O-M networks are formed, increasing the polymerisation of silicate networks (Si-O-Si) (Toplis

et al., 1994). In doing so, phosphorus increases the activity coefficient of silica in the melt ($\gamma_{SiO_2}^{liquid}$), which, at a given $X_{SiO_2}^{liquid}$, increases the $a_{SiO_2}^{liquid}$. This has a two-fold effect:

1. Increasing $a_{SiO_2}^{liquid}$ pushes equilibrium *4.4.* to the left, facilitating the preservation of pigeonite with respect to fayalite
2. It favours the formation of plagioclase (and indeed feldspars in general) owing to their more polymerised structure

The first point may be tested quantitatively. Using $K_D{}_{OPX-Liq}^{Mg-Fe}$ ≈ 0.23 from Bedard (2007), it can be seen that the most ferriferous pigeonite in the Red Hill suite (En_{23}) should be in equilibrium with a melt of Mg# ≈ 18.

A melt of this composition is also marked by the crystallisation of cumulus apatite, and a concomitant decrease in phosphorus content thereafter (*figure 4.9.*). The effect of phosphorus in polymerising the melt is ameliorated, and $a_{SiO_2}^{liquid}$ should experience a relative decrease. Thus, the disappearance of pigeonite may also be aided by the saturation of apatite.

Pigeonite's replacement of orthopyroxene as the low-Ca pyroxene and consequent perseverance is a product of the rapid decrease in Mg# with temperature in tholeiitic systems. The eventual disappearance of pigeonite and subsequent appearance of Ca-poor phases (fayalite, magnetite) permits the Ca enrichment of augite, as the predominant Ca-bearing phase. The point at which this occurs is a strong function of $a_{SiO_2}^{liquid}$, but may also be subordinately affected by changes in a_{FeO}^{liquid} (which depends on fo_2) and phosphorus content.

4.3.1d Compositional Zonation

The pyroxenes of the Red Hill intrusion display prominent and extensive compositional zoning throughout the doleritic section of the sequence (*section 2.3.2.*). Orthopyroxene phenocrysts present in the chilled dolerites (and Kangaroo Island basalts) are the exception, being of a homogeneous En_{83} composition. For the majority of the differentiation history, however, the pyroxenes may be subdivided into the pigeonite series and augite series, defined by their low and high Ca-contents, respectively. The successive zones of overgrowth reflect the cooling history, melt chemistry, and entrance and exit of other crystals phases.

In order to characterise these changes, a comprehensive dataset was compiled through EPMA analyses (*section 1.4.*), and consists of ≈650 augite datapoints, ≈300 pigeonite datapoints, and ≈150 orthopyroxene data points, collected over 13 samples which are representative of the differentiation sequence.

All pyroxenes are normally zoned in terms of Fe-Mg exchange (*figure 4.10a*), consistent with the uniform drop in Mg# in the melt with differentiation as a result of early Fe-enrichment. A salient characteristic is that a single crystal shows almost as much variation in Fe-Mg as the entire set of doleritic whole rocks. For example, the pigeonite in figure *2.4a*; displays Mg# changes from 72 in the

core to 29 at the rim, nearly encapsulating the complete range of pigeonite compositions in all the samples studied.

Owing to Mn's analogous geochemical behaviour with respect to Fe^{2+} (e.g. Humayun, 2004); Mn trends largely mirror those of Fe in pyroxenes. This suggests that Fe is predominantly divalent in the pyroxenes of the Red Hill intrusion. Pigeonite and early orthopyroxene are displaced to systematically higher Fe and Mn concentrations at a given Mg# compared to augite (*figure 4.10a,d*). Recognition of such a relationship was reported by Huebner and Turnock (1980); and is attributed to the differing site preferences of Fe^{2+} (and therefore Mn^{2+}) in pyroxenes. Because the augite $^{VIII}M2$ site is nearly completely occupied by Ca^{2+}, there remains only one available site for Fe-Mg exchange ($^{VI}M1_{augite}$). However, the size of the $^{VI}M2_{low\text{-}Ca}$ site is more tailored towards hosting Fe^{2+} than is $^{VI}M1_{augite}$, and hence, at a given melt Mg#, the pigeonite crystallising in equilibrium with it will be more ferriferous than the coexisting augite (*figure 4.10a*). Further corroborating this is that the lowest pigeonite Mg# at the point of magnetite crystallisation is En_{23}, whereas augite at this interval displays Mg#s near 30. This feature cannot be explained by systematically earlier crystallisation of augite compared to pigeonite; which would confer a higher Mg# to the augite. Such a scenario is precluded because pigeonite is typically seen consertally intergrown with augite, and often cores it, despite its lower Mg# *(figure 4.11.*). Thus, it appears as though augite and pigeonite usually precipitated in concert, with augite post-dating pigeonite in some cases.

In general, the well-developed zoning necessitates that a given parcel of liquid was in equilibrium with the same pyroxene over an extended period of time, insinuating relatively static conditions within the magma chamber during cooling. However, the crystallisation occurred at such a rate that the earlier formed zones were unable to re-equilibrate with the new liquid composition, and the subsequent zone became more iron-rich. As iron enrichment occurs in the liquid, it becomes more dense, and therefore resistant to flow, which may prevent efficient mixing over the scale of the magma chamber, and therefore the volume of liquid around the crystallising pyroxene becomes increasingly depleting in MgO, causing resulting zones to have lower Mg#. The implications of this are elaborated upon in section *4.7*.
The extent of Fe-Mg zonation is non-existent in the pyroxenes of the most differentiated granophyres, range in composition from $Di_{25\text{-}10}$. These pyroxenes evolve towards the hedenbergite end-member at near-constant Mg#. This can be attributed to magnetite crystallisation, which depletes the liquid in Fe^{2+}, Fe^{3+} at a similar rate to the depletion of Mg by the pyroxenes, holding the Mg# of the liquid constant.

Calcium zonation is much less prominent and indeed more sporadic, especially in pigeonites, where it shows only a slight increase with decreasing Mg# (*figure 4.10c*). Augite shows the opposite trend, and has a propensity to decrease slightly when in coexistence with pigeonite (*section 4.3.1a*). The inflection of the trend towards higher Ca-contents in augite is synchronous with the disappearance of pigeonite, and precipitation of fayalite and magnetite (*section 4.3.1c*).

Ti in clinopyroxene may be incorporated as the $CaTiAl_2O_6$ molecule through the coupled substitution $^{VI}Ti^{4+} + 2^{IV}Al^{3+} = {}^{VI}M^{2+} + 2^{IV}Si^{4+}$, (Verhoogen, 1962; Villiger et al., 2007) indicating that both Ti and Al should increase. A Ti/Al ratio of ½ would be evidence for such a substitution. However, the Ti/Al

ratio of the Red Hill pyroxenes increases uniformly from ≈0.05 to ≈0.70 with decreasing Mg# (*figure 4.10b*). This can be reconciled through the differing behaviour of Al_2O_3 and TiO_2 in the melt.
Al_2O_3 in clinopyroxene is controlled by $a_{SiO_2}^{liquid}$, through the following equilibrium (Carmichael et al., 1970):

$$CaAl_2SiO_6 + SiO_2 = CaAl_2Si_2O_8 \qquad (4.8.)$$

Thus, the gradual decrease in Al_2O_3 in pyroxene can be explained by an increase in $a_{SiO_2}^{liquid}$, as calculated via fayalite-low calcium pyroxene equilibria (*section 4.3.1c*). Similarly, since pigeonite and augite co-crystallise with plagioclase, prompting $a_{Al_2O_3}^{liquid}$ to decrease, this may also contribute to the falling $X_{Al_2O_3}^{pyroxene}$ (Villiger et al., 2007).

Contrarily, $a_{TiO_2}^{liquid}$ is continually enriched prior to magnetite crystallisation. TiO_2 in pyroxene reflects this increase in the melt, and also shows a sharp but erratic decrease in the most differentiated hedenbergites (*figure 3.10b*). However this does not correlate with the timing of magnetite crystallisation, possibly reflecting local anomalies due to sluggish diffusion of Ti in the melt. In any case, the lack of correlation between Al and Ti suggests the $CaTiAl_2O_6$ component does not facilitate their incorporation in the Red Hill pyroxenes. Rather, Fe shows a strong positive correlation with Ti, similar to that observed in the whole rock trends. This may point to the presence of the $CaFeTi_2O_6$ molecule, or a $^{VI}Fe^{2+} + {}^{IV}Ti^{4+} = {}^{VI}M^{2+} + {}^{IV}Si^{4+}$ substitution.

Pyroxenes of the Red Hill intrusion show extensive Fe-Mg zonation, high Fe/(Fe+Mg), Mn, and low Na and Al, characteristic of tholeiitic pyroxenes (Nisbet and Pearce, 1977). The pyroxene trends elucidated upon here are also consistent with those identified in other tholeiitic systems (e.g. Turner et al., 1992), and particularly in the Ferrar province itself. The 8-9km deep, Jurassic, Dufek intrusion, located in the Pensacola Mountains, Antarctica, (Himmelberg and Ford, 1976) displays the same pyroxene succession as the Red Hill intrusion. There is a lack of magnesian olivine, and the most primitive magmas contain orthopyroxene (bronzite) and augite, before orthopyroxene gives way to inverted pigeonite + augite assemblages. Fayalite of exactly the same composition as in the Red Hill Fayalite Granophyres (Fa_{95}) replaces the inverted pigeonite, before green hedenbergite become the only ferromagnesian silicate. The pyroxenes in the Dufek intrusion are also depleted in Al, and it too decreases with Mg#, both indicative of high $a_{SiO_2}^{liquid}$.
On a study performed on the pyroxenes of the Tasmanian Dolerites (Hall et al., 1988), much the same trends were identified, particularly the complex Fe-Mg zoning of both augite and pigeonite, their increasing Ti/Al with differentiation, and the inference of low oxygen fugacity of the liquid during crystallisation.

4.3.2. Amphiboles

Amphiboles are rare in the Red Hill intrusion, commonly occurring as late-stage overgrowths on primary augites, though sometimes forming separate phases, in the more differentiated quartz dolerites and fayalite granophyres. They are conspicuously absent in the most alkali-enriched granophyres, however.

The amphiboles present belong to the calcic series (Ca > 1.5 atomic formula units (afu) per 23O), contain Na+K > 0.5 afu, and less than 0.5 afu Ti. They may then be classified according to the number of Si per afu and their Mg# (*figure 4.12.*).

The amphiboles are ferroedenites, but trend towards ferropargasitic compositions as their Mg# decreases. Their ferriferous nature is commensurate with their mantling of earlier-formed pyroxenes. Deer et al., (1997) show that amphiboles are systematically more iron-enriched than the pyroxenes they coexist with, i.e., $K_{D_{PX-Amph}}^{Fe/Mg} < 1$, consistent with the observations at Red Hill (*figure 4.4.*).

Amphiboles offer the possibility to derive pressure estimates for the crystallisation of the intrusion due to an increase in the occupancy of both tetrahedral (IV-fold) and octahedral (VI-fold) site by Al as pressure increases, an exchange vector of the form $^{IV}Al^{3+VI}Al^{3+}(Si^{4+}M^{2+})^{-1}$. However, this may also be affected by the edenite substitution, $NaAl([]Si)^{-1}$, and therefore quoted uncertainties are typically ±0.5 kbar in the range 2-8 kbars (Johnson and Rutherford, 1989). Their calibration is based on experimental charges of natural samples from both volcanic and plutonic rocks, and equilibrated at variable fo_2, yielding the following linear equation:

$$P(kbars) = -3.46(\pm 0.24) + 4.23(\pm .13)\ ^{T}Al\ (r^2 = 0.99) \qquad (4.9.)$$

The barometer requires that the amphiboles be in equilibrium with quartz, otherwise the concentration of Al becomes a function of $a_{SiO_2}^{liquid}$ in addition to pressure. Cumulus quartz is present in the samples where amphibole is present, thereby reducing the thermodynamic degrees of freedom, and hence this caveat does not apply. The pressure estimates are plotted in figure *4.13*.

Most amphiboles record pressures between 1 and 3 kbars, however, immediately obvious is a trending of increasing Al^T with decreasing Mg#, which is unexpected given that the amphiboles should record the same pressure (within uncertainty) throughout the entire sequence (*figure 4.13.*). This appears to be related to the edenite-pargasite substitution $^{IV}Al^{3+VI}Al^{3+}(Si^{4+}M^{2+})^{-1}$, indicating the Mg# of the melt may also affect this exchange. This may also be influenced by oxygen fugacity, due to the similar ionic characteristics of Fe^{3+} and Al^{3+}, wherein an increase in $Fe^{3+}/\Sigma Fe$ increases competition for site occupancy in the amphibole, stifling the exchange reaction. Given the systematics of the pressure-dependence of the exchange reaction, there is no reason *a priori* to favour any given analysis over another, and therefore crystallisation conditions are taken to be 1-3kbars. Typically, however, igneous amphiboles are unstable below 1.5 kbars, owing to insufficient dissolved H_2O in the melt, concomitant with the increase in the water-saturated rhyolite solidus with decreasing pressure (Merzbacher and Eggler, 1984).

4.3.3. Feldspars

Plagioclase feldspar is a ubiquitous mineral phase in most planetary basaltic magmas, and persists into the most fractionated granophyres in the Red Hill intrusion. It is joined however by cumulus alkali feldspar in the granophyres.

The feldspars are subdivided according to the solid solutions between K-Na and Na-Ca, but not Ca-K, due to the size mismatch in their ionic radii.

Over 500 plagioclase and alkali feldspar compositions were obtained via EPMA analysis, and are plotted on a molar K-Na-Ca ternary diagram (*figure 4.14*.).

Plagioclase feldspars delineate the expected increase in the albite endmember with increasing fractionation, reaching almost pure albite in the granophyres (Ab_{98}). However, there is considerable overlap in the doleritic compositions, with even the quartz dolerites preserving plagioclase cores as calcic as An_{84}, where the most calcic plagioclase recorded in the intrusion is An_{89}. Normal zoning may be particularly extensive, with some plagioclase crystals recording compositions of An_{80} in the core to An_{25} in the rim. At other times, the crystals may show relatively more homogeneous compositions.
By contrast, the alkali feldspar series do not demarcate any particular trend with respect to the whole rock, showing relatively restricted Na-K exchange, preferring K-rich compositions during its crystallisation history. Cumulus K-feldspar is present in the fayalite granophyres onwards, however, analyses from granophyric intergrowths in more mafic dolerites exhibit similar chemical properties.

The tendency for alkali feldspars to increase their Ca-content towards more albitic compositions, and, similarly, for the plagioclase series to incorporate more potassium with higher albite contents is consistent with the ionic radius of Na^+ being intermediate between that of Ca^{2+} and K^+. However, the most albite-rich plagioclase coexists with the most potassic alkali feldspars, and does not show an elevated K-content.

The feldspars lack any exsolution lamellae (perthitic textures) between albite and orthoclase, rather occurring as separate crystals. This observation, in tandem with the very low concentration of the complementary ion in sodic or potassic feldspar in the granophyres, indicates the crystallisation of two separate feldspars from the melt. Alkali feldspars in the fayalite granophyres, however, do exhibit intermediate compositions, with 30-45 mol% Na, indicative of a hypersolvus origin. The scenario where two feldspars crystallise arises in subsolvus granitoids, where crystallisation at relatively high water pressures (P_{H2O} > 0.5 GPa) depresses the crystallisation interval of albite and orthoclase such that it intersects the solvus (field of two feldspars) (Bowen and Tuttle, 1950). Ca-content may also affect the system in a similar manner by raising the solvus, whereby the exclusion of H_2O and Ca from the alkali feldspars acts to stabilise the liquid phase in the system Or-Ab-Liquid, through a general reaction:

$$(Na, K)AlSi_3O_8 + H_2O + CaO = Liquid \qquad (4.10.)$$

This attests to the moderate pressures as identified by amphibole barometry (up to 3kbars), and significant portions of dissolved H_2O and CaO to instigate precipitation of separate alkali feldspars which are sufficiently close to their end-member compositions such that they do not undergo spinoidal decomposition. This may also be reflective of relatively quick cooling conditions, under which exsolution was not able to proceed.

4.4. Oxygen Fugacity

As detailed in the preceding sections, magnetite exerts a considerable influence on the evolution of the tholeiitic trend by not only controlling total iron contents, but also the ratio of $Fe^{3+}/\Sigma Fe$, which in turn controls the Mg# ($Mg/(Fe^{2+}+Mg)$) of the evolving melt. Considering that the prevailing oxygen fugacity is the main control on the saturation of magnetite, as evidenced through experimental studies (e.g. Snyder et al., 1993; Toplis and Carroll, 1995), it requires quantification if the evolution of a tholeiitic intrusion is to be thoroughly understood.

There are two common methods applicable for quantifying oxygen fugacity in intrusive bodies:

1. $Fe^{3+}/\Sigma Fe$ ratios of the whole rock (e.g. Kress and Carmichael, 1991; Nikolaev et al., 1996; Jaysuriya et al., 2004; O'Neill et al., 2006)
2. The magnetite-ilmenite thermobarometer (Buddington and Lindsley, 1964)

Both methods have their benefits and deficiencies, however, and the difficulties in applying them to plutonic complexes are considered prior to their application.

Due to the abundance of Fe compared to other polyvalent elements, the $Fe^{3+}/\Sigma Fe$ should control the redox state of the magma, with the chemical relation between the two being expressed by the equation:

$$Fe^{2+}O + \frac{1}{4}O_2 = Fe^{3+}O_{1.5} \qquad (4.11.)$$

At infinite dilution of FeO^T, the activity coefficients of Fe^{3+} and Fe^{2+} should be constant because the interactions between the two ions in the melt tend to zero (Jayasuriya et al., 2004). Thus, they act as trace elements and obey Henry's Law at low concentrations. However, Fe, as a major element in magmas, occurs up to 13.5wt% (Fe as $Fe_2O_3^{(T)}$) in the Red Hill intrusion. Thermodynamic modelling of experimental datasets suggests that non-ideal interactions in the melt occur with increasing $Fe_2O_3^{(T)}$ between the two iron valence states, leading to the formation of Fe^{3+}-Fe^{2+} complexes in the melt. This effect was corrected for linearly by assuming a lower coefficient than dictated by the stoichiometry of the reaction (.207 instead of .25, *equation 4.11.*) in the empirical equations of Kress and Carmichael (1991) and Nikolaev et al. (1996). However, it was subsequently shown that this correction method is erroneous for the cases in which there are minimal interactions between iron in the melt (i.e., where its concentration is low and hence the exponent is ideal; equal to 0.25) (Jayasuriya et al., 2004).

The accuracy of the method also relies upon robust corrections for the presence of alkalis, which are shown to promote the formation of Fe^{3+} in tetrahedral co-ordination, by the substitution $Fe^{3+}A^{+}(Si^{4+})^{-1}$ (Farges et al., 2004; Mysen and Richet, 2005; Jackson et al., 2005; Bingham et al., 2007). Increasing pressure imparts the opposite effect on the melt's oxygen fugacity, decreasing the $Fe^{3+}/\Sigma Fe$ through the preferential stabilisation of more densely-packed $^{VI}Fe^{2+}$ (O'Neill et al., 2006). The equation of O'Neill et al., (2006) accounts for all of these considerations, and was applied to the Red Hill suite:

$$\log f_{O_2} = 4\log\left(\frac{X_{Fe^{3+}O_{1.5}}}{X_{Fe^{2+}O_{1.5}}}\right) - \frac{28144}{T} + 13.95 + 3905\frac{X_{MgO}}{T} - 13359\frac{X_{CaO}}{T} - 14858\frac{X_{NaO_{0.5}}}{T} - 9805\frac{X_{KO_{0.5}}}{T} + 10906\frac{X_{AlO_{1.5}}}{T} + 110971\frac{X_{PO_{2.5}}}{T} - 11952\frac{(X_{Fe^{2+}O_{1.5}} - X_{Fe^{3+}O_{1.5}})}{T} + \left(\frac{33122}{T} - 5.24\right)\left[(1+0.241P)^{\left(\frac{3}{4}\right)} - 1\right] - \left(\frac{39156}{T} - 6.17\right)\left[(1+0.132P)^{\left(\frac{3}{4}\right)} - 1\right] \quad (4.12.)$$

The equation necessitates the conversion of weight % oxides to molar monoxides, and the pressure, in GPa, used was 0.3 (3 kbars). The temperatures (in °K) are taken from the whole-rock temperature estimates from Sisson and Grove (1993). The calculated fo_2s were plotted relative to the fayalite-magnetite-quartz (FMQ) buffer to account for the temperature-dependence of absolute fo_2 and facilitate comparison between samples (*section 3.2.9.*), and was calculated according to Ballhaus, (1991) because it includes a pressure term.

$$\log f_{O_2}^{FMQ} = 82.75 + 0.00484T - \frac{30681}{T} - 24.45\log T + \frac{940P}{T} - 0.02P \quad (4.13.)$$

The ΔFMQ values plotted in *figure 4.15.* are calculated according to:

$$\Delta FMQ_{Sample} = \log f_{O_2}^{Sample} - \log f_{O_2}^{FMQ} \quad (4.14.)$$

As elucidated in section *3.2.9.*, the chilled dolerites and Kangaroo Island basalts display oxygen fugacities between FMQ and one log unit below FMQ (FMQ-1). Dolerites and quartz dolerites with lower Mg# and MgO trend to higher values, up to FMQ+1.5, before the fayalite granophyres show the greatest positive deviation from the FMQ buffer at FMQ+3.5 (*figure 4.15*). The most differentiated granophyres then delineate a trend towards lower oxygen fugacities, reaching redox conditions as reduced as FMQ+1.5.

This initial increase in relative oxygen fugacity before an abrupt decrease coincident with magnetite saturation is indicative of differentiation in a system closed to oxygen exchange (Snyder et al., 1993; Toplis and Carroll, 1996). Under these conditions, there is a finite amount of oxygen available to the system, that is, the concentration of O_2 in the melt and total solids must remain constant. Early crystallisation of pyroxenes as the volumetrically dominant Fe-bearing phases drive the $Fe^{3+}/\Sigma Fe$ of the liquid to higher values, because the pyroxenes preferentially incorporate $^{VI}Fe^{2+}$ (Carmichael and Ghiorso, 1990; McCanta et al., 2004), and therefore, by mass balance, Fe^{3+} must be enriched in the coexisting melt phase (*equation 4.11.*). The $Fe^{3+}/\Sigma Fe$ content of the pyroxene in equilibrium with the melt is shown to be a positive linear function of the $Fe^{3+}/\Sigma Fe$ of the melt (McCanta et al., 2004). Given the low fo_2, and hence low $Fe^{3+}/\Sigma Fe$ of the Red Hill starting melt, the pyroxenes are deemed to incorporate negligible Fe^{3+}, a hypothesis substantiated by the stoichiometry of the mineral re-calculations (see appendices). The changing $Fe^{3+}/\Sigma Fe$ of the pyroxenes in equilibrium with the melt is manifest as a linear trend in fo_2-Mg# space (*figure 4.15b*).

Magnetite crystallisation is clearly distinguished by the sudden drop in $Fe^{3+}/\Sigma Fe_{melt}$ at MgO ≈ 1.5 wt% or Mg#≈20, as identified in the major element and pyroxene trends (*sections 4.2., 4.3.1*). The maximum relative fo_2 at the inflection point, coincident with magnetite precipitation, is a clear indicator of its dependence of the redox state of the system (e.g. Berndt et al., 2005; Botcharnikov et

al., 2008). Its formation in a closed system causes $Fe^{3+}/\Sigma Fe$ of the melt to decrease due to the sequestration of Fe^{3+} in the newly crystallised magnetite.

The relative fO_2 values seem quite high for a system initially beginning near ≈FMQ-0.5. Experimental studies show that, even though the increase in fO_2 during fractionation should be greatest in a system with low oxygen fugacity due to the decreased stability of magnetite, the relative magnitude of the change is about 1 log unit to the FMQ buffer (Toplis and Carroll, 1996). The increase in fO_2 over 3 log units as calculated by equation *4.12.* suggests that the change in relative fO_2 may have been overestimated. Since water is shown to have low activity in silicate melts due to the formation of OH^- groups (Carmichael, 1991; Botcharnikov et al., 2005), the increasing alkalis towards the granophyres may be responsible for such a discrepancy. Such an overestimation of the fO_2 (though in comparison to the Kress and Carmichael, (1991) formulation, which does not account for alkalis) was also reported by Schuessler et al., (2007) for an ultrapotassic (7.5 wt% K_2O), rhyolitic melt, intimating that some of that the high Fe^{3+} is in part due to alkali enrichment. In order to deconvolve the effects of alkalis on the redox ratio, the magnetite-ilmenite geothermobarometer was applied.

The magnetite-ilmenite equilibrium yields estimates of both fO_2 and their temperature of equilibration, based on the activites of ferric and ferrous iron in the solid-solution exchange reaction between the cubic (magnetite-ülvospinel) and rhombohedral (ilmenite-haematite) oxide series. Since alkalis are excluded from both oxide solid solutions, they should have relatively little impact on the derived fO_2 values. Oxides in intrusive complexes, due to their slow cooling, undergo subsolidus oxidation-exsolution, which involves Fe-Ti exchange and therefore perturbs the original activities of Fe and Ti in the oxides (*section 3.2.9.*). This effect is caused by the temperature-dependence of absolute fO_2; as the oxides cool at constant absolute fO_2, their position with respect to solid-solid buffers such as FMQ results in an increase in relative fO_2. The trajectory of this exchange dictates that relative fO_2 can only be increased (Lindsley and Frost, 1992; Frost et al., 1988) and so these values are maximum estimates.

Ilmenite is the only stable oxide phase in the chilled margins, its presence attesting to low oxygen fugacities and sufficiently high TiO_2 contents of the melt. Titanomagnetite is present as exsolution lamellae in the dolerites soon after, but has a composition near $Mt_{40}Üsp_{60}$, consistent with the low fO_2 of the liquid inferred from thermodynamic considerations (*figure 4.15.*). The ülvospinel component in titanomagnetite gradually decreases up to the fayalite granophyres and the Red Hill granophyres, reaching $Mt_{95}Üsp_5$. The magnetite content of the titanomagnetite grains then decreases down to Mt_{80} in the most differentiated O'Brien's Hill granophyres, coincident with the drop in $Fe^{3+}/\Sigma Fe$ of the melt. Ilmenite composition is uniform at Il_{97}, in accord with experimental studies (Toplis and Carroll, 1995; Botcharnikov et al., 2008), which demonstrate the ilmenite compositions show little variation below FMQ+0.5, and are invariably rich in the ilmenite component.

Molar recalculations on original ilmenite and titanomagnetite analyses were performed according to the method of Carmichael (1967), and temperature and fO_2 estimates were derived from the geothermobarometer of Spencer and Lindsley (1981). The dataset compiled comprises 130 oxide (titanomagnetite and ilmenite) analyses from five samples which encompass the range of

compositions in the Red Hill intrusion (dolerite, quartz dolerite, fayalite granophyres, and two granophyres).

Barometric fO_2s calculated by the magnetite-ilmenite geothermobarometer delineate a trend reminiscent of that calculated using the fO_2-Fe^{3+}/Fe^{2+} thermodynamic calibration (*figure 4.16.*). The range of oxygen fugacities recorded is more restrained using the barometric fO_2 geothermobarometer, lending support to the hypothesis that alkalis enhanced the $Fe^{3+}/\Sigma Fe$ ratio of the melt, and therefore the fO_2 estimates calculated using the expression of O'Neill et al., (2006). The range reported for barometric fO_2s is similar (1.3 log units) to that expected from experimental work on the tholeiitic Skaergaard ferrobasalt composition SC1 (Toplis and Carroll, 1996).

The fayalite granophyres, with an assemblage of quartz-fayalite-ilmenite-magnetite, are buffered by the FMQ equilibrium, suggesting that they should record oxygen fugacities quite close to it.

$$3Fe_2SiO_4 + O_2 \rightleftharpoons 2Fe_3O_4 + 3SiO_2 \qquad (4.15.)$$

The fact that these rocks appear to record redox conditions almost 1 log unit higher may indicate a dilution of the Fe_2SiO_4 component in fayalite, which could contribute to higher fO_2s. The FMQ reaction in the fayalite granophyres continues to proceed to the right during precipitation of fayalite, resulting in the formation of magnetite and quartz while fO_2 remains constant. When a_{FeO}^{liquid} becomes too impoverished to continue to precipitate fayalite, the oxygen fugacity of the liquid is no longer buffered, and may move off the buffer curve. Continued precipitation of magnetite then drives the fO_2 of the melt to lower values.

The low starting fO_2 of the melt is taken to be representative of the oxygen fugacity of the mantle source (Carmichael, 1991; *section 3.2.9.*), and is a pre-requisite for the evolution of magmas according to a tholeiitic trend. It follows that differentiated tholeiitic rocks are rarely found in arc settings, where the initial fO_2 of the liquid is considerably higher (near FMQ+1), permitting the early crystallisation of magnetite. Magnetite is saturated only once the Red Hill liquid reaches relatively high fO_2s nearing FMQ+1, terminating ΣFe, Fe^{3+} and Ti enrichment in the melt.

4.5. Trace Element Evolution

Trace elements, by definition, are low in abundance in magmas (formally <0.1 wt%). This property ensures that their behaviour is passive (Henry's Law); dependent on the chemistry of the mineral phases as dictated by the chemical parameters outlined in the preceding section (P, T, fO_2, aH_2O, and major element compositions). They therefore do not influence a particular process; rather, they act as its tracers.

The trace element geochemistry of the starting melt composition, as approximated by the chilled dolerites, was subjected to a detailed treatment in section *3.3*. More pertinent to the evolution of the liquid during differentiation is how these trace element abundances differ with respect to this initial composition. In view of this, the trace element abundances have also been normalised to the average chilled dolerite, thereby isolating the effect of the fractionating phases. In addition, they are

reported with respect to primitive mantle (Palme and O'Neill, 2003) to highlight their heterogeneity compared to oceanic basalts and to enable comparison with other tholeiitic provinces. On the other hand, moderately incompatible and compatible elements are retained in their un-normalised form, in accord with convention.

Trace element evolution may be modelled using Nernst paritition coefficients (the ratio of the weight fraction of a given trace element between two phases), in conjunction with the Rayleigh equation (see Appendices - *Modelling Iron Enrichment in the Melt*). In order to solve for the concentration of the trace element in the liquid, the bulk partition coefficient of that trace element between the crystallising phases and the liquid must be known. It follows therefore that knowledge of the composition and modal abundances of the crystallising assemblage are required. In order to quantitatively derive these parameters, a linear least-squares regression was performed between two samples in the differentiation sequence (Stormer and Nicholls, 1978). The composition of the phases were fixed, and taken from averaged microprobe analyses of minerals in the parent rock. The least squares regression then solves for the total solids and the modal proportions of each phase which minimise the misfit between the modelled and actual derivative composition, making for an internally-consistent model.

After the modal proportions of the crystallising phases have been constrained, the partition coefficients for a given element must be considered. Partition coefficients may be accurately predicted by the elastic lattice strain model (Blundy and Wood, 1994; Blundy and Wood, 2003) which incorporates the variability involved with the ionic radius of the element and the crystallographic site, and the deformation (elastic response of the site) induced by the misfit of the ion. This relationship is shown to be parabolic, where the partition coefficient decreases rapidly away from that of an ideal element for that site. However, the elastic strain is dependent on the radius of the site, which changes with the mineral's composition. Owing to the large compositional variation in the Red Hill sequence, it was considered simpler to exploit trace element analyses in minerals (by LA-ICP-MS, *section 1.3.*) and formulate partition coefficients based on the samples themselves. These were calculated by averaging the partition coefficient over the range of whole-rock host samples (whose trace element abundances were measured via S-ICP-MS) for low-Ca pyroxene, augite, and plagioclase. An individual partition coefficient is calculated for a mineral/whole rock pair, for 20 augite analyses, 15 low-Ca pyroxene analyses, and 5 plagioclase analyses (*tables A15-A17*).

4.5.1 Compatible and Moderately Incompatible Elements – Ni, Cr, Co, V, Sc, Cu, Zn, Ga

Transition metals, most of which nominally have a divalent charge, are ideal for substitution in the octahedral pyroxene sites for Fe and Mg. The M2 site of augite exists in dodecahedral co-ordination, and is slightly too large to accommodate transition metal (M_T^{2+}) ions, preferring to host Ca^{2+}. Thus, low-Ca pyroxene has twice the number of sites available to incorporate divalent metals, suggesting that $D_{Aug-OPX}^{M^{2+}} \approx 0.5$, assuming ideal mixing (Huebner and Turnock, 1980). This relationship is observed by Ni^{2+}, Mn^{2+} and Zn^{2+}, to an extent, however the concentration of Co^{2+} is similar in both, although the most magnesian augites and orthopyroxenes appear to uphold the relationship (*figure*

4.17., table 4.1.). Co also decreases strongly at $Mg\#_{augite}$ = 0.4 indicative of its compatibility in magnetite (*figure 4.17c*).

On the other hand, cations with other valencies (usually 3+) favour the coexisting augite. The coupled substitution of $^{VIII}Na^{+VI}M^{3+}(^{VIII}Ca^{2+}M^{2+})^{-1}$ in which an alkali metal replaces calcium in the VIII-fold M2 site of augite facilitates the replacement of a divalent by a trivalent metal cation for charge balance. Interestingly, Cr, which is predominantly trivalent above FMQ-1.6 (Mallmann and O'Neill, 2009), and is more compatible in its 3+ state owing to the large ionic radius of Cr^{2+}, contravenes this behaviour, perhaps suggesting non-negligible Cr^{2+} even at FMQ-0.5. The discrepancy may also be related to the rapid change in Cr concentration with Mg#, making it difficult to estimate $D_{Aug-OPX}^{Cr}$.
Sc is a homovalent, 3+, element whose budget is dominated by the pyroxenes. It displays the expected relationship wherein $D_{Aug-OPX}^{M^{3+}} \approx 2$ (*figure 3.17a*). This also holds for Ti, which exhibits remarkably constant $D_{PX-Melt}^{Ti}$ above FMQ-2 (Mallmann and O'Neill, 2009), likely reflecting increasing amounts of Ti^{3+}, though the Ti^{4+}/Ti^{3+} ratio reaches 1 only near FMQ-8. The $D_{PX-Melt}^{Ti}$ values calculated from the Red Hill pyroxenes (0.25 and 0.63 for low-Ca pyroxene and augite, respectively) are in agreement with experimental partition coefficients from Mallmann and O'Neill (2009) at FMQ-0.5; about 0.1 and 0.55, respectively.

Vanadium partitioning is highly sensitive to fo_2 due to its existence in four valence states in terrestrial magmas (V^{2+-5+}) (Toplis and Corgne, 2002; Mallmann and O'Neill, 2009). At FMQ to FMQ-1, the proportion of V^{3+} is only about 5%, whereas that of V^{4+} is near 85% (with V^{5+} being near 15%), but the $D_{Mineral-Melt}^{V}$ is about an order of magnitude higher for trivalent vanadium compared to its tetravalent state, and so at a given Mg# for pyroxene, $D_{Mineral-Melt}^{V}$ is strongly dependent on fo_2. Toplis and Corgne (2002), however, also demonstrated a strong positive dependence of $D_{CPX-Melt}^{V}$ on the Fe# of the pyroxene, which is large enough to mask the trend of decreasing $D_{CPX-Melt}^{V}$ with increasing fo_2. For mantle-like pyroxenes, Mallmann and O'Neill (2009) calculated partition coefficients at FMQ-0.5 of about 3 for augite and 0.9 for orthopyroxene, in good agreement with 3.09 and 1.13 calculated for the Red Hill pyroxenes. Given the similarities between V^{3+} and Fe^{3+} in VI-fold co-ordination, and V^{4+} and Ti^{4+}, it seems likely that V enters the M1 site of augite (Toplis and Corgne, 2002). The strong depletion in V in augite after Mg# = 0.4 is due to the precipitation of magnetite, whose $D_{Mt-Melt}^{V}$ is sensitive only to oxygen fugacity.

Making use of the knowledge of $D_{Mineral-Melt}^{M}$ systematics of the Red Hill intrusion, the partition coefficients listed in table *4.1.* were used to calculate the evolution of the trace element abundances of the evolving liquid, as approximated by the whole rocks. To model perfect fractional crystallisation, the Rayleigh equation was used. Representative whole-rock transition metal trends are depicted in figure *4.18*.

The well-defined trends consistent with the calculated partition coefficients and phase proportions provide steadfast evidence that fractional crystallisation was the predominant mechanism of magma differentiation in the Red Hill intrusion, as first hypothesised by McDougall (1962). Cr and Ni (not shown) are highly compatible in fractionating pyroxenes and behave similarly. Co and Sc exhibit comparable trends, despite their different valence (3+ and 2+, respectively). Sc appears to be slightly compatible in magnetite (MgO <1.5 wt%), probably as a substitute for $^{VI}Fe^{3+}$. Zn^{2+} behaves as a

marginally incompatible element, with bulk D decreasing from ≈0.8 to ≈0.4 later in the sequence where the modal proportion of pyroxenes decrease.

4.5.2. Highly Incompatible Elements and Rare Earth Elements

By definition, highly incompatible elements are not readily incorporated into the fractionating phases at the beginning of a differentiation sequence (e.g. pyroxenes). Rather, these elements, after reaching a critical saturation point, may precipitate out in accessory phases such as zircon, apatite and titanite. Prior to this point, their enrichment in the melt should be a function of the proportion of crystallisation (fraction of melt remaining), because their $D^{E}_{Mineral-Melt}$ is near 0.
Figure *4.19.* illustrates a primitive-mantle normalised (Palme and O'Neill, 2003) trace element diagram, on which the entire suite of Red Hill rocks are plotted. The distinct characteristics of the Northern Ferrar Province are evident, namely the negative Nb , Ta, P, Sr and Ti anomalies, accompanied by positive Pb anomalies indicative of the involvement of continental crust during magmagenesis (*section 3.3.*).

Two properties of the trace element abundances of the more differentiated rocks argue for the involvement of fractional crystallisation as a source of the diversity observed in the Red Hill suite:

1. The general increase in their abundance is that expected during progressive removal and differentiation of crystallising phases with low $D^{E}_{Mineral-Melt}$, as inferred from the low concentrations of these incompatible elements in the minerals.
2. The parallelism of the primitive-mantle normalised signature in the entire suite of rocks. This property indicates that there was minimal involvement of any other foreign magma.

However, because the magmas already exhibit the trace element characteristics of the upper continental crust assimilant, it is difficult to unequivocally dismiss the role of progressive contamination by upper crustal material as a method of elevating their abundances. There are, however, small nuances evident in the primitive mantle normalised diagram that would argue against this as the dominant mechanism for differentiation. Most notably, the negative Sr and Eu anomaly increases with increasing differentiation, which is attributable to the fractionation of plagioclase. If crustal contamination was the culprit, then, while their abundances may decrease, the size of the anomaly must stay the same. Furthermore, simple graphical comparison indicate that the most incompatible trace element enriched sample, the O'Briens Hill Granophyre, is enriched in many incompatible elements (especially the HREE) over the upper continental crust (Rudnick and Gao, 2003), making it unsuitable to act as a contaminant (*figure 4.20.*).

While the two are ostensibly similar, the negative Sr, Eu and Ti anomalies, in addition to the enriched HREE of the granophyre clearly distinguishes it from the upper continental crust. Furthermore, it appears that the positive Pb anomaly has been dampened owing to its mild compatibility in plagioclase (*table 4.1.*). Clearly, if the crust did act as a contaminant, it would have attenuated the strong anomalies observed in the granophyres. The absence of crustal-level contamination is also evidenced by the constant $^{87}Sr/^{86}Sr_{(180)}$, $^{143}Nd/^{144}Nd_{(180)}$, in addition to initial Pb isotopes which do not delineate a trend to increasing values in the more differentiated rocks that

would be expected if crustal contamination had occurred. Clearly then, the distinctive trace element signatures of the differentiated rocks can only be attributed to fractional crystallisation. Such trace element features are reminiscent of those found in other A-type granites, such as the Topsails Igneous Suite (Whalen et al., 1996).

In order to track the change of trace element abundances with differentiation, the rocks were subdivided into their petrological groupings, and normalised to the chilled margin composition (*figure 4.21.*).

The trace element signature of the KI Basalts overall mirror that of the chilled margins, though the abundances are overall slightly lower, consistent with the slightly more differentiated major element characteristics of the Tasmanian chilled dolerites. Zr and Hf are enriched, while Rb, Nb and K are depleted with respect to the chilled dolerites.
The dolerites define a small range of compositions, with some showing trace element signatures below 1, suggestive of a partially cumulative origin. Zr, Hf enrichment is prominent for the dolerites that have signatures above 1, highlighting their very low $D_{Solid-Melt}$ compared to Nb and Sm, as corroborated by trace element abundances in pyroxenes and plagioclase (*table 4.1.*).
The quartz dolerites display more discernible trends, such as the formation of a strong negative Sr anomaly, which is onset by plagioclase crystallisation ($D^{Sr}_{Plagioclase-Melt} = 1.45$, *table 4.1.*). Zr and Hf continue to increase, while Ti develops a small positive anomaly with respect to Eu and Gd, the former of which is suppressed in plagioclase and augite.
In the fayalite granophyres, the negative Sr, Eu become more pronounced, and at the same time, the small positive Ti anomaly that had developed in the quartz dolerites has been reversed, coincident with magnetite crystallisation. Interestingly, the U/Th ratio increases, in contrast to predictions from partition coefficients (*table 4.1.*).
Finally, the most differentiated granophyres show enrichments of rare earth elements up to 4xgreater than the chilled dolerites. Negative Sr, Eu and Ti anomalies are the dominant features of the diagram, indicative of continued plagioclase and magnetite fractionation. These are accompanied by positive U anomalies and negative Nb anomalies in some samples. The degree of Zr and Hf enrichment appears to have relented, and these features may signal the precipitation of minor zircon and other accessory phases that may incorporate Nb, such as titanite. A slight negative Pb anomaly has developed, also in response to plagioclase fractionation, which has an estimated $D^{Pb}_{Plagioclase-Melt} = .35$ (*table 4.1.*).

To substantiate the hypothesis that these characteristics may be produced via fractional crystallisation, the Rayleigh model was applied to these incompatible elements. The calculations also yield estimates for the rough proportions of crystals/melt, if we assume $D^{Incompatible}_{Solid-Melt} \approx 0$, or by the modal mineral proportions, which are estimated through least squares.

As shown in figure *4.22.*, the model faithfully reproduces the salient features in the trace element signatures of the differentiated dolerites and granophyres. Negative Pb, Sr, Eu, Ti and positive Zr, Hf anomalies are emulated by the model. The model also indicates an increase in La_N/Sm_N with differentiation, owing to $K_{D\,PX-Melt}^{La-Sm} < 1$. Since the calculations only consider augite, low-Ca pyroxene and plagioclase (and magnetite for Ti and V), the impact of accessory phases (e.g. on Zr, Hf,

Nb, Th and U) has not been investigated, and therefore these elements do not match exactly. However, this is a limitation of the least squares regression, in that it only accounts for modal proportions based on major element concentrations, to which accessory phases do not contribute.

As suggested by the well-reproduced Sr anomaly in the model, the $D^{Sr}_{Plagioclase-Melt}$ value of 1.45 compares favourably with the experimental figures derived by Aigner-Torres et al., (2007), ranging between 1.42 and 1.715, depending on temperature. Similarly, for $D^{Eu}_{Plagioclase-Melt}$, Aigner-Torres et al., (2007) report values of ≈0.9 at fo_2 on the Iron-Wüstite (IW) buffer, and ≈0.2 at the FMQ buffer between 1220 and 1180°C. The value calculated for the Red Hill plagioclases yields 0.42, consistent with the initial melt being slightly more reduced than FMQ (*section 4.4.*), but more oxidised than IW, given that Eu is dominantly incorporated as Eu^{2+} through substitution for Ca^{2+}. The Eu^{2+}/Eu^{3+} increases with fo_2in a manner analogous to iron; $Eu^{2+}O + \frac{1}{2}O_2 = Eu^{3+}O_{1.5}$.

Given the paucity of a Ti anomaly prior to the fayalite granophyres, presumably attributed to the delay in magnetite crystallisation, it is pertinent to explore the magnitude of this change, expressed as Ti/Ti*, in comparison to stage of liquid evolution.

The plot of Ti/Ti* against MgO elegantly illustrates the role of fractional crystallisation in creating the prominent negative Ti anomalies in the differentiated rocks (*figure 4.23.*). Over the initial course of crystallisation, the Ti anomaly is constant, reflecting the incompatibility of Ti, analogous to K or Na, as identified in the major element trends. Subsequently, however, following magnetite crystallisation, which occurs at MgO ≈ 1.5 wt%, the Ti/Ti* ratio drops quickly due to its incorporation in the ülvospinel component (Fe_2TiO_4) in titanomagnetite. If crustal contamination was responsible for such a feature, one would anticipate a constant linear array (dashed line, *figure 4.23.*). The fact that this is not observed, in addition to the absence of upper crust with such a pronounced negative Ti anomaly also strongly supports fractional crystallisation as the dominant control on the trend.

Whole rock trace element signatures experience considerable enrichment to their abundances from dolerites with high Mg# to the low Mg# granophyres. In addition, increasing Sr, Eu and Ti depletions, coupled with Zr and Hf enrichments typify the evolution of the more evolved rocks compared with the chilled margins (*figure 4.21.*). In order to isolate the process responsible for such a continuum, Rayleigh modelling, in tandem with internally-consistent partition coefficients, was performed. It is demonstrated that the range of trace element compositions must be a result of protracted fractional crystallisation of phases dominated volumetrically by augite, pigeonite and plagioclase, in the proportions dictated through least squares regression analyses (see Appendices - *Modelling Iron Enrichment in the Melt*).

4.5.3. Rare-Earth Elements (REE) in Minerals

Considering the range of trace element concentrations displayed by the Red Hill magmas, any phase in equilibrium with the liquid should record a successive stage in its evolution. High-Ca pyroxene (augite) is the ideal phase with which to probe the stage of liquid evolution, given its persistence throughout the entire sequence, and its affinity for incompatible elements.

Even though whole rock rare-earth element (REE) abundances may only vary within within an order of magnitude, REEs in clinopyroxene reflect a 10^2 change from the most mafic chilled dolerites to the end-member granophyres (*figure 4.24.*). The augmentation of REE in clinopyroxene is concomitant with an exponential decrease in the compatible element concentrations of Cr and Ni, both in the liquid and clinopyroxene (cf *figure 4.18*).

Concurrent with the rising La_N/Sm_N ratios in the evolving liquid as expected through the crystallisation of pyroxenes which have $K_{D\,PX-Melt}^{La/Sm} < 1$ (*table 4.1.*), augites in equilibrium with this melt also exhibit increasing La_N/Sm_N ratios. The most discernible trend displayed by the augites is the increasing trough expressed by Eu, and quantified by the Eu/Eu* ratio, which records a decrease from .63 to .14, correlative with $Mg\#_{aug}$ of 83 to 13 (*figure 4.24.*). This demonstrates augite in equilibrium with a liquid which has had increasing amounts of plagioclase removed from it. Figure *4.25* depicts this evolution by comparing the Eu/Eu* of the pyroxene with that of its whole rock. The trend for the whole rocks is not as pronounced, due to the presence of plagioclase, which carries a complementary positive Eu anomaly. However, this monotonic decrease in Eu/Eu* is indicative of continuous crystal segregation from the liquid, precluding interaction between the two following their formation, approximating a fractional process.

Amphiboles display similar trace element patterns to evolved pyroxenes, with a similarly striking negative Eu anomaly (*figure 4.26.*). Both the ferroedenites and hedenbergites display LREE-enriched trace element patterns, which is atypical of these minerals (e.g. Rollinson, 1993), and reflects the enrichment of these elements in the coexisting melt.

4.6. Formation of A-Type Granitoids

The prevailing model for the formation of A-type granitoids is exemplified by the ≈490Ma Padthaway granites of southern South Australia, which are shown to have experienced a prolonged history of fractional crystallisation in order to give rise to their extreme characteristics (Turner et al., 1992). The distinctive characteristics of these A-types are summarised below:

- A-type granitoids occur in bimodal association with mafic rocks, generally in anorogenic settings
- Ferrohastingsite and Fe-rich biotite are common as the ferromagnesian phases, although hedenbergite and fayalite may also be present. This is in contrast to I- and S-type granites, which may have magnesian amphiboles or biotite, reflecting their higher water contents and fo_2.
- Decreasing Al_2O_3, CaO, MgO, $Fe_2O_3^{(T)}$ with increasing SiO_2, indicative of plagioclase, pyroxene and magnetite removal
- Similarly, decreasing compatible elements (Cr, Ni, Sc, V) are consistent with segregation of pyroxenes and magnetite. The enrichments in lithophile elements (K, Rb, Ga) can be reconciled by their exclusion in the fractionating phases.
- REE concentrations are up to 8x higher than their parent mafic magma, and this increase is accompanied by an $LREE_N$/M,$HREE_N$ enrichment, as would be anticipated for pyroxene fractionation, which has $K_{D\,PX-Melt}^{LREE/M,HREE} < 1$ (*table 4.1., figure 4.24.*). Negative Eu anomalies

which become progressively larger as the REE contents and SiO_2 increase is also attributable to plagioclase fractionation (e.g. *figures 4.21, 4.22, 4.25*)

These features are entirely consistent with the petrological and chemical evolution observed at Red Hill. However, the point of difference is that the entire sequence from the mafic parent magma to fractionated granophyres is preserved, which is in contrast to most granitic plutons, which may only contain clues as to the parent magma, or, as in the case of A-type granites, an absence of intermediate compositions.

Figure *4.27* outlines the origin of the bimodal association between A-type granites and mafic magmas. Over the first 50% (by mass) of crystallisation, the SiO_2 content increases by less than 3wt%, which, as elucidated in section *4.2*, is due to the relative buffering of SiO_2 content by plagioclase, augite and pigeonite, which, together, have an SiO_2content comparable to that of the melt. Contrastingly, from 40% melt remaining to the most fractionated compositions (20% melt remaining), the SiO_2 content of the melt increases by almost 10wt%, which reflects the onset of magnetite crystallisation. Magnetite is devoid of SiO_2 altogether, and therefore imparts rapid silica enrichment over small crystallisation intervals. Therefore, given this dichotomy, the chances of intermediate compositions (56wt%<SiO_2<66wt%) being preserved in granitic systems is low, because these compositions reflect only a volumetrically small part of the crystallisation sequence.

The pre-requisite for this interval is the delayed crystallisation of magnetite. If magnetite crystallised early, as occurs in calc-alkaline suites, then silica enrichment should be pronounced from the initiation of differentiation. The formation of A-type granites in bimodal association with mafic magmas is therefore intimately linked to the low fo_2 of the starting magma, so as to destabilise magnetite and allow initial crystallisation at near constant SiO_2. Turner (1996), characterised the differentiation history of the tholeiitic, ≈490Ma Delamerian Black Hill gabbroic complex (South Australia), which contains sequentially layered peridotites, trocolite, gabbronorites, and differentiated pyroxene monzonites. The presence of sulphides in the Black Hill intrusion, in addition to highly titanian ilmenite (Il_{99}) is indicative of the low oxygen fugacity during crystallisation (FMQ-4, according to the QUILF formulation of Frost et al., (1988)). These magmas have major and trace element characteristics, in addition to depleted mantle model ages suggestive of their parentage to the Padthaway A-type granites (Turner, 1996), a hypothesis further evidenced by the similarity between the rare mafic rocks preserved with the Padthaway granites and Black Hill dykes (Turner et al., 1992). The Padthaway A-type granites record fo_2s between FMQ-2 and FMQ-3 (QUILF, Frost et al., 1988), and amphibole barometry crystallisation pressures of about 2.5 kbars (Johnson and Rutherford, 1989). These characteristics are in broad agreement with the crystallisation conditions experienced in the Red Hill intrusion (FMQ-1; ≈3 kbars). The low fo_2 also promotes a sizeable increase in Fe# with differentiation due to the enrichment of Fe in the residual melt. At the same time, Na and K are also enriched because of their incompatibility in calcic plagioclase, and pyroxenes. Both of these parameters record enrichment with differentiation in figure *4.28*. However, peralkalinity is not reached ((Na+K)/Al > 1), likely due to the low concentrations of alkalis in the starting melt (Na_2O = 1.8 wt%; K_2O = 0.8 wt%; *figure 4.1.*), suggesting that the starting composition must already be enriched in alkalis (e.g. basanites in continental or oceanic alkaline suites) to form peralkaline A-type granites, or that the melt must crystallise to near completion.

Where the two granitic suites diverge is in their water content. While the Red Hill mafic magmas commence at low H_2O, its compatibility in fractionating phases causes its abundance to increase up to ≈2 wt% in the most differentiated granophyres (see appendices). By contrast, the Padthaway A-types display LOI values (taken to approximate $X_{H_2O}^{liquid}$) below 1 wt%, and typically near 0.5 wt%. This may explain why the feldspars in the Padthaway A-Types are coarsely perthitic, implying hypersolvus conditions (low P_{H_2O}), whereas the Red Hill granophyres contain two compositionally-distinct feldpsars without any exsolution features, consistent with their much higher water contents. It therefore follows that A-type granites need not necessarily contain perthitic feldspar, depending on whether or not the system permitted fluid escape during its evolution, and the rate at which it cooled.

A strong indicator for fractional crystallisation giving rise to A-type granites is the depletion in compatible elements and the concomitant enrichment in incompatible elements. This feature of the Red Hill suite has been illustrated in section *4.5.*

A common descriptor of the degree of incompatible element enrichment is the A-type discrimination diagram employed by Whalen et al., (1987; 1996), which plots four incompatible trace elements of varying affinity (two HFSEs (Nb, Zr), an LREE (Ce) and an HREE-like element (Y)) against Ga/Al. Al is removed effectively through plagioclase fractionation, whereas Ga only increases slightly during this process. The greater the degree of enrichment in both variables, the more fractional crystallisation is deemed to have taken place. However, can only be considered in a quantitative sense for a given suite, because the absolute concentrations vary with that of the mafic parent, whose trace element abundances are a function of its mantle source.

Evident in figure *4.29.* is the enriched nature of the granophyres and Padthaway A-types with respect to typical I- and S-type granitoids. In the case of Red Hill, crystal fractionation is delineated by a linear trend towards increasing Ga/Al and Zr+Nb+Ce+Y.

Based on the preceding discussion and interpretation of results from the Red Hill suite, it is posited that A-type granites are the end-members formed from the tholeiitic fractionation trend. We therefore propose the following criteria for the formation of non-peralkaline A-type granites from a tholeiitic magma.

- Low starting fo_2. This is a crucial parameter as it controls the timing of magnetite saturation. This variable is evidenced to exert a very strong control on a number of factors that characterise the tholeiitic trend. Its delay facilitates Fe, $Fe^{3+}/\Sigma Fe$ enrichment and silica constancy, while its eventual precipitation induces alkali and silica enrichment over short crystallisation intervals, promoting bimodal mafic-felsic associations.
- Low starting $X_{H_2O}^{liquid}$. Such a control ensures that plagioclase crystallisation occurs in the early stages of fractionation, accommodating Fe enrichment in the melt. It also explains the crystallisation of anhydrous ferromagnesian silicates in hedenbergite and fayalite, as observed in the Red Hill and Padthaway suite. Additionally, the crystallisation interval of silicate phases is shifted to higher temperatures, while that of oxides remains unchanged, further promoting iron enrichment. $X_{H_2O}^{liquid}$ may rise later in the differentiation sequence,

depending on whether the system was closed or open to fluid escape, and hence feldspars may be hypersolvus and perthitic, or subsolvus and non-perthitic.

- Low-moderate pressures of crystallisation. Low pressure favours plagioclase crystallisation, and also permits the crystallisation of nominally anhydrous minerals due to the decreased solubility of water in the melt. Migration of the melt to lower pressures is made possible following magnetite crystallisation, since it depletes iron from the liquid and decreases its density (e.g. Villiger et al., 2007).

These conditions explain the absence of A-type granitoids in convergent margin magmatic settings. Since the oxygen fugacity and water content of a basaltic magma are linked to that of their mantle source (e.g. Carmichael, 1991; *sections 3.2.9, 4.4.*), and because arc magmas are formed from hydrous-fluxed melting of the mantle wedge, they possess high $X_{H_2O}^{liquid}$ and fo_2. These characteristics enable early magnetite crystallisation and delay plagioclase crystallisation, resulting in a calc-alkaline trend which is typified by early SiO_2 enrichment and $Fe_2O_3^{(T)}$ depletion. Similarly, A-type granites are found only in anorogenic settings (continental rifts, ocean islands, mid-ocean ridges) due to the uniformly low oxygen fugacity of the mantle source, and melting provoked by either decompression or thermal-compositional anomalies rather than any excess water. Their ability to rise to upper crustal levels is also aided by the extensional setting in which they are emplaced.

4.7. Mechanisms of Differentiation

The classical method for producing a variety of compositions from a single magma is to invoke crystal settling (Bowen, 1928), whereby a growing crystal is segregated from the melt by its descent to the bottom of the magma chamber. This principle functions on the premise that, upon emplacement in a (conduit-fed) magma chamber, the intrusion cools from the roof and side-walls and crystals settle by virtue of their higher density and viscosity compared to the surrounding liquid. However, when a magma is emplaced within the upper crust, the country rock into which it is intruding was previously at uniform temperature. Seeing as the magma is much hotter than the country rock ($\Delta T \approx 1000°C$), the temperature should be identical everywhere around the perimeter of the body. The rate of cooling via conduction should then also be comparable around the margins of the intrusion. This realisation prompted Marsh (2002) to propose the solidification front as a viable mechanism by which magmas cool and differentiate.

Crystallisation fronts are defined as the temperatures bracketing the solidus and liquidus of the magma. These fronts are dynamic, in that they migrate depending on the prevailing thermal regime. In the upper crust, due to the strong thermal contrast between the magma and the country rock, the movement of these fronts is quite rapid, rendering crystal settling difficult. The rate of crystal settling may be roughly approximated by Stokes' Law:

$$V_s = C_s \frac{\Delta \rho g a^2}{\mu} \qquad (4.16.)$$

Where C_s is a constant (≈2/9), $\Delta\rho$ is the density contrast between the crystal and the melt, a is the crystal radius and μ is the viscosity of the melt. On the other hand, the rate of advancement of the solidification front may be given by:

$$V_F = b\left[\frac{K}{t}\right]^{1/2} \quad (4.17.)$$

Where K is the thermal diffusivity, t is time and b is a constant. Equating these two expressions, it is evident that as the viscosity increases (as it does due to increasing crystallinity and polymerisation of the melt with cooling), the crystal must become larger to settle out. Therefore, it may only be possible for settling to occur during the early stages of differentiation. Furthermore, the growing crystal may not exhibit a sufficient density contrast between itself and the melt. This may occur in the case of plagioclase, which may have a density of 2.65-2.7g/cm^3, and is exacerbated by the iron enrichment trend of the Red Hill liquid, which exhibits a comparable density as predicted by PELE (Boudreau, 1999). If the rate of crystal settling is able to exceed that of solidification front advance, it is prone to resorption in the central, hotter part of the magma chamber and settling does not occur until most of the intrusion has crystallised.

Theoretical considerations point to a paucity of crystal settling from a magma that does not already bear phenocrysts. The absence of crystal settling in the Red Hill intrusion is supported by the dearth of modal layering, in addition to lack of stratification in the lower, doleritic portion of the sill. Such a stratigraphy is akin to that of Sudbury Igneous Complex, which due to impact-induced superheating (up to 1700°C), did not carry any initial phenocrysts and subsequently doesn't exhibit modal layering. Evidence thus points to another mechanism for the creation of the sequence observed at Red Hill.

Turbulent flow in a low viscosity, Mg-rich liquid that is fractionating ferromagnesian minerals and magnetite gives rise to a lower density residual liquid in which pyroxene chemistry would be buffered due to the ease of mixing of the interstitial liquid. This would produce wide ranges of mineral composition in the early and late stages of the intrusion, but small ranges in zoning, as expected during the evolution of a calc-alkaline magma.

However, in the Red Hill intrusion , the early precipitation of plagioclase and suppression of Fe-Ti oxide nucleation produces a high density Fe-rich residue, restricting magma flow and therefore giving rise to sequential precipitation of progressively evolved phases as zoning of individual grains within essentially closed-system magma zones at the grain-scale (Hall et al., 1988). This would create specific boundary conditions around the grain.

The size of chemical boundary layers in magmas are invariably thin, and occur on a length scale on the order of centimetres, whereas thermal boundary layers may extend for tens of metres, depending on the dimensions of the intrusion (Marsh, 2007). Chemical diffusivity (10^{-6}-10^{-8} cm^2/s) is several orders of magnitude smaller than thermal diffusivity (≈4*10^{-3} cm^2/s), with the net effect being that the chemical components of the melt are not equilibrated in the absence of physical mixing over the length scale of the magma chamber. Additionally, lack of broad-scale magmatic differentiation brought about by Soret diffusion, in which diffusion of mass is driven by a

temperature gradient, further illustrates this point. During Soret diffusion, according to laboratory experiments, SiO_2, Al_2O_3, Na_2O, K_2O are thermophilic and FeO, MgO, TiO_2, CaO are thermophobic, and therefore opposite to what is observed in magmatic complexes.

Therefore, when a crystal (e.g. pyroxene) grows in a melt, chemical diffusion is so slow such that the components rejected from the crystal (e.g. Na, K, Al, Fe^{3+}) build up in the proximal melt. The following zone that grows therefore has a different composition, and in the case of Red Hill, this is manifest as strong Fe-Mg zoning in pyroxenes. Such zoning is a function of the iron enrichment in the melt surrounding the pyroxene, which in turn is induced by plagioclase crystallisation. The growing pyroxene therefore remained stationary with respect to the surrounding melt, and subsequently was able to develop extensive zoning.

More differentiated dolerites and quartz dolerites reflect new nucleation and growth of pyroxenes and plagioclase in the evolving melt. The first crystals to become saturated in the melt are also the most magnesian, but in addition to forming zones around these phases, new crystals are saturated as well. A dynamic process results, whereby the evolving melt contributes both to the overgrowth zones of one pyroxene, whilst at the same time forming the nucleus of another. The competition between the two presumably reflects the difference in free energy in forming a new nucleus compared to that of creating a new zone. The free energy of crystallisation can be expressed as (Vernon, 2004):

$$\Delta G_t = -\frac{4}{3}\pi r^3 \Delta G_v + 4\pi r^2 \Delta\gamma \qquad (4.18.)$$

The equation indicates that the stability of the nucleus is dependent on its volume (r^3) and negatively dependent on its interfacial area (r^2) and interfacial free energy, $\Delta\gamma$. Ordinarily, crystallisation via zoning is favoured, however nucleation may occur if it takes place heterogeneously, that is, on a pre-existing nucleus, such that the surface area (r^2) is reduced. Therefore, while zoning is widespread, the overgrowth of pigeonite by augite that is widespread in the dolerites and quartz dolerites (*figures 2.4b, 4.11.*) is suggestive of heterogeneous nucleation of new crystals as well.

Seeing as magnetite crystallisation has not occurred at this degree of fractionaton, the increasing concentration of iron acts to densify the liquid, ensuring that static conditions in the magma chamber are extant, without any appreciable homogenisation occurring through convection or melt mixing, so as to preserve the chemical heterogeneity that has developed.

Magnetite becomes saturated when approximately 50-60% of the melt has crystallised (*figure 4.27.*). According to Marsh (2002), at this level of crystallinity, the constituent crystals have reached the threshold for maximum packing, and form a cohesive framework. This network of crystals now acts as a dilatant solid, which is subject to deformation upon shearing. The remaining melt, which is interstitial to these crystals, may migrate via porous flow instigated by strain on the crystal mush. Melt migration is further enhanced at this percentage of crystallisation because magnetite begins to sequester the iron, resulting in a decrease in the density of the melt. However, this may be

counteracted to some degree by its increasing viscosity due to increasing melt polymerisation and cooling.

Notable in the Red Hill intrusion is the absence of pyroxene zoning in the fayalite granophyres onwards. This coincides with magnetite saturation, intimating a correlation between the two phenomena. The Mg# of the pyroxenes in the granophyres and fayalite granophyres stays fairly constant, reflecting the removal of Fe^{2+} by magnetite at a rate similar to that of Mg^{2+} by the pyroxenes, leaving a liquid with a fairly constant Mg# (*figure 2.8.*). The differentiated liquid is permitted to flow and coalesce, perhaps as a result of deformation, and aggregate in the region of lowest pressure. Increasing magmastatic pressure may result in the domal uplift of the roof rocks, perhaps concentrated in a certain area by a pre-existing structural weakness in the country rock. This stage of the history represents the formation of the fayalite granophyres and granophyres.

The dilemma however remains that the exposed section of the Red Hill intrusion is comprised of ≈230m of dolerite and almost 200m of differentiated granophyres. This presents a mass balance problem if the granophyres are deemed to have been formed through 70-80% crystallisation of the parent (chilled dolerite) magma (*figure 4.27.*). However, the regions of differentiated granophyre preserved at Red Hill, Hickman's Hill, and O'Brien's Hill is not continuous along the length of the intrusion (*figure 2.2.*). While a cross-section of Red Hill shows that the dolerite/granophyre ratio is 55/45 (*figure 2.8.*), taking the volume of the intrusion as a whole, the ratio is probably closer to 75/25. This suggests that the granophyre migrated from a large lateral extent and was concentrated in these weaker, more readily uplifted zones.

Conclusion

Coherent trends in major element space defined by the magmas that comprise the Red Hill suite suggest that the differentiated rocks fall on a liquid line of descent produced by the evolution of a single liquid through fractional crystallisation. The type and modal proportions of the minerals that segregated to give rise to this evolution are controlled by the chemical composition of the magma, which is a function of its mantle source, and the pressure and temperatures it evolved at. The predominance of early pyroxenes and plagioclase indicate low fo_2, low $X_{H_2O}^{liquid}$ and low to moderate pressures. Temperatures are constrained by whole rock and pyroxene thermometers, and range between ≈1200°C for the chilled dolerites, decreasing to ≈950°C in the most differentiated granophyres. The prolonged stability of pigeonite in the Red Hill intrusion is evidence of elevated $a_{SiO_2}^{liquid}$, which is further substantiated by the absence of magnesian olivine. The progressive increase in fo_2 relative to the FMQ buffer from the chilled dolerites up until the precipitation of magnetite suggests liquid evolution in a system closed to oxygen exchange, where the crystallising minerals, owing to their varying ferric-ferrous ratios, enact a change on the redox conditions of the magma. The extensive pyroxene zoning reflects such an evolution, as it occurs in response to the rapidly falling Mg# of the melt instigated by iron enrichment. Iron isotopes also record this change, where the $\delta^{57}Fe$ of the evolving melt increases as a result of the sequestration of light Fe in $^{VI}Fe^{2+}$-bearing pyroxenes, before magnetite depletes the $^{IV}Fe^{3+}$ that had accumulated in the melt, driving $\delta^{57}Fe$ of the liquid to lower values in the granophyres. Iron isotopes, in addition to the trace element characteristics of the Red Hill magmas, attest to their formation through protracted fractional crystallisation. The development of large negative Eu, Sr, and Ti anomalies with respect to the parent

magma, onset by plagioclase and magnetite crystallisation, are ubiquitous features of the most differentiated magmas. Such signatures are also evident in the coexisting mineral phases that grew in equilibrium with the melt, and therefore a numerical model using internally-consistent partition coefficients and mineral proportions is devised that accurately reproduces the trace element characteristics of the magma sequence. The Red Hill granophyres exhibit chemical and petrological properties akin to other A-type granitoids. A common model invoking prolonged crystal fractionation from a mafic parent magma to encapsulate the mechanisms for their petrogenesis is proposed.

5.0. Iron Isotope Variations

Abstract

We can now measure the small but significant fractionation that occurs, even at magmatic temperatures, between the stable isotopes of heavy elements and use these changes to test theories of magmatic differentiation. Iron, due to its ubiquity in silicate melts and polyvalent behaviour undergoes isotopic fractionations that facilitate the study of igneous differentiation from the micro- to planetary-scale (Poitrasson, 2009; Steinhofel et al., 2009). Processes that are able to enact a change in the iron isotope composition of a given magma include fluid exsolution (Poitrasson and Freydier, 2005), partial melting of the mantle (Weyer and Ionov, 2007), mantle metasomatism (Williams et al., 2005; 2009), fractional crystallisation (Teng et al., 2008; Schuessler et al., 2009), and changes in $Fe^{3+}/\sum Fe_{melt}$ (Schoenberg et al., 2009; Dauphas et al., 2009a; 2010; Foden et al., 2009; Liu et al., 2010). However, relative constancy of homovalent stable isotopes such as Li and Mg suggest that the driver for iron isotope fractionation is endemic to that element. Our results indicate that fractional crystallisation of phases with disparate isotopic compositions to the evolving melt, in a system closed to oxygen exchange, enforce a change in the oxidation state of iron. This produces a concomitant shift in its bonding environment, engendering the fractionation of its isotopes. The extent of the variation recorded is consistent with the shift expected from theoretical (Schauble, 2004), experimental (Polyakov and Mineev, 2000; Polyakov et al., 2007; Shahar et al., 2008) and natural samples (Beard and Johnson, 2004; Poitrasson and Freydier, 2005; Schoenberg and von Blanckenburg, 2006). We contend that crystal fractionation has a primary influence on the iron isotopic composition of the products of planetary magmatism.

5.1. Introduction

The Red Hill intrusion is a classic example of an evolving tholeiitic, doleritic melt in a closed sytem (McDougall, 1962). This forms part of the Jurassic Tasmanian Dolerites (Hergt et al., 1989a), and, prior to Gondwana break-up, an extension of the Antarctic Ferrar province (Hergt et al., 1991). Unlike most other Tasmanian sills, Red Hill exhibits a continuum of magma compositions from mafic dolerite to alkali-enriched granophyres. The products of the differentiation were produced from *in-situ* fractional crystallisation of a single injection of magma, which is approximated by the well-preserved chilled margins which line the contacts of the body. The intrusion takes the form of a sill, and is typically about 400m thick (McDougall, 1962), but is characterised by a protruding cupola-like structure, which hosts a considerable section of differentiated granophyre (almost 200m; McDougall (1962)).

The advent of multicollector inductively-coupled plasma mass spectrometry has allowed for the resolution of iron isotope ratios with an analytical uncertainty of ≈0.03‰ for $\delta^{56}Fe$ and ≈0.05‰ for $\delta^{57}Fe$ (Dauphas, 2009b). Such high precision is particularly pertinent at high temperatures, as the magnitude of mass-dependent stable isotope fractionation decays proportional to $\frac{1}{T^2}$. Terrestrial basalts form a tight cluster of compositions, $\delta^{57}Fe \approx 0.1‰ \pm 0.1‰$ (Weyer and Ionov, 2007; Dauphas et al., 2009a), whilst the depleted mantle reservoir is approximately chondritic, with $\delta^{57}Fe \approx 0.03‰$ (Dauphas et al., 2009a; 2010). Dauphas et al., (2009a), illustrated that the isotopic compositions of

terrestrial basalts may be modelled assuming a $\Delta^{57}_{Fe^{3+}-Fe^{2+}}$= +0.45‰, for an exchange reaction of the form:

$$^{54}Fe^{2+} + {}^{57}Fe^{3+} \rightleftharpoons {}^{57}Fe^{2+} + {}^{54}Fe^{3+} \qquad (5.1.)$$

Since Fe^{3+} is an order of magnitude more incompatible than Fe^{2+} during mantle melting, smaller percentage partial melts of the mantle, where $Fe^{3+}/\Sigma Fe$ is therefore greater, are predicted to show heavier isotopic compositions than large percentage melts where the Fe^{3+} content of the melt is diluted. Granitoids tend to evolve towards heavier compositions with differentiation, (Poitrasson and Freydier, 2005; Teng et al., 2008; Schuessler et al., 2009), particularly when that differentiation is dominated by fractional crystallisation.

5.2. Results

We obtained precise and accurate iron isotope data on 16 rocks which record successive stages in the evolutionary history of the Red Hill body. The span of isotopic compositions measured (+0.117‰±.058‰ < δ^{57}Fe < +0.307‰±.030‰) fall within the range expected for terrestrial igneous rocks (Beard and Johnson, 2004; Poitrasson and Freydier, 2005; Schoenberg and von Blanckenburg, 2006). . In order to examine the relationship between the redox state and the iron isotopic composition of the fractionating Red Hill magma, we also determined whole rock Fe^{2+}-Fe^{3+} ratios. $Fe^{3+}/\sum Fe$ commences at ≈0.13 for the chilled dolerites, increasing to a maximum of ≈0.5 for the fayalite granophyres, before decreasing to ≈0.35 in the most differentiated granophyres (*table A19*).

Typical tholeiitic evolution is controlled first by the fractionation of magnesian pyroxenes and plagioclase, producing iron enrichment with minor silica enrichment before magnetite becomes the dominant iron-bearing phase; its formation leading to rapid iron depletion and alkali-silica enrichment (Toplis and Carroll, 1995; Berndt et al., 2005; Botcharnikov et al., 2008). This order of crystallisation is akin to that observed at Red Hill (*figure 2.8.*). The iron isotope data is plotted against MgO, as a descriptor of igneous differentiation (*figure 5.1.*). δ^{57}Fe displays a systematic increase with falling MgO, like that observed at Kilauea Iki (Teng et al., 2008), even though olivine rather than pyroxene is the predominant fractionating ferromagnesian phase at Kilauea. Notable is the abrupt decrease in δ^{57}Fe below ≈1wt% MgO. The δ^{57}Fe of the whole rocks show a direct positive correlation with $Fe_2O_3^{(T)}$ throughout the differentiation sequence (*figure 5.2.*).

Since the magma underwent differentiation whilst remaining closed to oxygen exchange, the amount of oxygen available to the system throughout its evolution is fixed. However, the melt's redox state evolved as it differentiated through crystal segregation. During early fractionation, the bulk of the iron is removed by pyroxenes. $Fe^{3+}/\sum Fe_{augite}$ is shown to vary with $Fe^{3+}/\sum Fe_{melt}$ (McCanta et al., 2004; Mallmann and O'Neill, 2009; Schoenberg et al., 2009), and exhibits $Fe^{3+}/\sum Fe$ lower than the coexisting melts below the Fayalite-Magnetite-Quartz buffer (FMQ) (McCanta et al., 2004). Thus, $Fe^{3+}/\sum Fe_{melt}$ increases with progressive removal of pyroxene-plagioclase in response to a conservation of O_2 by mass balance, through:

$$\underset{\text{in pyroxene}}{Fe^{2+}O} + \frac{1}{4}O_2 = \underset{\text{in melt}}{Fe^{3+}O_{1.5}} \qquad (5.2.)$$

δ^{57}Fe of the whole rocks, when plotted against δ^{57}Fe (*figure 5.3.*), demonstrates an initial increase, before reaching a maximum coincident with magnetite precipitation near 1.5wt% MgO, which then simultaneously depletes the remaining melt in Fe^{3+} and δ^{57}Fe.

In order to predict the iron isotope fractionation between crystals and melt during differentiation, the isotopic compositions of the phases involved must be estimated. This depends on the co-ordination and bonding environment of iron. These variables can be more accurately characterised in minerals as opposed to silicate melts, and therefore experimentally-determined reduced isotopic partition functions (β-factors) and fractionation factors are more readily available for minerals (Polyakov and Mineev, 2000; Polyakov et al., 2007; Schuessler et al., 2007; Shahar et al., 2008). The β-factor describes the tendency for dissociated isotopes of a given element to associate with the substance of interest. Experimental data are in agreement with theoretical predictions for stable isotope fractionation mechanics (e.g. Schauble, 2004), where Fe shows the following characteristics:

1. Higher β-factors for minerals with higher $Fe^{3+}/\sum Fe$
2. Higher β-factors for minerals with covalently-bonded Fe^{2+}

$$f = \frac{1}{2\pi}\sqrt{\frac{k_s}{\mu}} \qquad (5.3.)$$

These trends may be reconciled with the higher spring constants, k_s (a proxy for bond strength), for oxidised species, which have greater charge density, given that they exist in lower co-ordination polyhedra, which in turn have shorter (and thus stronger) bonds. This is due to the relationship whereby the vibrational energy shift associated with an isotopic substitution in a given bond in its ground state ($n_i = 0$, the zero point energy) controls the extent of the isotopic fractionation.

$$E_{(vib)i} = \left(n_i + \tfrac{1}{2}\right) h f_i \qquad (5.4.)$$

Where h = Planck's constant (6.626×10^{34}), *n* is the quantum number for the i^{th} vibrational degree of freedom and f_i is the oscillatory frequency for the vibration.

In accord with the iron (β-factors) for Fe^{2+}-bearing pyroxene, pigeonite and augite may be significantly lighter than a typical tholeiitic melt (Polyakov and Mineev, 2000; Polyakov et al., 2007). Light Fe in mafic minerals is recorded in both the mantle (Beard and Johnson, 2004; Williams et al., 2005; 2009) and in magmatic rocks (Schoenberg et al., 2009; Teng et al., 2008). In a statistical assessment of analysed mantle-derived mineral separates, Shahar et al. (2008) found no appreciable differences in the isotopic compositions of clinopyroxene, orthopyroxene and olivine.

To model the fractionation, the Rayleigh equation was used, which assumes perfect fractional crystallisation and is therefore an end-member scenario. Mineral proportions were estimated from petrographic analyses, and constraints further tightened via least squares calculations (see Appendices – *Modelling Iron Enrichment in the Melt*). In addition, because stable isotopic fractionation is temperature-dependent, whole rock temperatures were estimated with the formulation of Sisson and Grove (1993) (*equation 4.1.*). Both pyroxenes were assumed to have identical β-factors, whilst the iron hosted in plagioclase was considered negligible.

Early gabbroic fractionation in the Red Hill suite is modelled with a fractionation factor of $\Delta^{57}Fe_{px-melt} = -0.25‰ \times 10^6/T^2$, resulting in effective fractionation factors of -0.115‰ to -0.135‰ between pyroxene and melt at the magmatic temperatures inferred for the rocks. Based on these values, a pyroxene in equilibrium with the most primitive melt (a Kangaroo Island basalt, δ^{57}Fe ≈ +0.145‰±0.031‰), would have a δ^{57}Fe of +0.03‰, which is commensurate with the estimated depleted mantle composition of δ^{57}Fe ≈ +0.03‰ (Dauphas et al., 2009a; 2010) and is typical of peridotitic pyroxenes (Beard and Johnson, 2004; Williams et al., 2005).

The inflection in δ^{57}Fe in the Red Hill sequence at ≈1 wt% MgO demarcates a significant petrological transition from pyroxenes to magnetite as the primary host of iron. Owing to the incorporation of Fe^{3+} in magnetite, $^{IV}(Fe^{3+})\ ^{VI}(Fe^{3+} + Fe^{2+})_2O_4$, as compared to the predominantly Fe^{2+}-bearing pyroxenes , $^{VIII}Ca^{VI}(Mg,Fe)^{IV}Si_2O_6$, both total Fe and $Fe^{3+}/\sum Fe$ enrichment in the melt ceases (*figure 5.3.*). It follows that magnetite stability is sensitive to the prevailing redox conditions (Toplis and Carroll, 1995), and is saturated at the maximum fo_2 in the Red Hill suite, in conjunction with the appearance of fayalite, controlled by the equilibrium below (FMQ):

$$Fe_2SiO_4 + O_2 = Fe_3O_4 + SiO_2 \qquad (5.5.)$$

Therefore, at the apex of the $Fe^{3+}/\sum Fe$-δ^{57}Fe trend, the fo_2 of the melt is buffered until a_{FeO}^{liquid} becomes impoverished enough such that fayalite becomes exhausted. Continued precipitation of magnetite then drives the fo_2 of the melt to lower values and concomitantly depletes it in ^{57}Fe. The decrease in δ^{57}Fe may be modelled using $\Delta^{57}Fe_{mtn-melt} = +0.2‰ \times 10^6/T^2$, resulting in effective, $\Delta^{57}Fe_{mtn-melt} = +0.1‰ - +0.13‰$ at the calculated temperatures.

5.3. Discussion

The $Fe^{3+}/\sum Fe$ of the granophyric rocks (≈0.5) is higher than that expected for fractional crystallisation where Fe^{3+} is perfectly incompatible. Since small but significant amounts of Fe^{3+} are in fact incorporated in plagioclase, and in pigeonite and augite (e.g. McCanta et al., 2004; Mallmann and O'Neill, 2009; France et al., 2009), this requires that some Fe^{3+} in the melt must be formed by oxidation of Fe^{2+} .

$X_{H_2O}^{liquid}$ in the differentiated granophyres is high as a function of its incompatibility in fractionating phases. However the capacity for H_2O to oxidise iron is insignificant, given that its activity is low in magmas due to its formation of OH^- groups (Carmichael, 1991; Wilke, 2002; Botcharnikov, et al., 2005).

On the other hand, alkalis, which are also enriched in the granophyres, may play such a role. Alkalis, inversely proportional to their ionisation potential, are known to stabilise Fe^{3+}, and in tetrahedral co-ordination (Dickenson and Hess, 1986; Farges et al., 2004; Mysen and Richet, 2005; Bingham et al., 2007). Furthermore, alkaline earth cations (Ca and Mg) impart the opposite effect, owing to the steric hindrance in charge-balancing $2^{IV}Fe^{3+}$ as well as their high ionisation potential. Iron thus exhibits selective behaviour, wherein at high alkali/alkaline earth ratios, both Fe^{2+} and Fe^{3+} are present in predominantly tetrahedral co-ordination, and the $Fe^{3+}/\sum Fe$ is high (Jackson et al., 2005; Bingham et al., 2007). With an enrichment of Na and K relative to Ca and Mg, comes the preferential

incorporation of Fe^{2+} and Fe^{3+} into tetrahedrally-co-ordinated sites. This alludes to a network-forming role of Fe in alkalic melts. Further, due to the more extensive edge-sharing between Fe tetrahedra and other (Al-, Si-bearing) tetrahedra, the covalent character of Fe-bonding increases (Farges et al., 2004). The combined effects of shorter (and therefore stiffer) ^{IV}Fe-O bonds, and accentuated covalence of the medium-range environment of Fe both serve to concentrate heavier isotopes (Polyakov and Mineev, 2000; Schauble, 2004). It is therefore conceivable that some of the $\delta^{57(56)}$Fe enrichment observed in the evolving Red Hill melt is a response to alkali enrichment (*figure 4b.4.*).

Contrastingly, following the formation of magnetite (Mt_{93}), for the final 15% of the crystallisation history, ∑Fe, $Fe^{3+}/\sum Fe$ and $\delta^{57(56)}$Fe fall, whilst Na and K continue to increase (albeit slightly). Evidently, any effects of alkali enrichment on the proportion of $^{IV}Fe_{melt}$ are overridden by the incorporation of heavy iron into magnetite. This is consistent with the high β-factors (Polyakov and Mineev, 2000; Polyakov et al., 2007) and experimental fractionation factors (Shahar et al., 2008) calculated for stoichiometric magnetite, which hosts half of its Fe^{3+} in IV-fold co-ordination, and has a $Fe^{3+}/\sum Fe = 2/3$.

5.4. Implications

Identification of the pivotal role magnetite plays in both the liquid line of descent of tholeiitic and calc-alkaline magmas and their redox ratio, may subsequently aid in the interpretation of a given magma's iron isotope composition. Basaltic magmas record a range of oxygen fugacities that vary over 8 orders of magnitude bracketing the FMQ buffer (Carmichael, 1991). The saturation of magnetite is redox-dependent, crystallising later in low fo_2 tholeiitic systems and hence enabling iron enrichment. To a first order, the extent of accumulation of heavy iron in the melt is therefore a function of the timing of magnetite precipitation. Pre-differentiation processes including the fo_2 of the mantle source, extent of melting, and the alkalinity of the melt may contribute to the dispersion in δ^{57}Fe of primitive basalts (Dauphas et al., 2009a; *figure 5.5.*). However, as differentiation proceeds, the redox state of magmas tend to converge, as low fo_2 magmas increase their $Fe^{3+}/\sum Fe$ (as attested to by experimental studies of closed tholeiitic systems (Snyder et al., 1993; Toplis and Carroll, 1995; Botcharnikov et al., 2008)) and high fo_2 magmas decrease theirs, due to delayed and early precipitation of magnetite, respectively. Thus, differentiation acts to modulate and homogenise the range of $Fe^{3+}/\sum Fe$ in siliceous magmas, as noted by Carmichael (1991). Therefore, although oxidised arc lavas may initially show enriched iron isotope compositions as a function of their high starting fo_2, early crystallisation of magnetite ensures that the melt retains a fairly constant isotopic composition during differentiation. On the other hand, the asthenospheric mantle and depleted lithospheric mantle, the source of most tholeiitic magmas, display uniformly low fo_2s, near FMQ-0.5±0.5 (Frost and McCammon, 2008), a trait reflected in the constancy of $Fe^{3+}/\sum Fe$ of derivative magmas, such as MORB (Bézos and Humler, 2005). Equally, the most primitive Ferrar tholeiites exhibit $Fe^{3+}/\sum Fe \approx 0.13$, comparable to MORB, a similarity which extends to their iron isotope compositions ($\delta^{57}Fe \approx 0.1$), after which differentiation under conditions closed to oxygen acts to increase the δ^{57}Fe of the melt until magnetite becomes saturated. The effect of magnetite saturation in decreasing δ^{57}Fe is more pronounced in tholeiitic magmas, because it is the predominant iron-bearing phase, whereas it co-precipitates with olivine and pyroxenes in arc magmas (*figure 5.5.*).

In the preceding discussion, we consider that the melt is unbuffered and closed to oxygen exchange, which is typical of intrusive rocks. However, the redox state of the melt may be buffered, for example, owing to open-system oxygen exchange or by a mineralogical buffer, as is expected in volcanic systems. In these cases, the melt evolves along fO_2 trajectories defined by that buffer or by the amount of oxygen exchanged. Natural systems often follow paths parallel to the FMQ buffer, which holds $Fe^{3+}/\Sigma Fe_{melt}$ constant (Carmichael, 1991; Toplis and Carroll, 1996). In a system open to O_2 exchange, with its melt buffered at FMQ, the $Fe^{3+}/\Sigma Fe$ of the bulk system effectively reflects that of the crystallising phases, since $Fe^{3+}/\Sigma Fe_{melt}$ is fixed. Therefore, during Fe^{2+}-bearing ferromagnesian silicate crystallisation, the $Fe^{3+}/\Sigma Fe$ of the bulk system falls slightly. It increases thereafter, owing to a lower volumetric proportion of melt and pyroxenes, and higher fractions of magnetite, which possess elevated $Fe^{3+}/\Sigma Fe$. If the iron isotope composition of a given rock sample reflects the $Fe^{3+}/\Sigma Fe$ of the bulk system, then it is reasonable to expect that $\delta^{57}Fe$ mirrors this change. Indeed, this trend is delineated by most natural samples (Schuessler et al., 2009; Dauphas et al., 2009a; *figure 5.5.*), while this study and that of Teng et al., (2008), taken to represent closed systems, reach a maximum in $\delta^{57}Fe$ at ≈60wt% SiO_2, the inferred time of the pyroxene to magnetite transition (*figure 5.5.*). Thus, magnetite, with its heavy Fe isotope composition, may impart opposing effects in systems closed and open to oxygen in which it is the dominant host of Fe.

Intrusive granitic magmas, which usually evolve as systems closed to oxygen, may reflect the tectonic setting from which they are derived. The average 'hypersolvus' (A-type) granites of Poitrasson and Freydier (2005) are distinctly heavier ($\delta^{57}Fe$ = +0.44‰) than their calc-alkaline counterparts ($\delta^{57}Fe$ = +0.15‰) (*figure 5.6.*). This disparity correlates with differences in their Fe#s ($Fe^{(T)}/Fe^{(T)}$ + Mg). I-type granites exhibit limited iron and $\delta^{57}Fe$ enrichment indicative of early magnetite crystallisation which dampens their increase, meaning observable fractionation during differentiation may not be apparent in calc-alkaline suites (*figure 5.5., 5.6.*). Conversely, elevated Fe#s in A-type granitoids are a response to the suppression of magnetite crystallisation by the low fO_2 of the magma, also enabling $\delta^{57}Fe$ enrichment (*figure 5.5., 5.6.*). Their enriched iron isotope composition fortifies the hypothesis that A-type granites are often produced by protracted fractional crystallisation of a low fO_2, tholeiitic magma (Turner et al., 1992) and are akin to the granophyres described here from the Red Hill intrusion.

Conclusion

The pronounced effect crystal fractionation imparts on the $Fe^{3+}/\sum Fe$ of a given melt during igneous differentiation controls its resultant iron isotopic composition (Teng et al., 2008; Schuessler et al., 2009). We have demonstrated that the iron isotope composition of a tholeiitic melt closed to oxygen will become heavier as a result of removal of early-fractionating mafic phases which deplete the melt in Fe^{2+}, and enrich it in Fe^{3+} and alkalis, stabilising tetrahedrally-co-ordinated iron. In the latter stages of differentiation, when fO_2 is sufficiently high, magnetite becomes the dominant iron-bearing phase and sequesters Fe^{3+}. Due to the preference of heavy iron for the stiffer bonds of magnetite, the $\delta^{57}Fe$ of the residual melt decreases. These considerations point to an intimate link between iron isotope fractionation and the oxygen fugacity of the melt, which affects the valence, and hence structural state of iron between phases. Iron isotopes may therefore act as effective probes of the redox state and tectonic settings of terrestrial magmas.

Acknowledgements

The author would like to make a proverbial tip of the cap to the following people: Undoubtedly, John Foden deserves a sizeable commendation for his invaluable contribution to the realisation of this thesis. Not only was he a constant font of knowledge that was able to satisfy my ostensibly insatiable bloodlust for igneous petrological tidbits, his openness and concern throughout the course of the year was highly appreciated. The ideas he was able to conjure flowed like careening rivulets of thought cascading into a waterfall of bountiful opportunities. Certainly this thesis would not be in the state you are reading it in now if it weren't for such ideas.
Others that have contributed in some way to this project include:

- David Bruce, ever-helpful in the pursuits of radiogenic isotope geology. The time he took out of his schedule to assist me with the finer nuances of the TIMS and wet chemical techniques contributed greatly to the author's incipient chemical nous.
- Ben Wade, always happy to delve into the details of ICP-MS, be it laser or solution. The author is also indebted to Ben for his willingness to help devise a new method for running S-ICP samples, and indeed to allow the author to inundate the sample and skimmer cones with solution after solution of marginally diluted rock samples.
- Angus Netting, for his trademark 'rough –as-guts' tour of the electron microprobe and sardonic sense of humour.
- John Stanley for his tireless XRF work on my seemingly never-ending stream of samples.
- Amdel for promptly performing FeO determinations
- Galen Halverson, a long-distance friend and confidant with stable isotope geochemistry. Information garnered by the author in his final year of undergraduate work held him in great stead in the analytical world of MC-ICP-MS. For this and for Sunday afternoon lab sessions, the author is deeply grateful.
- Dave K and JP for their frequent advice and friendship during the year.
- My partners in crime the Honours cohort, particularly Alex 'ABB, Buches' Buchanan, Andrew 'Sir, Knighty' Knight, Alec 'A-dubs, 006' Walsh, Dave 'Orange-haired Spaniard' Segui and Dave 'DPJ' Pedler-Jones.

References

Aigner-Torres, M. et al., 2007. Laser Ablation ICPMS study of trace element partitioning between plagioclase and basaltic melts : an experimental approach. *Contributions to Mineralogy and Petrology*, 153, 647-667.

Albarède, F., 1996. Introduction to Geochemical Modeling. *Cambridge University Press. New York*. pp.564.

Allégre C.J. & Minster J.F., 1978. Quantitative models of trace element behavior in magmatic processes. Earth Planet. Sci. Lett. 38 I.

Allegre, C.J. et al., 1982. Subcontinental versus suboceanic mantle, II. Nd-Sr-Pb isotopic comparison of continental tholeiites with mid-ocean ridge tholeiites, and the structure of the continental lithosphere. *Earth and Planetary Science Letters*, 57, 25-34

Anbar, A.D., 2000. Nonbiological Fractionation of Iron Isotopes. *Science*, 288(5463), 126-128.

Anderson, D.L., 1994. The sublithospheric mantle as the source of continental flood basalts; the case against the continental lithosphere and plume head reservoirs.pdf. *Earth and Planetary Science Letters*, 123, 269-280.

Arai, S., Shimizu, Y., Gervilla, F., 2003. Quartz diorite veins in a peridotite xenoliths from Tallante, Spain: implications for reaction and survival of slab-derived SiO_2-oversaturated melt in the upper mantle. *Proc. Japan Acad.,* 79, 145-150.

Asimow, P.D., Hirschmann, M.M., Stolper E.M., 1997. An analysis of variations in isentropic melt productivity. *Phil. Trans. R. Soc. London*. 355, 255-281.

Baker, M. & Stolper, E., 1994. Determining the composition of high-pressure mantle melts using diamond aggregates. *Geochimica et Cosomochimica Acta*, 58(13), 2811-2827.

Balan, E. et al., 2006. The oxidation state of vanadium in titanomagnetite from layered basic intrusions. *American Mineralogist*, 91, 953-956.

Ballhaus, C., 1991. High pressure experimental calibration of the olivine-orthopyroxene-spinel oxygen geobarometer: implications for the oxidation state of the upper mantle. *Contributions to Mineralogy and Petrology*, 107(1), 27-40.

Beard, B. & Johnson, C., 2004. Inter-mineral Fe isotope variations in mantle-derived rocks and implications for the Fe geochemical cycle. *Geochimica et Cosmochimica Acta*, 68(22), 4727-4743.

Bebout, G.E., 2007. Metamorphic chemical geodynamics of subduction zones. *Earth and Planetary Science Letters*, 260, 373 - 393.

Bedard, J., 2007. Trace element partitioning coefficients between silicate melts and orthopyroxene: Parameterizations of D variations. *Chemical Geology*, 244(1-2), 263-303.

Bézos, A., Humler, E., 2005. The $Fe^{3+}/\Sigma Fe$ ratios of MORB glasses and their implications for mantle melting. *Geochimica et Cosmochimica Acta.* 69 (3), 711-725.

Berndt, J., Koepke, J. & Holtz, F., 2005. An Experimental Investigation of the Influence of Water and Oxygen Fugacity on Differentiation of MORB at 200 MPa. *Journal of Petrology*, 46(1), 135-167.

Bingham, P. et al., 2007. Local structure and medium range ordering of tetrahedrally coordinated Fe3+ ions in alkali–alkaline earth–silica glasses. *Journal of Non-Crystalline Solids*, 353(24-25), 2479-2494.

Blundy, J.D. & Wood, B.J., 1994. Prediction of crystal-melt partition coefficients from elastic moduli. *Nature*, 372, 452-454.

Blundy, J.D., Falloon, T.J., Wood, B.J., Dalton, J.A., 1995. Sodium partitioning between clinopyroxene and silicate melts. *Journal of Geophysical Research,*100, 15,501-15,515.

Blundy, J. & Wood, B., 2003. Partitioning of trace elements between crystals and melts. *Earth and Planetary Science Letters*, 210, 383-397.

Botcharnikov, R.E. et al., 2005. The effect of water activity on the oxidation and structural state of Fe in a ferro-basaltic melt. *Geochimica et Cosmochimica Acta*, 69(21), 5071-5085.

Botcharnikov, R.E. et al., 2008. Phase Relations and Liquid Lines of Descent in Hydrous Ferrobasalt-Implications for the Skaergaard Intrusion and Columbia River Flood Basalts. *Journal of Petrology*, 49(9), 1687-1727.

Boudreau, A.E., 1999. PELE - A version of the MELTS software program for the PC platform. Computers and Geosciences, v. 25, pp. 21-203

Bourman, R.P. & Alley, N.F., 1999. Permian glaciated bedrock surfaces and associated sediments on Kangaroo Island , South Australia : implications for local Gondwanan ice-mass dynamics. *Australian Journal of Earth Sciences*, (46), 523-531.

Bowen, N.L., 1928. The Evolution of the Igneous Rocks. *Princeton*, NJ. Princeton University Press.

Bowen, N.L. & Tuttle, O., 1950. The System NaAlSi3O8-KA1Si3O8-H20. *The Journal of Geology*, 58(5), 489-511.

Brauns, C.M. et al., 2000. Os Isotopes and the Origin of the Tasmanian Dolerites. *Journal of Petrology*, 41(7), 905-918.

Bromiley, G.D. & Redfern, S.A., 2008. The role of TiO 2 phases during melting of subduction-modified crust: Implications for deep mantle melting. *Earth and Planetary Science Letters*, 267, 301 - 308.

Buddington A.F. & Lindsley D.H., 1964. Iron-titanium oxide minerals and synthetic equivalents. J Petrology, 5, 310-357.

Campbell, I. H., & Nolan, J., 1974. Factors effecting the Stability Field of Ca-Poor Pyroxene and the Origin of the Ca-Poor Minimum in Ca-Rich Pyroxenes from Tholeiitic Intrusions. *Contributions to Mineralogy and Petrology*, 48, 205-219.

Campbell I.H., 1998. The mantle's chemical structure: insights from the melting products of mantle plumes, *in*: I.N.S. Jackson (Ed.), *The Earth's Mantle: Composition, Structure and Evolution.* Cambridge University Press, Cambridge, pp. 259–310.

Canil, D., & O'Neill, H.S.C., 1996. Distribution of ferric iron in some upper mantle assemblages, J. Petrol., 37, 609–635.

Canil, D., 2004. Mildly incompatible elements in peridotites and the origins of mantle lithosphere. *Lithos*, 77, 375-393

Carlson, R.W., Pearson, D.G. & James, D.E., 2005. Physical, chemical, and chronological characteristics of continental mantle. *Rev. Geophys.* 43, 1-24.

Carmichael I.S.E., 1967. The iron-titanium oxides of salic volcanic rocks and their associated ferromagnesian silicates. *Contrib. Mineral. Petrol*., 14, 36-64

Carmichael, I.S.E., Nicholls, J. & Smith, A.L., 1970. Silica activity in igneous rocks. *The American Mineralogist*, 55.

Carmichael, I.S.E., Turner, F.J., Verhoogen, J., 1974. Igneous Petrology. McGraw-Hill, New York. pp.739.

Carmichael, I.S.E. and Ghiorso, M.S., 1990. The effect of oxygen fugacity on the redox states of natural liquids and their crystallizing phases. *In* J. Nicholls and J.K. Russell, Eds., *Modern methods of igneous petrology: understanding magmatic processes*, 24, p. 190.212. *Reviews in Mineralogy*, Mineralogical Society of America, Washington, D.C.

Carmichael, I.S.E., 1991. The redox states of basic and silicic magmas : a reflection of their source regions ? *Contributions to Mineralogy and Petrology*, (106), 129-141.

Clarke, M. J., & Banks, M. R. 1975. The stratigraphy of the lower (Permo-Carboniferous) parts of the Parmeener Super-Group, Tasmania. In: *Gondwana Geology.* A.N.U. Press, 453-67.

Coffin, M.F. & Eldholm, O., 1994. Large igneous provinces: structure; crustal structure, dimensions and external consequences. *Reviews of Geophysics*, 32, 1-36

Coltice, N., Phillips, B.R., Bertrand, H., Ricard, Y., Rey, P., 2007. Global warming of the mantle at the origin of flood basalts over supercontinents. *Geology*, 35, 391-394.

Condie, K.C., 2001. Mantle Plumes and Their Record in Earth History. *Cambridge University Press*. pp. 306. ISBN: 0-521-01472-7.

Cox, K.G., 1980. A Model for Flood Basalt Vulcanism. *Journal of Petrology*, 21(4), 629-650.

Dasgupta, R. , Hirschmann, M.M., Smith, N.D., 2007. Partial Melting Experiments of Peridotite + CO2 at 3 GPa and Genesis of Alkalic Ocean Island Basalts. *Journal of petrology*, 48 (11), 2093-3007

Dauphas, N. et al., 2009a. Iron isotopes may reveal the redox conditions of mantle melting from Archean to Present. *Earth and Planetary Science Letters*, 288(1-2), 255-267.

Dauphas, N., Pourmand, A. & Teng, F., 2009b. Routine isotopic analysis of iron by HR-MC-ICPMS: How precise and how accurate? *Chemical Geology*, 267(3-4), 175-184.

Dauphas, N., Teng, F. & Arndt, N.T., 2010. Magnesium and iron isotopes in 2.7 Ga Alexo komatiites: Mantle signatures, no evidence for Soret diffusion, and identification of diffusive transport in zoned olivine. *Geochimica et Cosmochimica Acta*, 74, 3274-3291.

DePaolo, D.J., 1981. Trace element and isotopic effects of combined wallrock assimilation and fractional crystallization. *Earth and Planetary Science Letters*, 53, 189-202.

Dickenson, M.P. & Hess, P.C., 1986. Contributions to Mineralogy and The structural role and homogeneous redox equilibria of iron in peraluminous , metaluminous and peralkaline silicate melts. *Contributions to Mineralogy and Petrology*, 92, 207-217.

Downes, H., 2007. Origin and significance of spinel and garnet pyroxenites in the shallow lithospheric mantle : Ultramafic massifs in orogenic belts in Western Europe and NW Africa. *Lithos*, 99, 1 - 24.

Ebadi, A. & Johannes, W., 1991. Beginning of melting and composition of first melts in the system Q z - A b - O r - H 2 0 - CO2. *Contributions to Mineralogy and Petrology*, 106, 286-295.

Edwards, A. B. 1942. Differentiation of the dolerites of Tasmania. *J. Geol.* 50, 451-480.

Eiler, J.M. et al., 1997. Oxygen isotope variations in ocean island basalt phenocrysts. *Geochimica et Cosmochimica Acta*, 61, 2281-2293.

Elliot, D.H. et al., 1999. Long-distance transport of magmas in the Jurassic Ferrar Large Igneous Province, Antarctica. *Earth and Planetary Science Letters*, 167, 89-104.

Elburg, M.A., and Dougherty-Page, J.S., 1997. Chemical Separation of Pb from Arc Magmas. *Clean Room Procedures.* University of Adelaide.

Elkins-Tanton, L.T., 2007. Continental magmatism, volatile recycling, and a heterogeneous mantle caused by lithospheric gravitational instabilities. *Journal of Geophysical Research*, 112, 1-13.

Encarnaciòn, J., Fleming, T.H., Elliot, D.H., Eales, H.V., 1996. Synchronous emplacement of Ferrar and Karoo dolerites and the early breakup of Gondwana. Geology 24, 535-538.

Ernst, W.G., 2009. Archean plate tectonics, rise of Proterozoic supercontinentality and onset of regional, episodic stagnant-lid behaviour. *Gondwana Research*, 15, 243-253.

Falloon, T.J. and Danyushevsky, L.V., 2000. Melting of Refractory Mantle at 1.5, 2 and 2.5 GPa under Anhydrous and H2O-undersaturated Conditions: Implications for the Petrogenesis of High-Ca Boninites and the Influence of Subduction Components on Mantle Melting. J. Petrology, 41(2): 257-283.

Farges, F. et al., 2004. The effect of redox state on the local structural environment of iron in silicate glasses: a combined XAFS spectroscopy, molecular dynamics, and bond valence study. *Journal of Non-Crystalline Solids*, 344(3), 176-188.

Feig, S.T., Koepke, J. & Snow, J.E., 2010. Effect of oxygen fugacity and water on phase equilibria of a hydrous tholeiitic basalt. *Contributions to Mineralogy and Petrology.* 10.1007/s00410-010-0493-3

Fenner, C.N., 1929. The crystallization of basalts. *American Journal of Science*. 5(18), 225-253.

Foden, J. et al., 2002. Geochemical evolution of lithospheric mantle beneath S.E. South Australia. *Chemical Geology*, 182, 663-695.

Foden, J. et al., 2006. The Timing and Duration of the Delamerian Orogeny: Correlation with the Ross Orogen and Implications for Gondwana Assembly. *Geology*, 114, 189-210.

Foden, J.D., Halverson, G.P., Sossi, P., Elburg, M.A., 2009. Changing conditions of mantle wedge melting across arc as illustrated by changing iron isotopes compositions. *American Geophysical Union*, Fall Meeting 2009, abstract #T31D-04.

Foden, J.D., 2010. The petrogenesis of A-type granite: an endmember of granite formation mechanisms. *Australian Earth Sciences Convention, Canberra, July 4-8, 2010*.

Frost, B.R., Lindlsey, D.H. & Andersen, D.J., 1988. Fe-Ti oxide-silicate equilibria: Assemblages with fayalitic olivine. *American Mineralogist*, 73, 727-740.

Frost, D.J. & McCammon, C.A., 2008. The Redox State of Earth's Mantle. *Annu. Rev. Earth Planet. Sci.*, 36, 389-420.

Gaetani, G.A. & Grove, T.L., 1998. The influence of water on melting of mantle peridotite. *Contributions to Mineralogy and Petrology*, 131, 323-346.

Gallagher, K. & Hawkesworth, C.J., 1992. Dehydration melting and the generation of continental flood basalts. *Nature*, 358, 57-59.

Gao, S. et al., 2008. Recycling deep cratonic lithosphere and generation of intraplate magmatism in the North China Craton. *Earth and Planetary Science Letters*, 270, 41-53.

Ghiorso, M. S., and Sack, R. O., 1995. Chemical Mass Transfer in Magmatic Processes. IV. A Revised and Internally Consistent Thermodynamic Model for the Interpolation and Extrapolation of Liquid-Solid Equilibria in Magmatic Systems at Elevated Temperatures and Pressures*. Contributions to Mineralogy and Petrology,* 119, 197-212.

Ghiorso, M. S., Hirschmann, M.M., Reiners, P.W., and Kress, V. C. III (2002) The pMELTS: An revision of MELTS aimed at improving calculation of phase relations and major element partitioning involved in partial melting of the mantle at pressures up to 3 GPa. *Geochemistry, Geophysics, Geosystems,* 3(5), 10.1029/2001GC000217

Grove, T.L. & Juster, T.C., 1989. Experimental investigations of low-Ca pyroxene stability and olivine-pyroxene-liquid equilibria at 1-atm in natural basaltic and andesitic liquids. *Contributions to Mineralogy and Petrology*, 103(3), 287-305.

Grove, T.L., 1993. Corrections to expressions for calculating mineral components in "Origin of Calc-Alkaline Series Lavas at Medicine Lake Volcano by Fractionation, Assimilation and Mixing and

Experimental Petrology of normal MORB near the Kane Fracture Zone":. *Contributions to Mineralogy and Petrology*, 114, 422-424.

Hall, R.P., Hughes, D.J. & Joyner, L., 1988. Fe-enrichment in tholeiitic pyroxenes: complex two-pyroxene assemblages in Mesozoic dolerites, southern Tasmania. *Geol. Mag.*, 125(6), 573-582.

Hart, S.R. et al., 1992. Mantle plumes and entrainment: isotopic evidence. *Science*, 256, 517-520.

Hauri, E.H., Gaetani, G.A. & Green, T.H., 2006. Partitioning of water during melting of the Earth ' s upper mantle at H 2 O-undersaturated conditions. *Earth and Planetary Science Letters*, 248, 715 - 734.

Hawkesworth, C. et al., 1999. Mantle processes during Gondwana break-up and dispersal. *Journal of African Earth Sciences*, 28(1), 239-261.

Hawkesworth, C.J. & Kemp, A.I., 2006. Evolution of the continental crust. *Nature*, 443, 811-817.

Hergt, J.M. et al., 1989a. Geochemical and isotopic constraints on the origin of the Jurassic dolerites of Tasmania. *Journal of Petrology*, 30, 841-883.

Hergt, J.M. et al., 1989b. The geochemistry of Jurassic dolerites from Portal Peak, Antarctica. *Contributions to Mineralogy and Petrology*, 102, 298-305.

Hergt, J.M., Peate, D.W. & Hawkesworth, C.J., 1991. The petrogenesis of Mesozoic Gondwana low-Ti flood basalts. *Earth and Planetary Science Letters*, 105, 134-148.

Hergt, J.M. & Brauns, C.M., 2001. On the origin of Tasmanian dolerites. *Australian Journal of Earth Sciences*, 543-549.

Hermann, J. & Spandler, C.J., 2008. Sediment Melts at Sub-arc Depths: an Experimental Study. *Journal of Petrology*, 49(4), 717-740.

Herzberg, C. et al., 2000. New experimental observations on the anhydrous solidus for peridotite KLB-1. *Geochemistry Geophysics Geosystems*, 1(11), 1051-1064.

Herzberg, C., 2006. Petrology and thermal structure of the Hawaiian plume from Mauna Kea volcano. *Nature.*, 444, 605-609.

Herzberg, C. & Asimow, P.D., 2008. Petrology of some oceanic island basalts: PRIMELT2.XLS software for primary magma calculation. *Geochemistry Geophysics Geosystems*.

Himmelberg, G.R., & Ford, A.B., 1976. Pyroxenes of the Dufek Intrusion, Antarctica. *Journal of Petrology*, 17(2), 219-243.

Hirose, K., 1997. Melting experiments on lherzolite KLB-1 under hydrous conditions and generation of high-magnesian andesitic melts. *Geology*, 25(1), 42-44.

Hirschmann, M.M., Ghiorso, M.S. & Stolper, E.M., 1999a. Calculation of Peridotite Partial Melting from Thermodynamic Models of Minerals and Melts . II . Isobaric Variations in Melts near the Solidus and owing to Variable Source Composition. *Journal of Petrology*, 40(2), 297-313.

Hirschmann, M., Asimow, P.D., Ghiorso, M.S., & Stolper, E.M., 1999b. Calculation of Peridotite Partial Melting from Thermodynamic Models of Minerals and Melts. III. Controls on Isobaric Melt Production and the Effect of Water on Melt Production. *Journal of Petrology*, 40(5), 831-851.

Hirschmann, M.M., Aubaud, C. & Withers, A.C., 2005. Storage capacity of H 2 O in nominally anhydrous minerals in the upper mantle. *Earth and Planetary Science Letters*, 236, 167 - 181.

Hofmann, A.W., 1997. Mantle geochemistry: the message from oceanic volcanism. *Nature*, 385, 219-229.

Holloway, J. R., 2004. Redox reactions in seafloor basalts: possible insights into silicic hydrothermal systems. *Chemical Geology*, 210, 225–230.

Huebner, J. & Turnock, A., 1980. The melting relations at 1 bar of pyroxenes composed largely of Ca- , Mg- , and Fe-bearing components. *American Mineralogist*, 65, 225-271

Humayun, M., Qin, L. & Norman, M.D., 2004. Geochemical evidence for excess iron in the mantle beneath Hawaii. *Science*, 306, 91-94.

Ionov, D.A. & Wood, B.J., 1992. The oxidation state of subcontinental mantle: oxygen thermobarometry of mantle xenoliths from central Asia. *Contributions to Mineralogy and Petrology*, 111(2), 179-193.

Ivanov, A.V. et al., 2008. Low-Ti melts from the southeastern Siberian Traps Large Igneous Province: Evidence for a water-rich mantle source? *J. Earth Syst. Sci.*, 117(1), 1-21.

Jackson, M.G. et al., 2007. The return of subducted continental crust in Samoan lavas. *Nature*, 448, 3-6.

Jackson, M.G. & Dasgupta, R., 2008. Compositions of HIMU, EM1, and EM2 from global trends between radiogenic isotopes and major elements in ocean island basalts. *Earth and Planetary Science Letters*, 276, 175-186.

Jackson, W. et al., 2005. Multi-spectroscopic study of Fe(II) in silicate glasses: Implications for the coordination environment of Fe(II) in silicate melts. *Geochimica et Cosmochimica Acta*, 69(17), 4315-4332.

Jahn, B.M., Wu, F., Lo, C.-H., Tsai, C.-H., 1999. Crust–mantle interaction induced by deep subduction of the continental crust: geochemical and Sr–Nd isotopic evidence from post-collisional mafic–ultramafic intrusions of the northern Dabie complex, central China. *Chemical Geology,* 157(1-2), 119-146.

Jang, Y.D., Naslund, H.R. & Mcbirney, A.R., 2001. The differentiation trend of the Skaergaard intrusion and the timing of magnetite crystallization: iron enrichment revisited. *Earth and Planetary Science Letters*, 189, 189-196.

Jaques, A.L. & Green, D.H., 1980. Contributions to Mineralogy and Petrology Anhydrous Melting of Peridotite at 0-15 Kb Pressure and the Genesis of Tholeiitic Basaits. *Contributions to Mineralogy and Petrology*, 310, 287-310.

Jayasuriya, K.D. et al., 2004. A Mössbauer study of the oxidation state of Fe in silicate melts. *American Mineralogist*, 89(1991), 1597-1609.

Johnson, C.M., Beard, B.L. & Albarede, F., 2004. Overview and General Concepts. *Reviews in Mineralogy and Geochemistry*, 55(1), 1-24.

Johnson, M.C. & Rutherford, M.J., 1989. Experimental calibration of the aluminum-in-hornblende geobarometer with application to Long Valley caldera (California) volcanic rocks. *Geology*, 17(9), 837.

Johnston, A.D., 1986. Mineralogy and Anhydrous P-T phase relations of near-primary high-alumina basalt from the South Sandwich Islands Implications for the origin of island arcs and tonalite-trondhjemite series rocks. *Contributions to Mineralogy and Petrology*, 92, 368-382.

Karner, J.M. et al., 2008. Valence state partitioning of V between pyroxene-melt: Effects of pyroxene and melt composition, and direct determination of V valence states by XANES. Application to Martian basalt QUE 94201 composition. *Meteoritics & Planetary Science*, 43(8), 1275-1285.

Kay, R.W. & Kay, S.M., 1993. Delamination and delamination magmatism. *Tectonophysics*, 219, 177-189.

Kelemen, P.B., Hart, S.R. & Bernstein, S., 1998. Silica enrichment in the continental upper mantle via melt/rock reaction. *Earth and Planetary Science Letters*, 164(1-2), 387-406.

Kelsey, C.H., 1965. Calculation of the CIPW norm. *Mineralogical Magazine*. Mineralogical Society, 34, 276-282.

Kinzler, R.J., Grove, T.L., 1992. Primary Magmas of Mid-Ocean Ridge Basalts 1. Experiments and Methods. *Journal of Geophysical Research,* 97, 6885-6906.

Kinzler, R.J., 1997. Melting of mantle peridotite at pressures approaching the spinel to garnet transition: Application to mid-ocean ridge basalt petrogenesis. *Journal of Geophysical Research*, 102, 853-874.

Klein, E.M., Langmuir, C.H., 1987. Global Correlations of Ocean Ridge Basalt Chemistry with Axial Depth and Crustal Thickness. *Journal of Geophysical Research,* 92, 8089-8115.

Klemme, S., Blundy, J.D. & Wood, B.J., 2002. Experimental constraints on major and trace element partitioning during partial melting of eclogite. *Geochim. Cosmochim. Acta*, 66, 3109-3123.

Kushiro, I., Yoder, H.S. & Nishikawa, M., 1968. Effect of Water on the Melting of Enstatite. *Geological Society Of America Bulletin*, 79, 1685-1692.

Kushiro, I., 1996. Partial melting of a fertile mantle peridotite at high pressures: an experimental study using aggregates of diamond. In: (Basu, A., Hart, S.R., (eds Geophysical Monograph 95: *Earth Processes, Reading the Isotopic code*. *American Geophysical Union.* pp. 441.

Kogiso, T., Hirschmann, M.M. & Pertermann, M., 2004. High-pressure Partial Melting of Mafic Lithologies in the Mantle. *Petrology*, 45(12), 2407-2422.

Kress, V.C. & Carmichael, I.S.E., 1991. The compressibility of silicate liquids containing Fe2O3 and the effect of composition, temperature, oxygen fugacity and pressure on their redox states. *Contributions to Mineralogy and Petrology*, 108(1-2), 82-92.

Kushiro, I., 1972. Effect of water on the composition of magmas formed at high pressures. *Journal of petrology* , 13 (2), p. 311

Lambart, S., Laporte, D. & Schiano, P., 2009. An experimental study of pyroxenite partial melts at 1 and 1.5GPa: Implications for the major-element composition of Mid-Ocean Ridge Basalts. *Earth and Planetary Science Letters*, 288(1-2), 335-347.

Leake, B.E. et al., 1997. Nomenclature of Amphiboles: Report of the Subcommittee on Ampbiholes of the International Mineralogical Association, Commission on New Minerals and Mineral Names. *The Canadian Mineralogist*, 35, 219-246.

Lee, C.A., Brandon, A.D. & Norman, M.D., 2003. Vanadium in peridotites as a proxy for paleo-fO 2 during partial melting : Prospects , limitations , and implications. *Geochimica et Cosmochimica Acta*, 67(16), 3045-3064.

Lee, C.-T.A., Leeman,W.P., Canil, D., Li, Z.-X.A., 2005. Similar V/Sc systematics in MORB and arc basalts: implications for the oxygen fugacities of their mantle source regions*. J. Petrol.* 46, 2313–2336.

Lee, C.A., 2006. Geochemical / Petrologic Constraints on the Origin of Cratonic Mantle. *Geophysical Monograph*, 1-26.

Lee, C.-T.A., Cheng, X., Horodyskyj, U. The development and refinement of continental arcs by primary basaltic magmatism, garnet pyroxenite accumulation, basaltic recharge and delamination: insights from the Sierra Nevada, California. *Contrib. Mineral. Petrol.* 151, 222-242.

Lee, C.A. et al., 2009. Constraints on the depths and temperatures of basaltic magma generation on Earth and other terrestrial planets using new thermobarometers for mafic magmas. *Earth and Planetary Science Letters*, 279, 20-33.

Leitch, A.M. & Davies, G.F., 2001. Mantle plumes and flood basalts: from plume ascent and an eclogite Enhanced component melting. *Journal of Geophysical Research*, 106, 2047 - 2059.

Le Roux, V., Lee, C.A. & Turner, S.J., 2010. Zn/Fe systematics in mafic and ultramafic systems: implications for detecting major element heterogeneities in the Earth's mantle. *Geochimica et Cosmochimica Acta.* DOI: 10.1016/j.gca.2010.02.004

Lindsley, D.H. & Munoz, J.L., 1969. Subsolidus relations along the join hedenbergite-ferrosilite. *American Journal of Science*, 267, 295-324.

Lindlsley, D.H., 1983. Pyroxene thermometry. *American Mineralogist*, 68, 477-493.

Lindsley, D.H. & Frost, B.R., 1992. Equilibria among Fe-Ti oxides, pyroxenes, olivine, and quartz; Part I, Theory. *American Mineralogist,* 77(9-10), 987-1003.

Liu, Y. et al., 2010. Oxygen and iron isotope constraints on near-surface fractionation effects and the composition of lunar mare basalt source regions. *Geochimica et Cosmochimica Acta*. (In Press)

Ludwig, K.R., 2003. Isoplot 3.00: a geochronological toolkit for Microsoft Excel. *Berkeley Geochronology Center Special Publication*

Lustrino, M., 2005. How the delamination and detachment of lower crust can influence basaltic magmatism. *Earth Science Reviews*.

Mallmann, G., O'Neill, H.S. & Klemme, S., 2009. Heterogeneous distribution of phosphorus in olivine from otherwise well-equilibrated spinel peridotite xenoliths and its implications for the mantle geochemistry of lithium. *Contributions to Mineralogy and Petrology*, (158), 485-504.

Mallmann, G. & O'Neill, H.S., 2009. The Crystal/Melt Partitioning of V during Mantle Melting as a Function of Oxygen Fugacity Compared with some other Elements (Al, P, Ca, Sc, Ti, Cr, Fe, Ga, Y, Zr and Nb). *Journal of Petrology*, 50(9), 1765-1794.

Manton, W.I., 1988. Separation of Pb from young zircons by single-bead ion exchange. *Chemical Geology (Isotope Geoscience Section)*, 73, 147-152.

Maréchal, C., Télouk, P., Albarède, F., 1999. Precise analysis of copper and zinc isotopic compositions by plasma-source mass spectrometry. *Chemical Geology*, 156(1-4), 251-273.

Marsh, B.D., 2002. On bimodal differentiation by solidification front instability in basaltic magmas , part 1 : Basic mechanics. *Geochimica et Cosmochimica Acta*, 66(12), 2211-2229.

Marsh, B.D., 2004. A magmatic mush column rosetta stone: The McMurdo Dry Valleys of Antarctica. *EOS, Transactions of the American Geophysical Union*. 85(47) 497-502.

Marsh, B.D., 2007. Magmatism, Magma, and Magma Chambers. *In: Treatise in Geophysics: Volume 6 - Crustal and Lithosphere Dynamics*. 276-333. A. B. Watts, Oxford: Elsevier.

Mathez, E. A., 1984. Influence of degassing on oxidation states of basaltic magmas. *Nature* 310, 371–375.

McBirney, A.R. & Naslund, H.R., 1990. The differentiation of the Skaergaard Intrusion A discussion of Hunter and Sparks (Contrib Mineral Petrol 95:451-461). *Contributions to Mineralogy and Petrology*, 104, 235-247.

McCanta, M.C. et al., 2004. Iron partitioning between basaltic melts and clinopyroxene as a function of oxygen fugacity. *American Mineralogist*, 89, 1685-1693.

McDonough, W. F. (1990), Constraints on the composition of the continental lithospheric mantle, Earth Planet. Sci. Lett., 101, 1–18.

McDonough, W.F. & Sun, S., 1995. The composition of the Earth. *Chemical Geology*, 120, 223-253.

McDougall, I., 1962. Differentiation of the Tasmanian Dolerites: Red Hill Dolerite-Granophyre Association. *Geological Society of America Bulletin*, 73, 279-316.

McDougall, I. & Wellman, P., 1976. Potassium-argon ages for some Australian Mesozoic igneous rocks. *Australian Journal of Earth Sciences*, 23(1), 1-9.

Mckenzie, D.P. & Bickle, M.J., 1988. The volume and composition of melt generated by extension of the lithosphere. *Journal of Petrology*, 29, 625-679.

Merzbacher, C., Eggler, D.H., 1984. A magmatic geohygrometer: Application to Mount St. Helens and other dacitic magmas. *Geology*, 12(10), 587-590

Molzahn, M., Reisberg, L. & Worner, G., 1996. OS, Sr, Nd, Pb, O isotope and trace element data from the Ferrar flood basalts, Antarctica: evidence for an enriched subcontinental lithospheric source. *Earth and Planetary Science Letters*, 144, 529-546.

Milnes, A.R., Cooper, B.J., Cooper, J.A., 1982.The Jurassic Wisanger Basalt of Kangaroo Island, South Australia. Transactions of the Royal Society of South Australia, 106, 1-13.

Moore, L.J. et al., 1982. Absolute Isotopic Abundance Ratios and Atomic Weight of a Reference Sample of Strontium. *Journal Of Research Of The National Bureau Of Standards*, 87(1), 1-9.

Mysen, B.O. & Richet, P., 2005. *Developments in Geochemistry: Silicate Glasses and Melts - Properties and Structure*, Amsterdam: Elsevier, B.V.

Nicholls, J., Carmichael, I.S. & Stormer Jr., J.C., 1971. Silica activity and P total in igneous rocks. *Contributions to Mineralogy and Petrology*, 33(1), 1-20.

Nikolaev, G.S., Borisov, A.A. & Ariskin, A.A., 1996. Calculation of the Ferric – Ferrous Ratio in Magmatic Melts : Testing and Additional Calibration of Empirical Equations for Various Magmatic Series. *Geochemistry International*, 34(8), 641-649.

Nisbet, E.G. & Pearce, J.A., 1977. Contributions to Mineralogy and Clinopyroxene Composition in Marie Lavas from Different Tectonic Settings. *Contributions to Mineralogy and Petrology*, 160, 149-160.

O'Hara, M.J.,1968. The bearing of phase equilibria studies in synthetic and natural systems on the origin and evolution of basic and ultrabasic rocks. *Earth-science reviews* , 4, 69-133

O'Neill, C., Lenardic, A., Jellinek, A.M., Moresi, L., 2009. Influence of supercontinents on deep mantle flow. *Gondwana Research*, 15, 276-287.

O'Neill, H.S.C., 1981. The Transition Between Spinel Lherzolite and Garnet Lherzolite, and Its Use as a Geobarometer. *Contributions to Mineralogy and Petrology*, 77, 185-194.

O'Neill, H.S.C. 1987. Quartz-fayalite-iron and quartz-fayalite-magnetite equilibria and the free energy of formation of fayalite (Fe_2SiO_4) and magnetite (Fe_3O_4). *American Mineralogist.* 72 (1-2), 67-75.

O'Neill, H.S.C. et al., 2006. An experimental determination of the effect of pressure on the Fe3+-ΣFe ratio of an anhydrous silicate melt to 3.0GPa.pdf. *American Mineralogist*, 91, 402-412.

Palme, H., & O'Neill H.S.C., 2003. Cosmochemical estimates of mantle composition, *in Treatise on Geochemistry, vol. 2, The Mantle and Core*, edited by R. W. Carlson, H. D. Holland, and K. K. Turekian, pp. 1–38, Elsevier, New York.

Papike, J.J., Karner, J.M., Shearer, C.K., 2005. Comparative planetary mineralogy: Valence state partitioning of Cr, Fe, Ti, and V among crystallographic sites in olivine, pyroxene, and spinel from planetary basalts. *American Mineralogist*, 90(2-3), 277-290.

Parman, S.W. & Grove, T.L., 2004. Harzburgite melting with and without H 2 O : Experimental data and predictive modeling. *Journal of Geophysical Research*, 109, 1-20.

Pearce, N.J. et al., 1997. A Compilation of New and Published Major and Trace Element Data for NIST SRM 610 and NIST SRM 612 Glass Reference Materials. *Journal of Geostandards and Geonanalysis*, 21(1), 115-144.

Pertermann, M. & Hirschmann, M.M., 2003. Anhydrous Partial Melting Experiments on MORB-like Eclogite : Phase Relations , Phase Compositions and Mineral-Melt Partitioning of Major Elements at 2-3 GPa. *Journal of Petrology*, 44(12), 2173-2201.

Pickering-Witter, J. & Johnston, A.D., 2000. The effects of variable bulk composition on the melting systematics of fertile peridotitic assemblages. *Contributions to Mineralogy and Petrology*, 140(2), 190-211.

Plank, T. & Langmuir, C.H., 1998. The chemical composition of subducting sediment and its consequences for the crust and mantle. *Chemical Geology*, 145, 325-394.

Poitrasson, F. & Freydier, R., 2005. Heavy iron isotope composition of granites determined by high resolution MC-ICP-MS. *Chemical Geology*, 222(1-2), 132-147.

Poitrasson, F., 2009. Probes of the Ancient and the Inaccessible. *Science*, 323, 882-883.

Polyakov, V.B. & Mineev, S.D., 2000. The use of Mossbauer spectroscopy in stable isotope geochemistry. *Geochimica et Cosmochimica Acta*, 64(5), 849 - 865.

Polyakov, V.B. et al., 2007. Equilibrium iron isotope fractionation factors of minerals : Reevaluation from the data of nuclear inelastic resonant X-ray scattering and Mossbauer spectroscopy. *Geochimica et Cosmochimica Acta*, 71, 3833-3846.

Puffer, J.H., 2001. Contrasting high field strength element contents of continental flood basalts from plume versus reactivated-arc sources. *Geology*, 29, 675-678.

Qin, L. & Humayun, M., 2008. The Fe/Mn ratio in MORB and OIB determined by ICP-MS. *Geochimica et Cosmochimica Acta*, 72, 1660-1677.

Rapp, R.P. et al., 2008. Subduction recycling of continental sediments and the origin of geochemically enriched reservoirs in the deep mantle. *Earth and Planetary Science Letters*, 271, 14-23.

Roeder, P.L. & Emslie, R.F., 1970. Olivine-Liquid Equilibrium. *Contributions to Mineralogy and Petrology*, 29, 275-289.

Rollinson, H.R., 1993. Using geochemical data : evaluation, presentation, interpretation. Longman Scientific & Technical, New York, pp. 352

Rudnick, R.L. & Fountain, D.M., 1995. Nature and composition of the continental crust: a lower crustal perspective. *Reviews of Geophysics*, (95), 267-309.

Rudnick, R.L., Gao, S., 2003. Composition of the continental crust. *In: Rudnick, R.L. (Ed.), Treatise on Geochemistry, vol. 3, The Crust*. Elsevier, pp. 1–64.

Rutherford, L. et al., 2006. Continental ca 1.7 – 1.69 Ga Fe-rich metatholeiites in the Curnamona Province, Australia: a record of melting of a heterogeneous, subduction-modified lithospheric mantle. *Australian Journal of Earth Sciences*, 53(3), 501-519.

Sack, R.O. & Ghiorso, M.S., 1994. Thermodynamics of multicomponent pyroxenes : II . Phase relations in the quadrilateral. *Contributions to Mineralogy and Petrology*, 116, 287-300

Schauble, E.A., 2004. Applying Stable Isotope Fractionation Theory to New Systems. In C. M. Johnson, B. L. Beard, & F. Albarede *Geochemistry Of Non-traditional Stable Isotopes*. Washington, DC: Mineralogical Society Of America, pp. 65-111.

Schertl, H.-P., Schreyer, W., 2008. Geochemistry of coesite-bearing "pyrope quartzite" and related rocks from the Dora-Maira Massif, Western Alps. *European journal of mineralogy (Stuttgart) (0935-1221)*, 20 (5), p. 791.

Schmidt, P.W., McDougall, I., 1977. Palaeomagnetic and potassium-argon dating studies of the Tasmanian Dolerites, *Australian Journal of Earth Sciences*, **24**, 5-6, 321-328

Schoenberg, R. & von Blanckenburg, F., 2005. An assessment of the accuracy of stable Fe isotope ratio measurements on samples with organic and inorganic matrices by high-resolution multicollector ICP-MS. *International Journal of Mass Spectrometry*, 242(2-3), 257-272.

Schoenberg, R. & Blanckenburg, F., 2006. Modes of planetary-scale Fe isotope fractionation. *Earth and Planetary Science Letters*, 252(3-4), 342-359.

Schoenberg, R. et al., 2009. Fe isotope systematics of coexisting amphibole and pyroxene in the alkaline igneous rock suite of the Ilímaussaq Complex, South Greenland. *Chemical Geology*, 258(1-2), 65-77.

Schuessler, J. et al., 2007. The experimental calibration of the iron isotope fractionation factor between pyrrhotite and peralkaline rhyolitic melt. *Geochimica et Cosmochimica Acta*, 71(2), 417-433.

Schuessler, J.A., 2008. Controls on stable iron isotope variations in magmatic systems. *Unpublished PhD Thesis*, University of Hannover.

Seymour, D.B., Calver, C.R., 2001. Explanatory notes for the Time–Space Diagram and Stratotectonic Elements Map of Tasmania. *Tasmania Geological Survey Record, 1995-2001.* pp. 62.

Shahar, A., Young, E.D. & Manning, C.E., 2008. Equilibrium high-temperature Fe isotope fractionation between fayalite and magnetite : An experimental calibration. *Earth and Planetary Science Letters*, 268, 330 - 338

Simpson, E.S.W., Slater, J.G., Parsons, B., Norton, I.O., Meinke, L., 1979. Mesozoic magnetic lineations in the mozambique basin. Earth Planetary Science Letters 43, 260-264.

Singletary, S.J. & Grove, T.L., 2003. Early petrologic processes on the ureilite parent body. *Meteoritics & Planetary Science*, 38(1), 95-108.

Sisson, T.W. & Grove, T.L., 1993. Temperatures and H2O contents of low-MgO high-alumina basalts. *Contributions to Mineralogy and Petrology*, 113(2), 167-184.

Smith, P.M. & Asimow, P.D., 2005. Adiabat_1ph: A new public front-end to the MELTS, pMELTS, and pHMELTS models. *Geochemistry Geophysics Geosystems*, 6(2), 1-8.

Snyder D., Carmichael I.S.E., Wiebe R.A., 1993. Experimental study of liquid evolution in an Fe-rich, layered mafic intrusion: constrains of Fe-Ti oxide precipitation on the T- fO2 and T-ρ paths of tholeiitic magmas. *Contrib Mineral Petrol* 113, 73–86.

Sobolev, A.V. et al., 2005. An olivine-free mantle source of Hawaiian shield basalts. *Nature*, 434, 590-597.

Sobolev, A.V. et al., 2007. The Amount of Recycled Crust in Sources of Mantle-Derived Melts. *Science*, 316, 412 - 417.

Spandler, C. et al., 2008. Phase Relations and Melting of Anhydrous K-bearing Eclogite from 1200 to 16008C and 3 to 5 GPa. *Petrology*, 49(4), 771-795.

Spandler, C., Yaxley, G. & Green, D.H., 2010. Experimental phase and melting relations of metapelite in the upper mantle : implications for the petrogenesis of intraplate magmas. *Contributions to Mineralogy and Petrology*. DOI: 10.1007/s00410-010-0494-2

Spencer, K.J., Lindsley, D.H., 1981. A solution model for coexisting iron-titanium oxides. *American Mineralogist*. 66, 1189-1201.

Steinhofel, G., Horn, I. & Blanckenburg, F.V., 2009. Micro-scale tracing of Fe and Si isotope signatures in banded iron formation using femtosecond laser ablation. *Geochimica et Cosmochimica Acta*, 73(18), 5343-5360.

Stormer Jr., J.C. & Nicholls, J., 1978. XLFRAC: a program for the interactive testing of magmatic differentiation models. *Computers & Geosciences*, 4(2), 143-159.

Strelow, F.W., 1980. Improved separation of iron from copper and other elements by anion-exchange chromatography on a 4% cross-linked resin with high concentrations of hydrochloric acid. *Talanta*, 27, 727-732.

Sun, S.-S., McDonough, W.F., 1989. Chemical and isotopic systematics of oceanic basalts: implications for mantle composition and processes. *In*: Saunders, A.D., Norry, M.J. Eds. , *Magmatism in the Ocean Basins*. Blackwell, Oxford, UK, pp. 313–346.

Takahahshi, E., Nakajima, K. & Wright, T.L., 1998. Origin of the Columbia River basalts : melting model of a heterogeneous plume head. *Science*, 162, 63-80.

Tanaka, T. et al., 2000. JNdi-1: a neodymium isotopic reference in consistency with LaJolla neodymium. *Chemical Geology*, 168(3-4): 279-281.

Teng, F., Dauphas, N. & Helz, R.T., 2008. Iron Isotope Fractionation in Kilauea Iki Lava Lake. *Science*, 320, 1620-1622

Tiepolo, M. et al., 2000. Nb and Ta incorporation and fractionation in titanian pargasite and kaersutite: crystal-chemical constraints and implications for natural systems. *Earth and Planetary Science Letters*, 176, 185-201.

Todt W., Cliff R.A., Hanser A. and Hofmann A.W., 1996. Evaluation of a 202Pb-205Pb double spike for high-precision lead isotope analysis. *In*: A. Basu and S.Hart (eds), *Earth Processes: reading the isotopic code*. American Geophysical Union Geophysical Monograph, 95, 429-437.

Toplis, M.J. et al., 1994. The role of phosphorus in crystallisation processes of basalt : An experimental study. *Geochimica et Cosmochimica Acta*, 58(2), 797-810.

Toplis, M.J. & Carroll, M.R., 1995. An Experimental Study of the Influence of Oxygen Fugacity on Fe-Ti Oxide Stability , Phase Relations , and Mineral- Melt Equilibria in Ferro-Basaltic Systems. *Journal of Petrology*, 36(5), 1137-1170.

Toplis, M.J. & Carroll, M.R., 1996. Differentiation of Ferro-Basaltic Magmas under Conditions Open and Closed to Oxygen : Implications for the Skaergaard Intrusion and Other Natural Systems. *Journal of Petrology*, 37, 837-858.

Toplis, M.J. & Corgne, A., 2002. An experimental study of element partitioning between magnetite , clinopyroxene and iron-bearing silicate liquids with particular emphasis on vanadium. *Contributions to Mineralogy and Petrology*, 144, 22-37.

Toplis, M.J., 2005. The thermodynamics of iron and magnesium partitioning between olivine and liquid: criteria for assessing and predicting equilibrium in natural and experimental systems. *Contributions to Mineralogy and Petrology*, 149(1), 22-39.

Tormey, D.R., Grove, T.L. & Bryan, W.B., 1987. Contributions to Mineralogy and Experimental petrology of normal M O R B near the Kane Fracture Zone : 220-25 ~ N , mid-Atlantic ridge. *Contributions to Mineralogy and Petrology*, 96, 121-139.

Turner, S.P., Foden, J.D. & Morrison, R.S., 1992. Derivation of some A-type magmas by fractionation of basaltic magma: An example from the Padthaway Ridge, South Australia. *Lithos*, 28, 151-179.

Turner, S.P. et al., 1993. Sm-Nd isotopic evidence for the provenance of sediments from the Adelaide fold belt and southeastern Australia with implications for episodic crustal addition: Geochimica et. *Geochimica et Cosmochimica Acta*, 57, 1837-1857.

Turner, S. & Hawkesworth, C.J., 1995. The nature of the sub-continental mantle: constraints from the major-element composition of continental flood basalts. *Chemical Geology*, 120, 295-314.

Turner, S.P. et al., 1996. Source of the Lachlan fold belt flysch linked to convective removal of the lithospheric mantle and rapid exhumation of the Delamerian-Ross fold belt. *Geology*, 941-944.

Turner, S.P., 1996. Petrogenesis of the late-Delamerian gabbroic complex at Black Hill, South Australia: implications for convective thinning of the lithospheric mantle. *Mineralogy and Petrology*, 56, 51-89.

Tuttle, O.F. and Bowen, N.L., 1958. Origin of granite in the light of experimental studies in the system $NaAlSi_3O_8$-$KAlSi_3O_8$-SiO_2-H2O. *Geol. Soc. Am. Mem.,* 74, pp. 153

Verhoogen, J., 1962. Distribution of titanium between silicates and oxides in igneous rocks. *American Journal of Science* 260, 211-220.

Vernon, R.H., 2004. A practical guide to Rock Microstructure. *Cambridge University Press.* pp. 594. ISBN: 0 521 89133 7.

Villiger, S., Ulmer, P. & Muntener, O., 2007. Equilibrium and Fractional Crystallization Experiments at 0.7GPa; the Effect of Pressure on Phase Relations and Liquid Compositions of Tholeiitic Magmas. *Journal of Petrology*, 48(1), 159-184.

Wade, B.P., Hand, M., Maidment, D.W., Close, D.F. and Scrimgeour, I.R., 2008. Origin of metasedimentary and igneous rocks from the Entia Dome, eastern Arunta region, central Australia: a U and Pb LA-ICPMS, SHRIMP and Sm and Nd isotope study. *Australian Journal of Earth Sciences: An International Geoscience Journal of the Geological Society of Australia*, 55(5): 703 - 719.

Walter, M.J., 1998. Melting of Garnet Peridotite and the Origin of Komatiite and Depleted Lithosphere. *Journal of Petrology*, 39(1) 29–60.

Wasylenki, L.E. et al., 2003. Near-solidus Melting of the Shallow Upper Mantle: Partial Melting Experiments on Depleted Peridotite. *Journal of Petrology*, 44(7), 1163-1191.

Weyer, S. & Schwieters, J.B., 2003. High precision Fe isotope measurements with high mass resolution MC-ICPMS. *International Journal of Mass Spectrometry*, 226, 355-368.

Whalen, J.B., Currie, K.L., Chappell, B.W., 1987. A-type granites: geochemical characteristics, discrimination and petrogenesis. *Contributions to Mineralogy and Petrology* **95**, 407-419.

Whalen, J.B., Jenner, G.A., Longstaffe, F.J., Robert, F., Gariepy, C., 1996. Geochemical and Isotopic (O, Nd , Pb and Sr) Constraints on A-type Granite Petrogenesis Based on the Topsails Igneous Suite , Newfoundland Appalachians*. Journal of Petrology* **37**, 6, 1463-1489.

Whittaker, J.M., Müller, R.D., Goncharov, A., 2008. Australia-Antarctica rifting. *PESA Eastern Australasian Basins Symposium III Sydney, 14–17 September, 2008*. 271-274.

Wilke, M., 2005. Fe in magma – An overview. *Annals of Geophysics*, 48(4/5), 609-617.

Willbold, M. & Stracke, A., 2010. Formation of enriched mantle components by recycling of upper and lower continental crust. *Chemical Geology*, 276(3-4), 188-197.

Williams, H.M. et al., 2005. Systematic iron isotope variations in mantle rocks and minerals : The effects of partial melting and oxygen fugacity. *Earth and Planetary Science Letters*, 235, 435 - 452.

Williams, H.M. et al., 2009. Fractionation of oxygen and iron isotopes by partial melting processes : Implications for the interpretation of stable isotope signatures in mafic rocks. *Earth and Planetary Science Letters*, 283(1-4), 156-166.

Williams, I. S. & Hergt, J. M. U–Pb dating of Tasmanian dolerites: a cautionary tale of SHRIMP analysis of high-U zircon. In: Woodhead J. D., Hergt J. M. & Noble W. P. eds. Beyond 2000: New frontiers in Isotope Geoscience, Lorne, 2000, pp. 185–188. School of Earth Sciences, University of Melbourne, Melbourne

Wilson A. D., 1960. The micro-determination of Fe^{2+} in silicate minerals. Anal. 85, 823–827.

Workman, R.K. & Hart, S.R., 2005. Major and trace element composition of the depleted MORB mantle (DMM). *Earth Planet. Sci. Lett.*, 231, 53-72.

Wu, Y. et al., 2009. The fate of subducted Upper Continental Crust: An experimental study. *Earth and Planetary Science Letters*, 282(1-4), 275-284.

Yaxley, G. M. & Green, D. H., 1998. Reactions between eclogite and peridotite: mantle refertilisation by subduction of oceanic crust. *Schweizerische Mineralogische und Petrographische Mitteilungen* 78, 243-255.

Yaxley, G.M., 2000. Experimental study of the phase and melting relations of homogeneous basalt + peridotite mixtures and implications for the petrogenesis of flood basalts. *Contrib. Mineral. Petrol.*, 139, 326-338.

Tables

2.0. General

Table 2.1: Approximate modal mineral proportions in the Red Hill sequence deduced from petrographic analyses

	Chilled Dolerites/KI	Dolerites	Quartz Dolerites	Fayalite Granophyres	Granophyres
Orthopyroxene	5				
Augite	40	25	15	10	5
Pigeonite	5	15	10		
Plagioclase	45	50	55	30	20
Quartz	<1	5	15	25	35
Alkali Feldspar				15	25
Fayalite				5	
Magnetite				10	10
Ilmenite	1-2	3	5	5	5
Glass	<2 (KI only)				

3.0. The Mantle Source

Table 3.1.: A comparison of Tholeiitic Basalts. Chemical data from the Tasmanian dolerites, Parana Low-Ti basalts, Karoo (Nuanetsi), and the Deccan (Ambenali) province corrected for fractionation to MgO = 8 wt% (from Turner and Hawkesworth, 1995). N-MORB data from Workman and Hart, (2005).

	Tasmania$_{(8.0)}$	**N-MORB$_{(8.0)}$**	**Parana Low Ti$_{(8.0)}$**	**Karoo$_{(8.0)}$**	**Deccan$_{(8.0)}$**
SiO_2 %	52.88	50.50	49.92	51.14	48.14
CaO/Al_2O_3	0.72	0.71	0.68	0.88	0.79
$Fe_2O_3^T$ %	9.01	12.15	10.81	11.41	13.98
Mg#	67.00	59.00	65.00	59.00	57.00
Na_2O %	1.72	2.18	2.27	2.11	2.09
TiO_2 %	0.56	2.83	0.88	3.43	1.85
Ce/Pb	4.7	30.6	5.1	15.7	12.8
Nb/U	6.4	46.4	11.1	-	24.8
Nb/La	0.41	0.77	0.62	0.49	0.96
Ti/Zr	40.00	140.95	61.00	56.00	99.00
$\varepsilon Nd_{(i)}$	-5.85	8.40	-4.49	-6.54	2.94

Table 3.2. A comparison of Fe/Mn and Zn/Fe ratios of planetary reservoirs, and the K_D values used in the calculations (*figure 3.8.*) Fe/Mn data from Qin and Humayun, (2008); Zn/Fe from Le Roux et al., (2010), UCC calculated from Rudnick and Gao (2003). Uncertainties are 1σ for published data, and 2σ for data in this study.

	Olivine	OPX	CPX	Garnet	DMM	MORB	OIB	UCC	Tas + KI	Tas	KI
$K_{D_{Min-Liq}}^{Fe/Mn}$	1.30	0.85	0.69	0.60	1.1	-	-	-	-	-	-
Fe/Mn	≈70	≈44	-	-	60±10	54±1.2	56-67	50.59	52.34±.71	53.49±.31	50.20±.44
$K_{D_{Min-Liq}}^{Zn/Fe}$	0.92	0.96	0.56	0.20	0.9	-	-	-	-	-	-
Zn/Fe	-	-	-	-	9.75±1.25	10±1.5	10-16	17.1	10.39±.21	10.67±.10	9.97±.23

Table 3.3.: Model parameters for Zn/Fe and Fe/Mn mantle source modelling. K_Ds taken from Le Roux et al., (2010), with Fe/Mn_{source} from Qin and Humayun (2008).

	Garnet Peridotite	Cratonic Mantle	OPX-enriched Mantle	MORB-like Pyroxenite
Modes	Ol: 0.61 OPX: 0.25 CPX: 0.104 Gt: 0.036	Ol: 0.8 OPX: 0.2 CPX: - Gt: -	Ol: 0.68 OPX: 0.3 CPX: 0.02 Gt: -	Ol: - OPX: 0.2 CPX: 0.6 Gt: 0.2
Fe/Mn_{Source}	60	60	60	54
$K_{D(\frac{peridotite}{melt})}^{Fe/Mn}$	1.10	1.21	1.17	.704
$\left(\frac{Fe}{Mn}\right)_{melt}$	54.60	49.59	52.04	76.70
Zn/Fe_{source}	9.5	9.5	9.5	10
$K_{D(\frac{peridotite}{melt})}^{Zn/Fe}$	0.87	0.93	0.92	0.568
$\left(\frac{Zn}{Fe}\right)_{melt}$	10.96	10.23	10.27	17.6

Table 3.4.: Starting compositions, compositions of fractionated phases and the resultant model compositions calculated by mass balance addition of plagioclase, orthopyroxene and olivine. See section 3.2.5 for details.

	Average Chilled Margin	Plagioclase	OPX	CM + 25% OPX-Plag	CM + 25% OPX-Plag +3% Ol	CM + 25% OPX-Plag + 12% Ol	Ferrar Dolerite, Darwin Glacier (DG49)
SiO_2 %	53.79	47.95	55.02	53.21	52.83	51.76	52.96
Al_2O_3 %	14.62	32.25	0.93	15.11	14.66	13.30	16.41
FeO	7.80			7.23	7.34	7.36	7.32
Fe_2O_3	1.30			1.06	1.03	0.94	1.22
FeO^T	8.97	0.50	11.18	8.18	8.27	8.20	8.41
$Fe_2O_3{}^T$ %	9.96			9.10	9.19	9.12	9.35
$Fe^{3+}/\sum Fe$	0.13			0.13*	0.13*	0.13*	0.13*
MnO %	0.17	0.02	0.26	0.16	0.16	0.14	0.17
MgO %	6.72	0.26	30.09	8.83	10.02	13.84	8.67
CaO %	10.86	16.82	2.40	10.55	10.23	9.28	10.63
Na_2O %	1.82	2.07	0.02	1.63	1.58	1.43	1.64
K_2O %	0.82	0.11	0.01	0.63	0.61	0.56	0.47
TiO_2 %	0.62	0.01	0.09	0.48	0.47	0.42	0.50
P_2O_5 %	0.11			0.08	0.08	0.07	0.06
SO_3 %	0.02			0.01	0.01	0.01	-
LOI %	0.33			0.25	0.24	0.22	-
Mg#	60.56	N/A	82.75	68.54	70.87	77.01	67.87
Fo Olivine	83.66	N/A	N/A	87.90	89.02	91.78	87.56
Total %	**99.85**	**99.99**	**100.00**	**99.13**	**99.26**	**99.33**	**100.04**

Table 3.5.: Major element compositions of typical mantle clinopyroxene and orthopyroxene. Data from Workman and Hart, 2005. The 70:30 CPX/OPX column represents their relative contribution to mantle melts.

Element	CPX	OPX	70:30 CPX:OPX	Difference 3-4
SiO_2	50.61	53.36	51.435	1.925
TiO_2	0.63	0.16	0.489	-0.329
Al_2O_3	7.87	6.27	7.39	-1.12
Cr_2O_3	1.2	0.76	1.068	-0.308
$FeO^{(T)}$	2.94	6.27	3.939	2.331
MnO	0.09	0.12	0.099	0.021
MgO	16.19	30.55	20.498	10.052
NiO	0.06	0.09	0.069	0.021
CaO	19.52	2.18	14.318	-12.138
Na_2O	0.89	0.05	0.638	-0.588
Mg#	90.75	89.67	90.27	
Total	100	99.81	99.94	

Table 3.6. Major element compositions of depleted cratonic mantle, terrigenous sediment, and the resultant hybrid used in the pMELTS model.

	Low-T Craton (after Carlson, 2005; after McDonough, 1990)	Terrigenous Sediment (EPSM) (Spandler et al., 2010)	Peridotite + 3% EPSM
SiO_2	44.18	69.02	44.93
TiO_2	0.05	0.57	0.06
Al_2O_3	1.6	14.74	1.99
Fe_2O_3	0.5	0.8	0.51
Cr_2O_3	0.44	0	0.43
FeO^T	7.6	4.5	7.51
MnO	0.12	0	0.12
MgO	44	2.52	42.76
NiO	0.27	0	0.26
CaO	1.45	2.46	1.48
Na_2O	0.09	2.52	0.16
K_2O	0.02	1.8	0.07
P_2O_5	0.01	0.22	0.02
H_2O	0	1	0.03
Mg#	91.16	49.95	91.03
TOTAL	100.33	100.15	100.32

Table 3.7. Calculated phase proportions and melt compositions produced from the modelled source composition (column 2) in adiabat_1ph, using the pMELTS algorithm (Smith and Asimow, 2005).

Mineral	**Mode %**				**Ferrar Parent**
1GPa	**Subsolidus**	**1325°C**	**1350°C**	**1375°C**	**1377±19°C**
Ol	64.79	64.91	65.21	65.49	N/A
OPX	29.00	26.73	24.74	22.15	N/A
CPX	4.60	0	0	0	N/A
Spinel	1.61	1.16	1.05	0.93	N/A
Melt	0	*7.52*	*9.33*	*11.75*	*9.71±1.65*
SiO_2	44.93	52.36	52.36	52.48	51.76
TiO_2	0.06	0.72	0.66	0.58	0.42
Al_2O_3	1.99	14.21	13.16	11.90	13.30
Fe_2O_3	0.51	0.74	0.79	0.83	0.94
Cr_2O_3	0.43	0.12	0.15	0.18	-
FeO	7.51	5.76	6.51	7.23	7.36
MnO	0.12	0.01	0.02	0.02	0.14
MgO	42.76	12.61	14.45	16.50	13.84
NiO	0.26	0.01	0.01	0.01	-
CaO	1.48	9.80	8.93	7.90	9.28
Na_2O	0.16	2.06	1.69	1.36	1.43
K_2O	0.07	0.98	0.79	0.63	0.56
P_2O_5	0.02	0.22	0.17	0.14	.07
H_2O	0.03	0.40	0.32	0.26	0.22
Mg#	91.03	79.61	79.83	80.25	77.01

Table 3.8. Distinctive trace element ratios, their abundances in certain terrestrial reservoirs, and the inferred process for their fractionation.

Ratio	UCC	LCC	DMM	N-MORB	Ferrar	Signficance
Nb/U	4.44	12.64	48.00	49.57	6.03	Nb retained in rutile during slab melting
Th/U	3.89	3.77	2.22	2.55	3.91	Relatively constant ratio
Ce/Pb	3.71	4.60	30.07	25.00	4.62	Pb mobilised during sediment/slab dehydration
Rb/Sr	0.26	0.05	0.00	0.01	0.22	Sr compatible in plagioclase
P/Nd	24.25	67.14	70.48	69.86	29.29	P compatible in nesosilicates (olivine, garnet) and apatite
Ti/Zr	19.88	83.07	152.26	102.70	46.40	Ti retained in rutile during slab melting
Nb/Ta	13.33	9.57	15.43	17.65	10.96*	Fractionated by rutile ($D^{Ta} > D^{Nb}$)
Zr/Hf	36.42	33.33	33.61	36.10	37.13	CPX – $D^{Hf} > D^{Zr}$
Ba/Nb	52.00	22.39	2.63	2.70	41.96	Ba mobilised in slab fluids, Nb sequestered in rutile (± amphibole)
Hf/Sm	1.13	0.66	0.60	0.78	0.78	
Sr/Pr	45.07	82.14	70.02	68.18	45.06	Sr compatible in plagioclase
Nb/La	0.39	0.61	0.64	0.93	0.44	Nb retained in rutile during slab melting (± amphibole)
Sr/Y	15.24	12.11	1.95	3.21	6.19	Sr compatible in plagioclase, Y in garnet
Ba/Rb	7.43	12.50	11.35	11.25	7.17	Ba mobilised in slab fluids, both held in phlogopite
Eu/Eu*	0.69	1.13	1.01	1.00	0.81	Eu^{2+} compatible in plagioclase
$La_{(N)}/Sm_{(N)}$	4.14	2.18	0.40	0.60	2.44	Indicator of LREE enrichment ($D_{LREE} < D_{H,MREE}$)
Pb/Pb*	2.98	2.32	0.27	0.36	2.30	Quantifies Pb enrichment

Table 3.9. Trace element concentrations of depleted DMM, the upper continental crust, the calculated hybried, the modelled melt, and the actual average Ferrar tholeiite.

Element	DMM Source (Workman and Hart, 2005)	UCC (Rudnick and Gao, 2003)	DMM + 3% UCC	Modelled Melt (pMELTS)	Average Ferrar
Rb	0.02	84	2.54	27.24	32.60
Ba	0.227	624	18.94	203.23	199.77
Th	0.004	10.5	0.32	3.43	3.23
U	0.0018	2.7	0.083	0.89	0.81
Nb	0.0864	12	0.44	4.55	5.18
Ta	0.0056	0.9	0.03	0.33	0.46
La	0.134	31	1.06	11.30	11.24
Ce	0.421	63	2.30	24.44	24.49
Pb	0.014	17	0.52	5.61	5.24
Pr	0.087	7.1	0.30	3.14	3.04
Nd	0.483	27	1.28	13.43	12.35
Sr	6.092	320	15.51	164.04	137.18
Zr	4.269	193	9.93	93.63	79.73
Hf	0.127	5.3	0.28	2.97	2.14
Sm	0.21	4.7	0.34	3.59	2.92
Eu	0.086	1	0.11	1.17	0.83
Gd	0.324	4	0.43	4.46	3.4
Tb	0.064	0.7	0.08	0.85	0.55
Dy	0.471	3.9	0.57	5.81	3.61
Ho	0.108	0.83	0.13	1.30	0.77
Y	3.129	21	3.67	37.61	22.27
Er	0.329	2.3	0.39	3.87	2.30
Yb	0.348	2	0.40	3.81	2.27
Lu	0.056	0.31	0.06	0.60	0.34

Table 3.10. Isotopic compositions and depleted mantle model ages for Red Hill samples and that derived of the contaminant and the value for D-DMM of Workman and Hart (2005).

	Chilled dolerite (PS65)	Dolerite (PS48)	Quartz Dolerite (PS50)	Fay. Granophyre (PS54)	Granophyre (PS38)	Granophyre (PS14)	UCC Contaminant	D-DMM
Neodymium								
Nd ppm	12.68	11.87	20.75	35.23	38.31	38.96	27.00	0.48
Sm ppm	2.91	2.77	4.48	8.55	8.38	8.56	4.70	0.21
143/144 Nd (measured)	0.51232 ±.0000086	0.51229 ±.0000094	0.51227 ±.0000105	0.51226 ±.0000072	0.51228 ±.0000096	0.51225 ±.0000120	0.51178	0.51326
T_{mod}:dep (Ga)	1.16	1.21	1.13	1.33	1.14	1.18	1.45	-
$143/144Nd_{(180)}$	0.51215	0.51213	0.51212	0.51209	.51212	0.51209	0.51166	0.51295
$\varepsilon Nd_{(180)}$	-4.96	-5.47	-5.58	-6.22	-5.59	-6.08	-14.64	10.61
Strontium								
Sr ppm	127.6	120.3	150.8	121.2	114.6	119.7	320	6.092
Rb ppm	33	31.2	58.1	99.7	110	113.7	84	0.02
$^{87}Sr/^{86}Sr$ (measured)	0.71256 ±.0000112	0.71250 ±.0000130	0.71354 ±.0000130	0.71651 ±.0000127	0.71762 ±.0000163	0.71700 ±.0000140	0.71780	0.70219
$^{87}Sr/^{86}Sr_{(180)}$	0.71064	0.71058	0.71069	0.71041	0.71051	0.70996	0.71585	0.70217
T_{mod}:dep (Ga)	0.95	0.94	0.70	0.41	0.38	0.37	1.43	-
Lead								
Pb ppm	5.1	8.1		16.3	17.2	14.9		
U ppm	.88	1.8		3	3.7	2.3		
Th ppm	3.3	4.7		10.4	9.6	11.9		
$^{206}Pb/^{204}Pb$	18.886±2	18.903±4		18.935±2	18.921±2	18.946±2		
$^{207}Pb/^{204}Pb$	15.624±2	15.624±3		15.629±2	15.624±1	15.626±1		
$^{208}Pb/^{204}Pb$	38.692±5	38.692±8		38.749±5	38.732±3	38.746±4		
$^{206}Pb/^{204}Pb_{(180)}$	18.281	18.499		18.600	18.921	18.665		
$^{207}Pb/^{204}Pb_{(180)}$	15.594	15.604		15.612	15.624	15.612		
$^{208}Pb/^{204}Pb_{(180)}$	38.459	38.348		38.370	38.732	38.271		

4.0. Differentiation

Table 4.1.: Table of D-values used for the calculations

	Low-Ca Pyroxene	Augite	Plagioclase
P	0.09	0.08	0.13
Ti	0.25	0.63	0.03
Sc	1.24	3.46	0.06
V	1.13	3.09	0.03
Cr	13.65	9.03	0.03
Co	1.77	1.88	0.03
Ni	5.16	4.94	0.02
Cu	0.02	0.02	0.01
Zn	1.30	1.09	0.17
Ga	0.13	0.20	1.16
Rb	0.01	0.01	0.07
Sr	0.01	0.05	1.45
Y	0.35	0.63	0.01
Zr	0.04	0.08	0.00
Nb	0.01	0.01	0.01
Ba	0.00	0.01	0.16
La	0.05	0.09	0.04
Ce	0.06	0.15	0.04
Pr	0.07	0.20	0.03
Nd	0.09	0.29	0.03
Sm	0.15	0.46	0.05
Eu	0.07	0.36	0.43
Gd	0.21	0.57	0.00
Tb	0.26	0.62	0.04
Dy	0.33	0.71	0.00
Ho	0.36	0.74	0.00
Er	0.44	0.74	0.00
Yb	0.60	0.82	0.00
Lu	0.64	0.81	0.00
Hf	0.05	0.14	0.00
Pb	0.02	0.05	0.35
Th	0.01	0.01	0.01
U	0.10	0.04	0.00

Figures

1.0. Analytical Methods

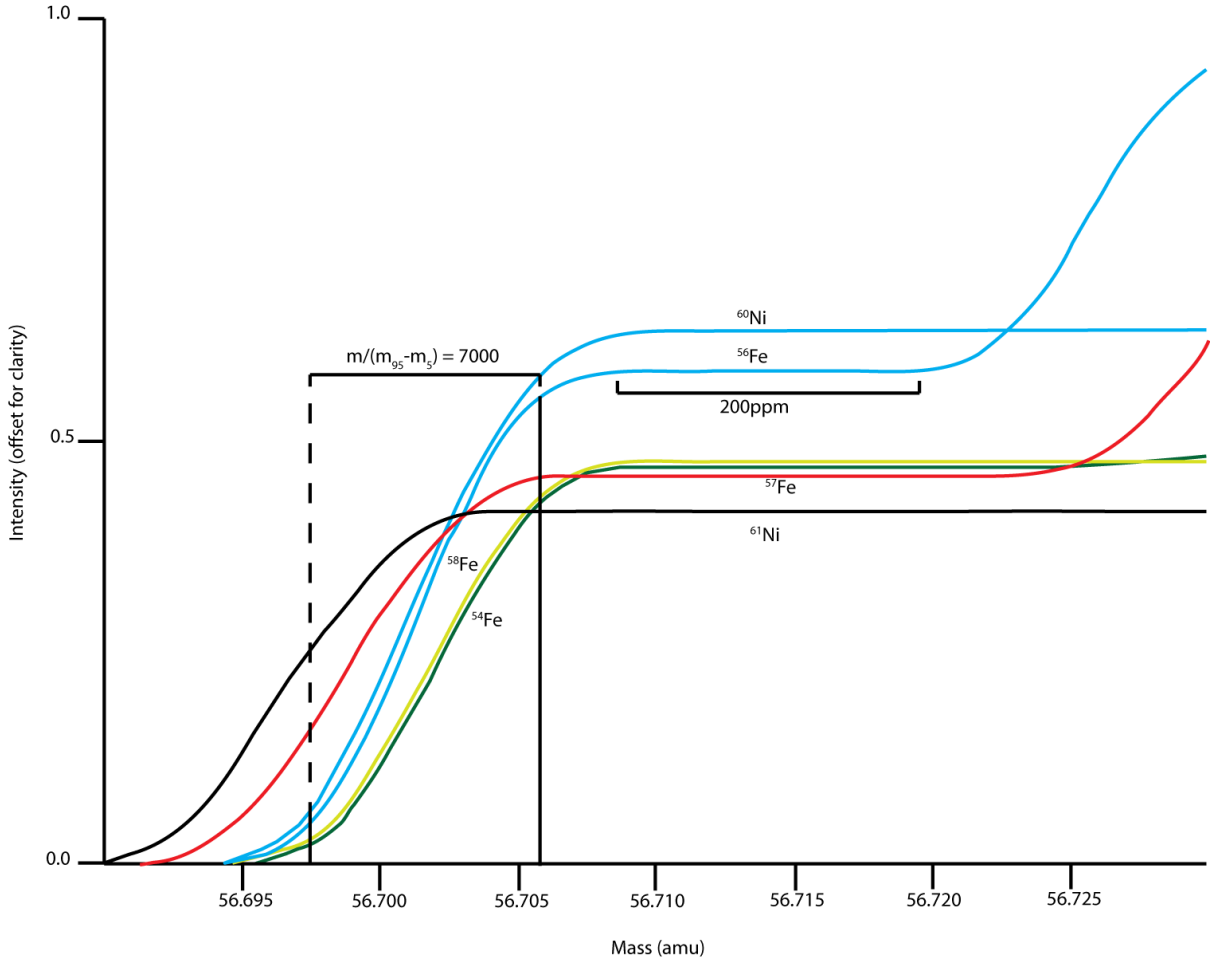

Figure 1.1. A typical mass scan in an Fe-Ni tune solution on the ThermoFinnigan Neptune MC-ICP-MS housed at the university of Adelaide (Waite Campus). The peak intensities are offset for clarity.

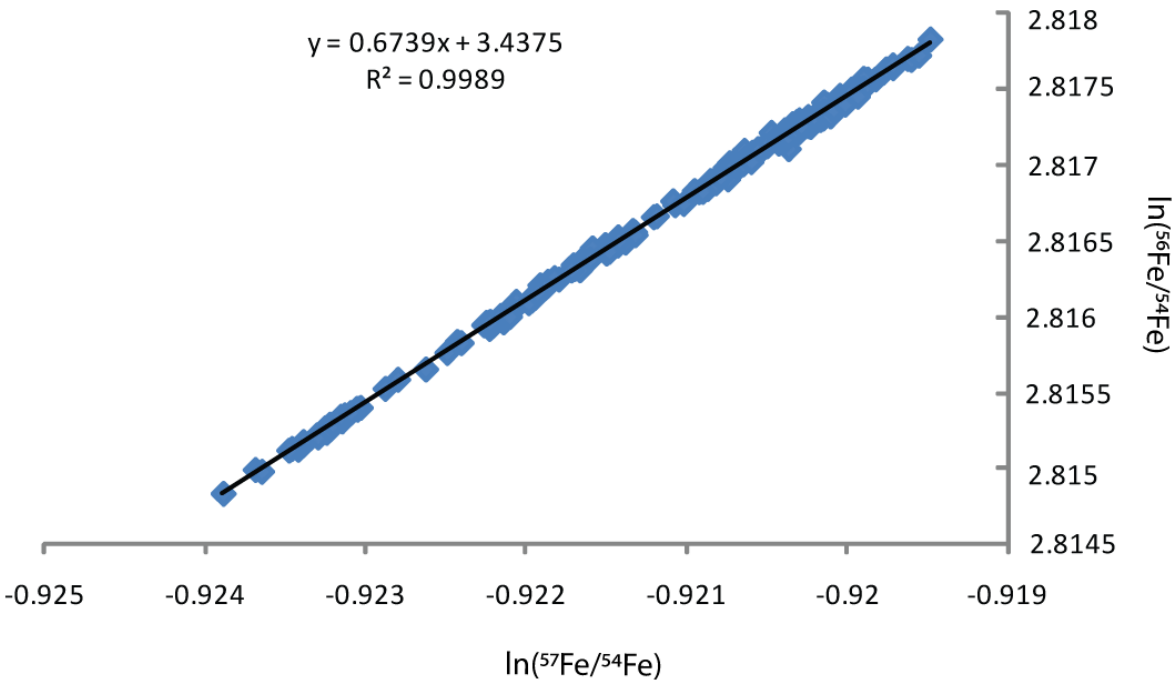

Figure 1.2. Shows a plot of raw ln(^{57}Fe/^{54}Fe) vs raw ln(^{56}Fe/^{54}Fe) for all individual analyses (*n* = 195) performed throughout the data collection period.

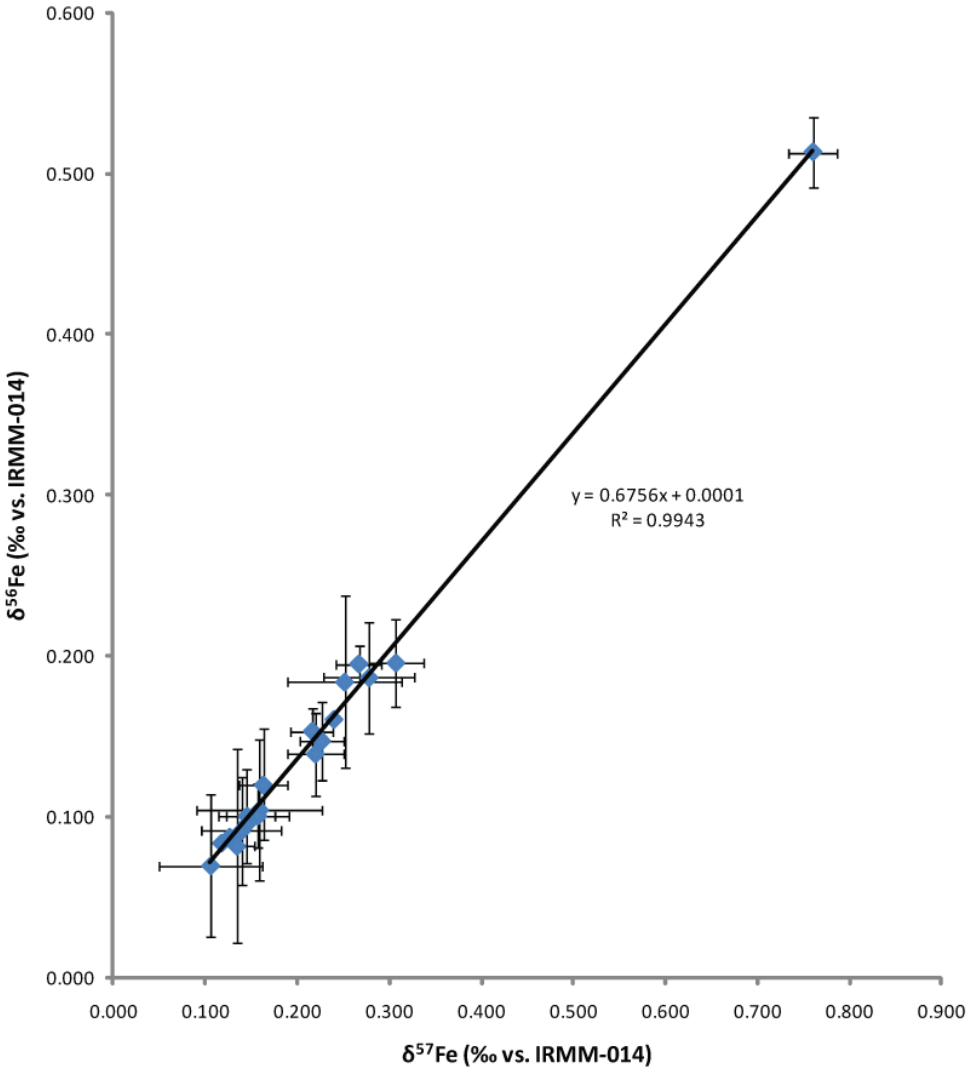

Figure 1.3. Displays the corrected δ^{56}Fe values against the corrected δ^{57}Fe values.

2.0. General

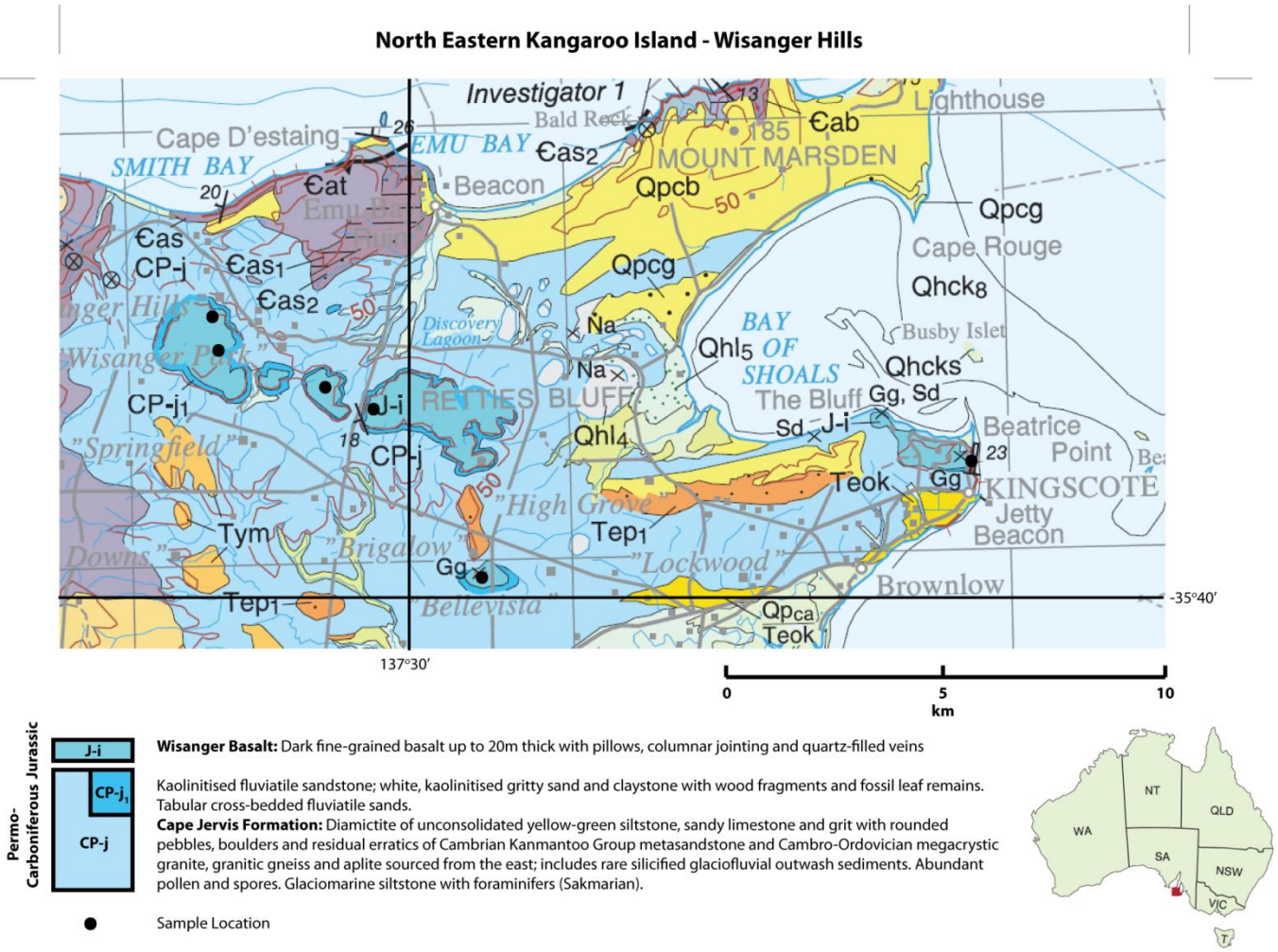

Figure 2.1. Geological map of North-Eastern Kangaroo Island, highlighting the outcrop and extent of the Kangaroo Island (Wisanger) basalts. Sample locations are also plotted. After Fairclough (2007).

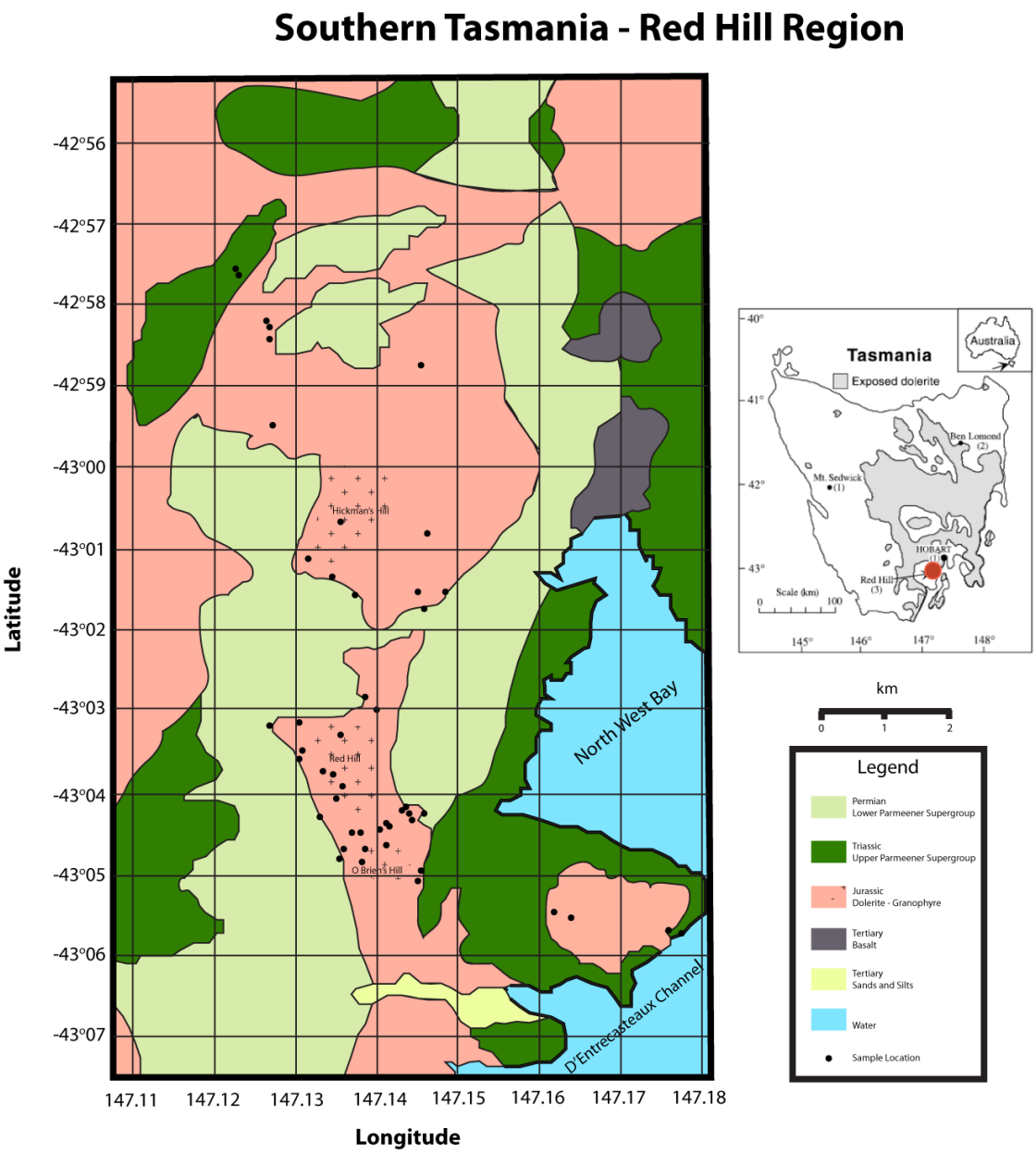

Figure 2.2. Geological map of Southern Tasmania, the Red Hill Region, highlighting the outcrop and extent of the Tasmanian Dolerites. The regions of granophyres are also delineated, in addition to the sample locations. See text for unit descriptions. After McDougall (1962).

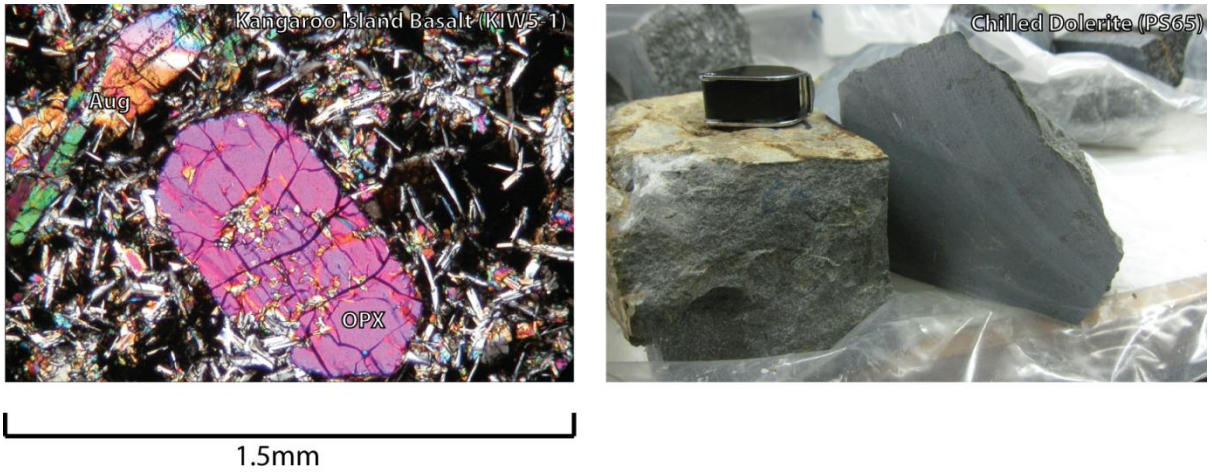

Figure 2.3. a) (XPL) Euhedral orthopyroxene microphenocryst (En_{83}**)** and smaller subhedral augite phenocrysts in a plagioclase-glass matrix in a Kangaroo Island basalt (KIW5-1). The swallow-tailed terminations on groundmass plagioclase and the presence of glass are indicative of quick cooling upon extrusion. *b)* Hand-specimen of a Tasmanian chilled dolerite (PS65), illustrating its very fine grain size.

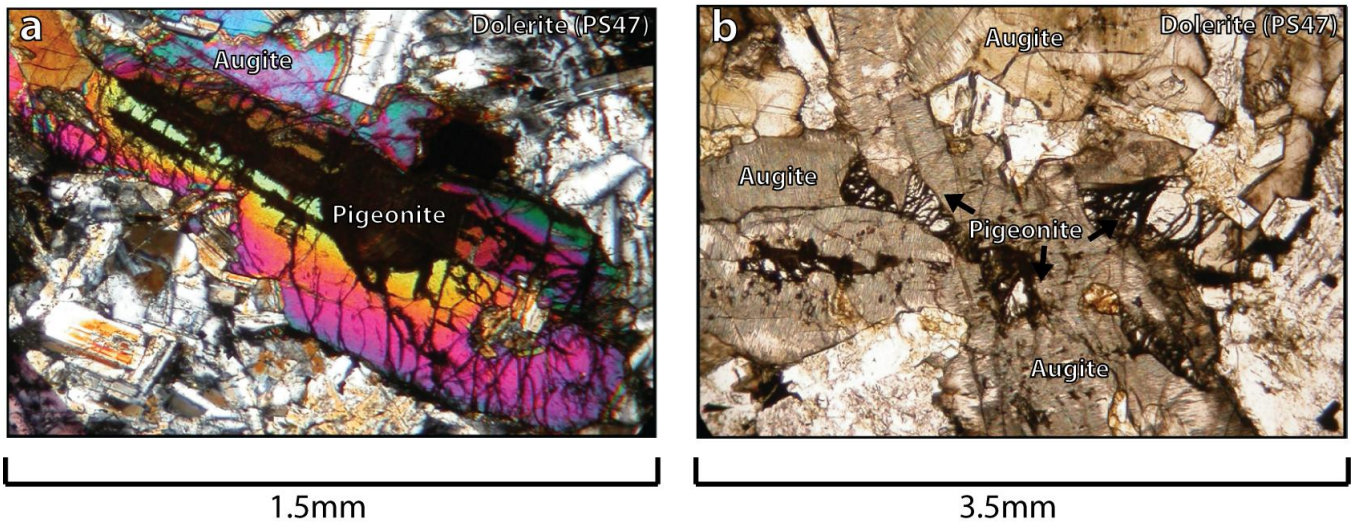

Figure 2.4. a) (XPL) Heavily zoned pigeonite (En_{75} to En_{30}) in a dolerite, also exhibiting an exsolved core, with lamellae along the [001], either side of a simple twin. Augite is also present with exsolution along [001]. *b)* (PPL) Consertally intergrown pigeonite and augite in a dolerite. Pigeonite appeared to nucleate first before it was itself used as a nucleus for augite, which subsequently grew at a greater rate. *c)* Typical quartz dolerite, possessing a mottled texture defined by pyroxene clusters and plagioclase.

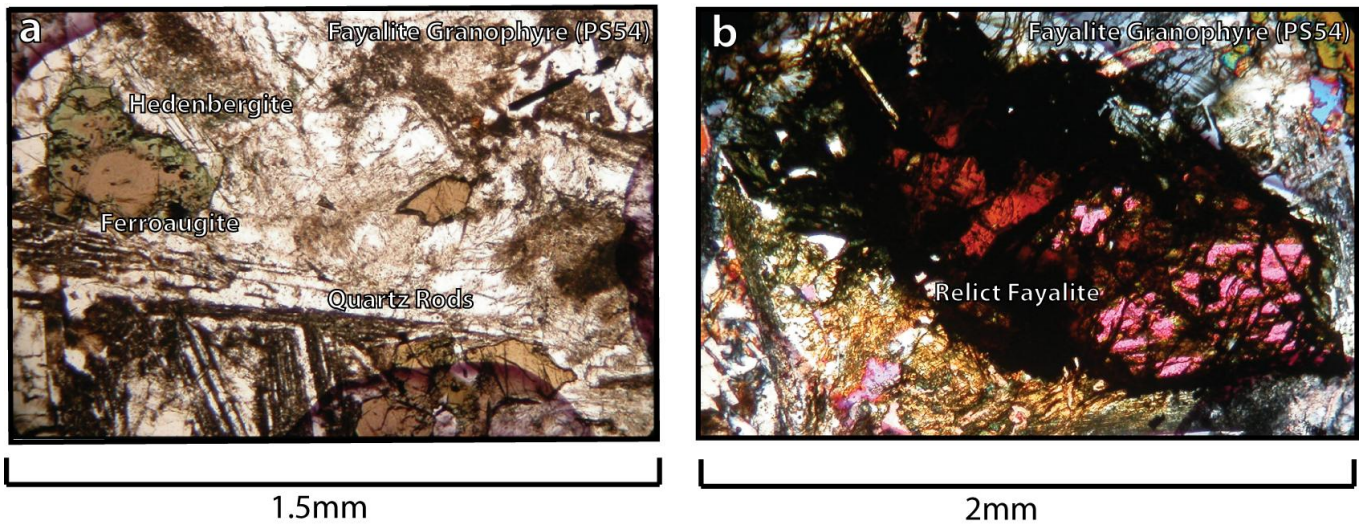

Figure 2.5. a) (PPL) Unzoned brown ferroaugite (Di_{25}) rimmed by vermicular hedenbergite (Di_{10}) in a fayalite granophyre, also showing rod-like quartz. *b)* (XPL) A large (≈2mm) relict euhedral fayalite grain, extensively inundated via oxidation along fractures by iron-rich alteration phases (laihunite). *c)* Distinctively spotted fayalite granophyres, where the spots consist of pyroxenes, fayalite and oxides, while the green-grey groundmass consists of alkali feldspar (orthoclase), plagioclase (mainly andesine) and quartz.

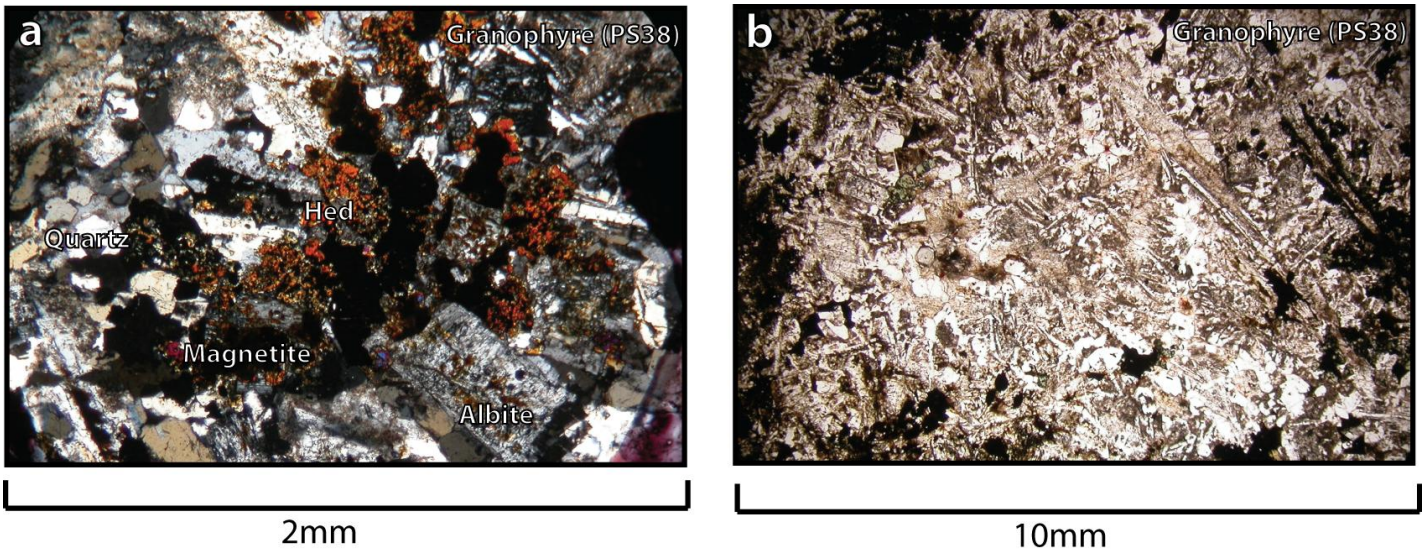

Figure 2.6. a) (XPL) Vermicular hedenbergite (Di_{10}) surrounded by magnetite and quartz, with subsidiary tabular albite. *b)* (PPL) Overview of a granophyre detailing the regions of intergrown skeletal quartz and orthoclase. *c)* Pale tan groundmass of quartz and orthoclase typify the granophyres, in addition to their elongate clusters of hedenbergite and associated magnetite.

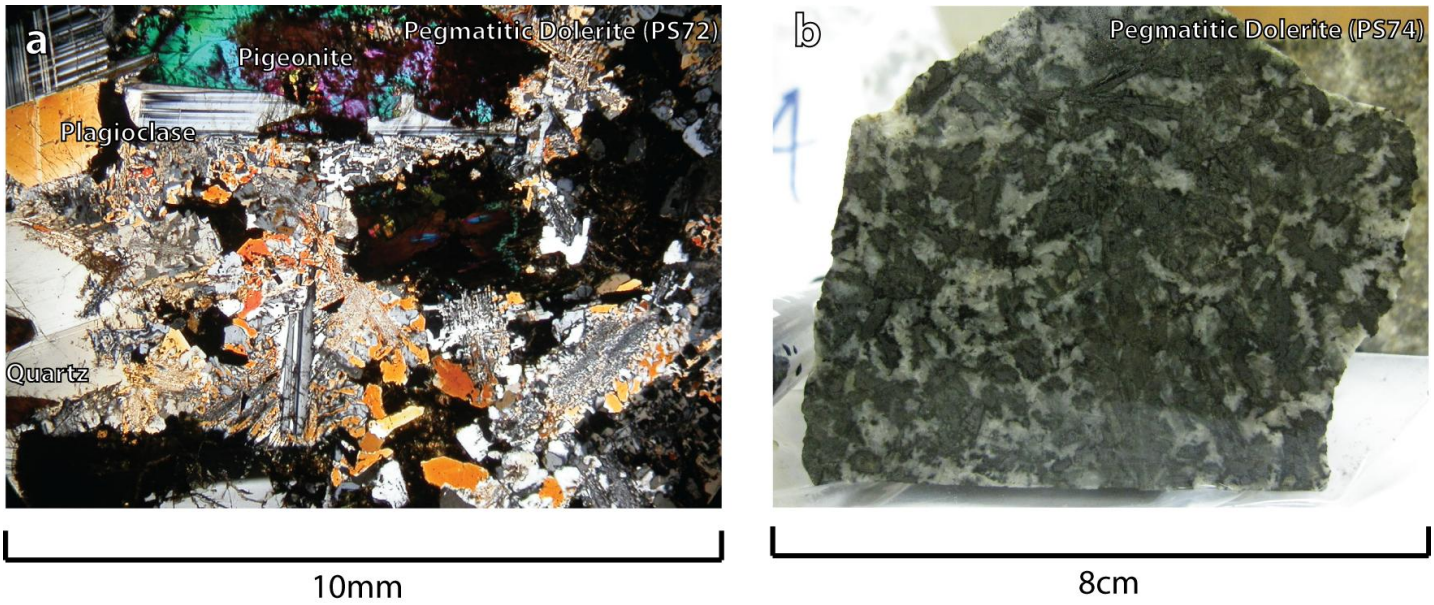

Figure 2.7. a) (XPL) A pegmatitic segregation displaying enlarged crystals of plagioclase and pyroxene, and an abundance of quartz-alkali feldspar granophyric intergrowths. *b)* Feathery pyroxenes readily evident in hand-specimen, as is the coarse grain size of the rock as a whole. This pegmatite is a mafic variety, and contains magnesian biotite and pyroxenes and bytownite-labradorite plagioclase.

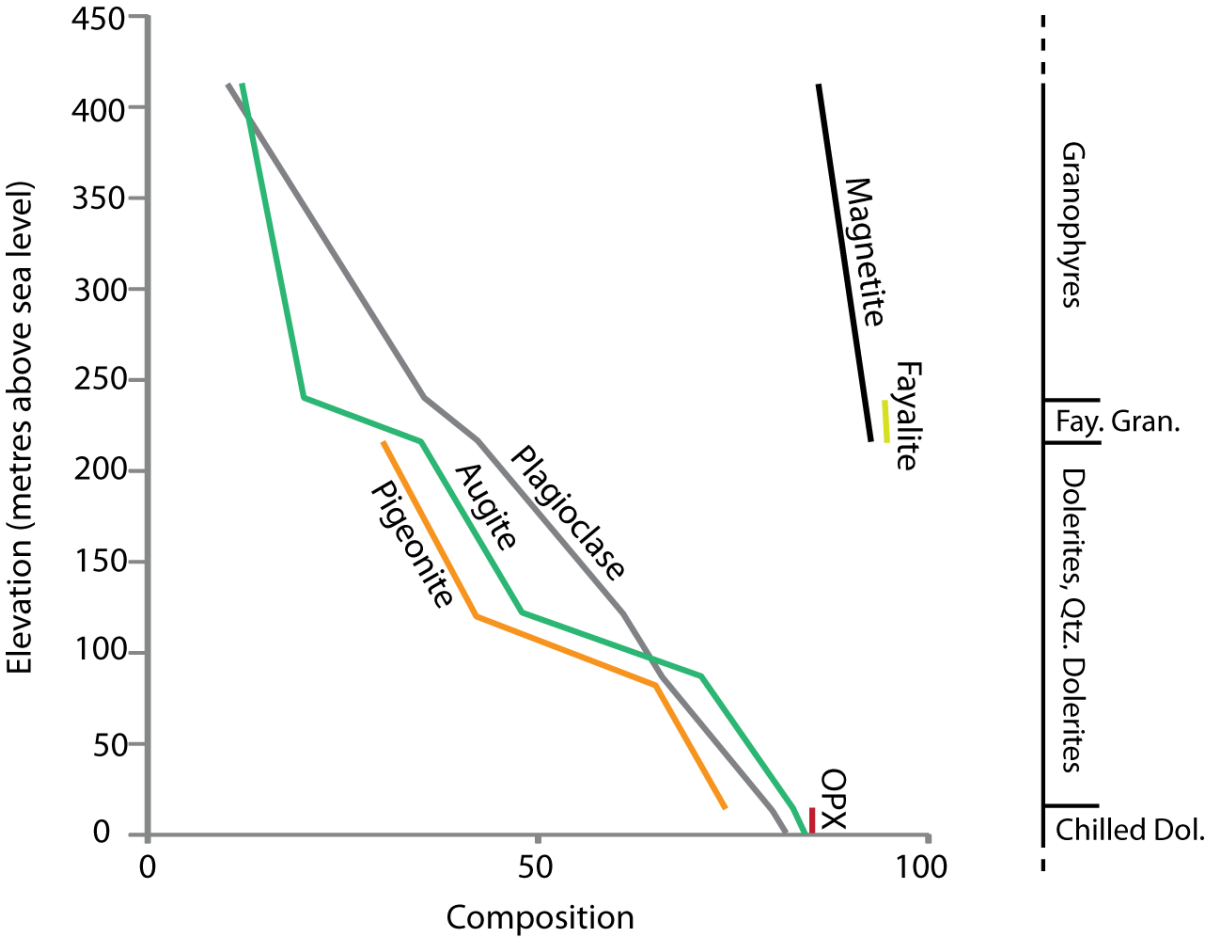

Figure 2.8. Illustration of the compositional variation in the main mineral phases at Red Hill. Compositions correspond to: Mg# (Pigeonite, Augite, OPX); Anorthite content (Plagioclase); Fayalite content (Fayalite); Magnetite content (Magnetite).

The data points were taken from average electron microprobe analyses of the minerals and correlated with the elevation of that sample in the sequence. Notable is the relative constancy of pyroxene Mg# after the disappearance of pigeonite and the arrival of magnetite, and is discussed in section 4.0.

3.0. Mantle Source

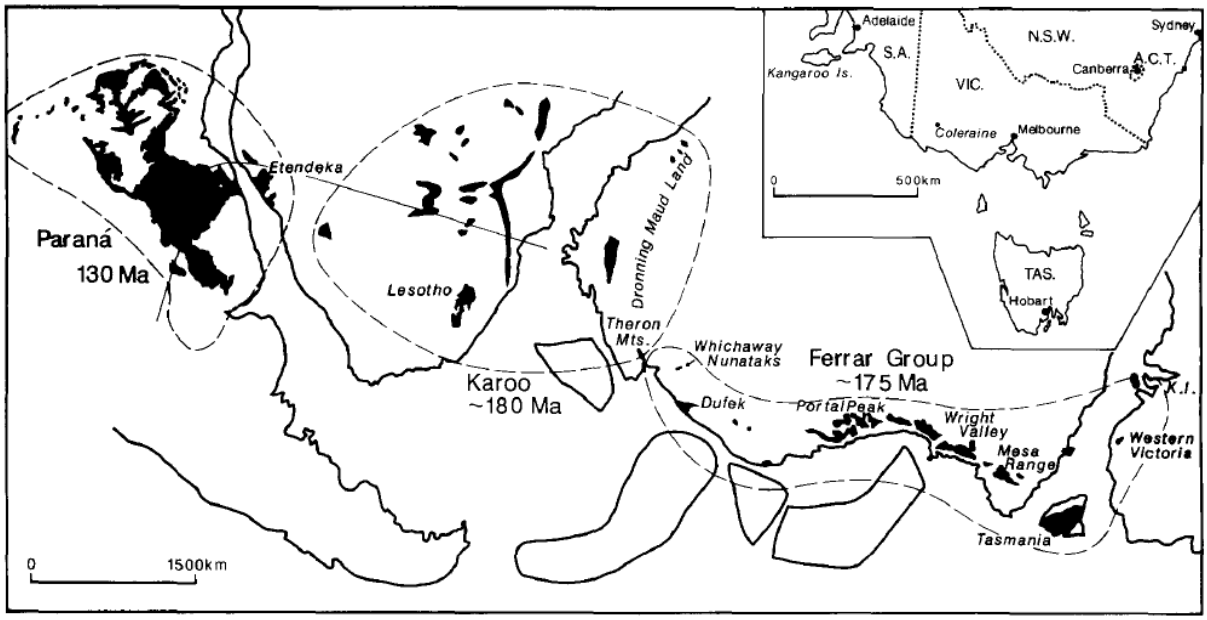

Figure 3.1. Gondwana reconstruction map illustrating the extent of Mesozoic magmatism which ultimately resulted in its break-up. The Ferrar group magmas have particularly homogeneous major element compositions throughout the length of the belt, from Dronning Maud Land to Kangaroo Island, and also share radiogenic isotopic characteristics with the Karoo low-Ti basalts. Map after Hergt et al., (1991).

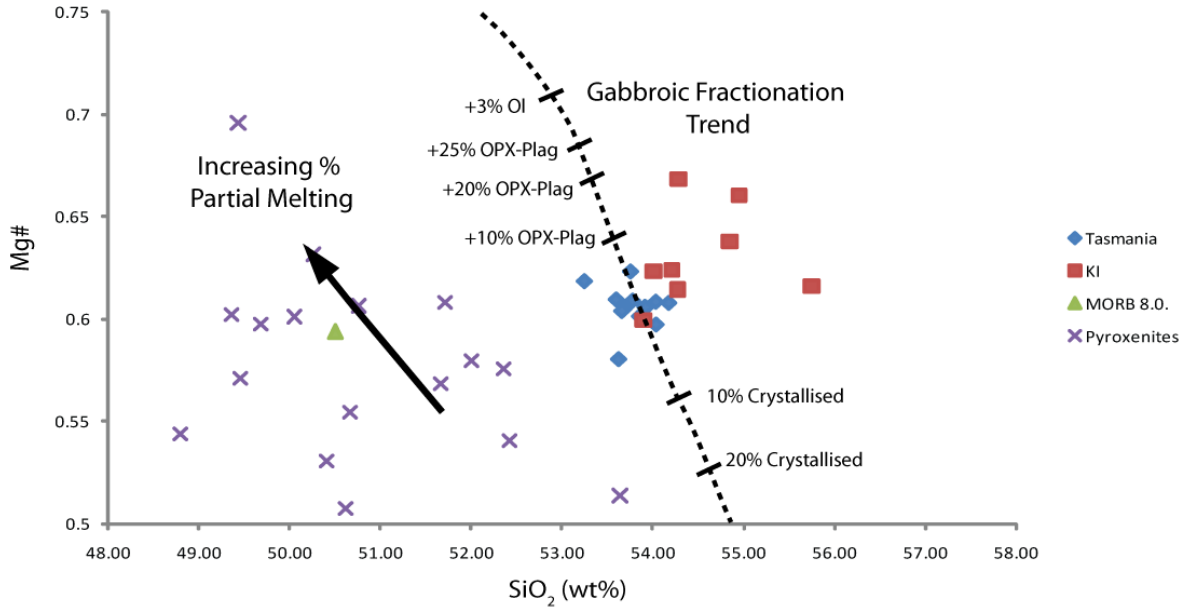

Figure 3.2. Mg# vs SiO_2 for pyroxenites, N-MORB and Ferrar magmas. See section 3.2.1 for discussion.

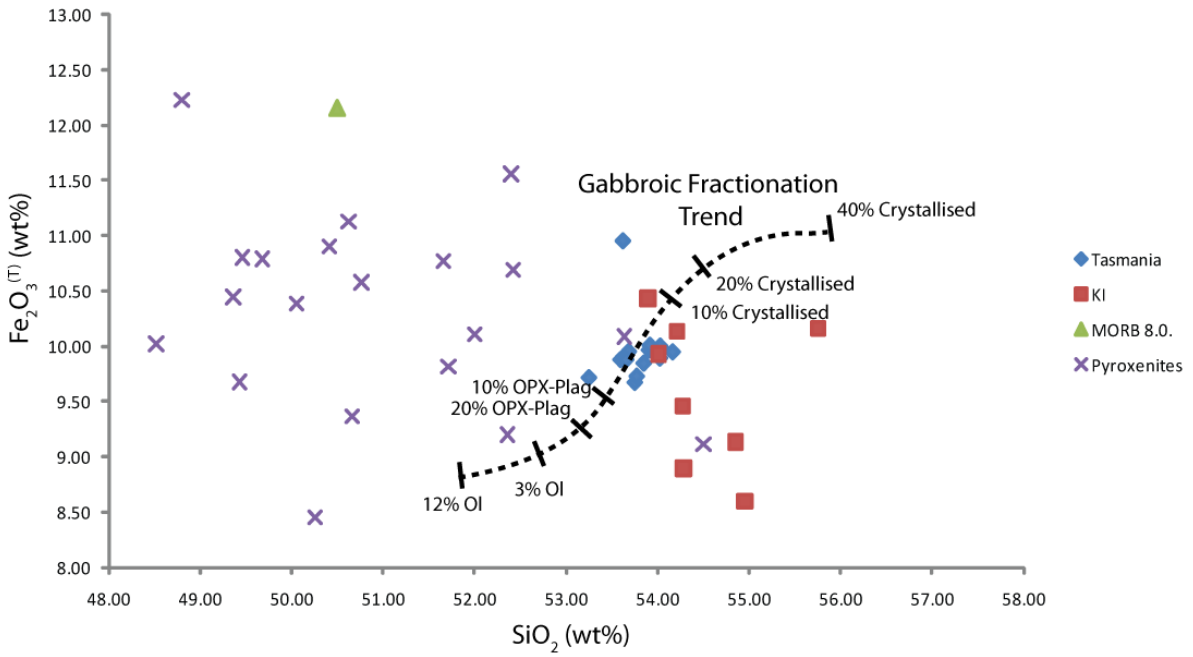

Figure 3.3. $Fe_2O_3^{(T)}$ vs SiO_2 for pyroxenites, N-MORB and Ferrar magmas. See section 3.2.1 for discussion.

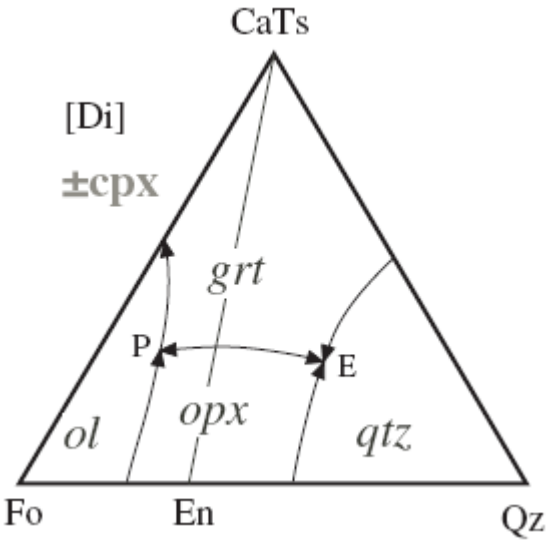

Figure 3.4. Schematic liquidus phase boundaries in the pseudoternary system CaTs Pyroxene-Forsterite-Quartz projected from Diopside (after O'Hara, 1968, after Kogiso et al., 2004). The arrows show the direction of falling temperature.

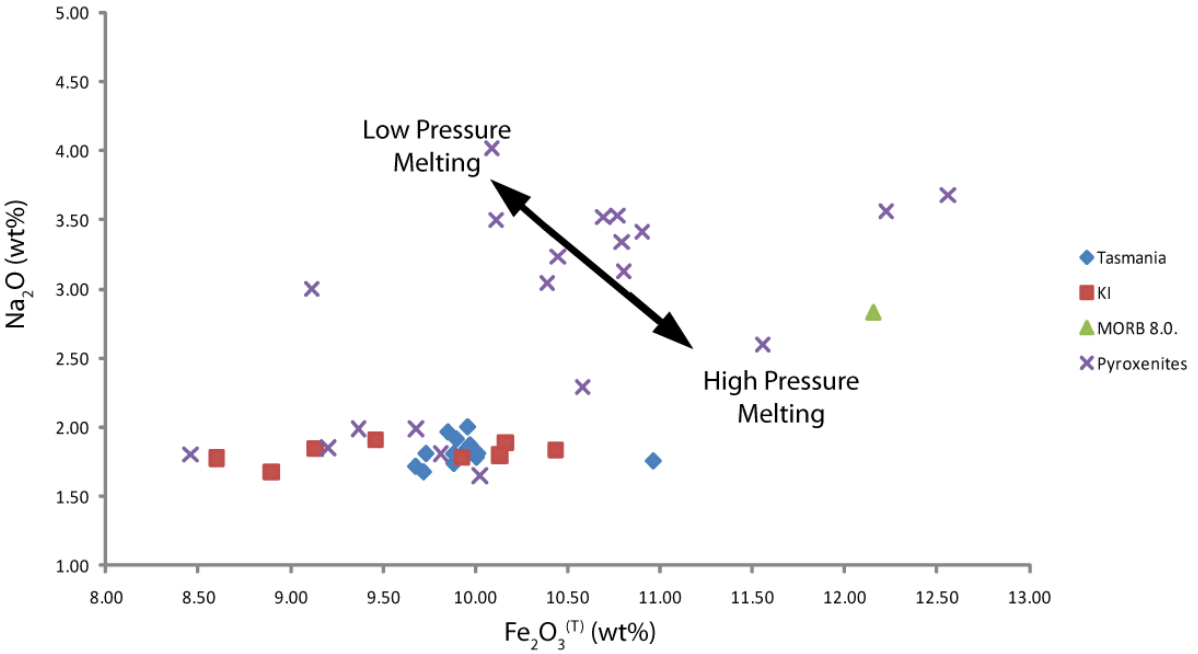

Figure 3.5. Na_2O vs $Fe_2O_3^{(T)}$ for pyroxenites, N-MORB and Ferrar magmas. See section 3.2.2 for discussion.

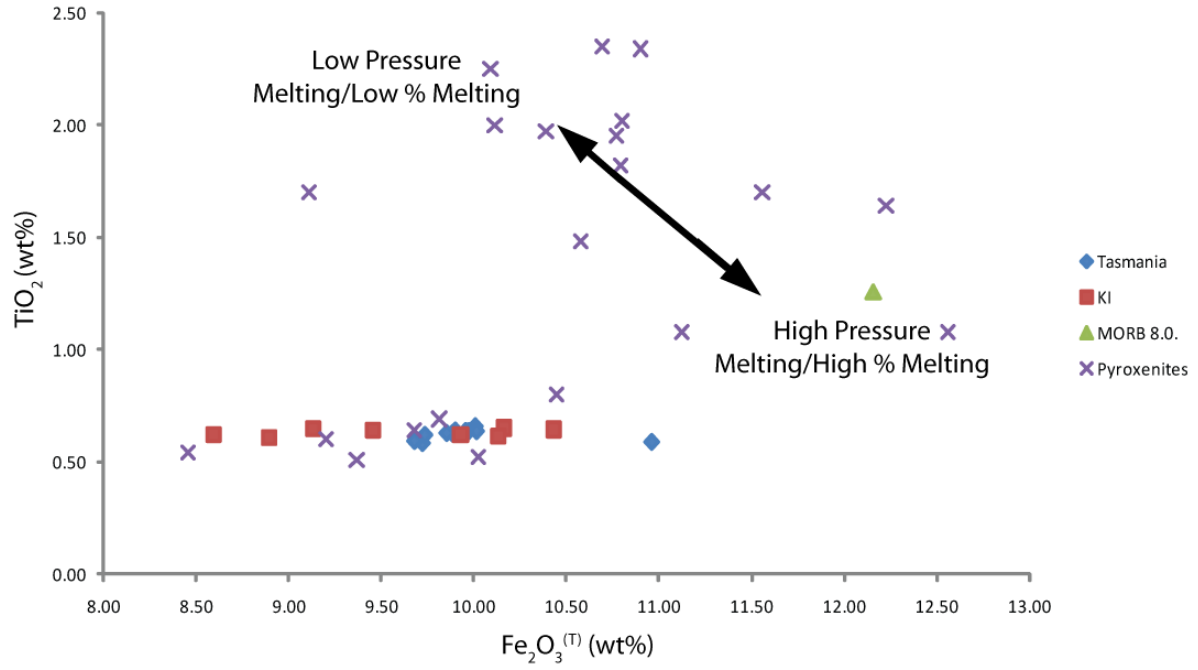

Figure 3.6. TiO_2 vs $Fe_2O_3^{(T)}$ for pyroxenites, N-MORB and Ferrar magmas. See section 3.2.2 for discussion.

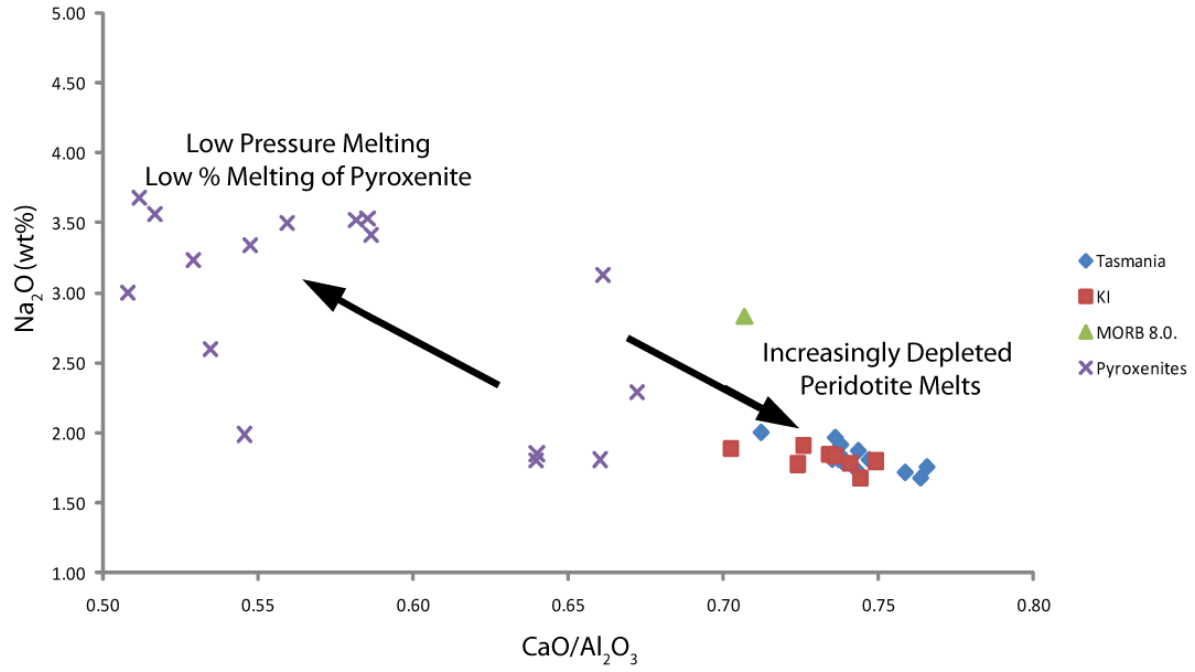

Figure 3.7. Na_2O vs CaO/Al_2O_3 for pyroxenites, N-MORB and Ferrar magmas. See section 3.2.3 for discussion.

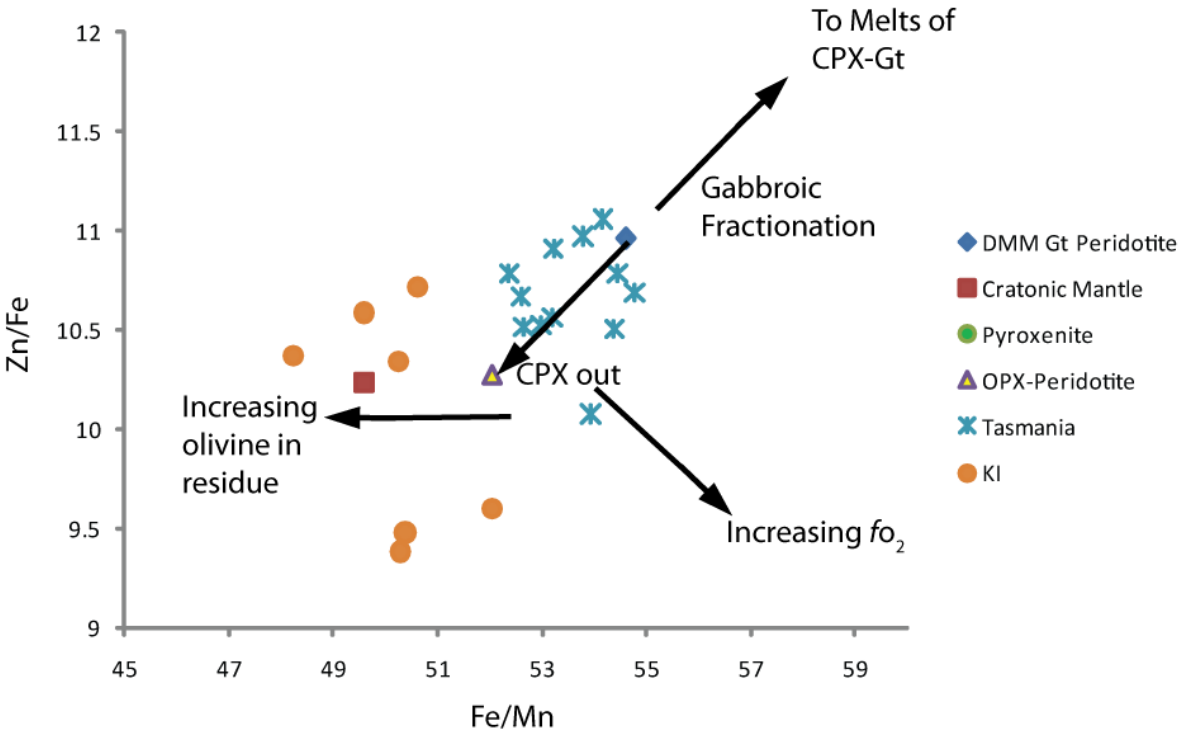

Figure 3.8.: Plot of Zn/Fe vs Fe/Mn illustrating the modelled melt compositions with the Northern Ferrar magmas (KI and Tasmania) superimposed. 'DMM Gt Peridotite' is an expected MORB melt.

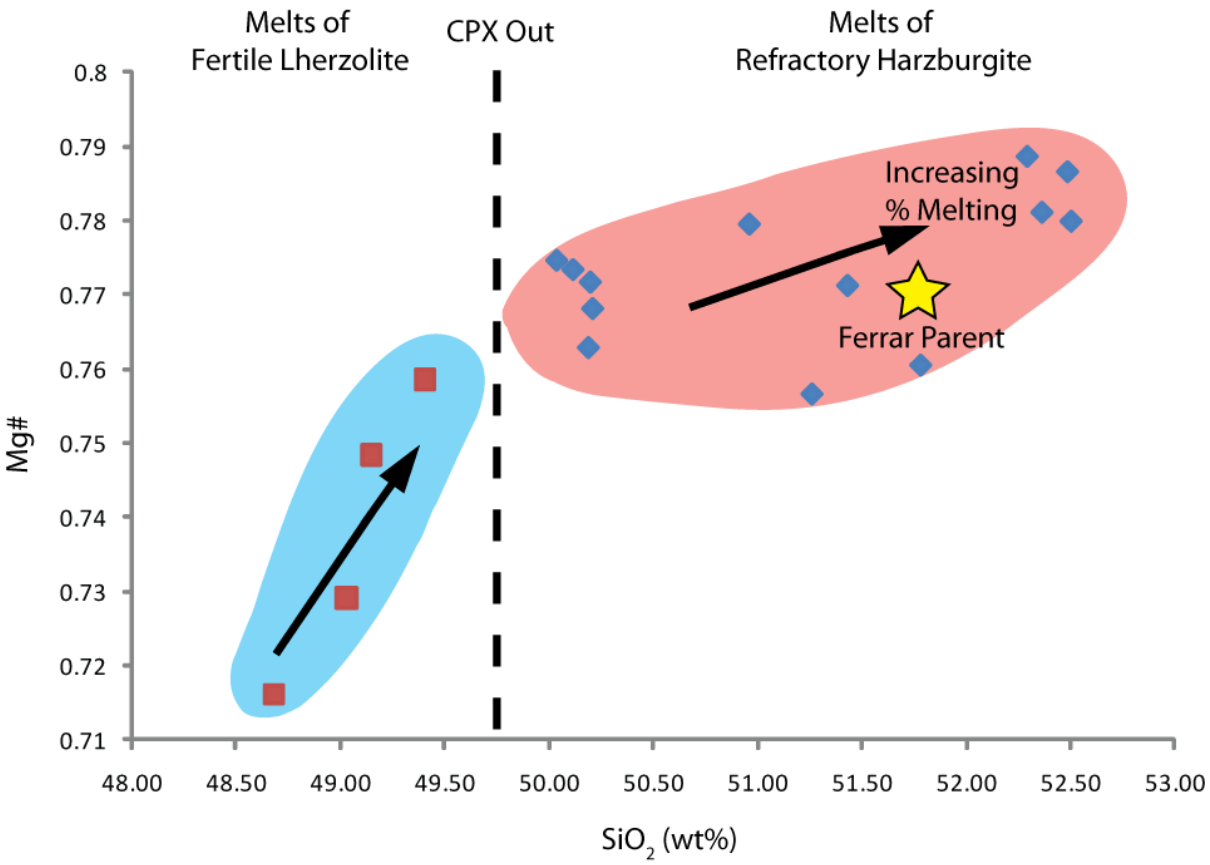

Figure 3.9. Mg# vs SiO_2 for experimental melts of lherzolite and harzburgite, in addition to melt compositions derived from harzburgite with adiabat_1ph using the pMELTS algorith (Smith and Asimow, 2005). The calculated primary Ferrar magma is also plotted (*table 3.4., col 7*). Arrows delineate trends of increasing partial melting/increasingly depleted peridotite sources.

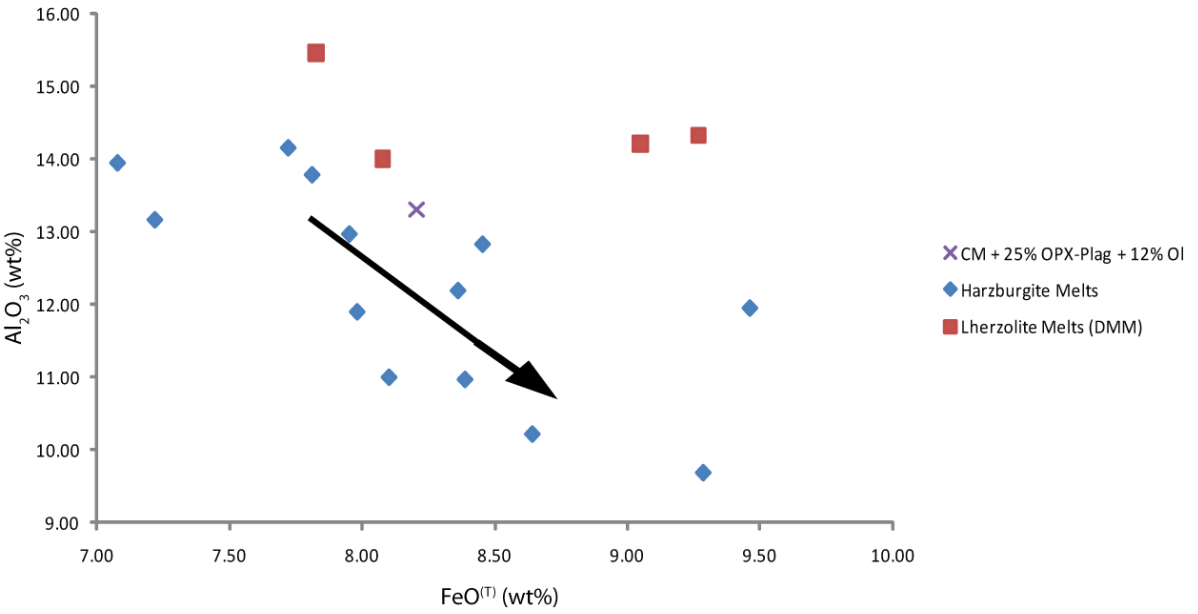

Figure 3.10. Al_2O_3 vs $FeO^{(T)}$ for experimental melts of lherzolite and harzburgite, in addition to melt compositions derived from harzburgite with adiabat_1ph using the pMELTS algorith (Smith and

Asimow, 2005). The calculated primary Ferrar magma is also plotted (*table 3.4., col 7*). Arrow delineates a trend of increasing partial melting/increasingly depleted peridotite sources.

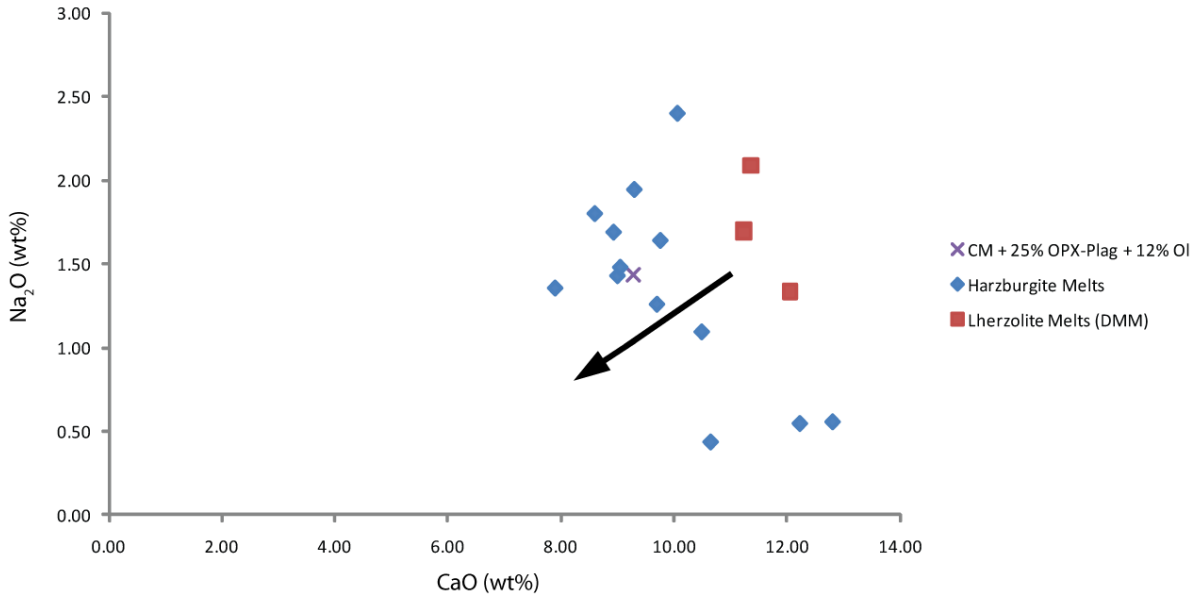

Figure 3.11. Na_2O vs CaO for experimental melts of lherzolite and harzburgite, in addition to melt compositions derived from harzburgite with adiabat_1ph using the pMELTS algorith (Smith and Asimow, 2005). The calculated primary Ferrar magma is also plotted (*table 3.4., col 7*). Arrow delineates a trend of increasing partial melting/increasingly depleted peridotite sources.

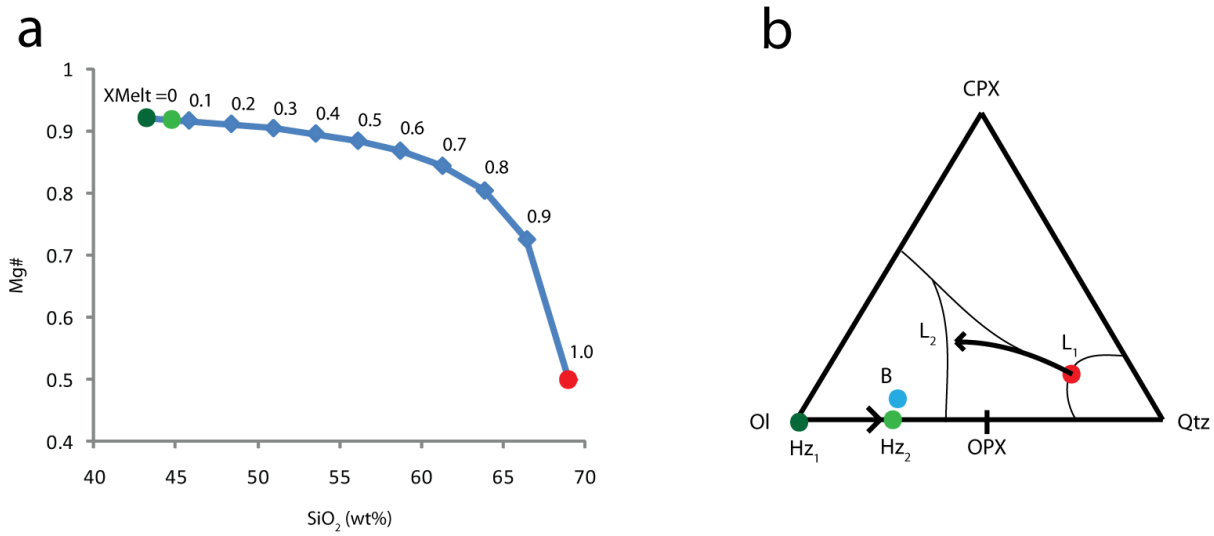

Figure 3.12. a) Mass-balance reactive model between low-T cratonic mantle (Carslon et al., 2005; after McDonough, 1990) and terrigenous sediment (Spandler et al., 2010), showing the relatively constant Mg# up to even 50% sediment addition but a drastic increase in SiO_2. *b)* Schematic representation of melt-rock reaction on a normative Ol-CPX-Qtz ternary phase diagram. A highly melt-depleted residue (e.g. an OPX-poor harzburgite, Hz_1), mixes with a silicic melt, L_1, in proportions such that the new bulk composition is given by B. Assuming that this system is in equilibrium, the

predicted phase proportions and compositions are denoted by the new equilibrium melt composition (L_2) and its harzburgite (Hz_2). After Lee, 2006.

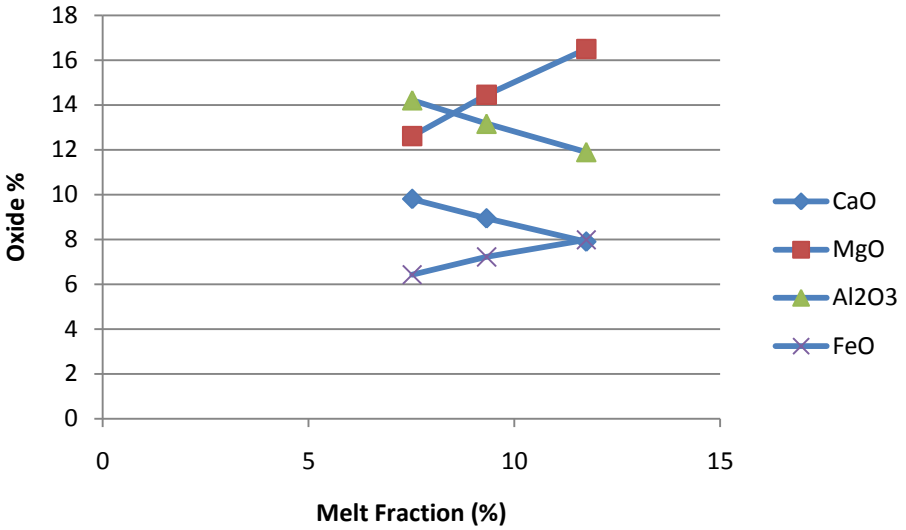

Figure 3.13. Plot of pMELTS compositions from the "Peridotite + 3% EPSM" composition (*table 3.6.*), showing the variations of the main oxides with increasing melt fraction (and therefore temperature) at 1GPa. Equations fit to these trends were used to estimate the percentage of melting required to generate the major element compositions of the Ferrar parent magma.

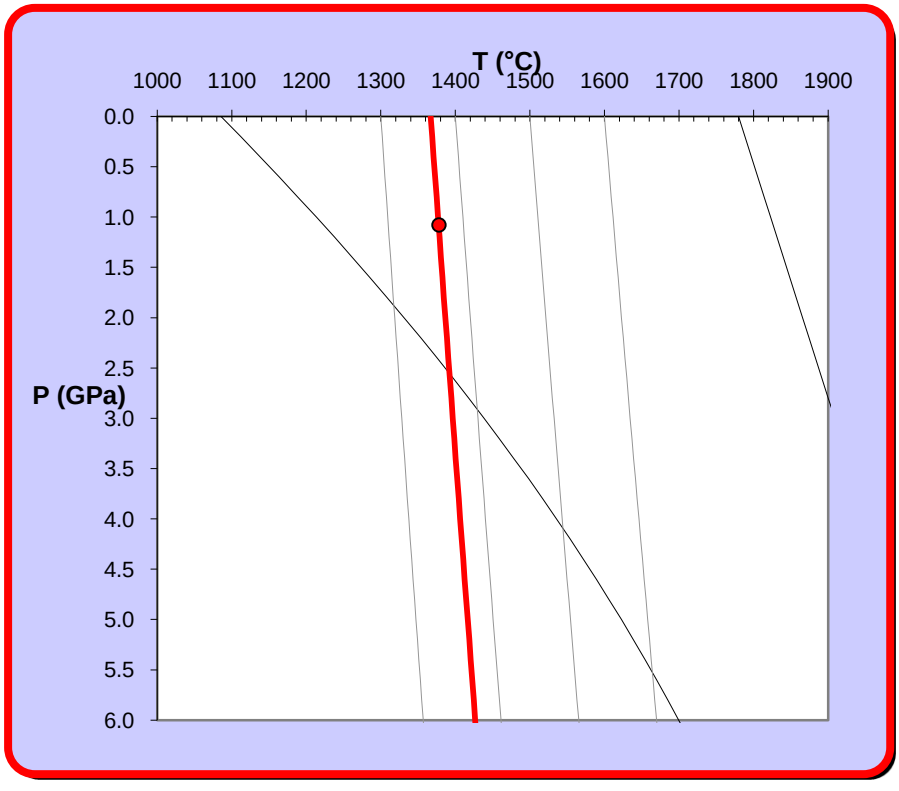

Figure 3.14. P-T diagram which shows the conditions of melting for the Ferrar primary magma, as calculated by the geothermobarometer of Lee et al., (2009). Also plotted are mantle adiabats for 1300°C, 1370°C, 1400°C, 1500°C, 1600°C and the melting envelope for dry depleted peridotite (McKenzie and Bickle, 1988).

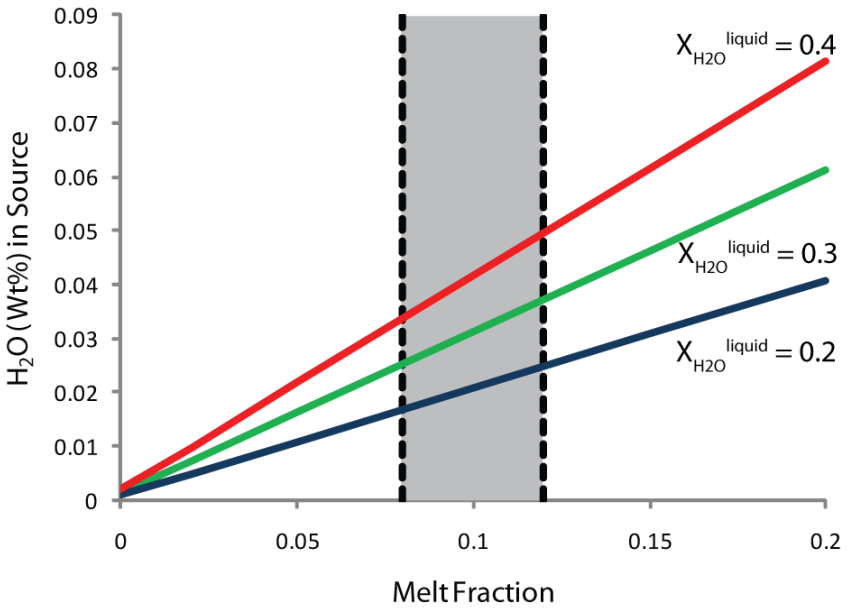

Figure 3.15. H_2O in source based on partition coefficients for water in nominally anhydrous minerals (Hauri et al., 2006) and the water content of the melts. X_{Ol} = 64.79; D^{H2O}_{Ol} = .0015; X_{OPX} = 29; D^{H2O}_{OPX} = .01; X_{CPX} = 4.6; D^{H2O}_{CPX} = .02. Calculated using the batch melting equation.

$$\frac{C_l}{C_o} = \frac{1}{F + D(1 - F)}$$

C_l is the concentration of water in the liquid, C_o is the calculated concentration of water in the source, F is the melt fraction, and D is the partition coefficient for water beenthe mineral and melt.

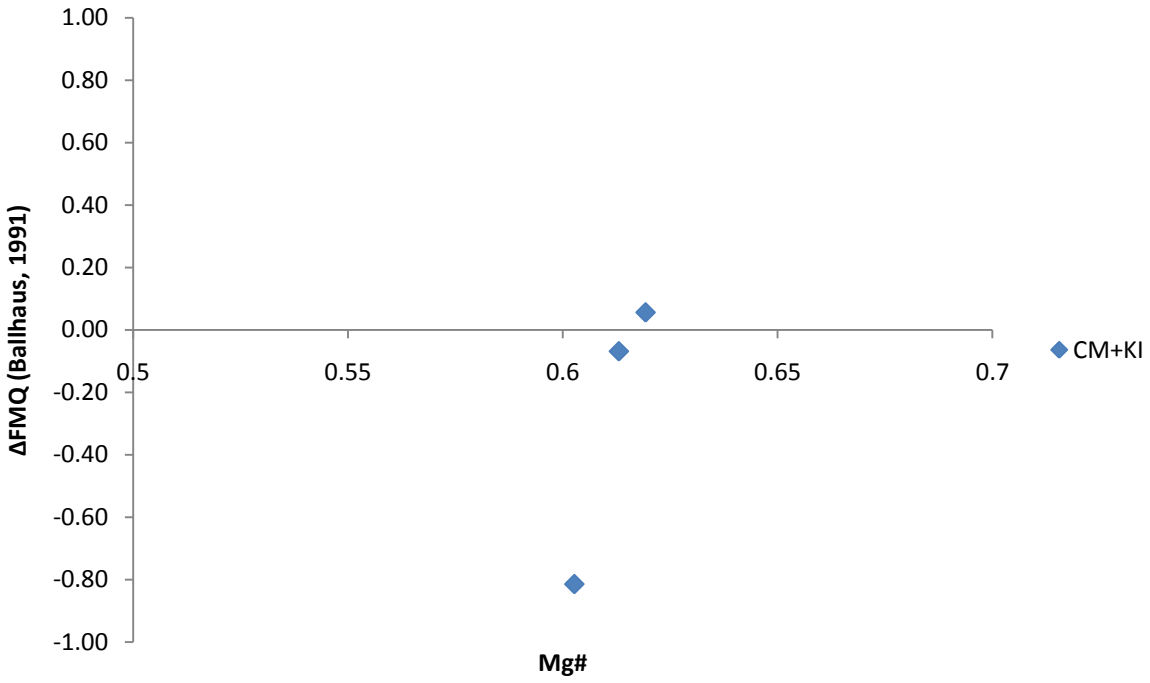

Figure 3.16. fo_2 relative to FMQ (Ballhaus, 1991) of Tasmanian chilled dolerites and Kangaroo Island basalts calculated from their $Fe^{3+}/\Sigma Fe$ ratios by the equation of O'Neill et al., (2006). The redox conditions recorded suggest equilibration with a mantle source with an fo_2 between FMQ and FMQ-1.

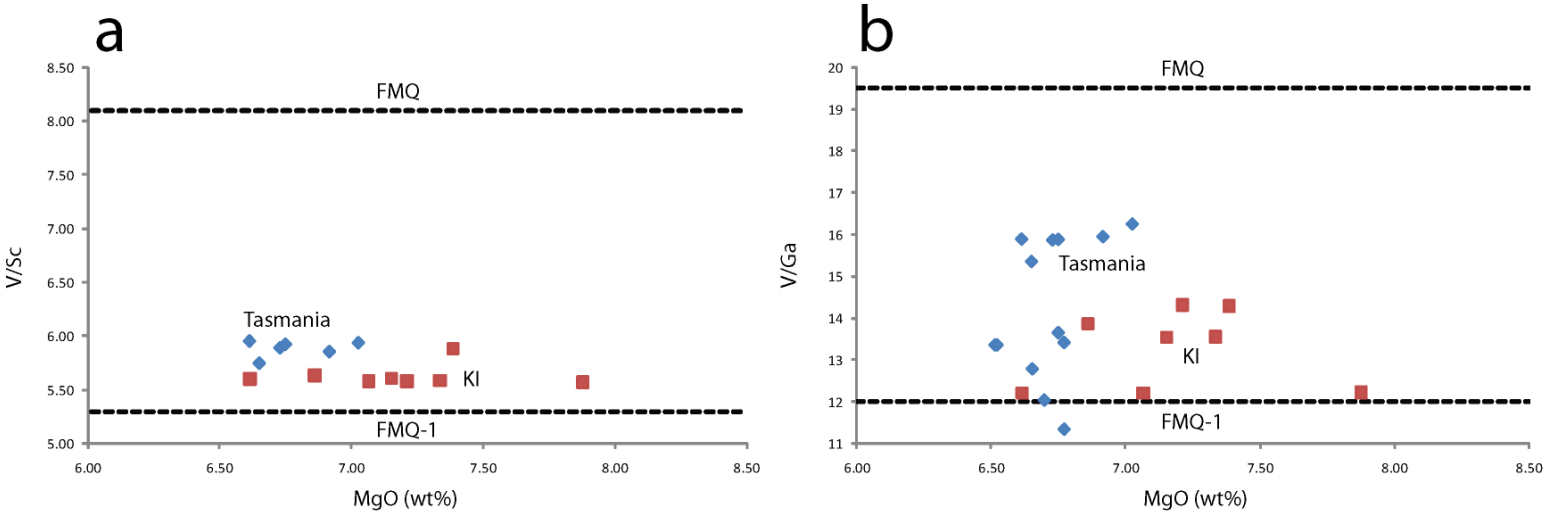

Figure 3.17. V/Sc and V/Ga ratios of the Tasmanian chilled dolerites and the Kangaroo Island basalts, calibrated for fo_2 estimates. The V/Sc $-fO_2$ and V/Ga $-fO_2$ contours are plotted for 10% melting of spinel lherzolite at 1.5GPa (Lee et al., 2005; Mallmann and O'Neill, 2009).

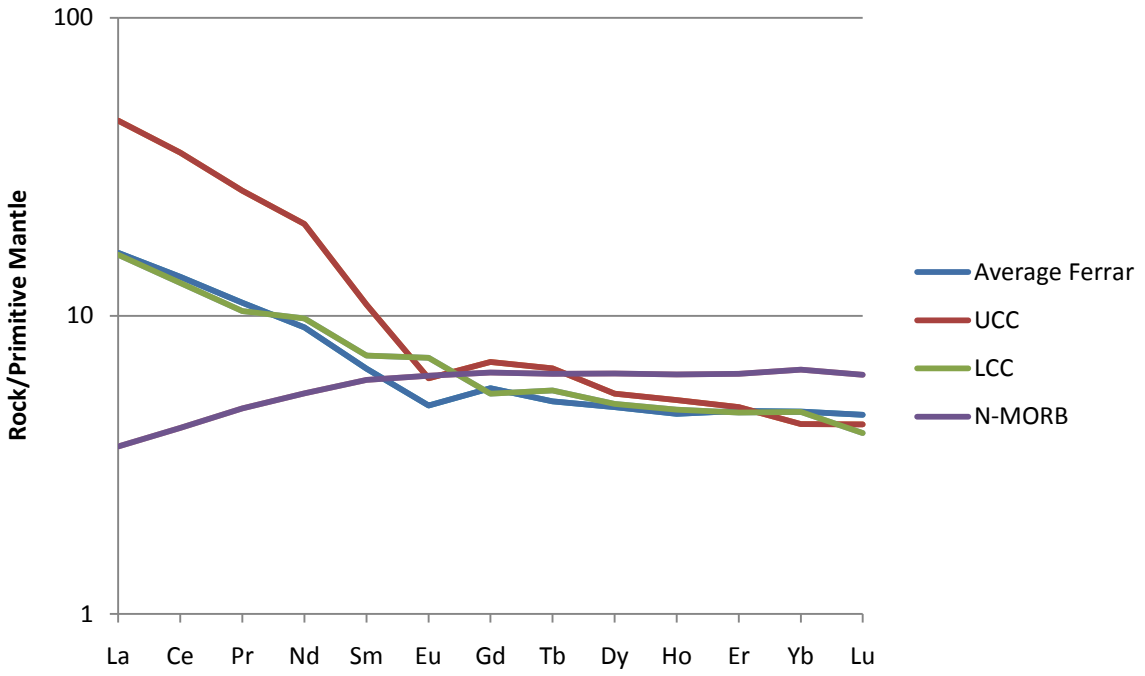

Figure 3.18.: REE abundances in the average Northern Ferrar tholeiite, upper and lower contintental crust (Rudnick and Gao, 2003) and N-MORB (Workman and Hart, 2005). Normalised to primitive mantle of Palme and O'Neill (2003).

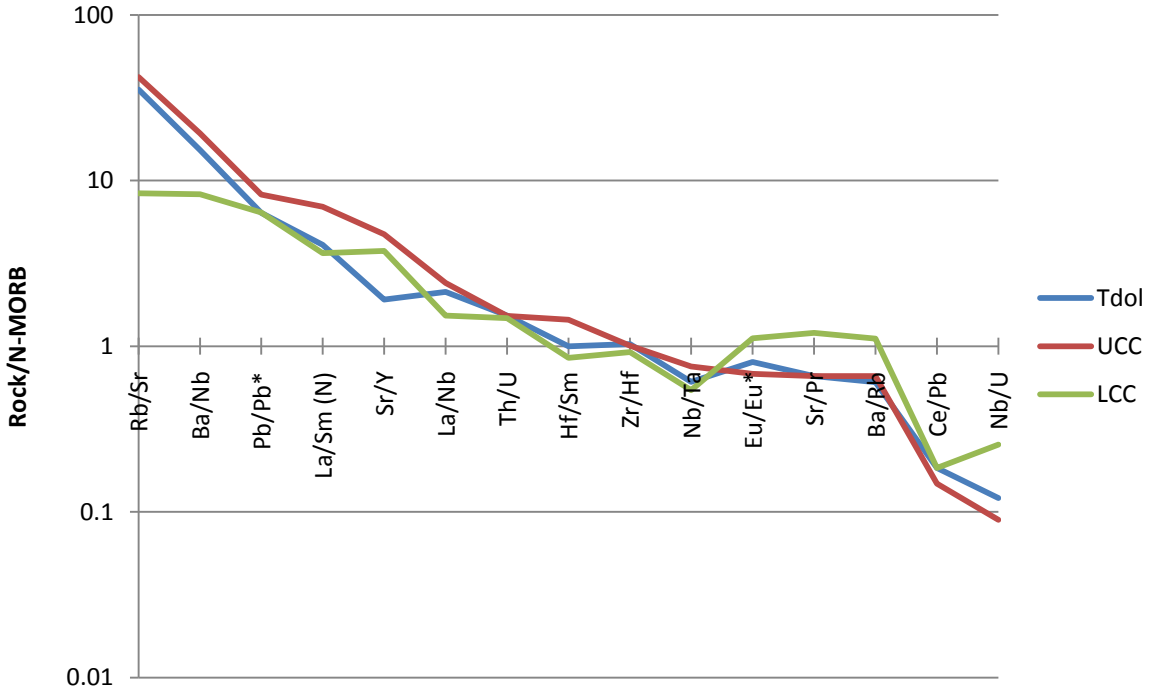

Figure 3.19. Diagnostic element ratios plotted for the average Northern Ferrar tholeiite, Upper and Lower Contintental Crust (Rudnick and Gao, 2003) and normalised to N-MORB (Workman and Hart, 2005).

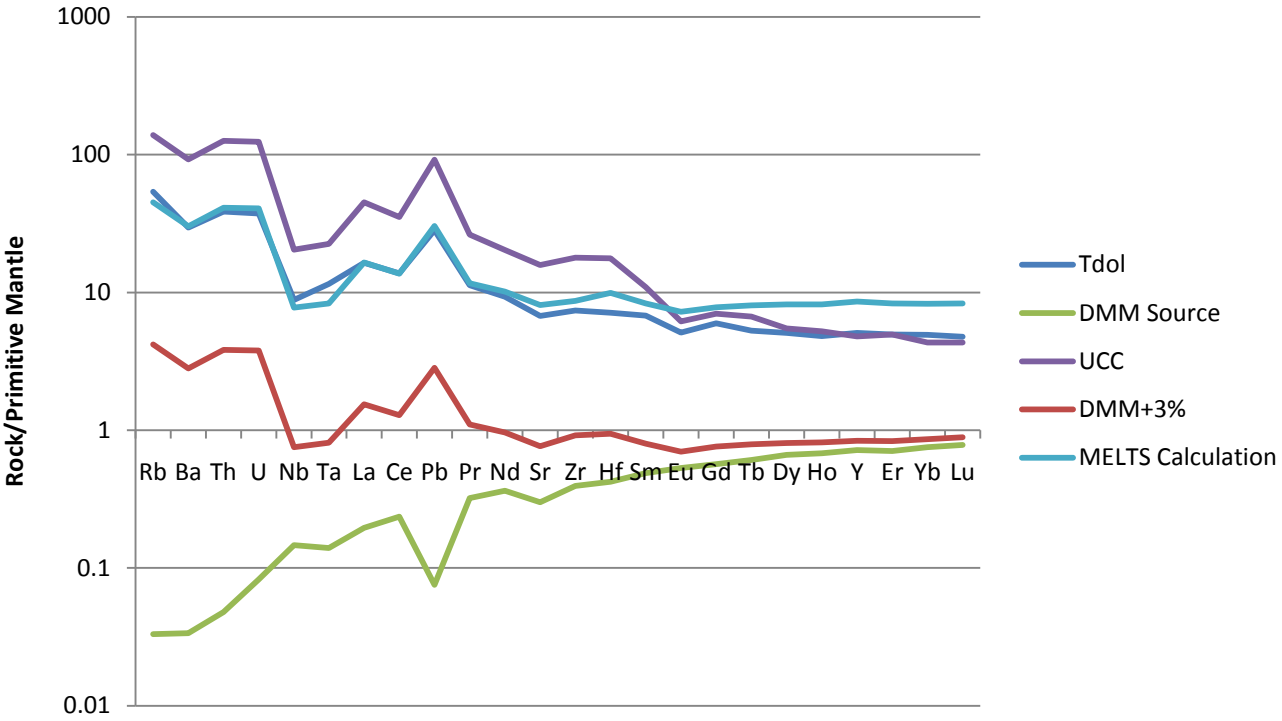

Figure 3.20.: Primitive-mantle normalised (Palme and O'Neill, 2003) incompatible trace element abundances of the depleted DMM mantle (Workman and Hart, 2005), upper continental crust (Rudnick and Gao, 2003) the calculated hybrid (*table 3.9.*) and average Ferrar tholeiite.

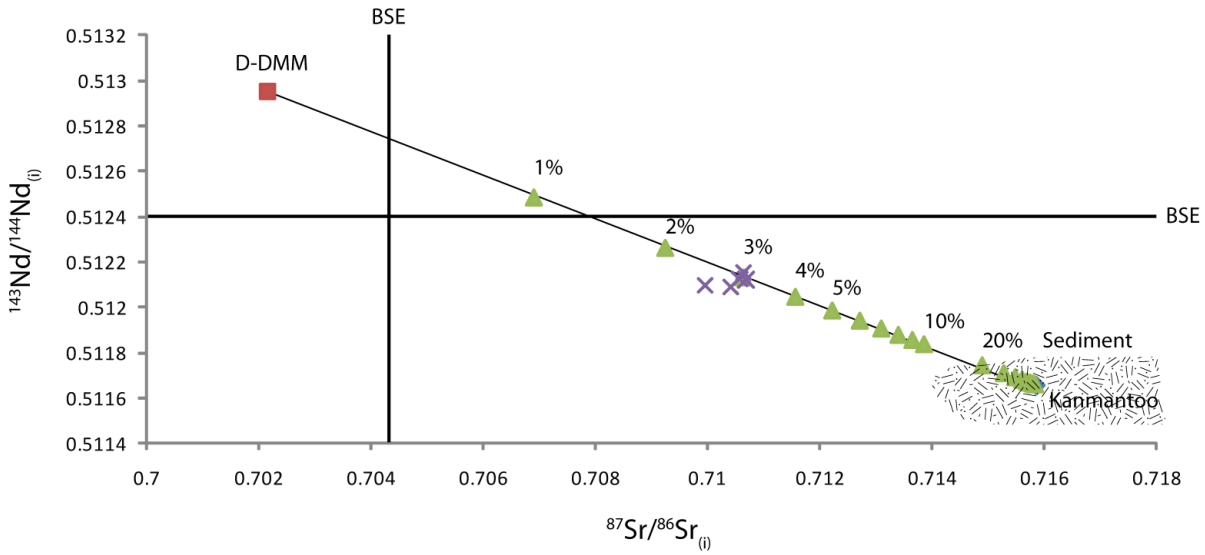

Figure 3.21.: Mixing diagram between depleted DMM, taken to represent the trace element composition of the Ferrar mantle source (Workman and Hart, 2005), and the sedimentary component (Rudnick and Gao, 2003). Also plotted are the range of Kanmantoo sediment compositions (Turner et al., 1993).

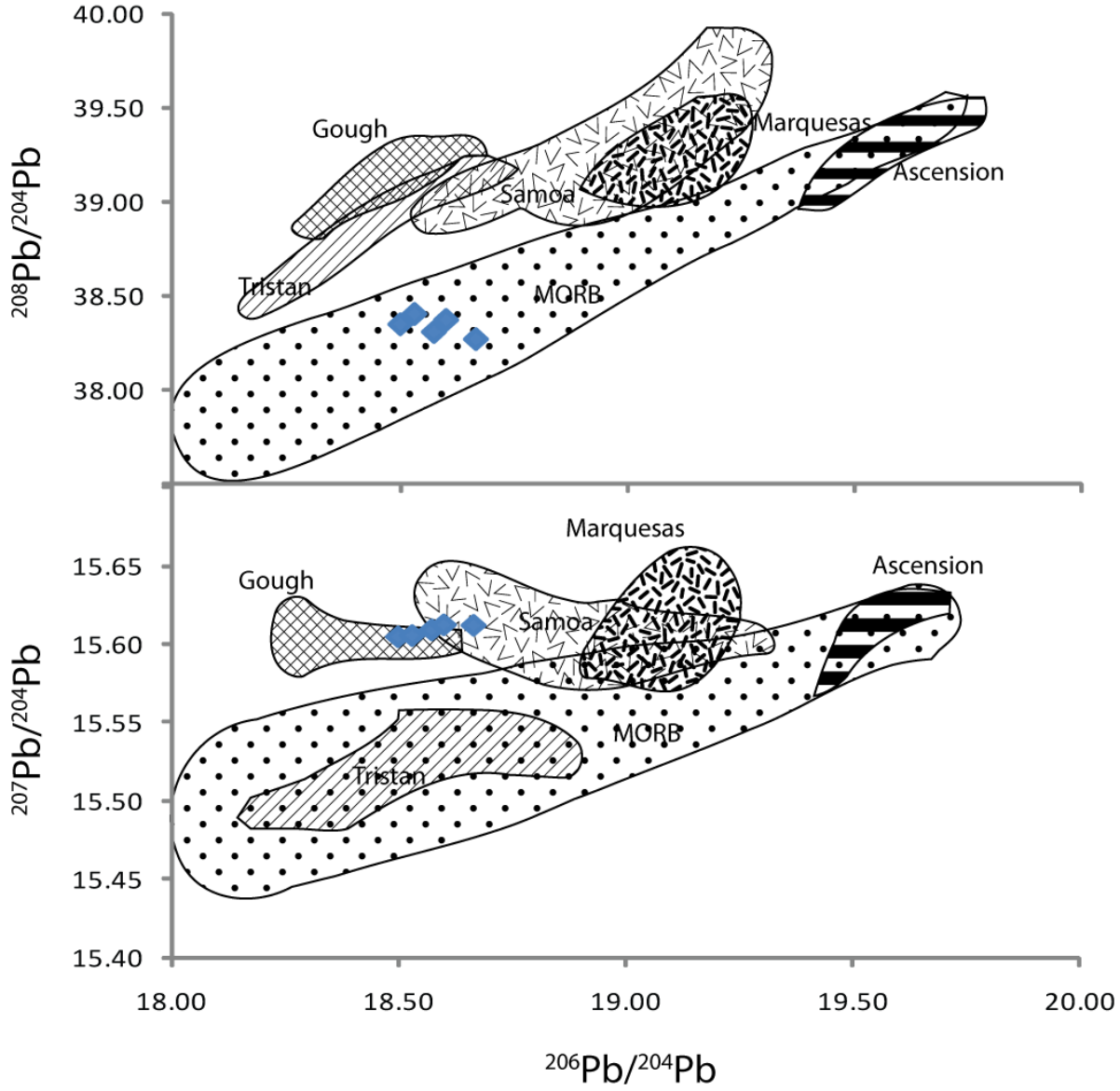

Figure 3.22: Pb isotopic compositions of the Ferrar tholeiites (*table 3.10.*) and ocean island basalts (data after Hergt et al., 1989a).

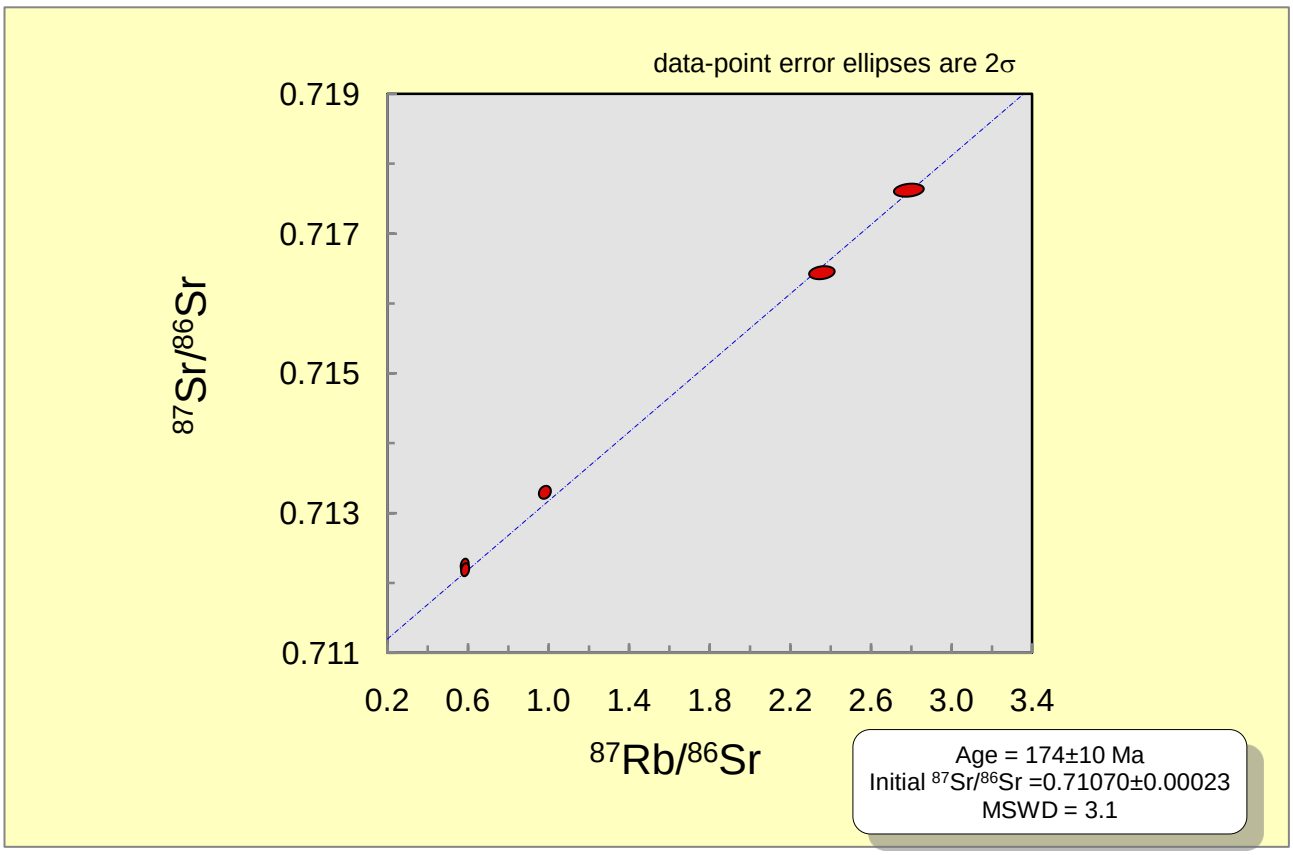

Figure 3.23. Rb-Sr isochron of 5 Red Hill samples, defining an age of 174±10Ma (2σ), using Isoplot (Ludwig, 2003)

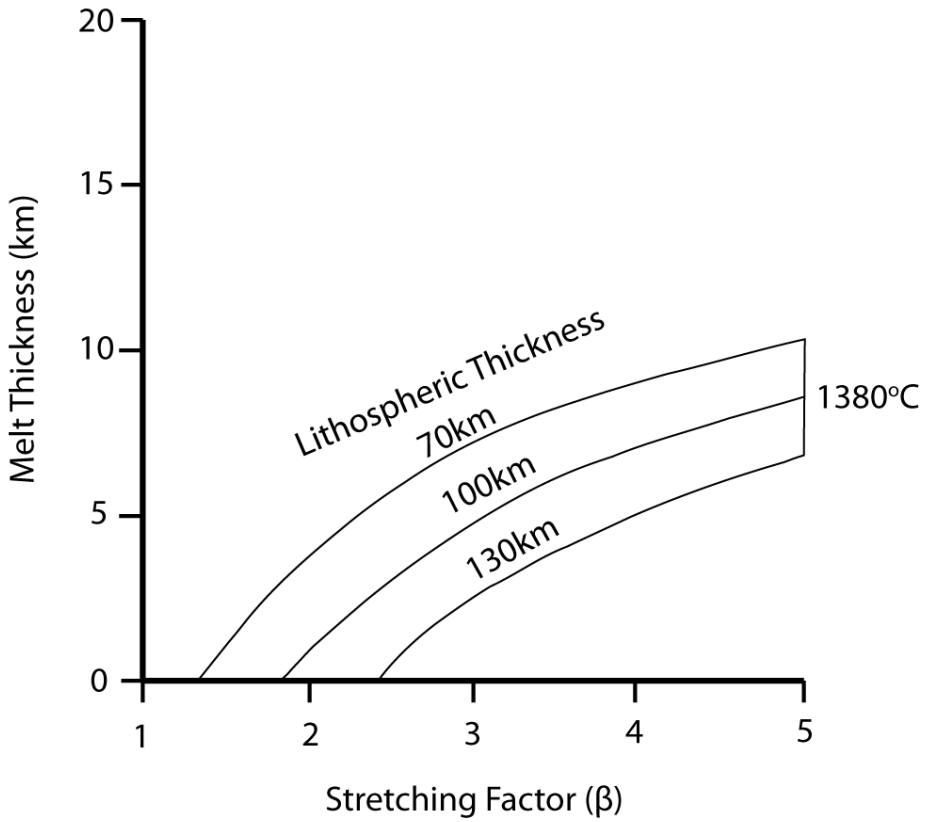

Figure 3.24. Plot of thickness of melt produced compared to the stretching factor for the lithosphere, with an initial thickness of 70km, 100km and 130km, and a mantle potential temperature of 1380°C. After McKenzie and Bickle, 1988.

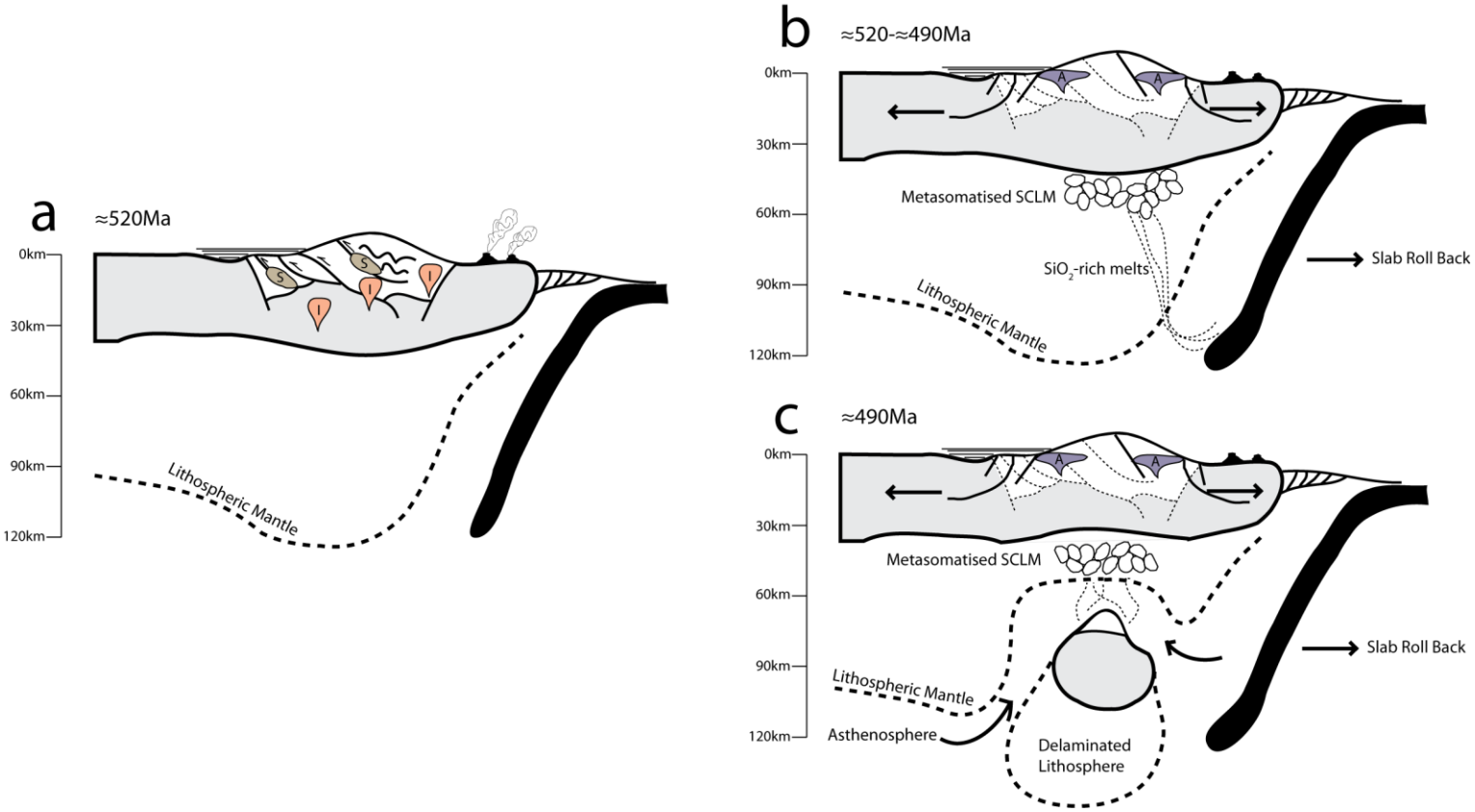

Figure 3.25. Schematic diagrams illustrating the tectonic setting on the eastern margin of Gondwana during the Cambrian. See section *3.5.* for discussion.

a) Lithospheric structure associated with the Delamerian Orogeny, highlighting the intrusion of synorogenic I- and S-type granitoids, which are by-products of magmatism caused by west-directed slab subduction.
b) Orogenic collapse which signals the termination of compression at ≈490Ma, coincident with asthenosphere-derived magmatism and A-type granites. During this period of subudction, SiO_2-rich melts derived from the sedimentary component of the slab may have reacted with olivine in the SCLM to create metasomatised domains.
c) The rapid cessation of convergent deformation at ≈490Ma is compatible with a delamination scenario wherein a fraction of the lithosphere becomes unstable due to a density excess. It is conceivable that newly-deposited Kanmantoo Group sediments were also transported into the mantle, where they readily melted and metasomatised the overlying peridotite.

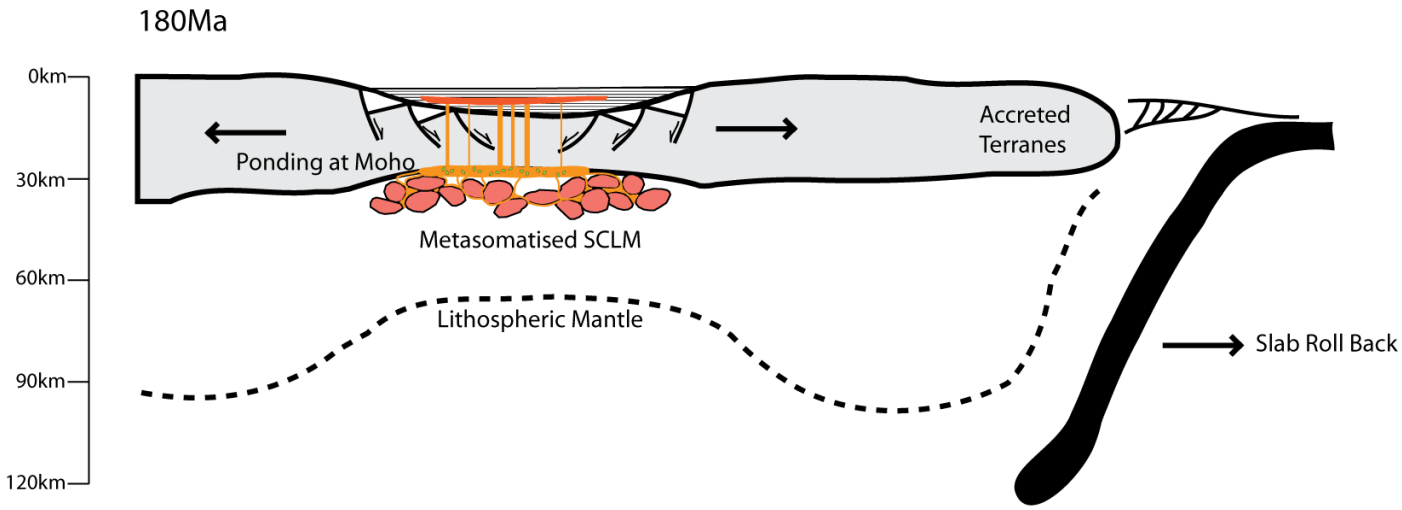

Figure 3.26. Schematic diagram of the tectonic environment extant during extensional magmatism of the Ferrar province on the Eastern margin of Gondwana. The slab is outboard of the magmatic locus, and does not refrigerate the mantle that was metasomatised during the Cambrian-Ordovician. This mantle is high-heat producing and melts due to extension and subsequent decompression at ≈180Ma. See section *3.5.* for discussion.

4.0. Differentiation

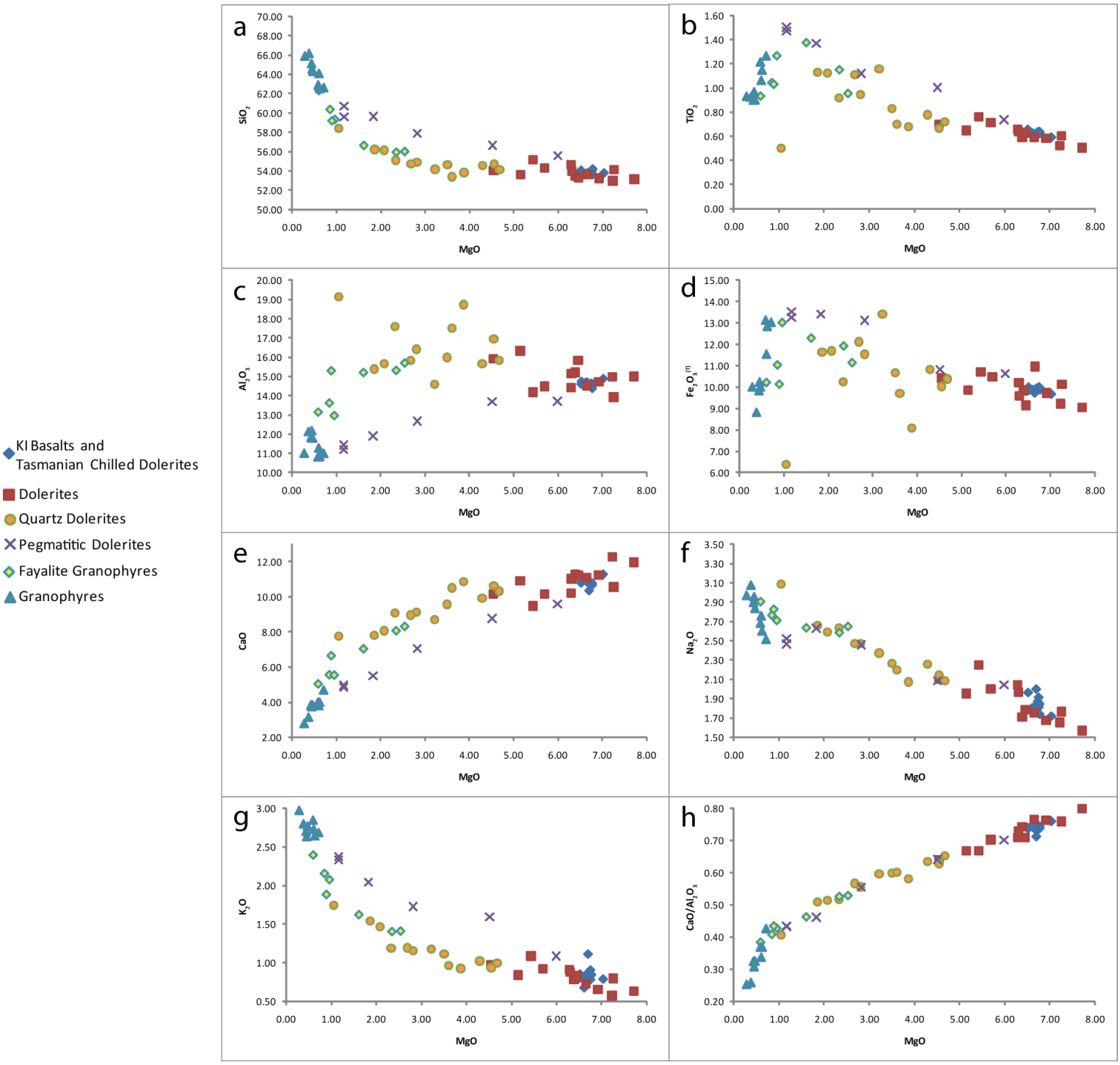

Figure 4.1. Major element binary plots illustrating the range of continuous compositions that comprise the Red Hill intrusion. See section *4.2.* for discussion.

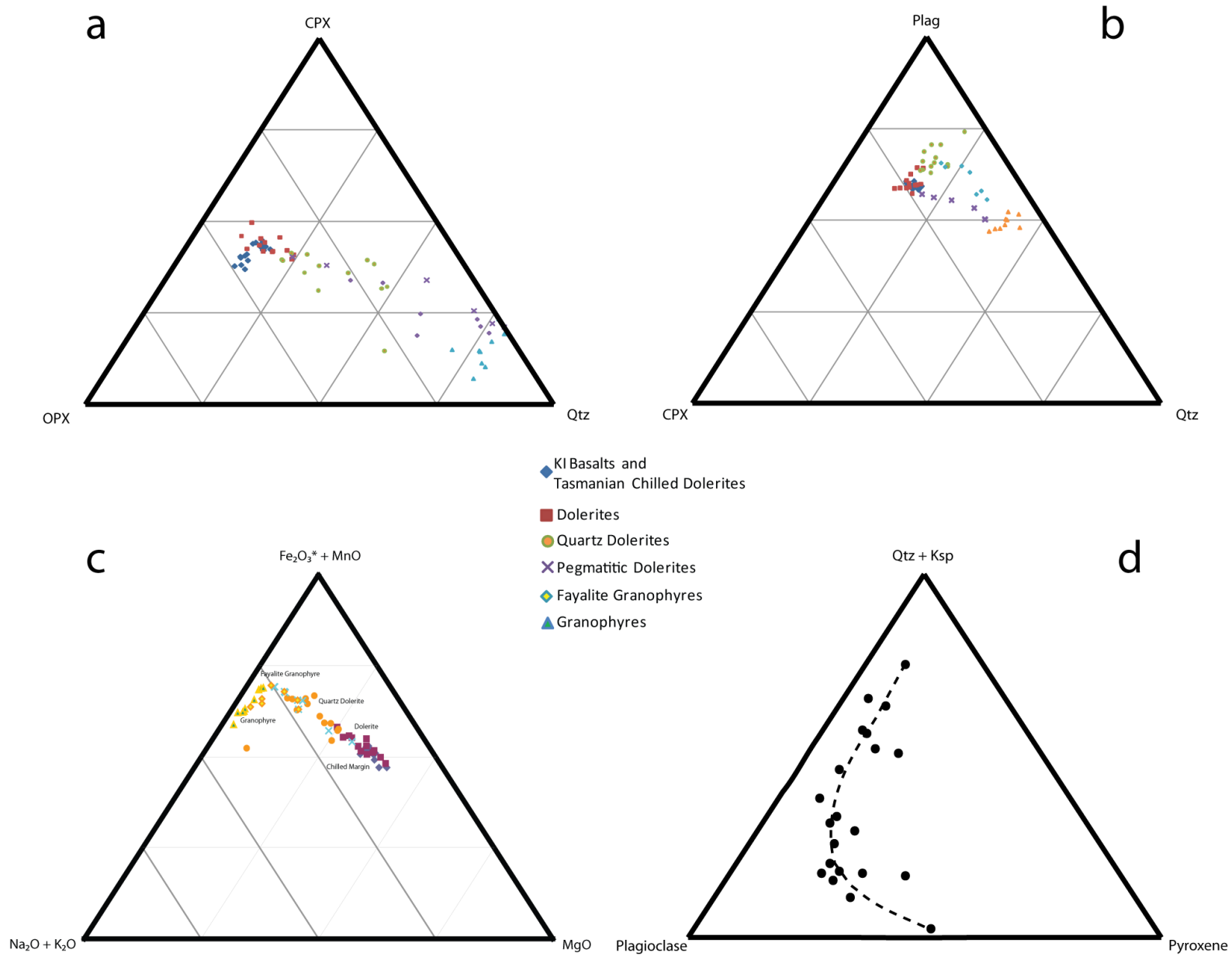

Figure 4.2. Ternary diagrams. *a)* Normative projection from olivine (Kelsey, 1965); *b)* Normative projection from olivine, with mineral proportions calculated manually from Grove (1993) (after Tormey et al., 1987); *c)* Alkalis-Fe-Mg (AFM) diagram; *d)* Modal point-count analyses showing the phases present in the Red Hill sequence (after McDougall, 1962). See section *4.2.* for discussion.

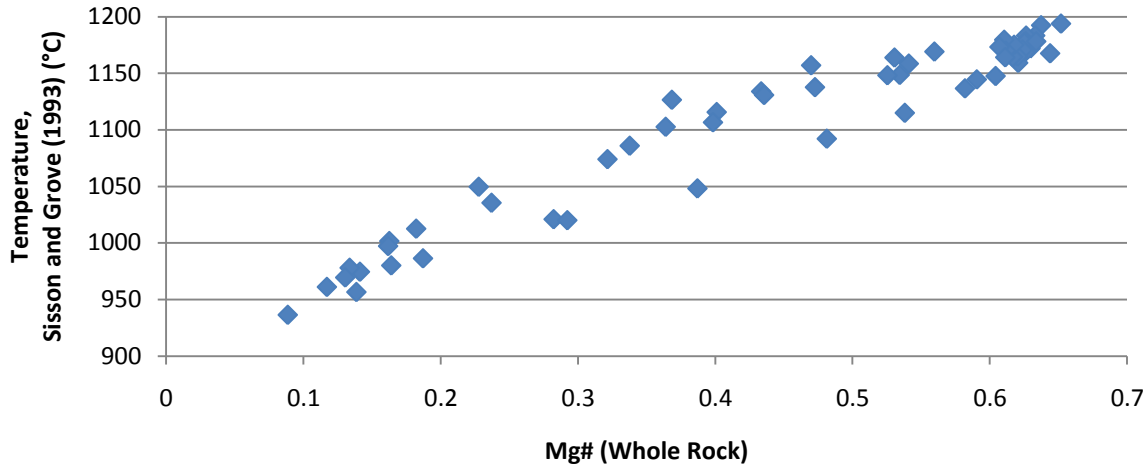

*Figure 4.3.*Temperature estimates for the suite of Red Hill rocks using the geothermometer of Sisson and Grove (1993). See section *4.2.7.* for discussion.

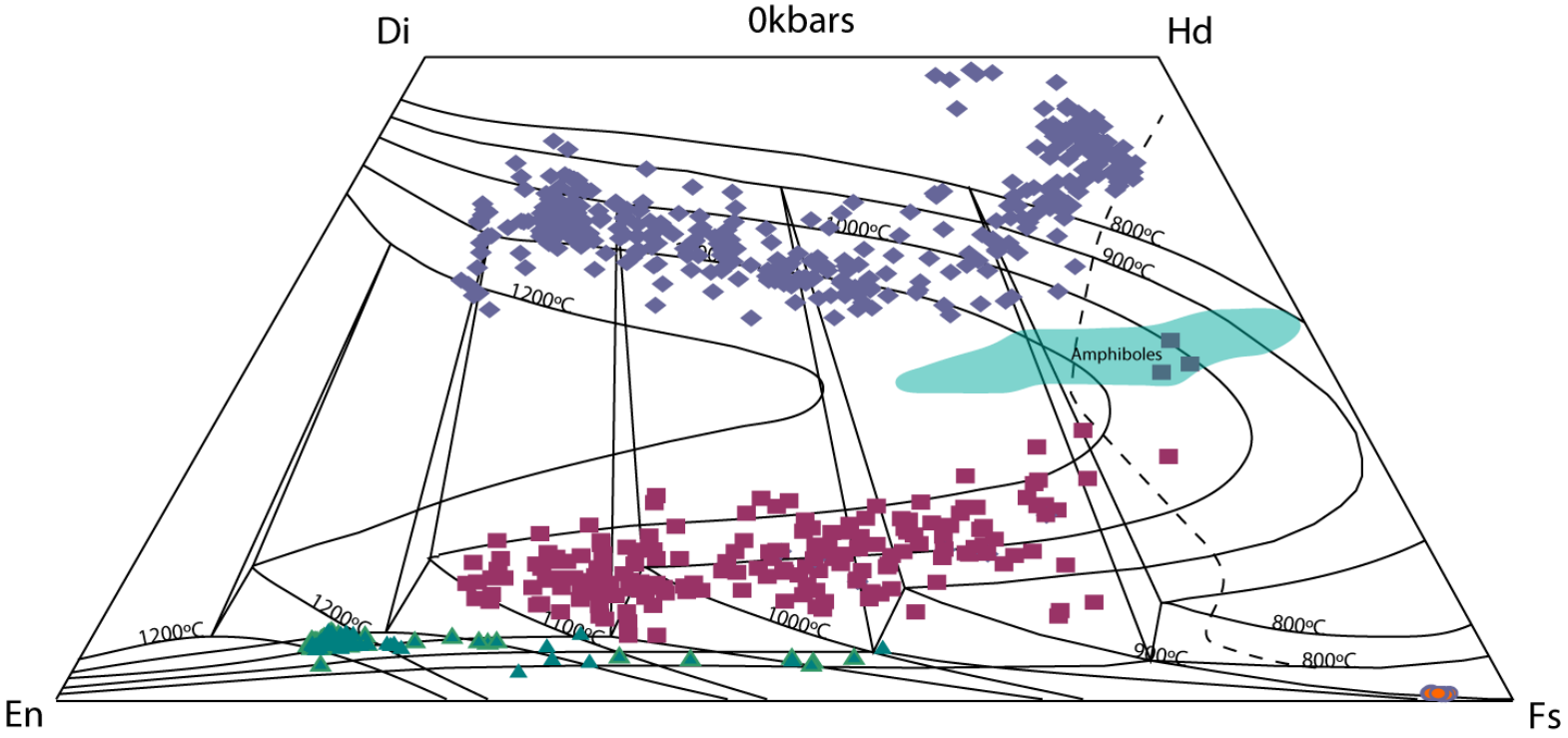

Figure 4.4. Pyroxene quadrilateral with isotherms (solid lines) after Sack and Ghiorso (1994) and the 5 kbars forbidden zone (dashed line) after Lindsley (1983). Plotted are augites (blue diamonds), pigeonites (pink squares), orthopyroxenes (green triangles), fayalites (orange circles) and amphiboles depicting progressive iron enrichment.

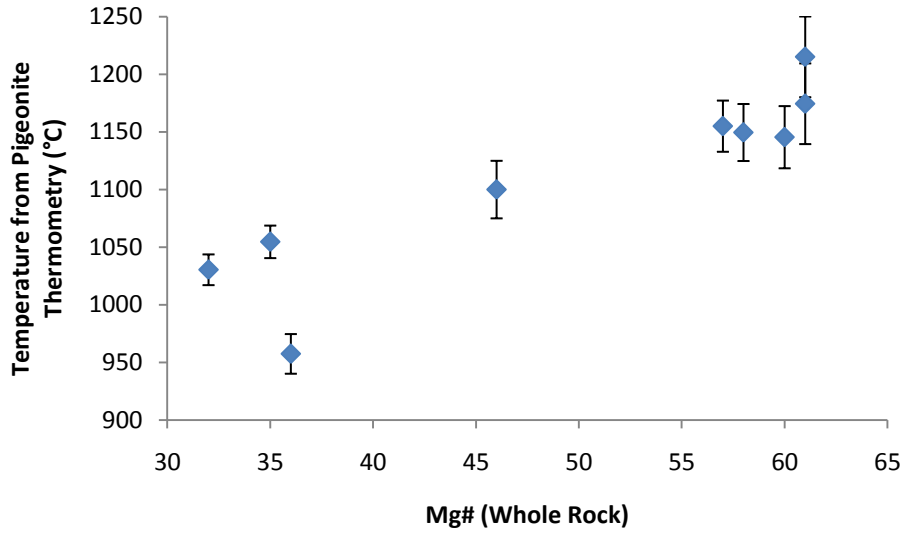

Figure 4.5. Temperature estimates for whole rocks using pigeonite thermometry on electron microprobe pigeonite analyses averaged for each rock compositon. Thermometer from Singletary and Grove (2003).

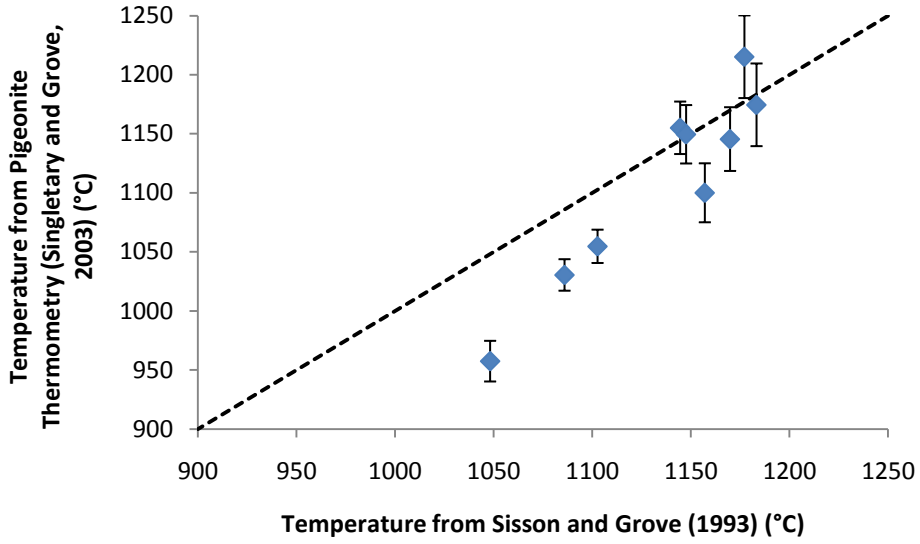

Figure 4.6. Comparison of the temperature estimates for whole rocks from pigeonite thermometry (Singletary and Grove, 2003) and from the bulk rock formulation of Sisson and Grove (1993).

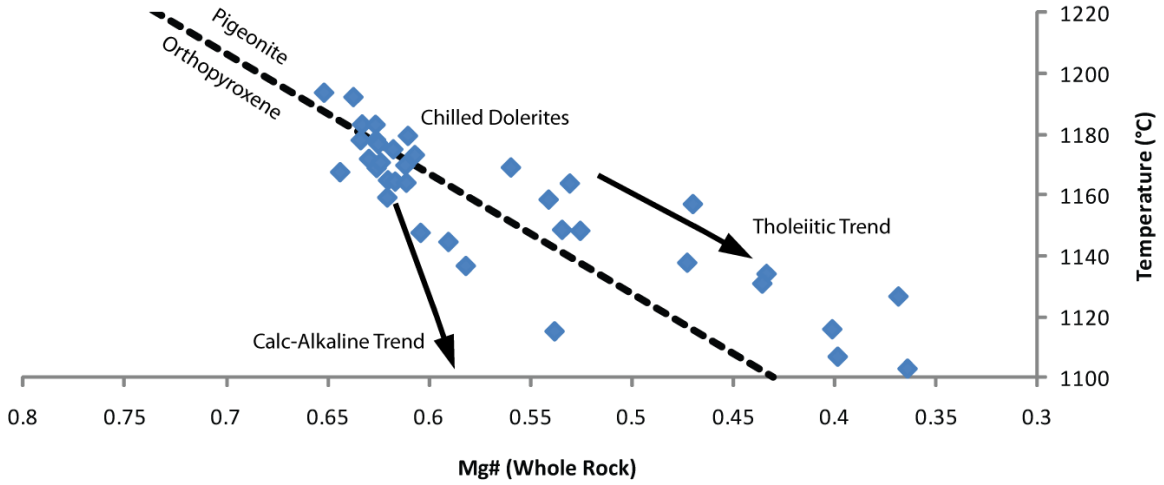

Figure 4.7. Pigeonite-Orthopyroxene equilibrium calculated at QFM, (Grove and Juster, 1989).Temperatures of whole rocks calculated from Sisson and Grove (1993). Arrows denote the putative tholeiitic and calc-alkaline trends.

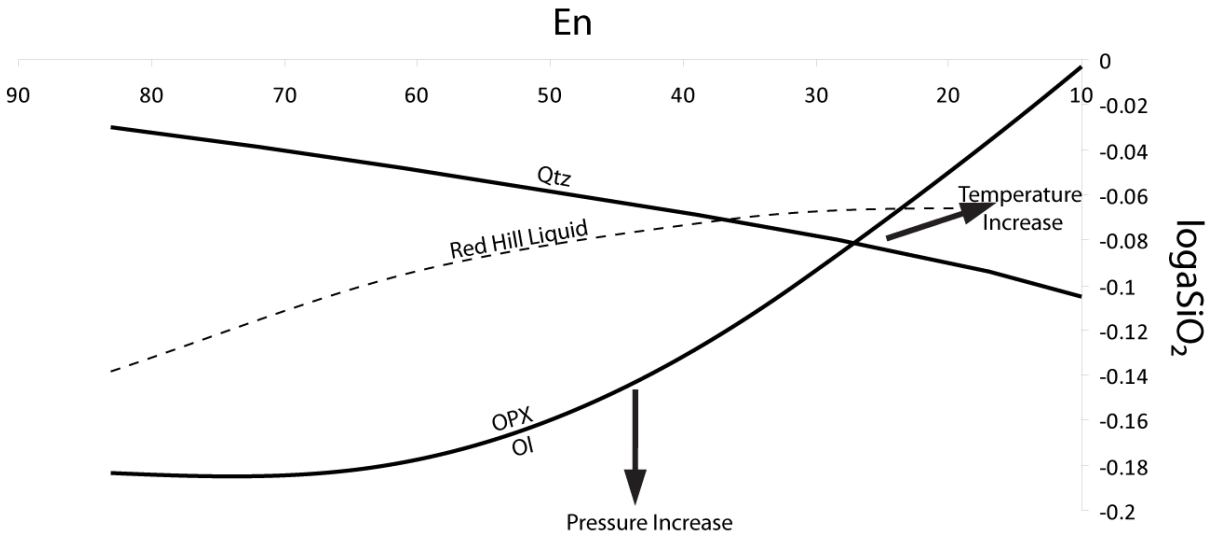

Figure 4.8. En% (pigeonite) vs $\log a_{SiO_2}^{liquid}$ calculated for Red Hill pigeonites at 3kbars (after Campbell and Nolan, 1974). Arrows show the vectors of increasing temperature and pressure on the position of the Ol-OPX and Qtz equilibria.

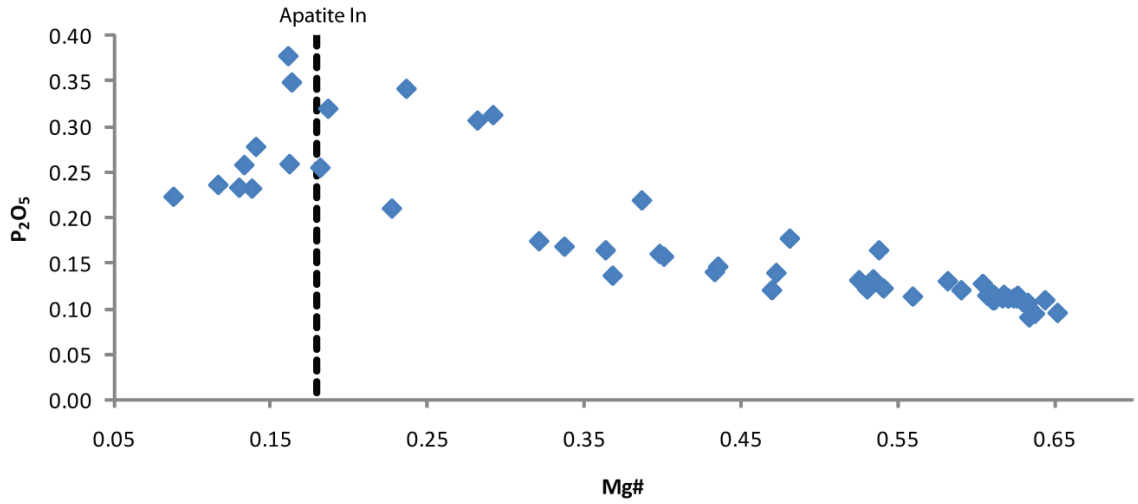

Figure 4.9. Illustration of the P_2O_5 content of the melt as it differentiates (decreasing Mg#). The Mg# at which apatite saturation occurs, insinuated by a drop in P_2O_5 in the melt, coincides with the Mg# of the melt coexisting with the most ferriferous stable pigeonite.

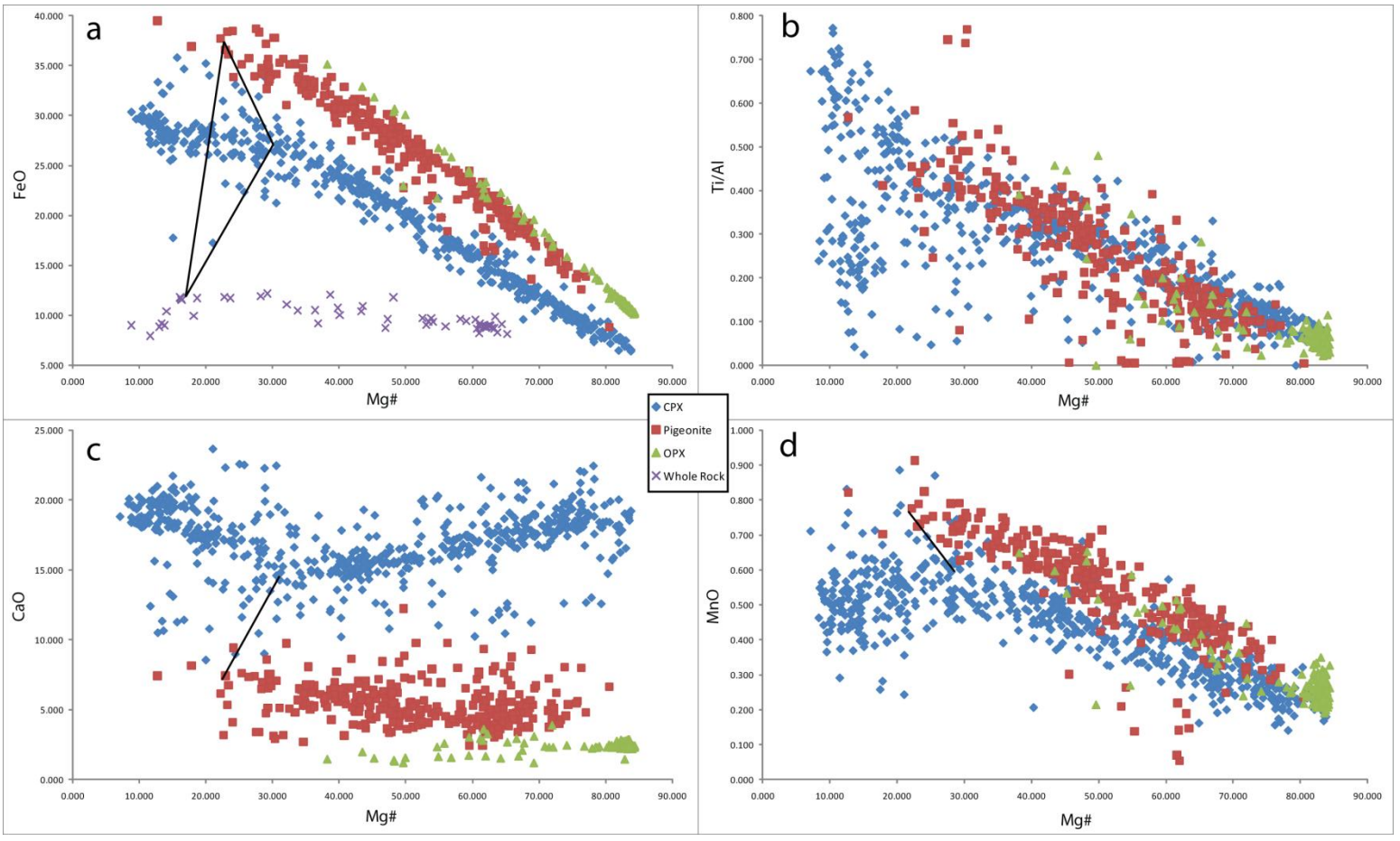

Figure 4.10. Binary plots detailing the chemical trends of pyroxenes with differentiation. Tie lines between augite and pigeonite (and the liquid, (*a*)) at the point of pigeonite exhaustion evidences the lower Mg# of pigeonite at a given augite Mg#. See section *4.3.1d* for discussion.

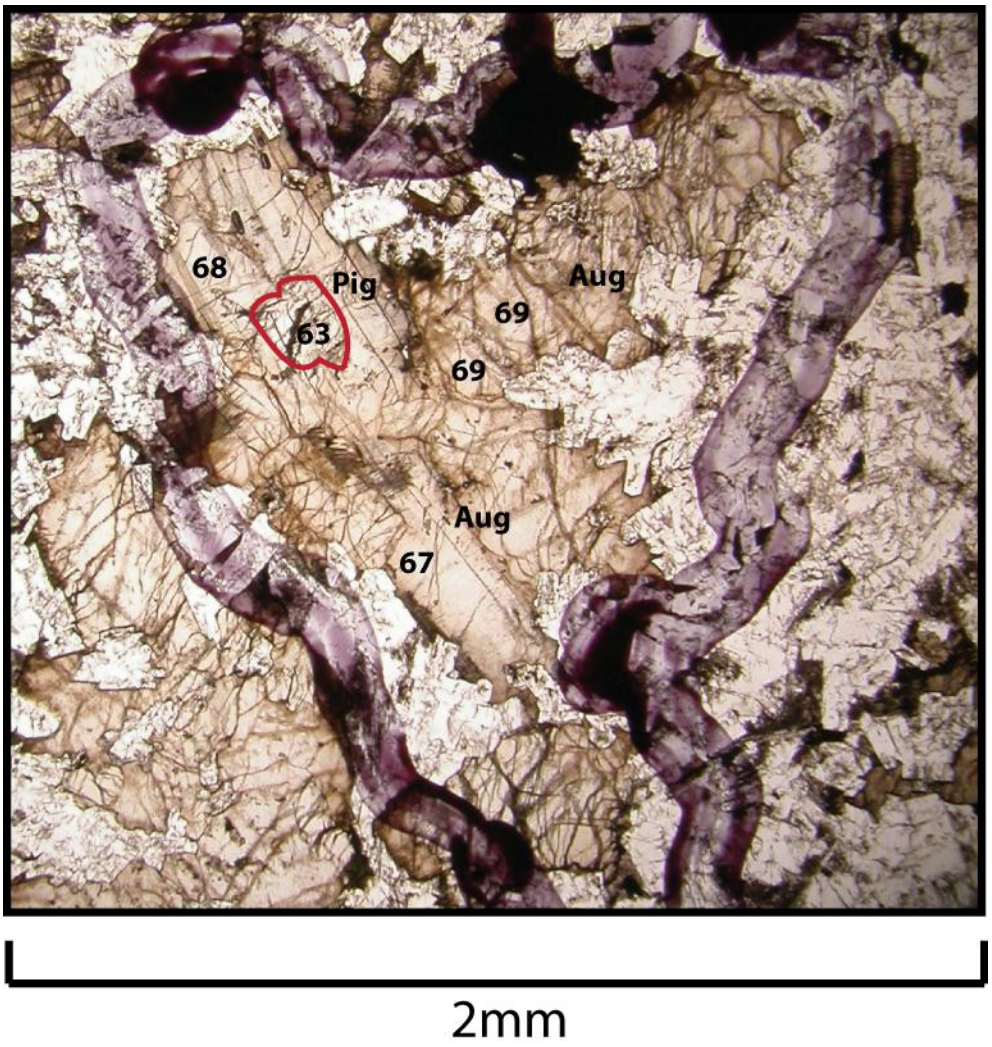

Figure 4.11. Thin section photomicrograph (PPL) of pigeonite coring augite in a dolerite (PS35). The pigeonite, despite having precipitated prior to the augite, exhibits lower Mg# (63) compared to surrounding augite (68).

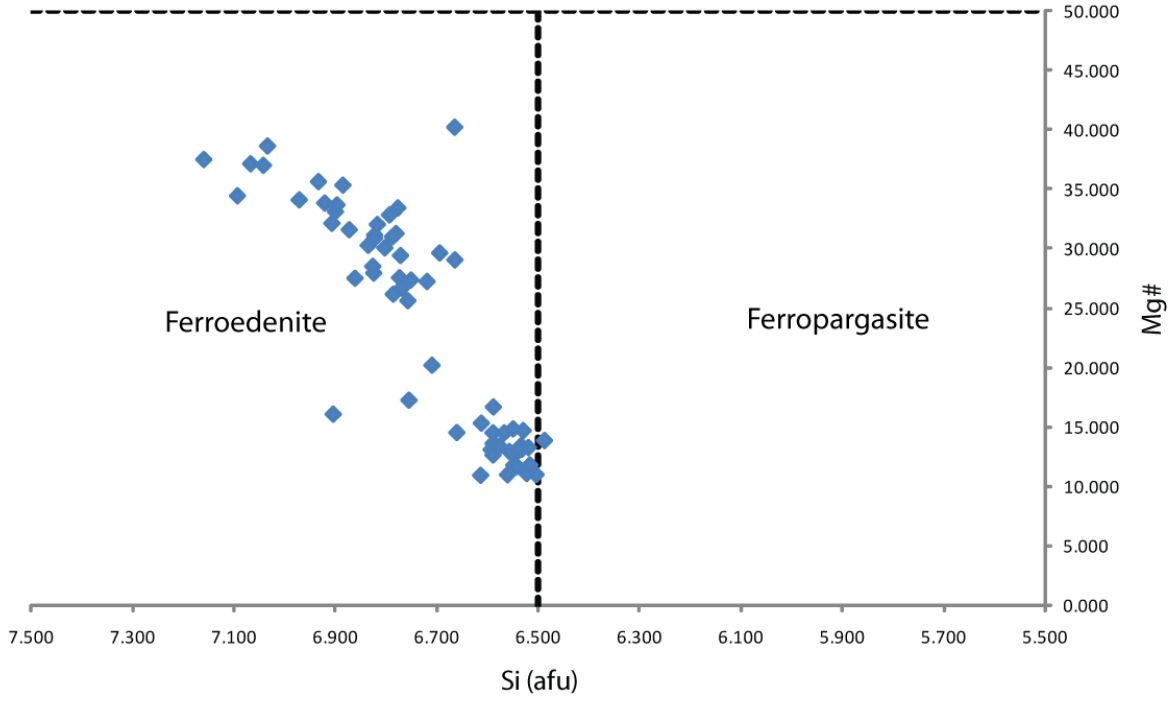

Figure 4.12. Classification of amphiboles from the Red Hill intrusion, showing their iron-enriched character. (After Leake et al., 1997).

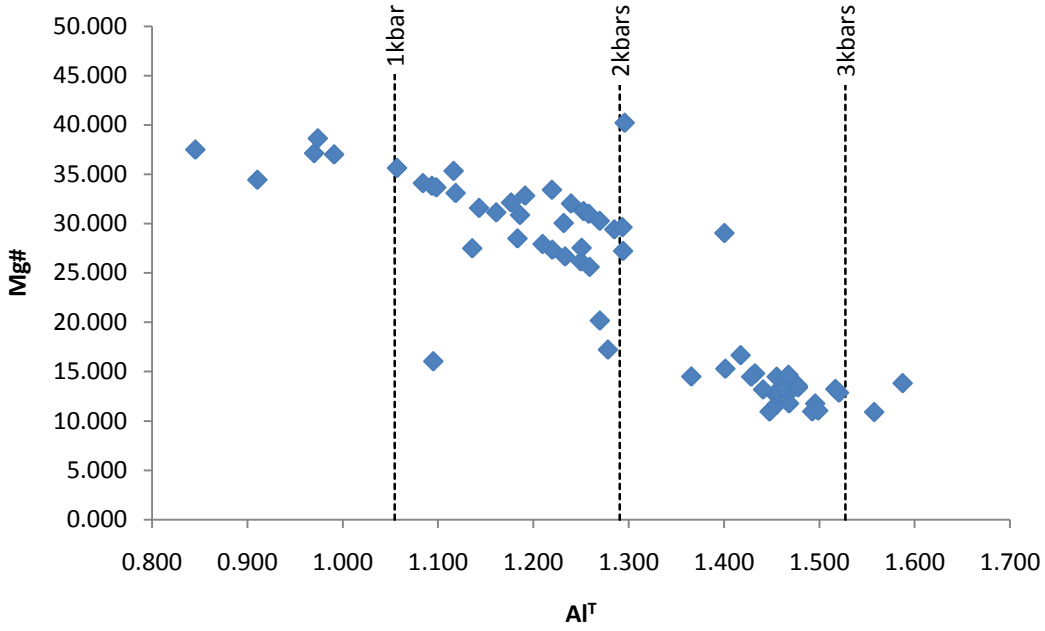

Figure 4.13. A plot of Mg# against Al^{total}, with pressure contours from the geobarometer of Johnson and Rutherford (1989) (*equation 4.9.*).

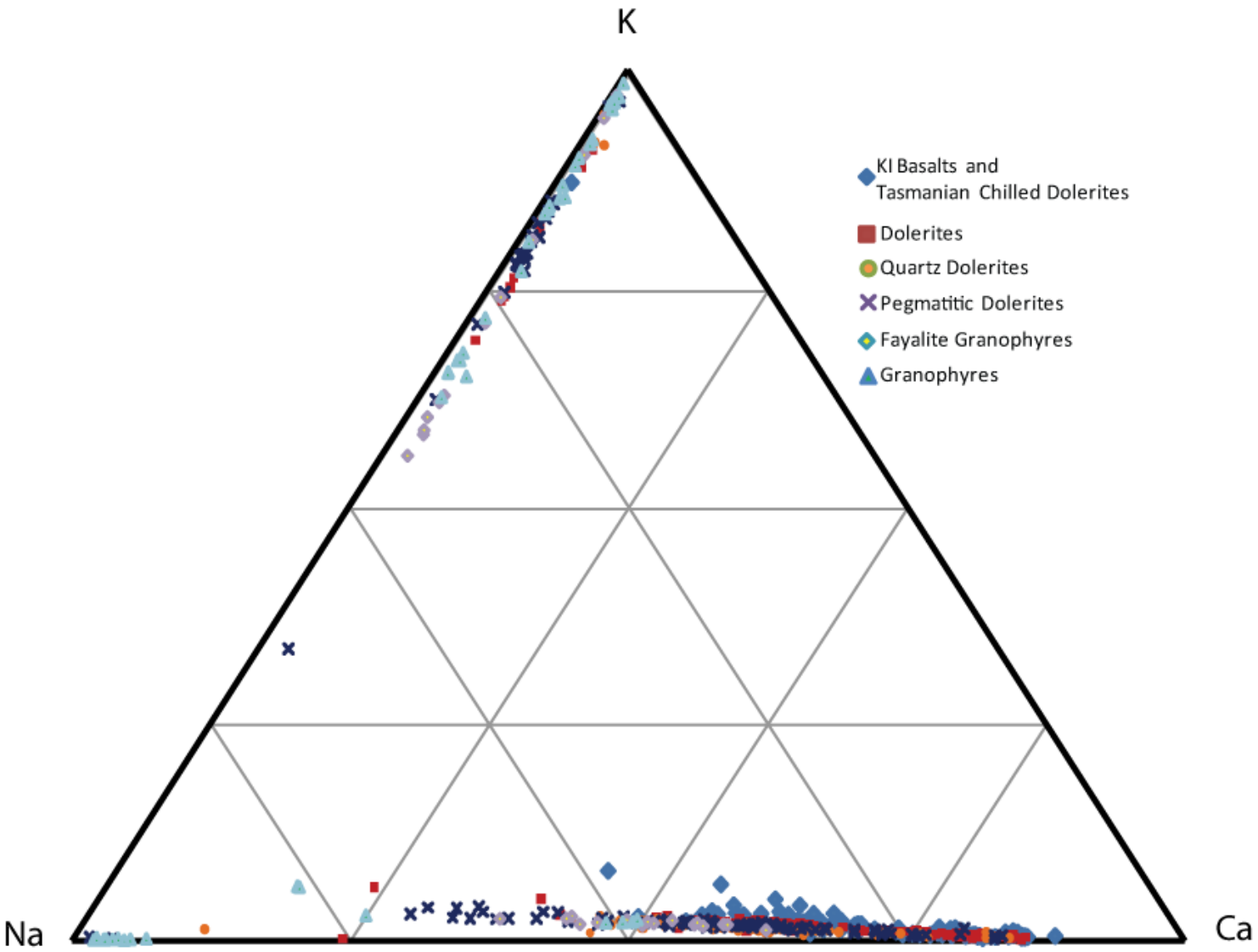

Figure 4.14. Feldspar ternary diagram which plots molar quantities of K, Na and Ca. See section *4.3.3.* for discussion.

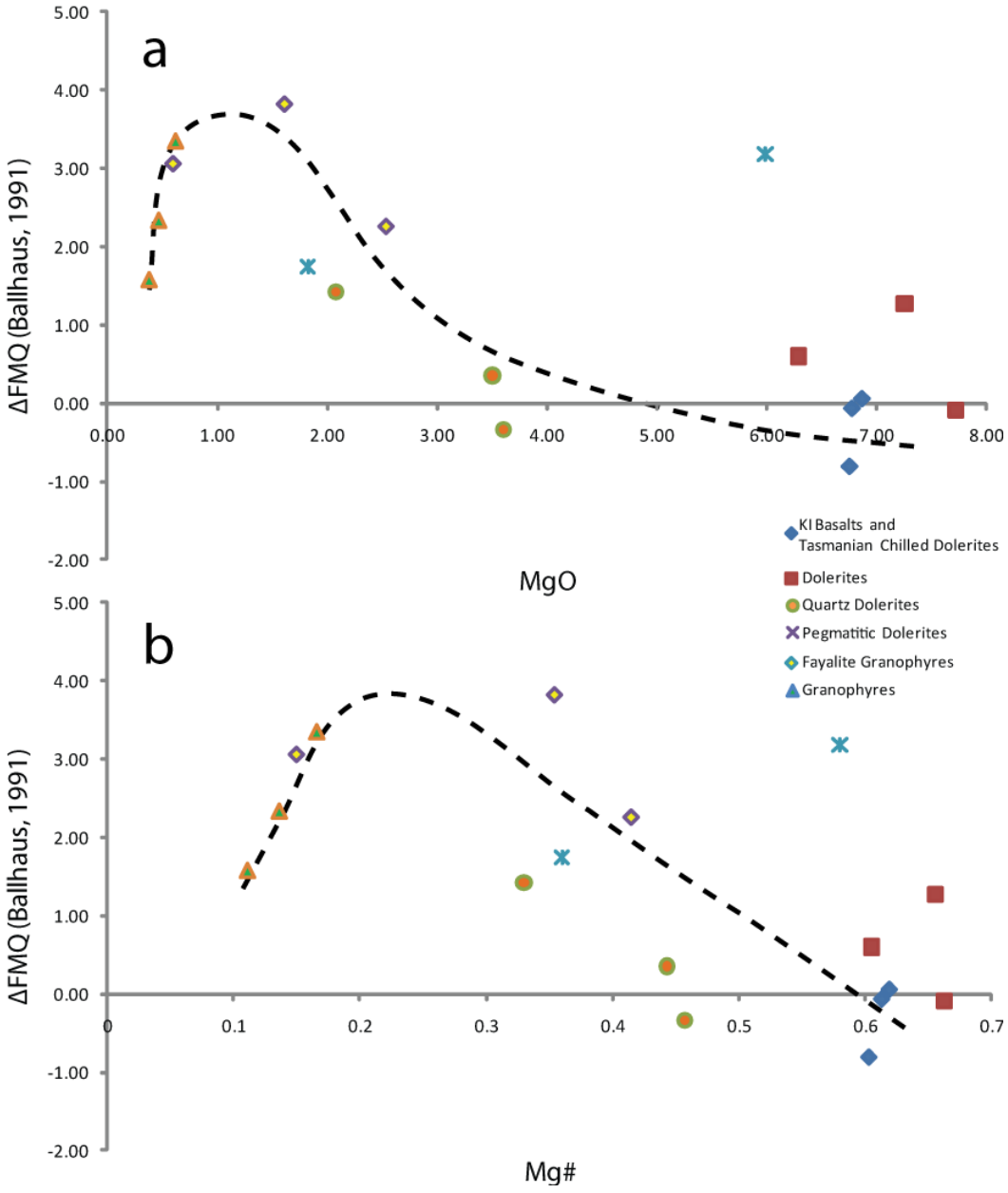

Figure 4.15. Thermodynamically- calculated oxygen fugacity of Red Hill samples (relative to the FMQ buffer, Ballhaus, 1991), illustrating its increase during gabbroic fractionation (*a)* MgO and *b)* Mg#) prior to an abrupt decrease heralding the saturation of magnetite. See section *4.4.* for calculation methods and discussion.

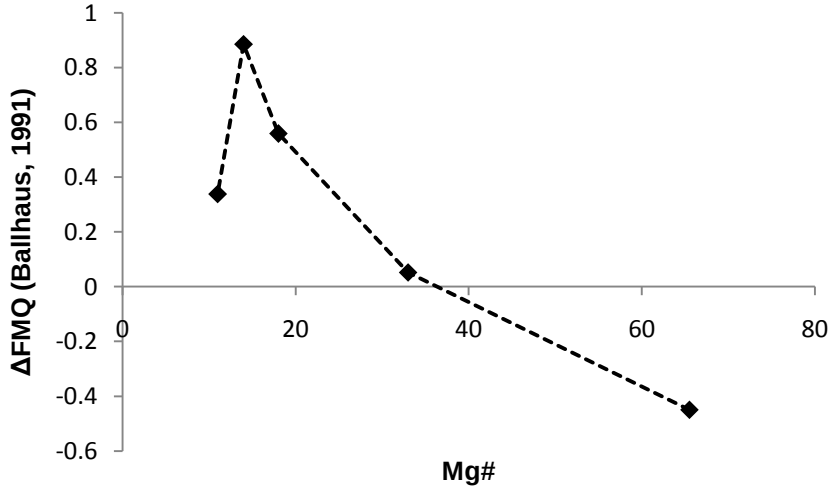

Figure 4.16. Oxygen fugacity of Red Hill samples (relative to the FMQ buffer, Ballhaus, 1991), calculated using the magnetite-ilmenite geothermobarometer. The redox evolution recorded is in agreement with that calculated thermodynamically, however, the range of absolute fo_2 changes relative to FMQ is smaller.

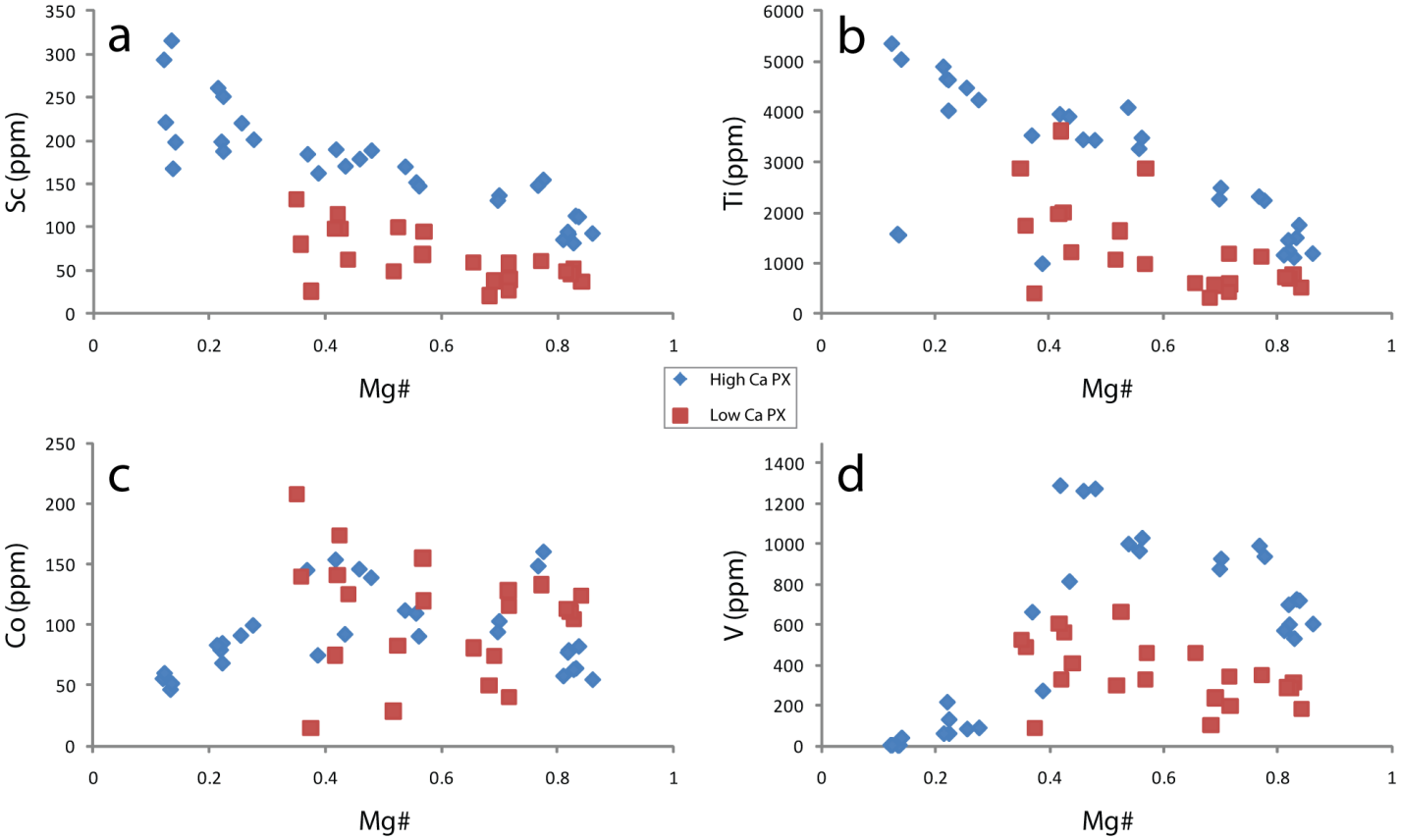

Figure 4.17. Moderately incompatible to compatible trace elements in low-Ca pyroxene and high-Ca pyroxene as a function of their state of differentiation (Mg#). See section *4.5.1.* for discussion.

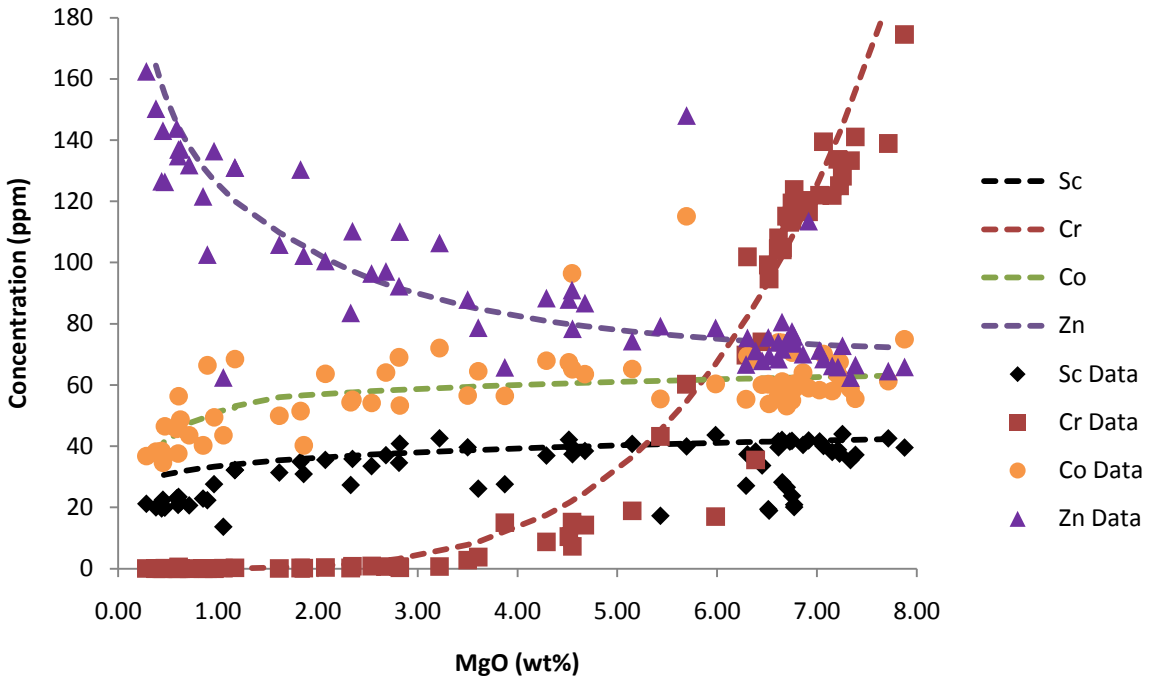

Figure 4.18. Abundances of moderately incompatible to compatible trace elements in the whole rocks of the Red Hill sequence. Their evolution by fractional crystallisation is modelled using internally-consistent partition coefficients and phase proportions (dashed lines). See section *4.5.1.* for further details.

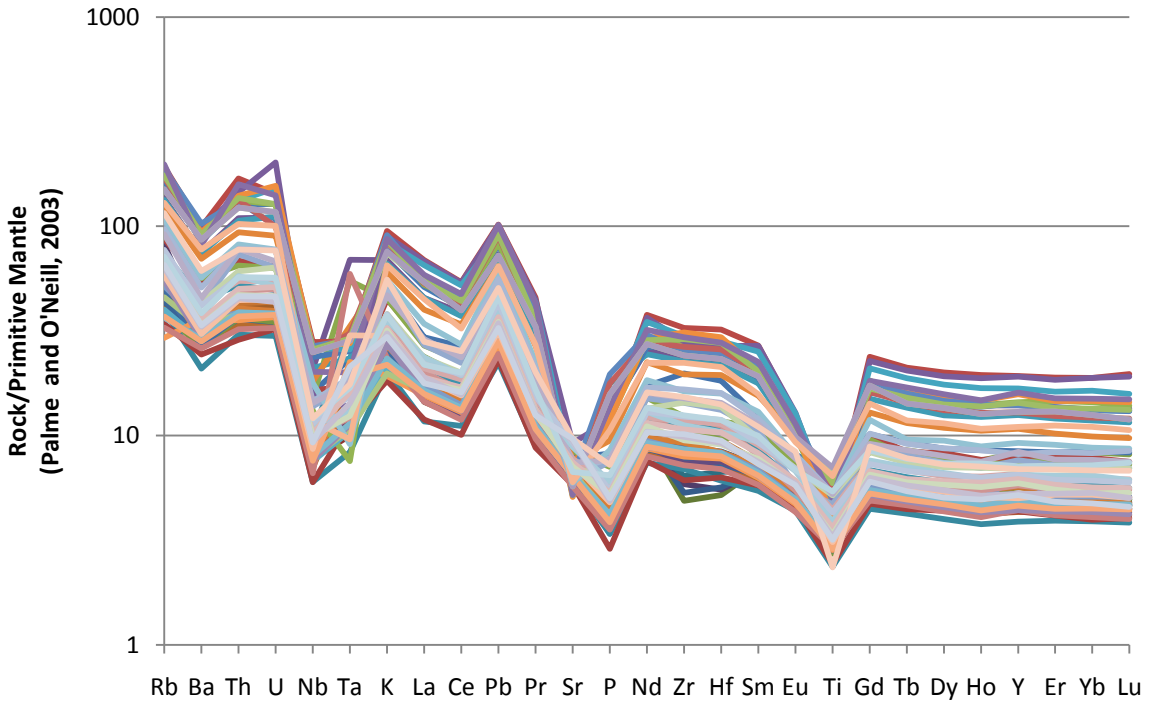

Figure 4.19. Incompatible trace element abundances of the entire Kangaroo Island-Red Hill sequence, normalised to the primitive mantle of Palme and O'Neill (2003). Identifiable is the strong positive Pb anomaly, and the pronounced negative Nb, Ta, Sr, P, Eu and Ti anomalies, reflective of the crustally-contaminated mantle source (*section 3.3.*).

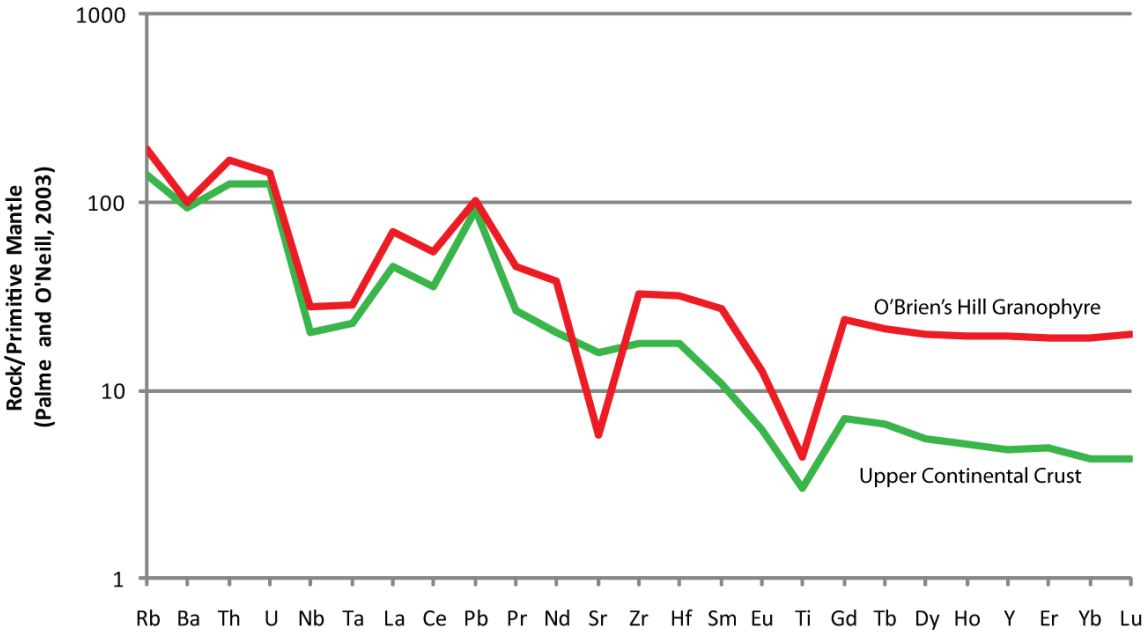

Figure 4.20. The most incompatible-element enriched granophyre (O'Brien's Hill Granophyre) in comparison to the upper continental crust (Rudnick and Gao, 2003), precluding the contamination of the former by the latter. Normalised to primitive mantle of Palme and O'Neill (2003).

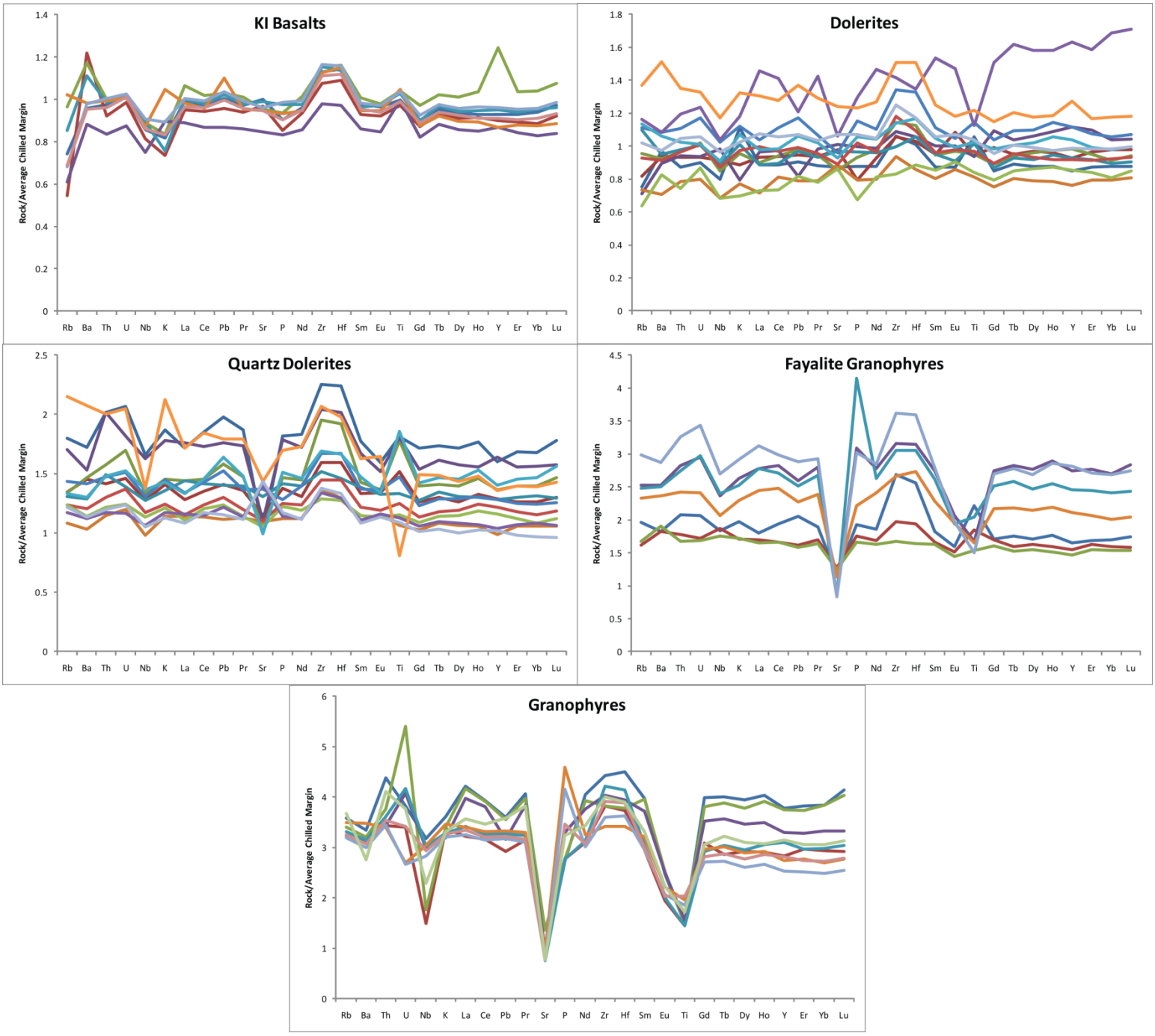

Figure 4.21. Samples normalised to the average chilled margin (*table 3.9.*), and subdivided by petrological grouping. Note the different scale for each of the diagrams, where the early dolerites represent much smaller deviations from the chilled dolerites.

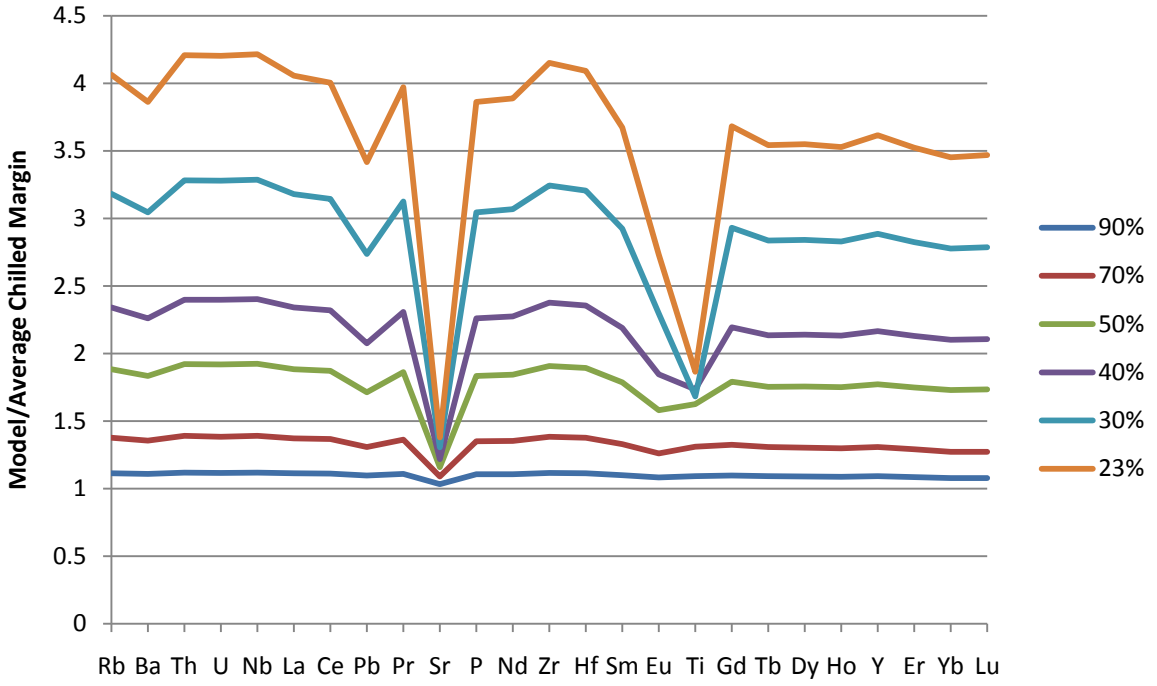

Figure 4.22: Modelled compositions based on partition coefficients calculated from LA-ICP-MS analyses of individual minerals in the Red Hill intrusion. Percentages refer to the fraction of melt remaining.

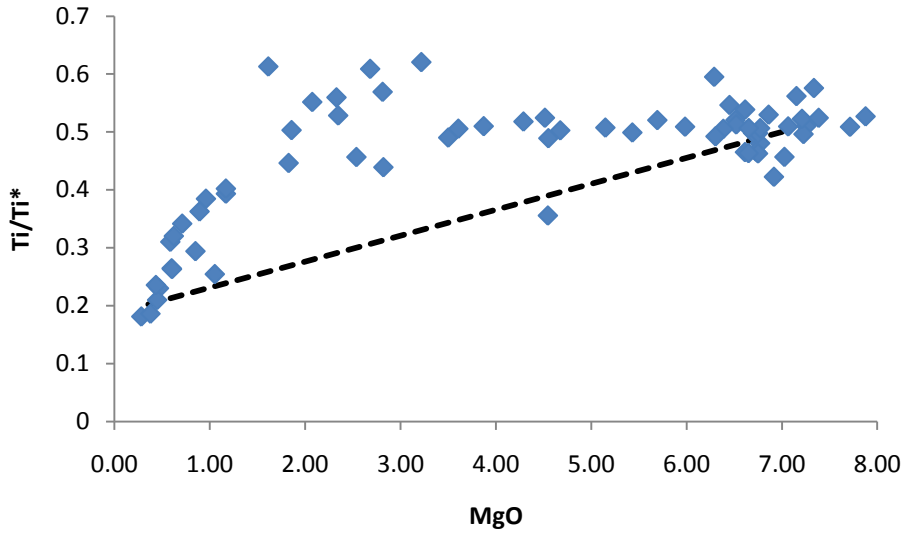

Figure 4.23. A plot quantifying the whole rock negative Ti anomaly that develops in the fayalite granophyres in response to magnetite precipitation. Where Ti/Ti* is $Ti_N/(Nd_N^{-0.0555}*Sm_N^{0.333}*Gd_N^{0.722})$, where N denotes normalisation to primitive mantle of Palme and O'Neill (2003). Expected crustal contamination vector is denoted by the dashed line.

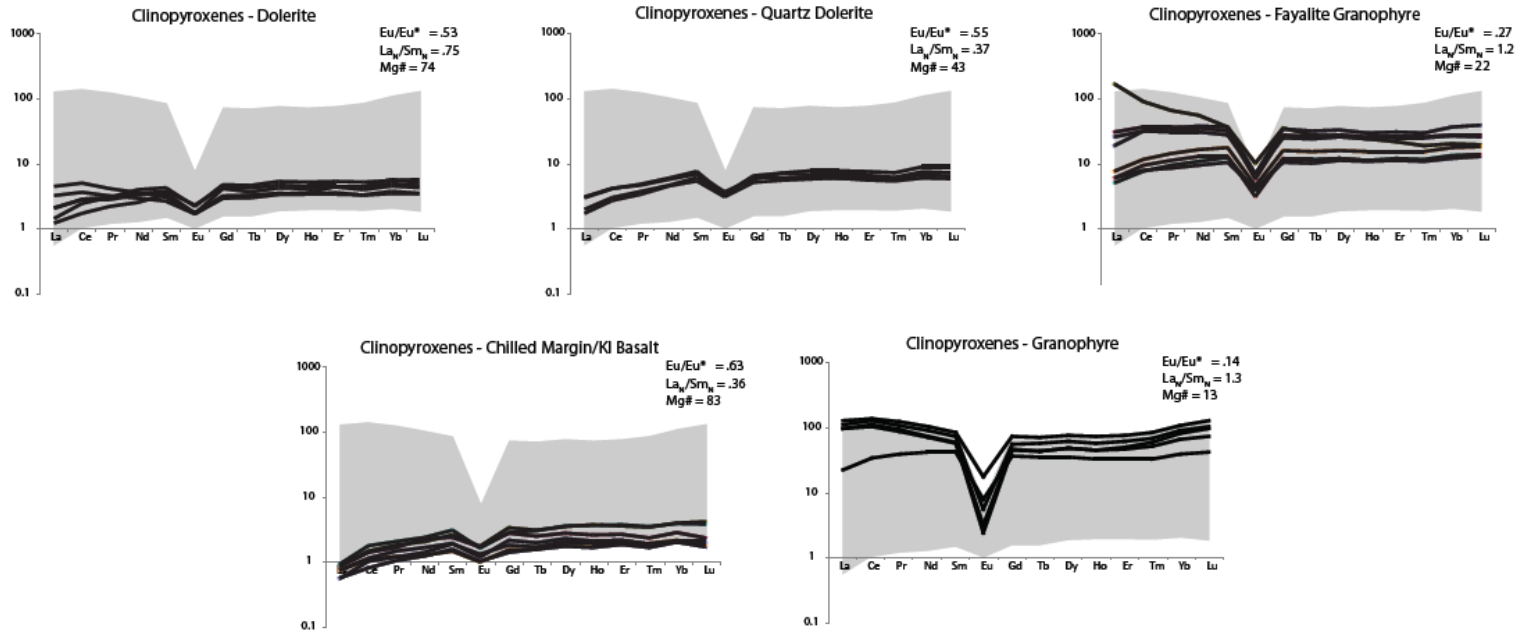

Figure 4.24. REE plots of augites from the Red Hill intrusion, subdivided by lithology and normalised against primitive mantle (Palme and O'Neill). The increase LREE enrichment and Eu depletion mirrors that of the whole rocks.

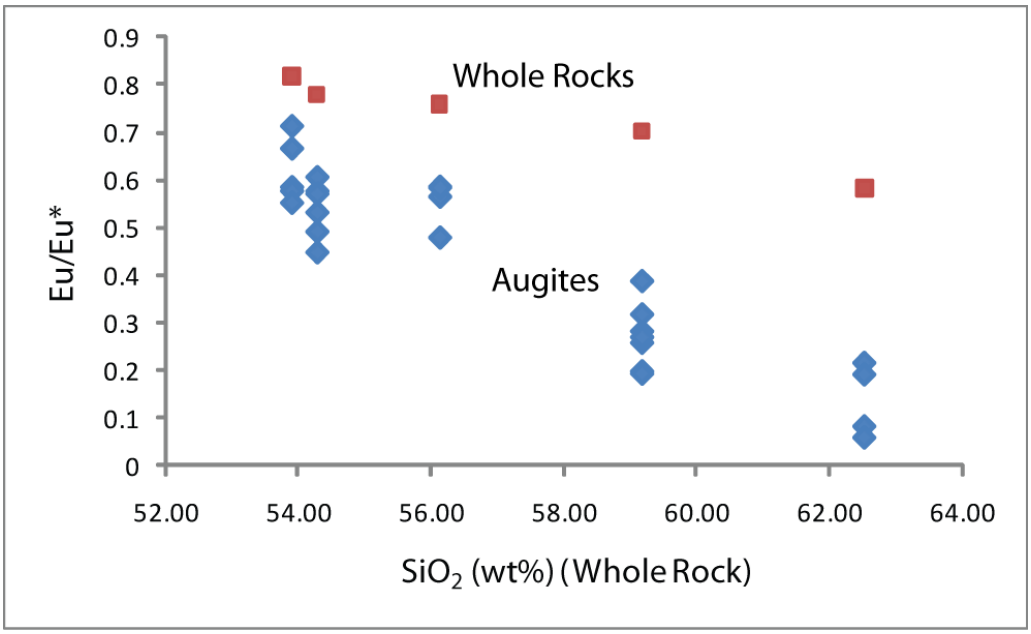

Figure 4.25. The evolving Eu anomaly of the whole rocks and the pyroxenes in that whole rock quantified by the Eu/Eu* (where Eu/Eu* = $Eu_N/((Gd+Sm)/2)$, where N denotes normalisation to primitive mantle of Palme and O'Neill (2003)), compared to the SiO_2 content of the whole rock.

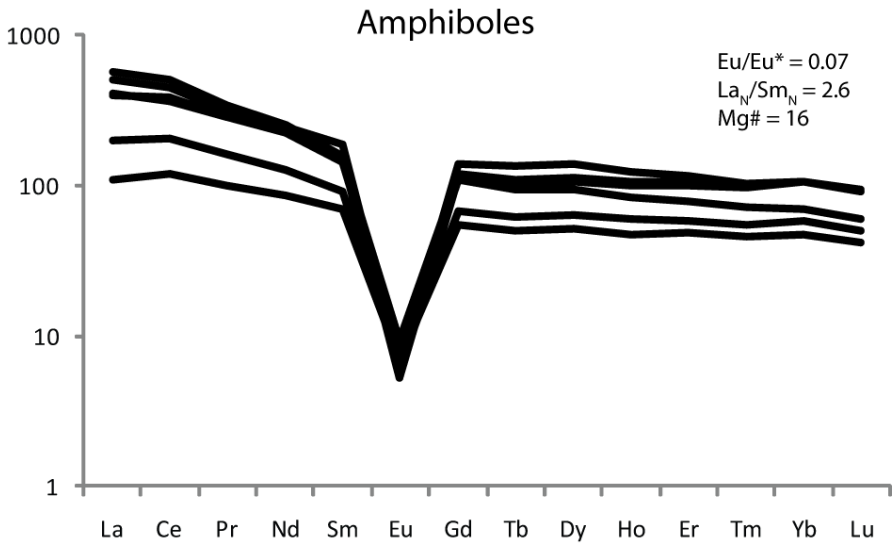

Figure 4.26. REE plots of amphiboles from the Red Hill intrusion normalised against primitive mantle (Palme and O'Neill). They display LREE enriched patterns with prolific negative Eu anomalies, reminiscent of the ferriferous augites and hedenbergites they coexist with.

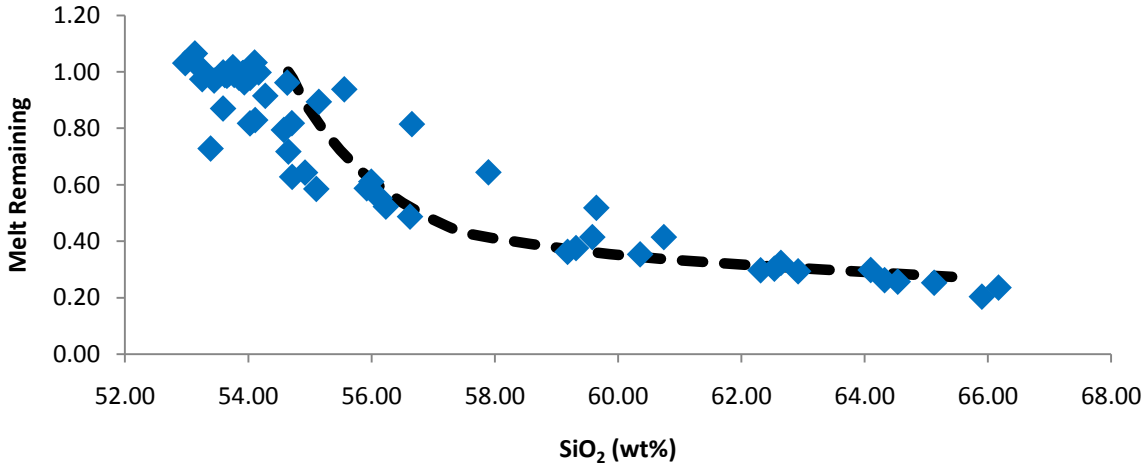

Figure 4.27. Melt remaining for the Red Hill suite (as calculated for the model in the appendices), depicting rapid silica enrichment following the crystallisation of magnetite near 60wt% SiO_2. Also shown is the liquid line of descent from a Tasmanian chilled dolerite composition as predicted by PELE (Boudreau, 1999). Crystallisation conditions were: Fractional crystallisation, Liquidus T(°C) = 1198, Pressure (kbars) = 4, fo_2 (initial) = FMQ-1, XH_2O (initial) = 0.3wt%. See section *4.6.* for discussion.

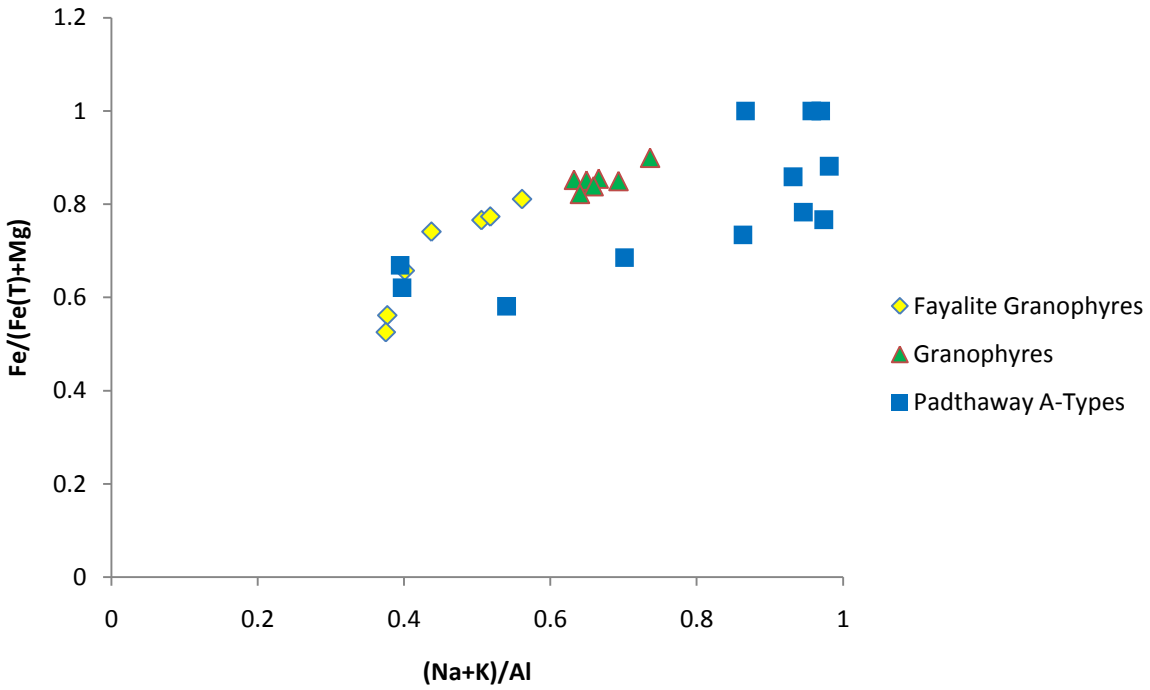

Figure 4.28: Fe# (calculated as Fe/(Fe$^{(T)}$+Mg) against peralkalinity (Na+K)/Al, depicting their increase with fractionation. For the Red Hill suite, Fe# enrichment is rapid with respect to peralkalinity prior to magnetite crystallisation, but becomes muted thereafter. The reverse applies for Na and K. See section *4.6.* for discussion.

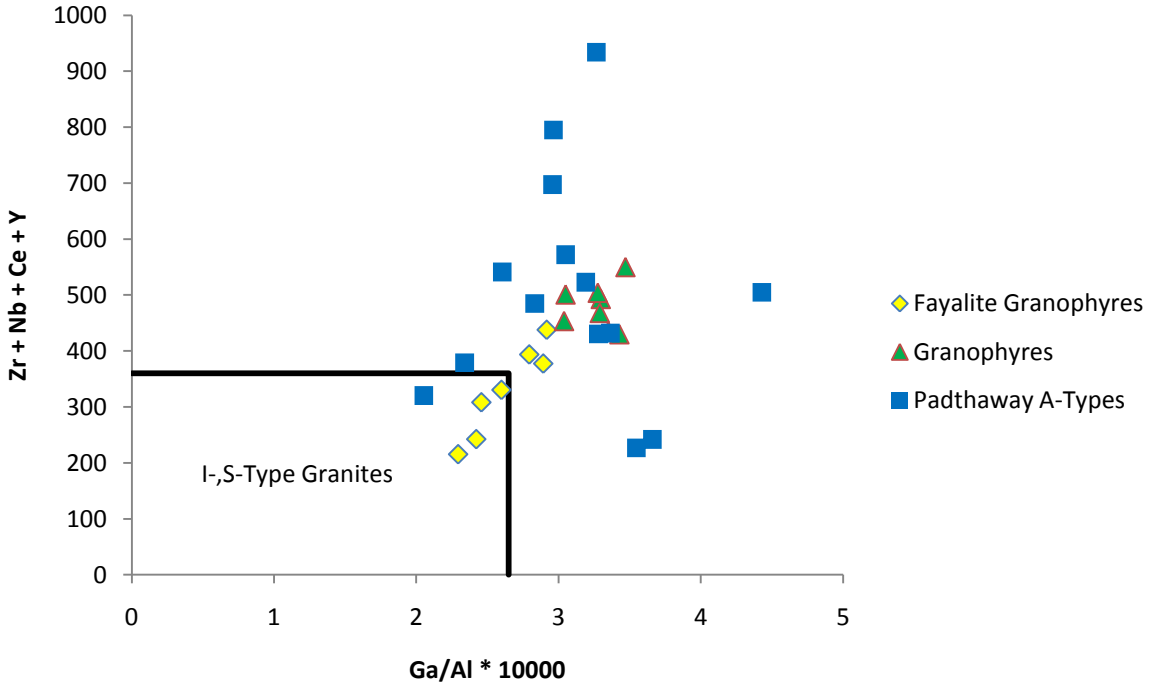

Figure 4.29: Ga/Al (*10000) against Zr+Nb+Ce+Y. Also denoted are the typical fields for I- and S-type granites, as estimated by Whalen et al., (1987; 1996). See section *4.6.* for discussion.

5.0. Iron Isotopes

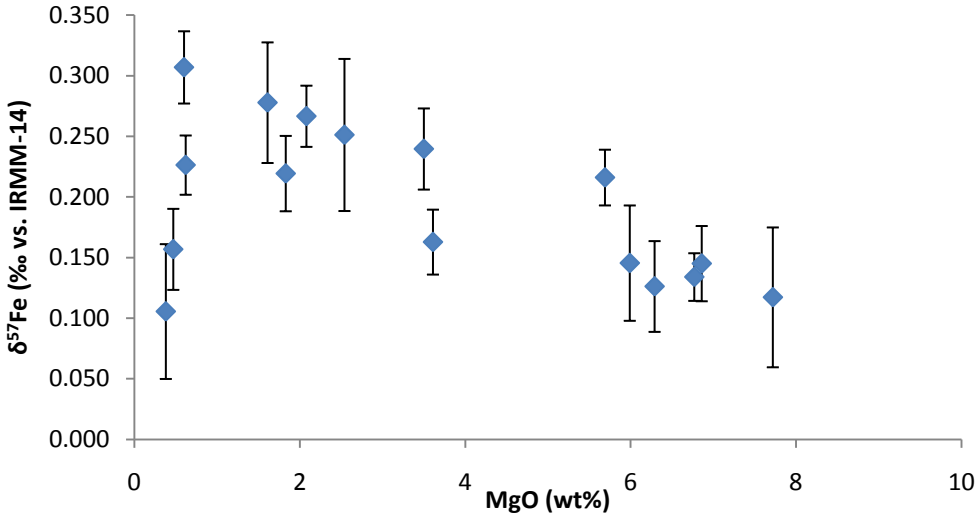

Figure 5.1. Plot of δ^{57}Fe against MgO (wt%) of the whole rocks, delineating an initial increase before falling near 1 wt% MgO.

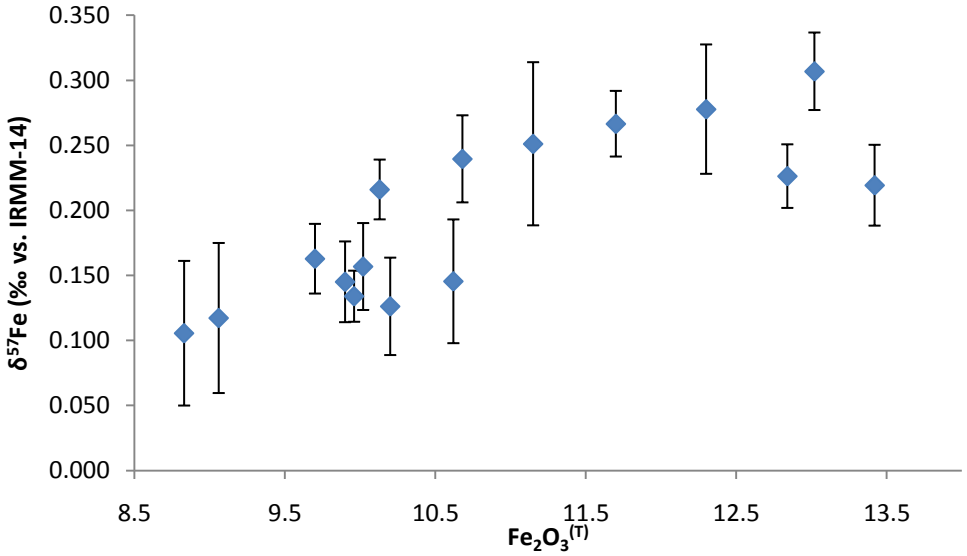

Figure 5.2. Plot of δ^{57}Fe against $Fe_2O_3^{(T)}$ (wt%) of the whole rocks, showing a broadly linear correlation throughout the intrusion.

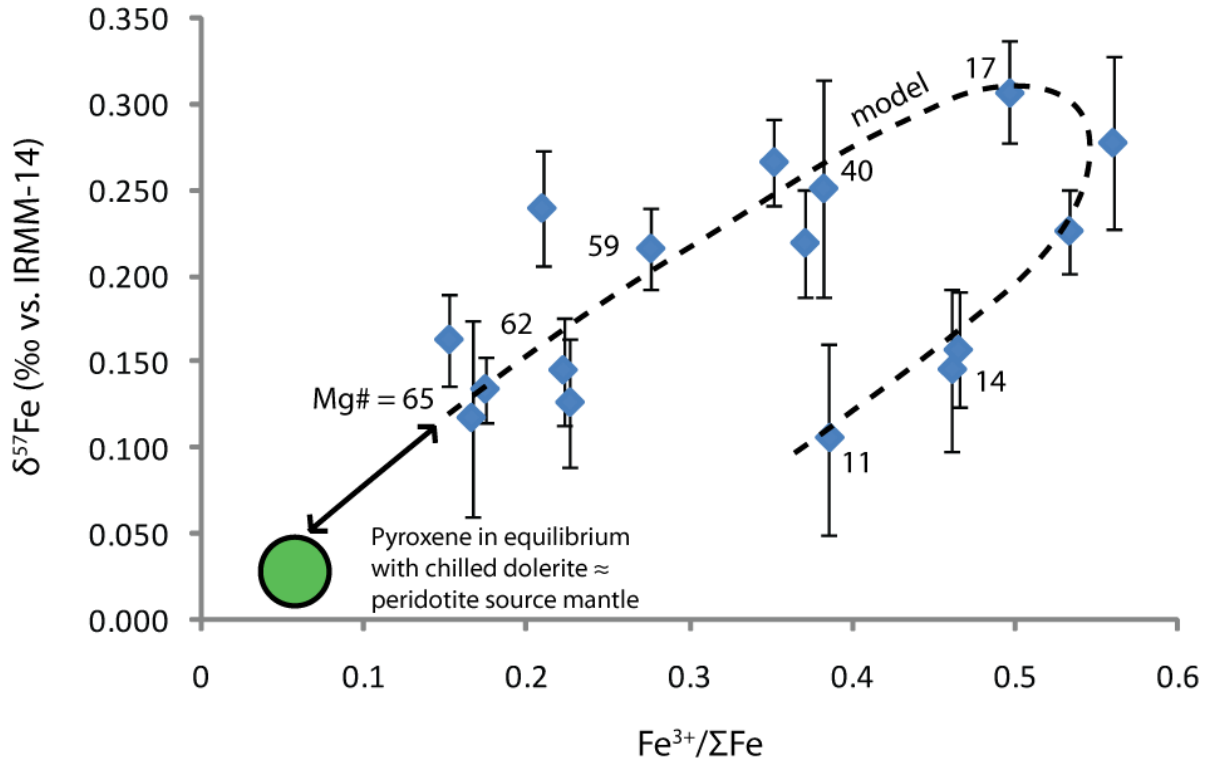

Figure 5.3. Plot of δ^{57}Fe against $Fe^{3+}/\sum Fe$ of the whole rocks, which illustrate the inflection in the trend coincident with magnetite crystallisation. The Rayleigh model (dashed line) assumes that $\Delta^{57}Fe_{px-melt} = -0.25‰ \times 10^6/T^2$ and that $\Delta^{57}Fe_{mtn-melt} = +0.2‰ \times 10^6/T^2$ such that the observed trends resulting from fractional crystallisation are reproduced. Also shown is the composition of the pyroxene in equilibrium with the most primitive compositions, predicted by Rayleigh modelling.

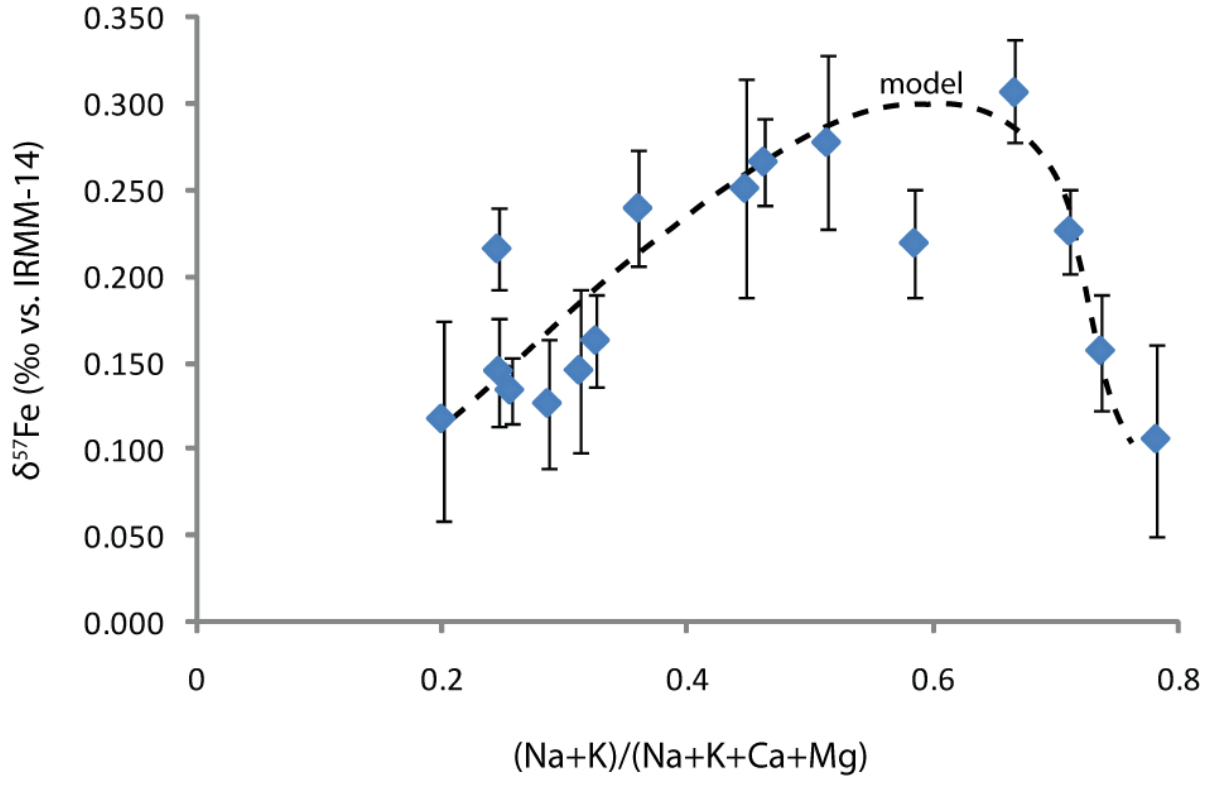

Figure 5.4. Plot of δ^{57}Fe against (Na+K)/(Na+K+Ca+Mg) of the whole rocks, which illustrate the inflection in the trend coincident with magnetite crystallisation. The initial increase in δ^{57}Fe is a positive linear function of the alkali content of the melt.

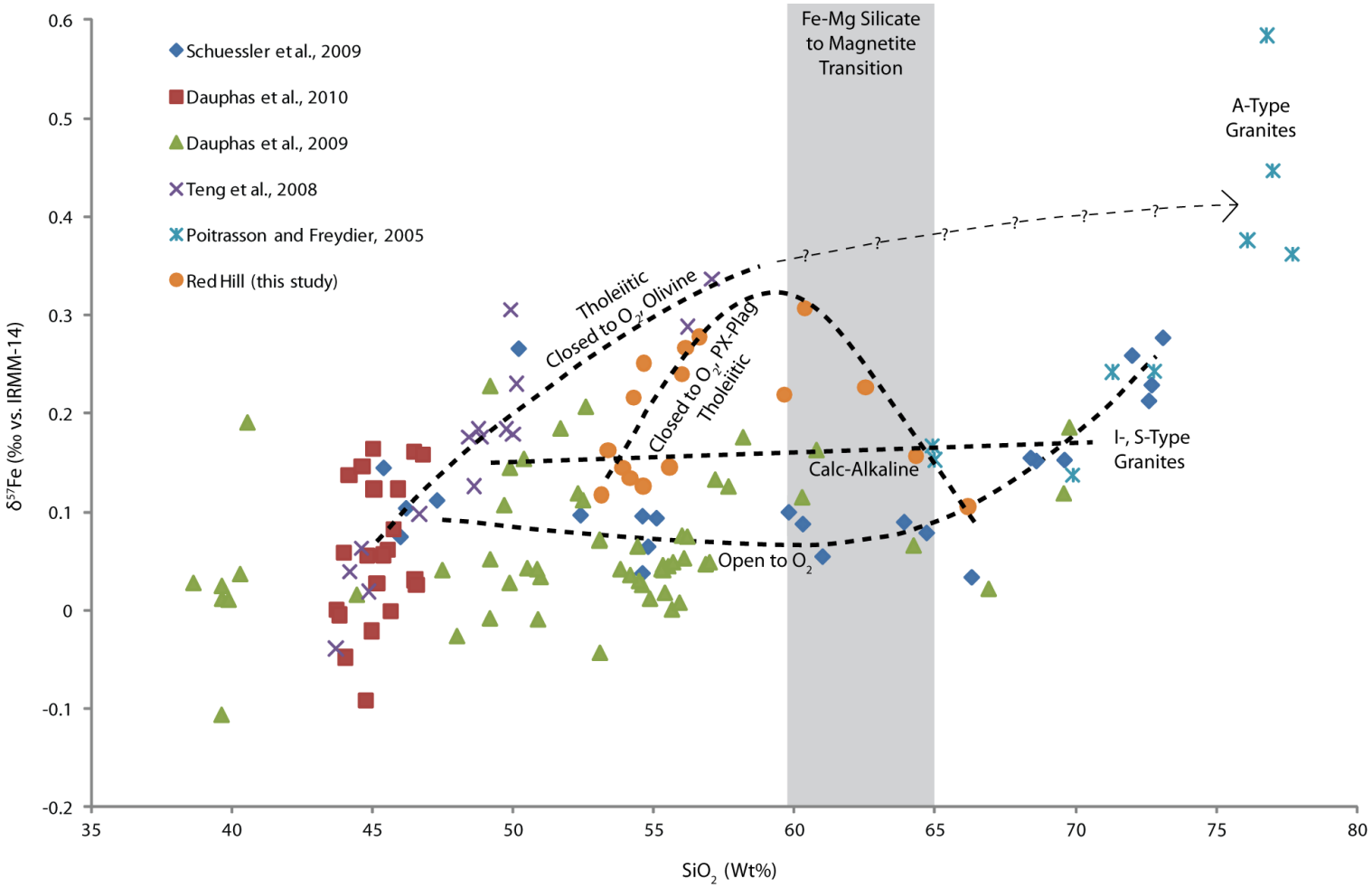

Figure 5.5. A compilation of δ^{57}Fe data (Poitrasson and Freydier, 2005; Teng et al., 2008; Schuessler et al., 2009; Dauphas et al., 2009; Dauphas et al., 2010) compared with that of this study, plotted against SiO_2 (Wt%). Delineated are the expected fractionation trends for different magmatic systems (tholeiitic and calc-alkaline) under conditions open and closed to oxygen exchange. Closed tholeiitic magmas, that have low fo_2, reach maxima in δ^{57}Fe coincident with magnetite saturation, near 60wt% SiO_2. The delay of magnetite crystallisation in low fo_2 magmas evolving as closed systems may give rise to the heavy isotopic compositions of A-type granites, in response to the protracted removal of ^{57}Fe-depleted ferromagnesian silicates. Conversely magmas open to oxygen trend along slightly decreasing δ^{57}Fe -SiO_2 trajectories before displaying a moderate increase in δ^{57}Fe when magnetite becomes the dominant Fe-bearing phase. Calc-alkaline magmas may show constant δ^{57}Fe -SiO_2 trends, giving rise to I-type granites with a similar isotopic composition to its parent magma. S-type granites could form from partial melts of such lithologies.

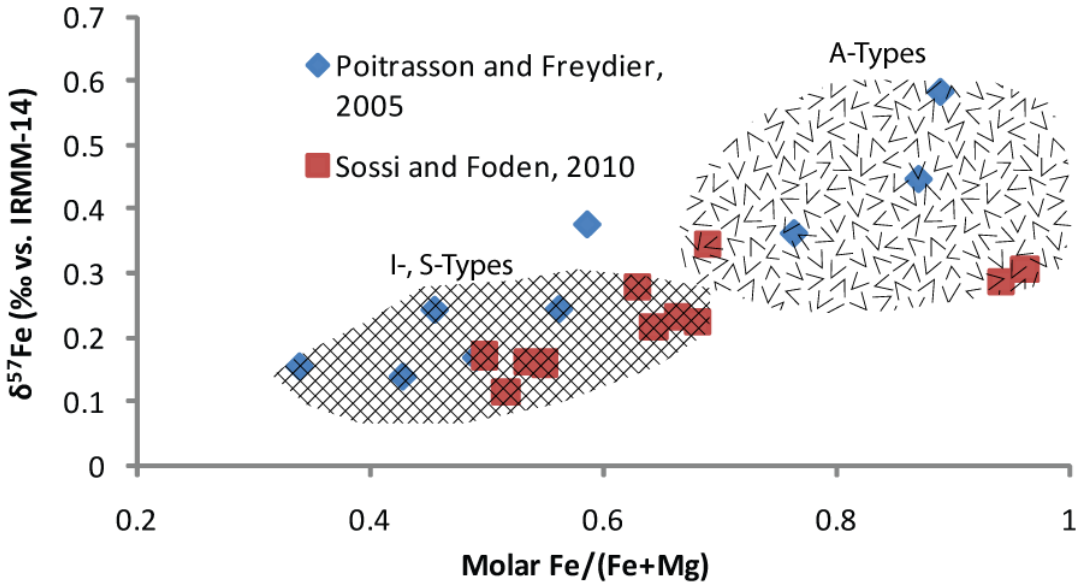

Figure 5.6. Plot of δ^{57}Fe against Fe/(Fe+Mg) of whole rocks from Poitrasson and Freydier (2005) and Sossi and Foden (2010, unpub. data), highlighting the compositional differences between more oxidised I- and S-type granites and reduced A-types.

Appendix

Table A1-A: In/Re-corrected trace element abundances (Li-Ga) measured by S-ICP-MS in the rock standards used for normalisation. All abundances in ppm.

Corrected With	In	In	In	In	In	In	In/Re	In/Re	In/Re	Re	Re	In	In
Element	Li	Be	B	P	Sc	V	Cr	Mn	Co	Ni	Cu	^{66}Zn	^{71}Ga
Sample													
GSP-2													
GSP1:4	36.50	1.60	0.55	1438.19	7.68	60.29	22.49	350.99	7.73	16.72	42.91	125.16	45.52
GSP0.5:4.5	41.29	1.65	0.53	1440.43	7.60	59.42	22.16	352.92	7.72	16.89	43.88	128.01	46.75
GSP0.25:4.75	41.71	1.73	0.13	1470.16	7.68	58.79	21.87	341.70	7.93	17.37	45.54	129.63	47.68
GSP2-2	28.17	1.22	0.12	1413.53	7.61	55.16	20.07	370.79	7.58	16.39	43.47	124.51	44.83
GSP2-4	23.40	0.91	-	1264.53	7.11	51.30	19.03	332.68	7.00	14.57	38.85	113.14	40.70
GSP2-1	42.34	1.63	-	1515.81	8.02	59.38	21.38	348.67	7.35	17.68	44.64	126.89	46.29
Average	**35.57**	**1.46**	**0.33**	**1423.78**	**7.62**	**57.39**	**21.17**	**349.63**	**7.55**	**16.60**	**43.21**	**124.56**	**45.30**
STDEV	8.00	0.32	0.24	85.53	0.29	3.48	1.34	12.74	0.33	1.10	2.32	5.89	2.46
2SE	6.35	0.25	0.19	67.85	0.23	2.76	1.07	10.11	0.26	0.87	1.84	4.68	1.95
Accepted	**41.22**	**1.50**		**1259.62**	**6.27**	**51.79**	**19.84**	**320.00**	**7.35**	**17.61**	**42.75**	**120.94**	**23.56**
% Difference	-13.71	-2.88		13.03	21.54	10.82	6.69	9.26	2.76	-5.74	1.09	2.99	92.26
BCR-2													
BCR2-4	10.33	1.99	1.62	1681.39	38.18	479.37	17.93	1694.54	39.53	11.97	16.64	137.83	25.60
BCR2-5	8.44	1.67	1.65	1639.85	37.82	469.27	17.47	1797.75	40.22	11.94	17.07	141.86	25.65
BCR2-7	5.73	1.16	0.63	1431.76	33.42	412.16	15.18	1516.35	35.01	10.42	15.42	126.61	23.64
BCR2-2	8.73	2.00	2.08	1692.99	35.90	451.54	17.73	1486.41	37.37	11.43	15.99	122.64	23.78
BCR2-3	8.68	2.33	1.85	1951.60	37.86	464.46	19.90	1523.45	37.77	13.05	18.90	121.28	26.72
BCR2-6	7.68	1.58	0.97	1731.13	34.25	398.65	18.64	1409.09	40.66	12.06	17.05	103.89	22.71
BCR2-1	11.34	2.26	1.15	1597.76	39.27	456.61	17.48	1687.76	38.25	11.02	16.49	145.17	26.45
BCR2-2(2)	8.52	1.60	-	1494.98	35.38	446.52	15.71	1539.56	33.18	9.74	14.33	127.14	24.52
Average	**8.68**	**1.82**	**1.42**	**1652.68**	**36.51**	**447.32**	**17.50**	**1581.86**	**37.75**	**11.45**	**16.49**	**128.30**	**24.89**
STDEV	1.67	0.39	0.52	158.03	2.08	28.06	1.51	130.37	2.58	1.04	1.34	13.31	1.44

2SE	1.10	0.26	0.34	103.90	1.37	18.45	0.99	85.71	1.69	0.69	0.88	8.75	0.95
Accepted	**9.00**	**2.35**		**1527.47**	**33.00**	**416.00**	**18.00**	**1520.00**	**37.00**	**18.00**	**21.00**	**127.00**	**23.00**
% Difference	-3.56	-22.36		8.20	10.64	7.53	-2.75	4.07	2.03	-36.37	-21.49	1.03	8.20
BHVO-2													
BHVO2-5	4.86	0.93	0.96	1263.65	36.56	373.19	326.10	1400.84	47.50	120.66	122.83	101.45	24.40
BHVO2-6	4.87	1.05	1.62	1373.52	35.01	356.08	334.19	1309.05	45.04	113.51	128.92	95.83	18.99
BHVO2-4 .25	4.94	1.19	0.45	1481.68	35.80	366.61	301.34	1333.65	43.14	113.00	148.58	124.93	22.16
BHVO2-4 .5	4.88	1.22	0.78	1500.24	36.17	363.36	302.73	1324.94	42.69	110.87	144.67	99.32	21.68
BHVO2-4 1	4.78	1.16	1.00	1513.05	36.38	362.28	306.65	1331.26	46.40	108.36	147.40	97.22	20.89
BHVO2-1	5.40	1.05	0.84	1308.97	37.60	388.49	321.80	1365.96	45.60	123.63	130.63	109.56	25.27
BHVO2-7	4.13	0.81	-	1307.61	33.08	336.94	270.19	1317.11	43.43	117.07	118.05	105.78	23.40
Average	**4.84**	**1.06**	**0.94**	**1392.67**	**35.80**	**363.85**	**309.00**	**1340.40**	**44.83**	**115.30**	**134.44**	**104.87**	**22.40**
STDEV	0.37	0.15	0.39	104.28	1.43	15.75	21.22	32.14	1.81	5.44	12.39	10.07	2.15
2SE	0.27	0.11	0.28	74.67	1.02	11.28	15.19	23.02	1.30	3.90	8.87	7.21	1.54
Accepted	**4.80**	**1.14**		**1266.50**	**32.00**	**317.00**	280.00	1315.90	45.00	119.00	127.00	103.00	22.00
% Difference	0.81	-6.84		9.96	11.87	14.78	10.36	1.86	-0.38	-3.11	5.86	1.82	1.82
TASBAS													
TASBAS3	11.64	2.52	2.20	4466.18	17.14	191.95	201.61	1396.86	55.68	145.61	53.44	117.20	29.25
TASBAS2	7.68	1.74	0.89	3837.38	14.75	158.19	170.28	1243.43	50.41	140.64	46.95	113.98	26.60
TASBAS4	9.88	2.31	2.15	4577.80	15.00	157.57	190.02	1197.08	48.74	110.87	54.96	112.56	26.01
TASBAS1	10.13	2.23	-	3691.09	13.94	149.37	173.60	1188.79	47.49	127.87	42.97	117.35	27.56
TASBAS4	11.50	2.49	-	4080.16	15.79	167.20	192.27	1332.80	48.42	144.59	46.44	118.37	28.05
Average	**10.17**	**2.26**	**1.74**	**4130.52**	**15.32**	**164.86**	**185.56**	**1271.79**	**50.15**	**133.92**	**48.95**	**115.89**	**27.49**
STDEV	1.60	0.31	0.74	385.45	1.21	16.41	13.22	90.33	3.27	14.70	5.06	2.49	1.27
2SE	1.44	0.28	0.67	347.35	1.09	14.79	11.91	81.40	2.94	13.24	4.56	2.24	1.14
Accepted				**4058.71**	**13.70**	**146.50**	**182.50**	**1315.90**		**147.60**			
% Difference				1.77	11.84	12.53	1.67	-3.35		-9.27			

Table A1-B: In/Re-corrected trace element abundances (Ge-Cs) measured by S-ICP-MS in the rock standards used for normalisation. All abundances in ppm.

Corrected With	In/Re	In	In	In	In	In	In	In/Re	In	Re	In	In	In
Sample	**Ge**	**As**	**Rb**	**Sr**	**Y**	**Zr**	**Nb**	**Mo**	**Ag**	**Cd**	**Sn**	**Sb**	**Cs**
GSP-2													
GSP1:4	17.06	9.88	287.31	278.84	26.98	165.43	29.36	2.32	0.15	0.14	6.41	0.40	1.25
GSP0.5:4.5	17.50	10.30	268.99	281.28	26.98	166.03	28.79	2.34	0.15	0.14	6.51	0.38	1.28
GSP0.25:4.75	18.03	10.25	268.65	262.70	26.90	158.44	28.58	2.28	0.15	0.14	6.22	0.35	1.27
GSP2-2	16.62	9.93	300.64	298.04	27.24	205.46	26.49	2.02	0.17	0.13	6.15	0.35	1.35
GSP2-4	15.85	9.52	277.67	288.33	26.52	232.40	27.29	2.21	0.14	0.14	6.40	0.34	1.38
GSP2-1	17.28	9.38	301.73	288.62	26.94	166.58	27.52	2.26	0.16	0.15	6.34	0.55	1.25
Average	**17.06**	**9.88**	**284.17**	**282.97**	**26.93**	**182.39**	**28.01**	**2.24**	**0.15**	**0.14**	**6.34**	**0.39**	**1.29**
STDEV	0.75	0.37	14.85	11.99	0.23	29.71	1.08	0.11	0.01	0.01	0.13	0.08	0.05
2SE	0.60	0.29	11.78	9.51	0.18	23.57	0.86	0.09	0.01	0.01	0.10	0.06	0.04
Accepted			**234.94**	**233.18**	**25.62**	**554.36**	**25.84**	**3.05**		**0.20**	**3.00**	**0.27**	**1.21**
% Difference			20.95	21.35	5.11	-67.10	8.38	-26.61		-31.82	111.30	45.98	6.63
BCR-2													
BCR2-4	6.21	1.70	51.79	387.78	36.06	202.27	13.13	267.61	0.13	0.45	2.12	0.28	1.20
BCR2-5	6.21	1.83	53.42	400.98	36.61	203.52	13.18	339.74	0.12	0.49	2.13	0.31	1.25
BCR2-7	6.05	1.56	52.79	405.01	35.53	199.58	11.70	225.29	0.13	0.41	2.07	0.23	1.30
BCR2-2	4.95	1.50	44.09	333.38	33.35	196.64	11.38	243.08	0.08	0.42	1.69	0.23	0.99
BCR2-3	5.95	1.87	48.32	365.11	35.08	190.48	11.64	244.02	0.08	0.45	1.89	0.34	1.06
BCR2-6	6.21	1.50	50.30	385.72	32.48	194.67	10.94	223.45	0.08	0.45	1.75	0.23	1.16
BCR2-1	6.19	1.60	50.97	393.97	36.02	190.38	12.20	262.24	0.14	0.41	2.06	0.33	1.22
BCR2-2(2)	6.01	1.35	50.17	398.43	35.24	189.57	11.24	289.39	0.13	0.40	2.12	0.24	1.22
Average	**5.97**	**1.62**	**50.23**	**383.80**	**35.05**	**195.89**	**11.93**	**261.85**	**0.11**	**0.44**	**1.98**	**0.27**	**1.18**
STDEV	0.43	0.18	2.95	23.83	1.42	5.53	0.84	38.43	0.03	0.03	0.18	0.05	0.10
2SE	0.28	0.12	1.94	15.66	0.93	3.64	0.55	25.27	0.02	0.02	0.12	0.03	0.07
Accepted			**46.90**	**340.00**	**37.00**	**184.00**	**12.60**	**250.00**		**0.75**			**1.10**
% Difference			7.10	12.88	-5.28	6.46	-5.34	4.74		-41.87			6.86
BHVO-2													

BHVO2-5	6.08	1.50	10.27	451.12	25.88	182.82	19.61	3.85	0.12	0.14	1.67	0.09	0.10
BHVO2-6	6.04	1.62	8.92	396.15	24.13	161.84	18.87	3.91	0.09	0.12	1.44	0.07	0.09
BHVO2-4 .25	6.08	1.71	9.37	433.42	23.84	160.12	16.91	3.17	0.08	0.13	1.70	0.08	0.09
BHVO2-4 .5	6.11	1.66	9.35	435.61	23.81	174.35	17.14	3.25	0.09	0.13	1.57	0.09	0.09
BHVO2-4 1	6.16	1.68	9.48	431.17	23.76	170.11	17.32	3.29	0.09	0.11	1.57	0.10	0.09
BHVO2-1	6.24	1.25	9.97	456.05	25.64	177.32	19.01	3.81	0.13	0.13	1.59	0.12	0.10
BHVO2-7	6.10	1.34	9.91	461.36	24.94	169.02	17.99	3.64	0.13	0.15	1.40	0.08	0.11
Average	**6.12**	**1.54**	**9.61**	**437.84**	**24.57**	**170.80**	**18.12**	**3.56**	**0.10**	**0.13**	**1.56**	**0.09**	**0.10**
STDEV	0.07	0.18	0.46	21.86	0.91	8.14	1.05	0.32	0.02	0.01	0.11	0.01	0.01
2SE	0.05	0.13	0.33	15.66	0.65	5.83	0.75	0.23	0.02	0.01	0.08	0.01	0.01
Accepted	**1.60**		**9.11**	**396.00**	**26.00**	**172.00**	**18.10**	**4.00**		**0.06**	**1.70**	**2.06**	**0.13**
% Difference	282.24		5.48	10.57	-5.49	-0.70	0.12	-11.04		113.22	-8.04	-95.55	-26.35
TASBAS													
TASBAS3	6.95	3.87	18.41	1208.09	21.13	284.04	67.64	7.53	0.16	0.16	2.58	0.10	1.14
TASBAS2	6.76	3.39	17.91	1184.78	20.28	273.65	64.78	6.95	0.16	0.15	2.40	0.08	1.13
TASBAS4	7.46	3.51	16.89	1140.34	20.91	277.85	65.53	8.24	0.15	0.11	2.08	0.08	1.03
TASBAS1	6.49	3.72	16.79	1149.47	19.70	281.11	65.49	7.92	0.15	0.15	2.55	0.09	1.09
TASBAS4	6.60	3.73	17.25	1181.62	20.33	287.06	67.84	8.21	0.16	0.15	2.58	0.10	1.15
Average	**6.85**	**3.64**	**17.45**	**1172.86**	**20.47**	**280.74**	**66.26**	**7.77**	**0.16**	**0.14**	**2.44**	**0.09**	**1.11**
STDEV	0.38	0.19	0.69	27.68	0.56	5.24	1.39	0.54	0.01	0.02	0.21	0.01	0.05
2SE	0.35	0.17	0.62	24.94	0.51	4.72	1.25	0.49	0.01	0.02	0.19	0.01	0.04
Accepted			**16.00**	**1006.50**	**21.10**	**256.90**	**54.65**						
% Difference			9.06	16.53	-2.98	9.28	21.24						

Table A1-C: In/Re-corrected trace element abundances (Ba-Yb) measured by S-ICP-MS in the rock standards used for normalisation. All abundances in ppm.

Sample	In Ba	In La	In Ce	In Pr	In Nd	In Sm	In Eu	In Gd	In Tb	In Dy	In Ho	In Er	In Yb
GSP-2													
GSP1:4	1599.05	205.47	479.34	61.77	230.50	27.05	2.48	14.93	1.53	6.04	1.00	2.62	1.53
GSP0.5:4.5	1629.57	209.62	483.23	63.69	230.59	27.19	2.50	14.94	1.52	6.03	1.00	2.63	1.54
GSP0.25:4.75	1683.14	214.13	485.32	59.20	214.79	27.19	2.47	14.84	1.52	5.99	0.99	2.61	1.53
GSP2-2	1675.45	209.89	481.20	63.36	231.92	26.74	2.45	14.88	1.47	5.84	0.95	2.46	1.42
GSP2-4	1736.69	216.15	481.80	64.37	212.95	26.97	2.46	14.71	1.48	5.67	0.96	2.51	1.53
GSP2-1	1758.57	201.76	475.84	61.65	230.35	26.21	2.41	14.50	1.48	5.78	0.95	2.47	1.43
Average	**1680.41**	**209.50**	**481.12**	**62.34**	**225.18**	**26.89**	**2.46**	**14.80**	**1.50**	**5.89**	**0.98**	**2.55**	**1.50**
STDEV	60.85	5.33	3.27	1.88	8.80	0.37	0.03	0.17	0.02	0.15	0.03	0.08	0.06
2SE	48.27	4.23	2.60	1.49	6.98	0.30	0.02	0.13	0.02	0.12	0.02	0.06	0.04
Accepted	**1316.46**	**184.17**	**437.92**	**53.72**	**211.00**	**26.53**	**2.25**	**12.41**	**1.33**	**5.86**	**1.02**	**2.33**	**1.69**
% Difference	27.65	13.76	9.86	16.05	6.72	1.35	9.29	19.25	12.92	0.50	-4.14	9.37	-11.24
BCR-2													
BCR2-4	802.08	28.61	57.75	7.09	29.07	6.63	2.05	6.79	1.08	6.33	1.31	3.70	3.39
BCR2-5	828.02	29.06	58.28	7.14	29.17	6.64	2.08	6.73	1.07	6.26	1.28	3.65	3.27
BCR2-7	860.58	26.95	58.27	7.18	29.09	6.66	2.07	6.63	1.06	6.25	1.28	3.55	3.28
BCR2-2	685.14	23.30	47.65	6.67	26.06	6.10	1.89	6.27	0.98	5.90	1.20	3.43	3.08
BCR2-3	708.84	23.90	47.55	7.30	28.87	6.57	2.03	6.67	1.03	6.21	1.23	3.54	3.14
BCR2-6	755.99	24.80	47.70	6.79	32.06	7.29	2.24	6.94	1.11	6.67	1.32	3.76	3.29
BCR2-1	747.98	27.84	57.20	6.79	28.28	6.56	2.04	6.67	1.08	6.34	1.30	3.67	3.41
BCR2-2(2)	780.31	28.70	58.55	6.96	29.10	6.70	2.09	6.84	1.11	6.54	1.35	3.83	3.53
Average	**771.12**	**26.65**	**54.12**	**6.99**	**28.96**	**6.64**	**2.06**	**6.69**	**1.07**	**6.31**	**1.28**	**3.64**	**3.30**
STDEV	58.94	2.32	5.38	0.22	1.63	0.32	0.10	0.20	0.04	0.23	0.05	0.13	0.14
2SE	38.75	1.52	3.54	0.15	1.07	0.21	0.06	0.13	0.03	0.15	0.03	0.09	0.09
Accepted	**677.00**	**24.90**	**52.90**	**6.70**	**28.70**	**6.58**	**1.96**	**6.75**	**1.07**	**6.41**	**1.28**	**3.66**	**3.38**
% Difference	13.90	7.02	2.30	4.34	0.91	0.97	5.11	-0.89	-0.43	-1.52	0.24	-0.55	-2.41
BHVO-2													
BHVO2-5	145.41	17.47	40.93	5.56	24.67	5.99	2.12	6.12	0.94	5.18	0.96	2.50	1.93
BHVO2-6	138.04	16.59	38.65	5.15	22.56	5.62	1.96	5.75	0.86	4.78	0.88	2.31	1.78
BHVO2-4 .25	126.18	16.70	39.99	5.51	24.09	5.95	2.06	5.99	0.89	5.14	0.93	2.44	1.79
BHVO2-4 .5	126.15	16.68	43.69	5.54	23.97	5.89	2.05	6.07	0.91	5.06	0.92	2.41	1.82
BHVO2-4 1	126.67	16.87	44.14	5.62	24.35	6.03	2.07	6.02	0.91	5.11	0.93	2.43	1.86
BHVO2-1	153.34	17.18	41.07	5.31	24.12	6.01	2.08	6.02	0.93	5.11	0.97	2.49	1.98
BHVO2-7	159.18	15.20	41.30	5.32	24.17	5.99	2.11	6.00	0.95	5.20	1.00	2.52	2.04
Average	**139.28**	**16.67**	**41.40**	**5.43**	**23.99**	**5.93**	**2.06**	**6.00**	**0.91**	**5.08**	**0.94**	**2.44**	**1.89**
STDEV	13.76	0.72	1.94	0.17	0.67	0.14	0.05	0.12	0.03	0.14	0.04	0.07	0.10

2SE	9.85	0.52	1.39	0.12	0.48	0.10	0.04	0.08	0.02	0.10	0.03	0.05	0.07
Accepted	131.00	15.20	37.50	5.35	24.50	6.07	2.07	6.24	0.92	5.31	0.98	2.54	2.00
% Difference	6.32	9.67	10.39	1.52	-2.09	-2.37	-0.26	-3.91	-0.99	-4.31	-3.88	-3.77	-5.72
TASBAS													
TASBAS3	217.16	42.94	80.57	10.25	38.99	7.73	2.49	6.67	0.90	4.48	0.75	1.82	1.26
TASBAS2	218.77	43.38	81.25	10.21	38.83	7.70	2.45	6.56	1.01	4.43	0.74	1.81	1.24
TASBAS4	215.85	42.01	81.75	10.09	38.02	7.73	2.55	6.83	0.95	4.65	0.75	1.82	1.22
TASBAS1	202.74	42.97	83.26	10.47	37.05	7.79	2.52	6.81	0.92	4.42	0.76	1.81	1.27
TASBAS4	208.75	43.58	83.86	10.05	38.59	7.77	2.48	6.68	0.92	4.42	0.75	1.81	1.25
Average	**212.65**	**42.98**	**82.14**	**10.22**	**38.30**	**7.75**	**2.50**	**6.71**	**0.94**	**4.48**	**0.75**	**1.82**	**1.25**
STDEV	6.74	0.60	1.38	0.16	0.79	0.04	0.04	0.11	0.04	0.10	0.01	0.01	0.02
2SE	6.07	0.54	1.24	0.15	0.71	0.03	0.03	0.10	0.04	0.09	0.01	0.01	0.02
Accepted	**188.85**	**40.43**	**79.34**	**9.51**	**37.67**	**7.55**	**2.41**	**6.54**	**0.92**	**4.45**	**0.76**	**1.73**	**1.26**
% Difference	12.60	6.30	3.53	7.42	1.67	2.59	3.71	2.60	2.21	0.71	-0.92	4.95	-0.87

Table A1-D: In/Re-corrected trace element abundances (Lu-U) measured by S-ICP-MS in the rock standards used for normalisation. All abundances in ppm.

	In	Re	Re	Re	Re	Re	Re	Re
Sample	**Lu**	**Hf**	**Ta**	**W**	**Tl**	**^{208}Pb**	**Th**	**U**
GSP-2								
GSP1:4	0.20	4.03	1.03	0.42	1.23	40.13	111.70	2.32
GSP0.5:4.5	0.21	3.92	1.01	0.40	1.25	38.92	112.42	2.30
GSP0.25:4.75	0.20	3.91	1.00	0.43	1.23	39.42	116.73	2.33
GSP2-2	0.21	4.53	0.86	0.33	1.22	40.45	112.78	2.24
GSP2-4	0.21	5.28	1.04	0.45	1.24	37.99	114.60	2.36
GSP2-1	0.20	4.07	0.97	0.36	1.24	42.16	117.30	2.29
Average	**0.20**	**4.29**	**0.98**	**0.40**	**1.23**	**39.84**	**114.25**	**2.31**
STDEV	0.00	0.54	0.07	0.05	0.01	1.43	2.35	0.04
2SE	0.00	0.43	0.05	0.04	0.01	1.14	1.86	0.03
Accepted	**0.24**	**14.78**	**0.86**	**0.33**	**1.10**	**41.98**	**108.52**	**2.38**
% Difference	-15.38	-70.99	14.62	20.86	12.23	-5.08	5.29	-3.03
BCR-2								
BCR2-4	0.50	5.03	0.94	0.54	0.25	9.02	5.78	1.67
BCR2-5	0.50	5.24	0.95	0.58	0.25	9.35	5.95	1.69
BCR2-7	0.50	5.08	1.08	0.36	0.23	9.03	5.93	1.67
BCR2-2	0.46	4.47	0.75	0.48	0.22	8.38	5.57	1.46
BCR2-3	0.47	4.47	0.70	0.47	0.21	8.52	5.54	1.46
BCR2-6	0.51	4.63	0.71	0.46	0.21	8.08	5.09	1.40
BCR2-1	0.51	4.88	0.77	0.59	0.25	9.71	5.98	1.71

BCR2-2(2)	0.53	5.17	0.81	0.65	0.25	9.24	6.24	1.77
Average	**0.50**	**4.87**	**0.84**	**0.52**	**0.23**	**8.92**	**5.76**	**1.61**
STDEV	0.02	0.31	0.14	0.09	0.02	0.54	0.35	0.14
2SE	0.02	0.20	0.09	0.06	0.01	0.36	0.23	0.09
Accepted	**0.50**	**4.90**	**0.74**			**11.00**	**5.70**	**1.69**
% Difference	-0.72	-0.57	13.23			-18.94	1.07	-4.99
BHVO-2								
BHVO2-5	0.27	4.48	1.24	0.30	0.02	1.39	1.17	0.41
BHVO2-6	0.25	3.88	1.09	0.20	0.02	1.17	1.01	0.36
BHVO2-4 .25	0.26	4.03	1.26	0.36	0.00	1.25	1.01	0.35
BHVO2-4 .5	0.27	3.99	1.28	0.26	0.01	1.27	0.99	0.35
BHVO2-4 1	0.26	3.98	1.29	0.23	0.01	1.30	1.02	0.34
BHVO2-1	0.28	4.35	1.28	0.19	0.02	1.60	1.19	0.42
BHVO2-7	0.28	4.38	1.26	0.23	0.01	1.31	1.24	0.43
Average	**0.27**	**4.16**	**1.24**	**0.25**	**0.01**	**1.33**	**1.09**	**0.38**
STDEV	0.01	0.24	0.07	0.06	0.01	0.14	0.10	0.04
2SE	0.01	0.17	0.05	0.04	0.00	0.10	0.07	0.03
Accepted	0.27	4.36	1.14	0.21		1.60	1.22	0.40
% Difference	-2.99	-4.68	9.04	20.95		-16.96	-10.73	-5.78
TASBAS								
TASBAS3	0.18	5.77	3.71	56.78	0.07	4.40	4.58	1.84
TASBAS2	0.18	5.71	3.58	53.25	0.06	4.49	4.65	1.85
TASBAS4	0.18	5.79	3.79	48.91	0.05	4.65	4.86	1.88
TASBAS1	0.18	5.50	3.50	53.48	0.06	4.67	4.62	1.84
TASBAS4	0.18	5.94	3.58	60.11	0.07	4.83	4.79	1.94
Average	**0.18**	**5.74**	**3.63**	**54.51**	**0.06**	**4.61**	**4.70**	**1.87**
STDEV	0.00	0.16	0.12	4.20	0.01	0.17	0.12	0.04
2SE	0.00	0.14	0.10	3.78	0.01	0.15	0.11	0.04
Accepted	**0.18**	**5.51**				**4.64**	**4.82**	**1.91**
% Difference	0.57	4.26				-0.69	-2.40	-2.05

Table A2: Sample Locations (decimal degrees, GDA94)

Sample Name	Latitude	Longitude
PS1	Mt Wellington Summit	
PS2	Mt Wellington Summit	
PS3	-43.0737	147.23584
PS4	-43.0783	147.23563
PS5	-43.074	147.23535
PS6	-43.0757	147.23035
PS7	-43.0791	147.22690
PS8	50m above PS7	
PS9	-43.0798	147.22534
PS10	-43.0806	147.22520
PS11	-43.0796	147.23096
PS12	-43.0796	147.23096
PS13	-43.0796	147.23096
PS14	-43.0792	147.25111
PS15	-43.0789	147.23122
PS16	-43.0789	147.23131
PS17	-43.0785	147.23141
PS18	-43.0784	147.23141
PS19	-43.0745	147.23436
PS20	-43.0968	147.29578
PS21*	-43.0968	147.29578
PS22	-42.9801	147.24283
PS23	-42.9801	147.24283
PS24	-42.9801	147.24283
PS25	-42.9801	147.24283
PS26	Furthest up NW river (200 N of PS27)	
PS27*	-42.9604	147.20485
PS28	-42.9614	147.20485
PS29	-43.0706	147.23970
PS30*	-43.0713	147.24039
PS31*	-43.071	147.24025
PS32	-43.0715	147.23988
PS33	-43.0715	147.23988
PS34	-43.0709	147.23875
PS35	-43.074	147.22923
PS36*	-43.0722	147.22159
PS37	-43.0633	147.22473
PS38	-43.0633	147.22473
PS39	-43.0633	147.22473
PS40	-43.0633	147.22473
PS41	100m N of 42	
PS42	-43.0685	147.22566

PS43	100m N of 42	
PS44	-43.0698	147.22545
PS45	-43.0705	147.24362
PS46	-43.0705	147.24362
PS47	-43.0917	147.27357
PS48	-43.0915	147.26985
PS49	-43.0828	147.24129
PS50	-43.0842	147.24161
PS51	-43.0839	147.24265
PS52	-43.0503	147.23392
PS53	-43.0556	147.22673
PS54, PS54X	-43.0582	147.22153
PS55	-43.0589	147.21783
PS56*	-43.0608	147.21683
PS57	-43.0465	147.23576
PS58*	-43.0484	147.23087
PS59*	-43.0539	147.20958
PS60*	-43.054	147.20914
PS61	-43.0533	147.21696
PS62*	-43.0292	147.24236
PS63	-43.012	147.24362
PS64	-43.0269	147.24161
PS65*	-43.0318	147.21936
PS67	-43.0193	147.22020
PS68	-43.0226	147.22392
PS69*	-42.9927	147.21280
PS70	-42.9718	147.21140
PS71	-42.9718	147.21155
PS72	-42.9724	147.21150
PS73	-42.9725	147.21150
PS74	-42.9724	147.21150
PS75	-42.9725	147.21150
PS76*	-43.0027	147.17189
PS77*	-43.0426	147.11726
KI09 Q	-35.67175	137.516724
KI09 SF	-35.67175	137.516724
KIW1-2	-35.63685	137.488711
KIW2-1	-35.62995	137.479816
KIW4-1	-35.61674	137.450063
KIW4-SF	-35.62982	137.457152
KIW5-1	-35.64554	137.641523
KIW6-NF	-35.67175	137.516724

Table A3: XRF Major Element Data

Sample Name	SiO_2 %	Al_2O_3 %	$Fe_2O_3^T$ %	MnO %	MgO %	CaO %	Na_2O %	K_2O %	TiO_2 %	P_2O_5 %	SO_3 %	LOI %	Total %	Classi-fication
PS27	53.59	14.38	9.89	0.17	6.77	10.68	1.74	0.84	0.63	0.11	0.02	0.42	99.23	CM
PS30	53.91	14.54	9.97	0.17	6.73	10.81	1.87	0.86	0.64	0.11	0.02	0.17	99.79	CM
PS31	54.03	14.46	9.90	0.17	6.75	10.67	1.92	0.91	0.64	0.11	0.02	0.10	99.66	CM
PS36	53.68	14.52	9.96	0.17	6.70	10.34	2.00	1.12	0.63	0.11	0.02	0.23	99.49	CM
PS58	53.65	14.69	9.89	0.16	6.61	10.97	1.81	0.67	0.63	0.11	0.02	0.64	99.86	CM
PS59	54.03	14.61	10.01	0.17	6.51	10.80	1.78	0.80	0.66	0.12	0.02	0.24	99.73	CM
PS60	53.92	14.65	10.02	0.17	6.75	10.77	1.81	0.78	0.64	0.11	0.02	0.19	99.83	CM
PS62	53.85	14.75	9.85	0.17	6.52	10.86	1.97	0.85	0.63	0.11	0.01	0.55	100.12	CM
PS65	54.17	14.63	9.96	0.17	6.77	10.79	1.84	0.84	0.64	0.11	0.02	0.00	99.93	CM
PS69	53.75	14.90	9.68	0.17	7.03	11.30	1.72	0.79	0.59	0.11	0.02	0.19	100.24	CM
PS77	53.77	14.71	9.74	0.17	6.65	10.85	1.81	0.84	0.62	0.11	0.03	0.76	100.05	CM
PS21	54.63	14.41	10.20	0.17	6.29	10.22	2.04	0.91	0.66	0.12	0.02	0.32	99.99	Dol
PS25	53.62	14.53	10.96	0.18	6.65	11.12	1.76	0.73	0.59	0.09	0.02	0.26	100.50	Dol
PS26	53.45	15.21	9.84	0.17	6.39	11.30	1.71	0.79	0.59	0.11	0.02	0.62	100.19	Dol
PS28	53.24	14.71	9.72	0.17	6.92	11.23	1.68	0.65	0.59	0.11	0.01	0.55	99.57	Dol
PS29	53.25	15.83	9.14	0.16	6.45	11.22	1.79	0.83	0.63	0.11	0.01	0.46	99.88	Dol
PS32	53.13	15.00	9.06	0.16	7.72	11.98	1.57	0.63	0.51	0.10	0.02	0.12	99.97	Dol
PS47	54.28	14.49	10.49	0.17	5.69	10.18	2.00	0.92	0.71	0.12	0.02	0.89	99.95	Dol
PS48	54.10	13.92	10.13	0.17	7.26	10.56	1.77	0.80	0.61	0.11	0.02	0.37	99.81	Dol
PS64	52.98	14.99	9.22	0.16	7.23	12.28	1.66	0.57	0.52	0.09	0.02	0.13	99.85	Dol
PS68	54.03	15.93	10.42	0.17	4.55	10.16	2.11	0.97	0.70	0.13	0.03	0.89	100.08	Dol
PS73	53.94	15.14	9.60	0.16	6.30	11.03	1.97	0.88	0.64	0.11	0.02	0.35	100.15	Dol
PS76	55.15	14.19	10.70	0.17	5.43	9.48	2.25	1.09	0.76	0.13	0.02	0.80	100.17	Dol
PS8	53.59	16.33	9.86	0.16	5.15	10.92	1.95	0.84	0.65	0.11	0.01	0.62	100.20	Dol
PS44	56.62	15.21	12.30	0.15	1.61	7.05	2.64	1.63	1.38	0.17	0.01	1.38	100.15	Fay Gran
PS51	55.92	15.32	11.94	0.16	2.35	8.08	2.59	1.41	1.15	0.16	0.02	0.95	100.05	Fay Gran
PS61	56.00	15.71	11.15	0.16	2.54	8.32	2.65	1.41	0.95	0.16	0.02	0.79	99.86	Fay Gran
PS11	60.36	13.62	11.05	0.15	0.85	5.57	2.77	2.16	1.04	0.26	0.02	1.70	99.54	Fay Gran
PS42	59.32	12.97	13.02	0.17	0.96	5.55	2.71	2.08	1.27	0.34	0.01	1.14	99.55	Fay Gran
PS53	59.18	15.30	10.15	0.13	0.89	6.66	2.83	1.89	1.03	0.21	0.03	1.47	99.76	Fay Gran
PS54	62.31	13.15	13.02	0.14	0.60	5.05	2.91	2.40	0.93	0.26	0.03	1.56	99.57	Fay Gran
PS13	65.90	11.01	10.01	0.23	0.28	2.78	2.97	2.97	0.93	0.22	0.01	1.85	99.18	Gran
PS14	64.32	11.81	10.02	0.14	0.47	3.84	2.84	2.77	0.91	0.23	0.02	2.06	99.41	Gran
PS15	66.17	12.15	8.83	0.12	0.38	3.14	3.08	2.80	0.93	0.24	0.01	1.60	99.44	Gran
PS17	64.54	12.19	10.24	0.14	0.45	3.75	2.96	2.63	0.97	0.26	0.01	1.46	99.59	Gran
PS18	65.13	11.84	9.84	0.13	0.44	3.84	2.90	2.70	0.90	0.23	0.01	1.62	99.58	Gran
PS37	62.92	10.82	13.13	0.16	0.59	3.99	2.69	2.85	1.22	0.38	0.01	0.78	99.52	Gran
PS38	62.54	10.84	12.84	0.16	0.62	3.99	2.61	2.64	1.15	0.35	0.01	1.39	99.12	Gran
PS39	62.64	11.01	13.03	0.17	0.71	4.69	2.52	2.68	1.27	0.32	0.01	1.50	100.53	Gran
PS67	64.10	11.29	11.54	0.15	0.60	3.80	2.76	2.73	1.07	0.28	0.04	1.42	99.77	Gran
KI09 Q	54.01	14.62	9.93	0.18	7.21	10.84	1.78	0.67	0.62	0.11	0.02	0.07	100.06	KI Basalt

KI09 SF	54.28	14.49	8.90	0.16	7.88	10.78	1.68	0.60	0.61	0.11	0.02	0.52	100.02	KI Basalt
KIW1-2	54.85	14.52	9.13	0.16	7.07	10.67	1.85	0.69	0.65	0.11	0.02	0.49	100.19	KI Basalt
KIW2-1	54.95	14.81	8.60	0.16	7.34	10.72	1.78	0.74	0.62	0.11	0.02	0.24	100.08	KI Basalt
KIW4-1	54.28	15.19	9.46	0.17	6.62	11.03	1.91	0.62	0.64	0.12	0.02	0.15	100.20	KI Basalt
KIW4-SF	55.75	14.74	10.16	0.16	7.15	10.36	1.89	0.86	0.65	0.11	0.01	0.38	102.22	KI Basalt
KIW5-1	53.89	14.52	10.43	0.18	6.86	10.69	1.83	0.73	0.65	0.11	0.03	0.12	100.05	KI Basalt
KIW6-NF	54.21	14.42	10.13	0.18	7.39	10.80	1.80	0.68	0.62	0.11	0.02	0.03	100.38	KI Basalt
PS24	56.66	13.68	10.82	0.17	4.52	8.77	2.09	1.60	1.00	0.16	0.02	0.91	100.38	Pegmatite
PS74	55.56	13.71	10.62	0.18	5.99	9.61	2.05	1.09	0.74	0.13	0.01	0.46	100.13	Pegmatite
PS70	59.58	11.21	13.26	0.16	1.17	4.86	2.47	2.33	1.47	0.31	0.03	1.14	97.98	Pegmatite
PS70-t	60.74	11.44	13.54	0.17	1.17	4.96	2.52	2.37	1.50	0.31	0.03	1.21	99.96	Pegmatite
PS71	57.90	12.68	13.13	0.18	2.82	7.05	2.46	1.73	1.12	0.18	0.02	0.74	99.98	Pegmatite
PS63	59.65	11.91	13.42	0.17	1.83	5.50	2.63	2.04	1.37	0.22	0.02	1.05	99.79	Pegmatite
PS1	56.23	15.38	11.64	0.16	1.86	7.82	2.66	1.54	1.13	0.17	0.03	1.27	99.88	Qtz Dol
PS19	54.92	16.42	11.54	0.17	2.81	9.14	2.47	1.16	0.95	0.14	0.02	0.79	100.52	Qtz Dol
PS5	54.71	15.83	12.12	0.17	2.68	8.96	2.47	1.19	1.11	0.15	0.02	0.74	100.16	Qtz Dol
PS50	56.13	15.67	11.70	0.16	2.08	8.06	2.59	1.47	1.12	0.16	0.03	1.00	100.16	Qtz Dol
PS52	54.65	15.98	10.68	0.16	3.50	9.57	2.27	1.12	0.83	0.14	0.02	0.84	99.76	Qtz Dol
PS57	54.71	16.94	10.03	0.16	4.55	10.65	2.15	0.94	0.66	0.12	0.02	0.65	101.58	Qtz Dol
PS6	55.10	17.60	10.24	0.14	2.33	9.08	2.63	1.19	0.92	0.14	0.02	0.99	100.37	Qtz Dol
PS75	54.58	15.66	10.82	0.17	4.29	9.92	2.26	1.02	0.78	0.13	0.01	0.70	100.33	Qtz Dol
PS34	54.11	15.83	10.39	0.16	4.68	10.33	2.08	1.00	0.72	0.12	0.01	0.60	100.03	Qtz Dol
PS35	53.39	17.51	9.70	0.15	3.61	10.52	2.20	0.96	0.70	0.12	0.02	0.83	99.70	Qtz Dol
PS3D	54.18	14.60	13.40	0.19	3.22	8.72	2.37	1.17	1.16	0.15	0.03	0.67	99.86	Qtz Dol
PS3L	58.43	19.14	6.38	0.09	1.05	7.76	3.09	1.75	0.50	0.16	0.02	1.61	99.98	Qtz Dol
PS9	53.82	18.74	8.09	0.13	3.87	10.88	2.07	0.93	0.68	0.13	0.02	0.75	100.09	Qtz Dol

Table A4-A: Trace Element Concentrations (Be-Y) of whole rocks measured by S-ICP-MS. All abundances in ppm.

Sample	Classification	Be	P	Sc	V	Cr	Mn	Co	Ni	Cu	Zn	Ga	Ge	Rb	Sr	Y
PS27	CM	0.68	388.65	20.86	243.24	123.85	1313.98	58.73	74.38	81.35	75.87	21.43	1.21	36.88	141.10	22.59
PS30	CM	0.80	389.03	41.48	244.38	113.17	1310.56	73.62	79.12	76.70	75.23	15.40	1.28	33.90	133.16	22.81
PS31	CM	0.82	391.96	41.71	247.07	119.52	1310.52	54.93	79.14	78.71	75.56	15.55	1.28	33.28	148.62	22.32
PS36	CM	0.68	370.71	26.55	237.90	115.17	1312.61	53.12	71.84	75.00	74.31	19.75	1.13	49.56	173.11	21.13
PS58	CM	0.75	384.94	41.55	247.30	104.45	1262.40	73.85	76.47	75.80	73.89	15.56	1.26	25.25	131.08	21.56
PS59	CM	0.68	375.46	19.40	233.38	99.26	1264.94	60.24	68.39	80.38	75.51	17.46	1.16	30.98	126.81	21.72
PS60	CM	0.69	368.84	23.77	233.21	113.81	1262.82	70.55	77.98	79.56	77.48	17.07	1.14	30.54	127.34	22.78
PS62	CM	0.61	363.05	18.92	224.32	94.65	1204.23	53.83	64.06	76.60	69.45	16.79	1.13	35.88	131.67	20.99
PS65	CM	0.69	371.40	20.08	237.61	118.49	1253.13	60.35	78.23	77.57	73.57	17.70	1.15	34.88	131.34	22.92
PS69	CM	0.76	352.64	41.53	246.56	122.04	1255.69	58.35	83.02	70.79	71.24	15.17	1.26	29.27	128.88	22.88
PS77	CM	0.66	363.80	28.20	233.37	104.16	1232.10	61.10	76.18	74.08	71.62	18.24	1.13	33.62	137.33	22.29
PS21	Dol	0.57	321.69	27.06	203.83	69.76	1041.96	55.34	54.47	63.94	66.68	17.33	0.99	24.46	119.56	18.90
PS25	Dol	0.85	291.89	42.03	241.70	104.80	1347.61	73.82	74.58	97.13	80.54	15.74	1.31	26.59	134.24	20.67
PS26	Dol	0.66	342.46	38.24	256.84	35.49	1296.65	68.28	74.36	68.15	71.11	15.67	1.02	31.06	117.37	21.88
PS28	Dol	0.82	365.61	41.85	245.11	116.58	1298.85	58.95	85.02	73.05	113.53	15.36	1.30	23.19	138.71	24.83
PS29	Dol	0.60	354.71	33.66	239.93	74.12	1217.42	60.06	81.17	59.76	67.87	15.59	1.00	35.72	132.85	20.62
PS32	Dol	0.60	291.83	42.52	245.58	138.89	1236.69	61.22	91.05	56.63	64.53	15.78	1.10	24.00	121.71	16.99
PS47	Dol	0.88	423.57	39.89	266.76	60.25	1308.14	115.11	68.78	84.97	148.05	16.65	1.10	36.26	131.39	24.87
PS48	Dol	0.69	375.29	43.92	249.65	128.16	1344.96	61.64	82.35	74.12	72.81	18.83	1.15	30.25	122.46	20.46
PS64	Dol	0.51	247.17	37.56	252.97	125.11	1169.86	67.50	86.40	62.48	282.62	14.28	0.96	20.71	118.15	19.02
PS68	Dol	0.92	475.48	39.69	231.58	15.17	1314.78	96.44	45.94	96.72	91.01	22.57	1.34	37.88	145.65	36.36
PS73	Dol	0.73	388.26	37.31	254.43	101.86	1254.21	69.52	78.27	73.38	75.38	16.27	1.06	36.94	126.94	23.15
PS76	Dol	0.76	451.68	17.25	231.86	43.19	1262.55	55.43	45.30	87.42	79.23	30.32	1.24	44.70	170.15	28.32
PS8	Dol	0.79	393.08	40.72	233.97	18.88	1250.85	65.21	50.95	84.99	74.31	20.29	1.29	33.24	147.04	21.93
PS44	Fay Gran	1.16	706.31	31.35	301.41	0.07	1121.13	49.96	8.31	109.76	105.86	19.78	1.35	63.78	158.55	36.79
PS51	Fay Gran	1.36	646.29	35.81	266.94	0.78	1199.06	55.19	14.11	148.41	110.24	19.64	1.54	52.70	174.84	34.48
PS61	Fay Gran	1.26	609.94	33.45	215.19	0.86	1172.78	54.11	17.10	125.99	96.42	19.07	1.42	54.61	171.47	32.57
PS11	Fay Gran	1.72	1135.41	22.86	24.15	0.00	1136.19	40.27	0.69	56.70	121.61	20.15	1.45	82.29	117.36	61.02
PS42	Fay Gran	1.59	1523.89	27.57	37.33	0.01	1285.37	49.39	0.96	58.17	136.42	19.86	1.56	80.98	113.82	54.80
PS53	Fay Gran	1.44	813.52	22.33	53.26	0.00	977.75	66.41	1.80	55.09	102.59	21.05	1.26	75.78	154.86	47.04
PS54	Fay Gran	1.78	1109.84	20.79	16.70	0.01	1111.88	37.63	0.60	48.28	134.79	20.30	1.45	97.31	115.10	62.56
PS13	Gran	2.30	1003.70	21.17	1.08	0.07	1890.70	36.75	0.13	35.17	162.48	20.23	1.67	116.82	116.98	84.10
PS14	Gran	2.29	1019.13	19.90	10.25	0.11	1034.98	46.52	0.33	40.34	126.38	18.99	1.69	105.56	109.35	63.02
PS15	Gran	2.36	1018.86	19.98	9.99	0.00	883.66	38.20	0.36	40.33	150.28	21.20	1.56	111.08	186.76	83.61
PS17	Gran	2.19	1213.17	22.49	11.79	0.00	1073.82	34.63	0.35	41.85	143.09	21.14	1.67	104.90	130.77	73.44
PS18	Gran	2.06	1021.01	19.64	12.78	0.00	1052.63	38.42	0.35	38.82	126.55	19.11	1.52	108.10	103.30	68.90
PS37	Gran	1.86	1687.16	22.96	4.96	0.01	1258.50	45.67	0.09	37.46	143.80	19.63	1.72	113.92	128.78	61.05
PS38	Gran	1.86	1527.07	21.64	5.68	0.00	1168.06	48.69	0.11	36.59	137.16	19.22	1.61	103.86	107.22	56.31
PS39	Gran	1.96	1274.04	20.64	9.23	0.00	1110.35	43.56	0.23	37.70	131.86	19.17	1.56	105.98	105.26	62.60
PS67	Gran	2.16	1191.10	23.42	14.06	0.51	1112.97	56.36	0.59	44.02	136.94	68.22	1.58	119.56	105.50	70.13
KI09 Q	KI Basalt	0.53	331.78	38.79	216.48	133.74	1288.98	63.37	67.56	68.89	65.83	15.12	1.11	24.21	137.03	20.69
KI09 SF	KI Basalt	0.50	313.39	39.51	220.09	174.48	1141.99	74.92	85.43	71.73	65.88	18.00	1.07	17.74	132.58	20.04
KIW1-2	KI Basalt	0.61	343.25	40.03	223.37	139.47	1194.10	70.08	70.06	58.81	68.46	18.31	1.12	31.38	131.00	27.66

KIW2-1	KI Basalt	0.48	305.32	35.42	197.91	133.33	1037.33	58.78	91.31	63.36	62.39	14.61	0.98	19.84	115.93	19.29
KIW4-1	KI Basalt	0.59	358.98	39.58	221.70	108.05	1260.05	56.31	64.92	75.60	68.42	18.17	1.16	27.77	135.57	21.12
KIW4-SF	KI Basalt	0.56	342.13	38.08	213.46	121.91	1066.51	57.99	64.29	72.33	66.21	15.76	1.09	33.28	129.96	19.28
KIW5-1	KI Basalt	0.59	361.67	40.38	227.43	120.32	1324.62	64.04	66.75	75.57	70.04	16.40	1.13	22.16	131.64	21.37
KIW6-NF	KI Basalt	0.54	331.93	37.14	218.54	141.02	1285.76	55.48	69.57	69.72	66.49	15.29	1.09	22.49	129.82	20.25
PS24	Pegmatite	1.03	645.94	42.08	255.86	10.46	1301.96	67.36	48.63	81.10	87.92	28.77	1.32	65.51	123.44	33.39
PS74	Pegmatite	0.82	464.62	43.60	249.83	16.97	1353.13	60.35	62.17	86.90	78.65	23.08	1.23	43.89	139.72	25.30
PS70	Pegmatite	1.91	1356.61	32.17	196.91	0.26	1223.24	68.46	3.11	90.93	131.04	19.82	1.83	90.87	116.27	56.85
PS70-t	Pegmatite	1.91	1356.61	32.17	196.91	0.26	1223.24	68.46	3.11	90.93	131.04	19.82	1.83	90.87	116.27	56.85
PS71	Pegmatite	1.61	733.47	40.78	242.39	0.29	1375.71	53.31	17.46	150.11	110.10	19.16	1.75	65.80	120.72	40.33
PS63	Pegmatite	1.78	914.36	34.90	207.12	0.20	1161.99	51.48	6.86	105.35	130.39	19.43	1.76	78.44	121.52	48.18
PS1	Qtz Dol	1.35	667.96	30.88	250.65	0.15	1189.04	40.28	9.79	115.96	102.25	19.44	1.26	58.70	138.41	35.66
PS19	Qtz Dol	0.91	505.13	34.54	257.49	0.67	1289.24	69.04	18.60	130.26	92.27	18.69	1.14	43.93	157.14	28.70
PS5	Qtz Dol	0.99	539.49	37.03	297.17	0.70	1312.98	64.05	17.61	137.84	97.09	18.89	1.21	43.56	143.14	30.35
PS50	Qtz Dol	1.23	656.57	35.48	268.52	0.38	1181.15	63.65	9.99	125.04	100.50	38.61	1.54	55.55	150.88	36.52
PS52	Qtz Dol	1.05	518.92	39.61	239.27	2.75	1277.05	56.53	30.41	123.05	87.90	26.65	1.42	42.63	178.95	28.52
PS57	Qtz Dol	0.88	412.94	37.34	218.54	7.25	1211.78	65.15	42.39	92.37	78.36	21.85	1.36	35.26	149.92	21.98
PS6	Qtz Dol	0.96	471.55	27.30	217.92	0.23	1056.16	54.35	13.61	111.65	83.54	20.46	1.07	46.67	187.70	28.49
PS75	Qtz Dol	0.94	457.81	36.90	251.44	8.73	1333.96	67.93	43.90	112.14	88.37	17.98	1.11	40.33	151.37	27.07
PS34	Qtz Dol	0.94	449.34	38.41	263.29	14.22	1352.25	63.53	52.83	102.34	86.73	18.24	1.13	40.31	144.33	25.85
PS35	Qtz Dol	0.79	419.95	26.10	202.86	3.79	1135.79	64.48	30.30	112.37	78.70	21.34	1.39	38.31	193.25	23.04
PS3D	Qtz Dol	1.08	556.07	42.54	334.55	0.66	1424.82	72.06	19.83	138.73	106.40	18.38	1.32	43.34	136.24	31.18
PS3L	Qtz Dol	1.44	622.71	13.66	44.39	0.17	651.56	43.54	3.99	61.59	62.44	21.45	0.95	70.12	196.45	30.21
PS9	Qtz Dol	0.85	431.55	27.55	201.20	15.02	994.01	56.41	42.18	63.68	65.75	18.57	0.92	39.60	196.48	22.73

Table A4-B: Trace Element Concentrations (Zr-Eu) of whole rocks measured by S-ICP-MS. All abundances in ppm.

		Zr	Nb	Mo	Cd	Sn	Sb	Cs	Ba	La	Ce	Pr	Nd	Sm	Eu
Sample	**Classification**														
PS27	CM	95.24	5.06	0.55	0.04	0.88	0.11	1.97	260.28	12.22	26.43	3.27	13.15	3.10	0.87
PS30	CM	91.59	5.91	0.71	0.04	0.88	0.09	0.88	196.39	11.12	24.32	3.06	12.50	2.98	0.84
PS31	CM	52.80	6.21	0.59	0.04	0.90	0.16	0.84	205.88	11.49	25.30	3.18	12.91	3.00	0.83
PS36	CM	63.34	4.77	0.48	0.04	0.83	0.12	1.85	220.78	11.21	24.62	3.00	12.24	2.91	0.80
PS58	CM	69.17	6.24	0.84	0.04	0.84	0.46	0.78	184.34	11.23	24.80	3.04	12.44	2.97	0.83
PS59	CM	88.69	4.92	0.56	0.04	0.86	0.13	1.17	195.85	11.65	25.13	3.12	12.55	2.95	0.83
PS60	CM	57.54	4.83	0.63	0.04	0.84	0.12	1.13	193.30	11.66	25.09	3.12	12.70	2.95	0.83
PS62	CM	90.43	4.57	0.50	0.04	0.81	0.11	2.54	193.19	11.45	24.73	3.04	12.30	2.88	0.80
PS65	CM	81.14	4.79	0.54	0.04	0.85	0.12	1.40	198.78	11.47	24.72	3.06	12.38	2.93	0.81
PS69	CM	84.98	5.51	0.64	0.04	0.82	0.13	0.98	179.88	10.32	22.62	2.83	11.69	2.77	0.79
PS77	CM	90.40	4.68	0.55	0.05	0.81	0.10	0.77	202.48	10.94	23.87	2.95	11.98	2.84	0.80
PS21	Dol	84.57	4.13	0.49	0.04	0.73	0.11	0.51	193.54	9.95	21.67	2.67	10.84	2.54	0.72

PS25	Dol	84.24	4.73	0.62	0.04	0.81	0.09	0.67	187.22	10.50	22.95	2.84	11.47	2.78	0.90
PS26	Dol	91.01	4.41	0.49	0.15	0.89	0.07	0.83	184.01	10.10	23.05	2.87	12.05	2.76	0.80
PS28	Dol	86.86	5.09	0.55	0.04	0.81	0.16	1.04	178.66	10.83	23.85	2.99	12.21	2.92	0.83
PS29	Dol	79.43	4.59	0.45	0.14	0.90	0.12	1.51	189.59	9.98	21.93	2.83	11.83	2.77	0.75
PS32	Dol	74.72	3.53	0.41	0.04	0.69	0.08	0.89	141.11	8.03	19.84	2.40	9.87	2.35	0.71
PS47	Dol	107.02	5.30	0.87	0.22	1.12	0.15	1.30	216.91	11.64	27.25	3.24	13.61	3.25	0.87
PS48	Dol	94.24	4.52	0.49	0.04	0.82	0.11	1.07	182.18	11.20	23.74	2.90	11.90	2.81	0.81
PS64	Dol	66.17	3.53	0.48	0.17	0.69	0.09	0.65	164.60	8.18	18.02	2.37	10.01	2.49	0.75
PS68	Dol	112.88	5.38	0.86	0.06	1.01	0.12	1.68	216.55	16.35	34.51	4.33	18.08	4.48	1.22
PS73	Dol	90.78	4.71	0.47	0.15	0.96	0.12	1.63	212.08	11.00	24.03	3.10	12.89	3.06	0.82
PS76	Dol	120.22	6.07	0.62	0.04	1.00	0.16	1.13	301.65	14.69	31.24	3.92	15.63	3.64	0.98
PS8	Dol	99.74	4.98	0.58	0.04	0.89	0.12	1.24	194.05	12.06	25.89	3.14	12.92	3.08	0.89
PS44	Fay Gran	214.48	9.48	0.83	0.22	1.86	0.14	2.10	363.18	20.24	47.58	5.76	22.97	5.32	1.32
PS51	Fay Gran	157.47	9.67	0.93	0.07	1.50	0.17	1.09	364.40	19.02	40.85	5.15	20.76	4.84	1.25
PS61	Fay Gran	133.11	9.06	0.85	0.06	1.37	0.16	1.92	380.85	18.50	40.80	4.98	20.13	4.75	1.19
PS11	Fay Gran	251.36	12.21	0.97	0.26	2.22	0.16	1.99	505.26	31.19	69.19	8.52	34.32	8.00	1.71
PS42	Fay Gran	243.87	12.40	1.06	0.28	2.25	0.14	1.74	500.82	31.23	66.47	8.14	32.46	7.66	1.60
PS53	Fay Gran	212.04	10.69	1.07	0.26	2.11	0.18	1.95	472.01	27.43	60.75	7.26	29.77	6.69	1.62
PS54	Fay Gran	288.26	13.95	1.02	0.27	2.67	0.17	2.62	572.38	35.15	73.11	8.89	35.23	8.14	1.63
PS13	Gran	353.24	16.47	1.08	0.36	3.34	0.19	1.67	668.27	47.34	96.40	12.35	50.04	11.61	2.04
PS14	Gran	305.12	7.73	1.14	0.08	2.29	0.11	1.71	621.88	36.13	77.62	9.58	38.30	8.64	1.61
PS15	Gran	304.52	9.15	0.57	0.44	2.40	0.14	1.88	642.06	46.85	95.80	12.05	48.58	11.55	2.08
PS17	Gran	322.02	15.45	0.95	0.38	2.87	0.21	2.04	619.64	44.66	93.23	11.65	46.46	10.86	2.07
PS18	Gran	336.59	15.67	1.09	0.29	3.43	0.21	2.08	629.68	38.40	79.95	9.82	38.76	8.90	1.66
PS37	Gran	272.07	15.71	1.17	0.29	2.91	0.14	2.39	694.86	38.27	80.99	10.04	40.18	9.37	1.84
PS38	Gran	287.04	14.68	1.15	0.29	2.99	0.17	3.59	598.16	36.59	76.90	9.43	37.11	8.64	1.71
PS39	Gran	311.82	15.18	1.12	0.29	3.21	0.19	2.83	613.92	37.50	78.42	9.62	37.93	8.77	1.68
PS67	Gran	319.07	11.87	0.94	0.08	2.63	0.22	3.99	550.22	40.17	84.72	11.61	42.42	9.70	1.84
KI09 Q	KI Basalt	89.93	4.44	0.56	0.04	0.78	0.12	0.83	191.13	11.15	23.77	2.95	11.85	2.85	0.80
KI09 SF	KI Basalt	85.79	4.21	0.62	0.04	0.73	0.14	0.59	243.45	10.66	23.08	2.85	11.53	2.71	0.76
KIW1-2	KI Basalt	91.96	4.61	0.57	0.04	0.80	0.12	1.21	234.14	11.95	24.96	3.07	12.51	2.94	0.81
KIW2-1	KI Basalt	77.92	3.88	0.58	0.04	0.66	0.10	0.55	175.98	9.98	21.22	2.61	10.58	2.51	0.70
KIW4-1	KI Basalt	92.05	4.62	0.68	0.04	0.84	0.14	1.02	222.25	11.22	23.98	2.97	12.03	2.82	0.80
KIW4-SF	KI Basalt	89.60	4.51	0.60	0.04	0.79	0.10	0.85	196.48	11.02	23.47	2.90	11.69	2.76	0.78
KIW5-1	KI Basalt	92.93	4.70	0.59	0.04	0.80	0.11	0.64	195.78	11.27	24.30	3.02	12.25	2.87	0.80
KIW6-NF	KI Basalt	88.64	4.45	0.56	0.04	0.77	0.12	0.71	190.24	10.85	23.54	2.90	11.75	2.78	0.78
PS24	Pegmatite	154.64	8.10	0.88	0.05	1.54	0.14	2.19	284.75	18.63	39.78	4.90	19.96	4.59	0.93
PS74	Pegmatite	132.75	5.87	0.55	0.05	1.10	0.12	1.24	232.65	13.74	29.49	3.61	14.88	3.47	0.89
PS70	Pegmatite	260.42	14.70	1.44	0.08	2.33	0.15	2.59	582.91	37.12	70.81	8.95	36.44	8.28	1.59
PS70-t	Pegmatite	260.42	14.70	1.44	0.08	2.33	0.15	2.59	582.91	37.12	70.81	8.95	36.44	8.28	1.59
PS71	Pegmatite	176.00	10.48	0.87	0.06	1.52	0.14	1.24	383.36	23.44	48.56	6.05	24.43	5.59	1.30
PS63	Pegmatite	240.28	6.93	0.71	0.08	1.92	0.15	1.44	523.20	30.80	57.89	7.32	29.58	6.80	1.50

PS1	Qtz Dol	179.35	8.59	0.63	0.19	1.61	0.21	3.03	343.54	19.29	45.37	5.67	22.57	5.19	1.32
PS19	Qtz Dol	127.32	6.60	0.75	0.20	1.28	0.15	1.33	290.13	14.40	33.12	4.11	16.16	3.88	1.11
PS5	Qtz Dol	155.44	6.88	0.71	0.21	1.37	0.17	1.39	292.38	16.17	35.62	4.47	17.88	4.16	1.13
PS50	Qtz Dol	162.68	8.41	0.88	0.06	1.51	0.15	2.43	306.03	19.81	42.28	5.26	21.25	4.89	1.26
PS52	Qtz Dol	121.03	6.61	0.67	0.05	1.20	0.12	1.44	256.57	16.20	34.60	4.24	17.22	4.03	1.10
PS57	Qtz Dol	109.00	5.08	0.65	0.05	0.96	0.21	1.46	206.37	12.80	27.75	3.42	13.84	3.21	0.96
PS6	Qtz Dol	133.10	6.75	0.64	0.17	1.23	0.14	1.40	282.16	15.05	34.96	4.15	17.22	4.00	1.13
PS75	Qtz Dol	115.56	6.06	0.66	0.17	1.13	0.10	1.32	240.88	12.99	30.27	3.64	15.24	3.56	0.99
PS34	Qtz Dol	102.75	5.86	0.57	0.17	1.06	0.11	1.15	228.15	12.48	29.50	3.47	14.74	3.34	0.94
PS35	Qtz Dol	106.52	5.49	0.71	0.05	0.92	0.13	1.85	223.72	13.01	28.06	3.44	13.87	3.23	0.96
PS3D	Qtz Dol	134.89	7.07	0.78	0.21	1.45	0.16	1.32	259.29	14.98	35.61	4.48	18.04	4.30	1.11
PS3L	Qtz Dol	164.88	7.12	0.63	0.14	1.59	0.10	2.59	413.66	19.30	45.15	5.44	21.35	4.75	1.36
PS9	Qtz Dol	109.70	5.45	0.62	0.15	1.10	0.09	2.03	226.96	12.19	28.71	3.38	13.76	3.15	0.94

Table A4-C: Trace Element Concentrations (Gd-U) of whole rocks measured by S-ICP-MS. All abundances in ppm.

		Gd	Tb	Dy	Ho	Er	Yb	Lu	Hf	Ta	Tl	Pb	Th	U
Sample	**Classification**													
PS27	CM	3.34	0.59	3.75	0.79	2.36	2.34	0.36	2.52	0.41	0.24	5.78	3.47	0.87
PS30	CM	3.62	0.56	3.72	0.79	2.42	2.38	0.36	2.41	0.54	0.21	5.11	3.26	0.84
PS31	CM	3.68	0.55	3.71	0.79	2.34	2.28	0.34	1.56	0.44	0.25	5.29	3.30	0.81
PS36	CM	3.26	0.56	3.57	0.76	2.25	2.27	0.33	1.66	0.51	0.26	5.46	3.27	0.80
PS58	CM	3.57	0.53	3.59	0.75	2.29	2.26	0.34	2.01	0.72	0.17	4.93	3.14	0.80
PS59	CM	3.27	0.56	3.61	0.76	2.29	2.30	0.35	2.35	0.49	0.21	5.81	3.38	0.91
PS60	CM	3.33	0.58	3.69	0.78	2.34	2.34	0.35	1.70	0.50	0.22	5.46	3.28	0.81
PS62	CM	3.16	0.54	3.47	0.73	2.18	2.18	0.33	2.41	0.40	0.18	5.45	3.36	0.86
PS65	CM	3.26	0.55	3.54	0.75	2.23	2.25	0.34	2.17	0.41	0.27	5.52	3.28	0.82
PS69	CM	3.49	0.52	3.47	0.76	2.27	2.18	0.32	2.23	0.44	0.19	4.81	2.99	0.78
PS77	CM	3.17	0.54	3.46	0.73	2.17	2.18	0.33	2.34	0.43	0.22	5.26	3.17	0.78
PS21	Dol	2.89	0.49	3.16	0.67	2.01	1.99	0.30	2.16	0.73	0.15	4.75	2.81	0.73
PS25	Dol	3.37	0.53	3.50	0.73	2.22	2.22	0.33	2.20	0.52	0.19	4.95	3.01	0.76
PS26	Dol	3.04	0.52	3.47	0.75	2.18	2.07	0.32	2.41	0.49	0.18	5.12	3.11	0.83
PS28	Dol	3.72	0.57	3.84	0.83	2.53	2.36	0.36	2.26	0.44	0.17	4.28	3.04	0.76
PS29	Dol	2.96	0.51	3.31	0.72	2.12	2.03	0.31	2.26	0.42	0.20	5.08	3.15	0.82
PS32	Dol	2.55	0.45	2.84	0.60	1.82	1.80	0.28	1.83	0.33	0.13	4.13	2.53	0.65
PS47	Dol	3.53	0.61	3.95	0.87	2.47	2.40	0.37	2.84	0.82	0.20	6.13	3.57	0.95
PS48	Dol	3.05	0.53	3.36	0.70	2.10	2.10	0.32	2.34	0.54	0.20	5.19	3.11	0.82
PS64	Dol	2.70	0.47	3.11	0.67	1.93	1.83	0.29	1.89	0.46	0.12	4.28	2.39	0.71
PS68	Dol	5.13	0.89	5.71	1.21	3.64	3.84	0.58	2.88	0.81	0.27	6.33	3.86	1.01
PS73	Dol	3.35	0.56	3.67	0.81	2.28	2.22	0.34	2.50	0.51	0.19	5.56	3.31	0.82
PS76	Dol	3.91	0.67	4.25	0.91	2.69	2.67	0.40	3.22	1.21	0.29	7.18	4.35	1.08
PS8	Dol	3.25	0.56	3.58	0.75	2.26	2.24	0.34	2.51	0.53	0.21	5.61	3.38	0.86
PS44	Fay Gran	5.81	0.97	6.17	1.35	3.87	3.86	0.60	5.48	0.93	0.37	10.78	6.71	1.68

PS51	Fay Gran	5.76	0.88	5.86	1.22	3.73	3.62	0.54	4.15	0.69	0.38	8.48	5.72	1.40
PS61	Fay Gran	5.47	0.84	5.58	1.16	3.55	3.49	0.52	3.50	2.20	0.37	8.28	5.41	1.37
PS11	Fay Gran	9.34	1.56	9.98	2.22	6.37	6.14	0.97	6.74	2.77	0.51	13.61	9.11	2.40
PS42	Fay Gran	8.57	1.43	8.89	1.95	5.61	5.47	0.83	6.53	0.94	0.48	13.17	8.86	2.42
PS53	Fay Gran	7.37	1.21	7.76	1.68	4.75	4.57	0.70	5.84	1.33	0.46	11.92	7.80	1.97
PS54	Fay Gran	9.19	1.54	9.70	2.19	6.23	6.11	0.94	7.69	1.02	0.62	15.13	10.52	2.80
PS13	Gran	13.58	2.22	14.23	3.09	8.80	8.73	1.41	9.62	1.13	0.75	18.85	14.11	3.11
PS14	Gran	10.48	1.58	10.52	2.22	6.82	6.66	0.99	7.99	0.30	0.72	15.34	11.07	2.77
PS15	Gran	12.98	2.15	13.64	2.99	8.59	8.73	1.37	8.06	0.55	0.70	18.61	12.12	4.40
PS17	Gran	11.99	1.97	12.47	2.68	7.55	7.57	1.13	8.45	1.03	0.65	16.56	11.06	3.32
PS18	Gran	9.97	1.68	10.63	2.34	6.81	6.77	1.03	8.86	1.11	0.64	17.14	11.66	3.40
PS37	Gran	10.10	1.67	10.42	2.24	6.35	6.12	0.94	7.32	1.15	0.71	17.46	10.95	2.19
PS38	Gran	9.22	1.51	9.39	2.04	5.78	5.64	0.87	7.76	1.23	0.61	16.67	11.14	2.17
PS39	Gran	9.59	1.59	10.01	2.19	6.30	6.21	0.95	8.31	1.17	0.63	16.91	11.40	2.78
PS67	Gran	10.43	1.78	11.22	2.35	7.02	6.94	1.07	8.33	0.80	0.74	18.78	13.27	3.06
KI09 Q	KI Basalt	3.04	0.53	3.38	0.71	2.13	2.13	0.33	2.45	0.42	0.19	5.26	3.14	0.82
KI09 SF	KI Basalt	2.97	0.52	3.28	0.70	2.06	2.02	0.31	2.33	0.90	0.15	5.01	2.97	0.80
KIW1-2	KI Basalt	3.30	0.56	3.65	0.79	2.38	2.36	0.37	2.48	0.86	0.23	5.39	3.23	0.83
KIW2-1	KI Basalt	2.79	0.49	3.09	0.65	1.94	1.88	0.29	2.08	2.37	0.15	4.54	2.69	0.71
KIW4-1	KI Basalt	3.07	0.54	3.40	0.72	2.16	2.16	0.33	2.43	0.43	0.28	5.35	3.18	0.82
KIW4-SF	KI Basalt	2.98	0.51	3.23	0.68	2.02	1.99	0.30	2.46	0.45	0.22	5.76	3.20	0.82
KIW5-1	KI Basalt	3.14	0.54	3.45	0.74	2.20	2.18	0.34	2.47	0.46	0.15	5.42	3.24	0.83
KIW6-NF	KI Basalt	3.02	0.52	3.33	0.70	2.08	2.07	0.32	2.39	0.77	0.17	5.23	3.10	0.82
PS24	Pegmatite	4.91	0.84	5.29	1.11	3.36	3.34	0.50	3.99	0.70	0.45	8.02	6.13	1.39
PS74	Pegmatite	3.71	0.64	4.12	0.87	2.58	2.60	0.40	3.35	0.49	0.28	6.44	4.10	1.09
PS70	Pegmatite	9.92	1.50	9.63	2.02	6.06	5.79	0.86	6.96	1.13	0.67	13.39	10.24	2.55
PS70-t	Pegmatite	9.92	1.50	9.63	2.02	6.06	5.79	0.86	6.96	1.13	0.67	13.39	10.24	2.55
PS71	Pegmatite	6.79	1.01	6.73	1.41	4.21	4.05	0.62	4.77	0.36	0.47	11.45	6.83	1.69
PS63	Pegmatite	8.14	1.24	8.14	1.71	5.19	5.09	0.76	6.38	0.38	0.52	11.94	8.55	2.19
PS1	Qtz Dol	5.85	0.96	6.19	1.35	3.87	3.81	0.61	4.80	0.76	0.41	10.38	6.50	1.68
PS19	Qtz Dol	4.29	0.72	4.56	1.01	2.91	2.87	0.44	3.41	0.70	0.26	7.37	4.57	1.19
PS5	Qtz Dol	4.75	0.78	5.03	1.12	3.20	3.17	0.50	4.11	0.70	0.29	8.30	5.09	1.38
PS50	Qtz Dol	5.22	0.89	5.68	1.19	3.58	3.54	0.54	4.31	0.72	0.37	9.23	6.50	1.48
PS52	Qtz Dol	4.35	0.74	4.72	1.00	2.99	2.98	0.44	3.12	0.52	0.29	7.36	4.82	1.13
PS57	Qtz Dol	3.49	0.60	3.83	0.81	2.43	2.41	0.36	2.76	1.21	0.23	5.85	3.70	0.97
PS6	Qtz Dol	4.18	0.71	4.64	1.00	2.86	2.82	0.43	3.57	0.62	0.27	8.00	4.74	1.23
PS75	Qtz Dol	3.87	0.65	4.30	0.95	2.71	2.62	0.40	3.10	0.64	0.24	6.82	4.20	1.12
PS34	Qtz Dol	3.71	0.63	4.14	0.90	2.57	2.46	0.38	2.72	0.50	0.24	6.46	3.92	1.01
PS35	Qtz Dol	3.59	0.61	3.90	0.82	2.46	2.46	0.36	2.77	0.57	0.25	6.37	3.78	0.95
PS3D	Qtz Dol	4.85	0.81	5.24	1.17	3.34	3.34	0.53	3.55	0.68	0.30	8.58	4.78	1.24
PS3L	Qtz Dol	5.08	0.82	5.17	1.13	3.21	3.15	0.49	4.23	0.70	0.43	9.39	6.46	1.67
PS9	Qtz Dol	3.44	0.57	3.60	0.79	2.25	2.19	0.33	2.84	0.85	0.23	6.05	3.86	1.00

Table A5: CIPW Normative compositions (Kelsey, 1965)

Sample	Classification	Quartz	Orthoclase	Albite	Anorthite	Diopside	Hypersthene	Magnetite	Ilmenite	Apatite
PS27	CM	7.63	4.98	14.70	28.95	19.05	18.55	2.71	1.19	0.26
PS30	CM	7.12	5.11	15.84	28.71	19.75	17.97	2.87	1.21	0.26
PS31	CM	7.02	5.35	16.20	28.18	19.62	18.18	2.74	1.21	0.26
PS36	CM	5.99	6.60	16.95	27.33	19.00	18.29	2.85	1.19	0.26
PS58	CM	7.64	3.97	15.29	29.99	19.40	17.97	2.71	1.19	0.26
PS59	CM	8.23	4.72	15.08	29.51	19.04	17.67	2.94	1.25	0.27
PS60	CM	7.67	4.60	15.32	29.56	18.90	18.37	2.95	1.21	0.26
PS62	CM	6.69	5.04	16.64	28.90	19.83	17.58	2.65	1.19	0.26
PS65	CM	7.48	4.98	15.60	29.15	19.30	18.32	2.84	1.21	0.26
PS69	CM	6.55	4.65	14.52	30.63	20.22	18.96	2.34	1.13	0.25
PS77	CM	7.16	4.98	15.31	29.53	19.26	18.37	2.44	1.18	0.26
PS8	Dol	7.60	4.97	16.53	33.31	16.58	15.63	2.65	1.23	0.26
PS21	Dol	8.41	5.39	17.29	27.45	18.37	17.14	3.30	1.25	0.27
PS25	Dol	8.35	4.31	14.85	29.60	20.31	15.88	4.86	1.12	0.21
PS26	Dol	7.17	4.64	14.47	31.50	19.52	17.46	2.63	1.13	0.25
PS28	Dol	7.05	3.85	14.18	30.69	19.88	18.81	2.42	1.11	0.25
PS29	Dol	5.71	4.91	15.11	32.71	18.26	19.02	1.44	1.20	0.25
PS32	Dol	4.92	3.73	13.28	32.01	21.86	20.77	1.30	0.96	0.22
PS47	Dol	9.38	5.44	16.95	27.82	17.92	15.27	3.86	1.36	0.28
PS48	Dol	7.97	4.72	14.93	27.70	19.54	19.22	3.17	1.15	0.25
PS64	Dol	5.04	3.38	14.00	31.78	23.33	18.61	1.57	0.99	0.22
PS68	Dol	9.29	5.74	17.84	31.13	15.19	13.83	3.73	1.33	0.31
PS73	Dol	6.44	5.20	16.66	29.88	19.75	17.38	2.20	1.21	0.26
PS76	Dol	10.06	6.42	19.05	25.40	17.03	14.59	4.31	1.44	0.30
PS11	Fay Gran	21.44	12.76	23.40	18.38	6.55	6.91	5.05	1.98	0.59
PS42	Fay Gran	23.79	12.29	22.96	17.07	6.85	1.62	10.00	2.41	0.79
PS44	Fay Gran	17.90	9.61	22.31	24.86	7.46	4.87	8.05	2.62	0.40
PS51	Fay Gran	15.23	8.31	21.89	26.05	10.75	6.47	7.12	2.19	0.37
PS53	Fay Gran	21.11	11.15	23.92	23.50	6.80	1.39	10.36	1.96	0.49
PS54	Fay Gran	25.45	14.18	24.59	15.75	6.47	1.37	10.00	1.77	0.60
PS61	Fay Gran	13.21	8.35	22.43	26.78	11.26	8.81	5.29	1.81	0.36
PS13	Gran	30.21	17.58	25.15	7.93	3.86	3.57	6.17	1.77	0.52
PS14	Gran	28.14	16.35	24.01	11.31	5.38	3.14	6.18	1.72	0.54
PS15	Gran	29.12	16.54	26.04	11.07	2.58	5.00	4.61	1.76	0.55
PS17	Gran	28.29	15.53	25.02	12.24	4.03	3.49	6.51	1.84	0.60
PS18	Gran	28.83	15.94	24.54	11.33	5.38	3.18	5.93	1.71	0.54
PS37	Gran	28.76	16.82	22.72	9.06	6.93	0.34	10.30	2.31	0.88
PS38	Gran	28.85	15.60	22.04	10.08	6.33	1.72	9.48	2.19	0.81
PS39	Gran	28.56	15.85	21.31	10.80	8.70	0.03	10.01	2.41	0.74
PS67	Gran	27.58	16.12	23.36	10.34	5.81	5.52	6.17	2.02	0.64
KI09 Q	KI Basalt	6.25	3.97	15.08	29.92	18.98	22.17	2.01	1.18	0.25
KI09 SF	KI Basalt	6.38	3.57	14.21	30.21	18.48	24.10	2.01	1.15	0.25

KIW1-2	KI Basalt	7.22	4.05	15.63	29.31	18.80	21.83	2.01	1.23	0.25
KIW2-1	KI Basalt	6.85	4.35	15.04	30.25	18.23	22.83	2.01	1.18	0.25
KIW4-1	KI Basalt	6.44	3.67	16.14	31.06	18.85	20.68	2.01	1.22	0.27
KIW4-SF	KI Basalt	7.47	5.08	15.97	29.21	17.58	22.62	2.01	1.24	0.26
KIW5-1	KI Basalt	6.45	4.33	15.51	29.24	18.95	21.27	2.01	1.23	0.26
KIW6-NF	KI Basalt	6.22	4.04	15.21	29.25	19.38	22.44	2.01	1.17	0.25
PS24	Pegmatite	13.51	9.43	17.66	23.24	15.76	12.25	4.56	1.91	0.38
PS63	Pegmatite	24.54	12.06	22.25	14.67	8.92	1.48	11.14	2.60	0.51
PS70	Pegmatite	26.39	13.78	20.87	12.64	7.67	0.71	10.69	2.79	0.71
PS70-t	Pegmatite	27.34	14.02	21.35	12.88	7.31		11.49	2.86	0.73
PS71	Pegmatite	20.33	10.21	20.79	18.46	12.33	3.68	10.30	2.13	0.41
PS74	Pegmatite	10.70	6.42	17.30	25.01	17.84	15.79	4.14	1.40	0.29
PS1	Qtz Dol	15.41	9.09	22.51	25.49	10.22	6.21	6.41	2.14	0.39
PS3D	Qtz Dol	13.90	6.94	20.07	25.73	13.54	6.89	7.60	2.20	0.34
PS3L	Qtz Dol	14.05	10.31	26.13	33.22	3.63	7.15	7.60	0.95	0.36
PS5	Qtz Dol	13.68	7.06	20.93	28.56	12.31	6.16	7.60	2.10	0.34
PS6	Qtz Dol	10.67	7.04	22.26	32.68	9.68	10.82	3.37	1.74	0.32
PS9	Qtz Dol	9.22	5.48	17.54	39.08	11.51	11.27	6.54	1.29	0.30
PS19	Qtz Dol	12.48	6.84	20.92	30.28	11.72	8.46	6.18	1.79	0.32
PS34	Qtz Dol	9.08	5.89	17.63	30.90	16.09	13.74	3.67	1.37	0.28
PS35	Qtz Dol	7.81	5.69	18.61	35.05	13.63	13.28	2.37	1.33	0.28
PS50	Qtz Dol	15.17	8.66	21.91	26.81	10.12	6.70	6.54	2.13	0.38
PS52	Qtz Dol	11.18	6.60	19.19	30.13	13.65	11.23	4.27	1.57	0.32
PS57	Qtz dol	8.45	5.54	18.15	33.83	15.04	14.59	2.99	1.26	0.28
PS75	Qtz Dol	10.14	6.05	19.12	29.55	15.50	12.17	4.56	1.48	0.30

Table A6: Normalised oxygen units after Grove, 1993 (after Tormey, 1987)

Sample	**Classification**	**Qtz**	**Plag**	**Olv**	**CPX**	**Ilm-Hem-Chr**	**Or**	**Ap**
PS1	Qtz Dol	0.06	0.69	0.13	0.03	0.06	0.03	0.00
PS3D	Qtz Dol	0.05	0.65	0.17	0.04	0.07	0.02	0.00
PS3L	Qtz Dol	0.06	0.79	0.08	0.01	0.03	0.03	0.00
PS5	Qtz Dol	0.05	0.69	0.14	0.04	0.06	0.02	0.00
PS6	Qtz Dol	0.05	0.73	0.12	0.03	0.05	0.02	0.00
PS8	Dol	0.04	0.68	0.16	0.05	0.05	0.02	0.00
PS9	Qtz Dol	0.04	0.74	0.12	0.03	0.04	0.02	0.00
PS11	Fay Gran	0.09	0.65	0.12	0.02	0.06	0.05	0.01
PS13	Gran	0.14	0.58	0.12	0.01	0.06	0.07	0.01
PS14	Gran	0.13	0.60	0.12	0.02	0.06	0.07	0.01
PS15	Gran	0.13	0.62	0.11	0.01	0.05	0.07	0.01
PS17	Gran	0.12	0.62	0.12	0.01	0.06	0.06	0.01
PS18	Gran	0.13	0.61	0.11	0.02	0.06	0.07	0.01
PS19	Qtz Dol	0.05	0.70	0.14	0.04	0.05	0.02	0.00
PS21	Dol	0.05	0.64	0.19	0.06	0.05	0.02	0.00
PS24	Pegmatite	0.06	0.62	0.17	0.05	0.06	0.03	0.00

PS25	Dol	0.04	0.63	0.20	0.06	0.05	0.01	0.00
PS26	Dol	0.04	0.65	0.18	0.06	0.05	0.02	0.00
PS27	CM	0.05	0.63	0.20	0.06	0.05	0.02	0.00
PS28	Dol	0.05	0.64	0.19	0.06	0.05	0.01	0.00
PS29	Dol	0.04	0.66	0.18	0.06	0.04	0.02	0.00
PS30	CM	0.04	0.63	0.19	0.06	0.05	0.02	0.00
PS31	CM	0.04	0.63	0.19	0.06	0.05	0.02	0.00
PS32	Dol	0.04	0.64	0.19	0.07	0.04	0.01	0.00
PS34	Qtz Dol	0.04	0.68	0.16	0.05	0.05	0.02	0.00
PS35	Qtz Dol	0.04	0.72	0.13	0.04	0.04	0.02	0.00
PS36	CM	0.04	0.63	0.19	0.06	0.05	0.02	0.00
PS37	Gran	0.12	0.55	0.15	0.03	0.08	0.07	0.01
PS38	Gran	0.12	0.55	0.15	0.02	0.08	0.06	0.01
PS39	Gran	0.12	0.55	0.15	0.03	0.08	0.07	0.01
PS42	Fay Gran	0.09	0.62	0.15	0.02	0.07	0.05	0.01
PS44	Fay Gran	0.06	0.67	0.14	0.02	0.06	0.03	0.00
PS47	Dol	0.05	0.64	0.18	0.06	0.05	0.02	0.00
PS48	Dol	0.05	0.61	0.21	0.06	0.05	0.02	0.00
PS50	Qtz Dol	0.06	0.69	0.13	0.03	0.06	0.03	0.00
PS51	Fay Gran	0.06	0.68	0.14	0.03	0.06	0.03	0.00
PS52	Qtz Dol	0.05	0.69	0.14	0.04	0.05	0.02	0.00
PS53	Fay Gran	0.08	0.70	0.11	0.02	0.05	0.04	0.00
PS54	Fay Gran	0.10	0.65	0.11	0.02	0.06	0.05	0.01
PS57	Qtz dol	0.04	0.70	0.15	0.04	0.05	0.02	0.00
PS58	CM	0.05	0.64	0.19	0.06	0.05	0.01	0.00
PS59	CM	0.05	0.63	0.19	0.06	0.05	0.02	0.00
PS60	CM	0.05	0.63	0.19	0.06	0.05	0.02	0.00
PS61	Fay Gran	0.05	0.69	0.14	0.03	0.05	0.03	0.00
PS62	CM	0.04	0.64	0.18	0.06	0.05	0.02	0.00
PS63	Pegmatite	0.09	0.59	0.17	0.03	0.07	0.05	0.00
PS64	Dol	0.04	0.65	0.18	0.07	0.04	0.01	0.00
PS65	CM	0.05	0.63	0.19	0.06	0.05	0.02	0.00
PS67	Gran	0.13	0.57	0.14	0.02	0.07	0.07	0.01
PS68	Dol	0.05	0.68	0.16	0.05	0.05	0.02	0.00
PS69	CM	0.04	0.64	0.19	0.06	0.05	0.02	0.00
PS70	Pegmatite	0.11	0.56	0.16	0.03	0.08	0.06	0.01
PS70-t	Pegmatite	0.11	0.56	0.16	0.03	0.08	0.06	0.01
PS71	Pegmatite	0.07	0.60	0.17	0.04	0.07	0.04	0.00
PS73	Dol	0.04	0.66	0.17	0.06	0.05	0.02	0.00
PS74	Pegmatite	0.06	0.62	0.19	0.06	0.05	0.02	0.00
PS75	Qtz Dol	0.05	0.68	0.16	0.05	0.05	0.02	0.00
PS76	Dol	0.05	0.64	0.18	0.05	0.05	0.02	0.00
PS77	CM	0.05	0.64	0.19	0.06	0.05	0.02	0.00
KI09 Q	KI Basalt	0.05	0.63	0.20	0.06	0.05	0.01	0.00

KI09 SF	KI Basalt	0.05	0.62	0.21	0.06	0.04	0.01	0.00
KIW1-2	KI Basalt	0.05	0.64	0.19	0.06	0.04	0.01	0.00
KIW2-1	KI Basalt	0.05	0.64	0.19	0.06	0.04	0.01	0.00
KIW4-1	KI Basalt	0.05	0.65	0.18	0.06	0.04	0.01	0.00
KIW4-SF	KI Basalt	0.05	0.62	0.21	0.05	0.05	0.02	0.00
KIW5-1	KI Basalt	0.05	0.63	0.20	0.06	0.05	0.01	0.00
KIW6-NF	KI Basalt	0.05	0.62	0.21	0.06	0.05	0.01	0.00

Table A7-A: Representative augite compositions from EPMA.

Sample	**KIW5-1**	**KIW5-1**	**KIW5-1**	**PS47**	**PS47**	**PS47**	**PS50**	**PS50**	**PS50**
Type	**KI Basalt**	**KI Basalt**	**KI Basalt**	**Dol**	**Dol**	**Dol**	**Qtz Dol**	**Qtz Dol**	**Qtz Dol**
Oxide Total	99.55	100.65	99.38	99.69	99.54	98.18	100.42	101.16	100.29
SiO2	52.86	53.53	52.98	50.87	48.76	50.78	48.31	48.87	50.83
TiO2	0.16	0.20	0.14	0.40	0.72	0.28	0.18	0.45	0.32
Al2O3	1.47	1.52	1.23	1.18	1.07	2.73	0.54	0.70	0.79
Cr2O3	0.23	0.26	0.31	0.00	0.00	0.09	0.03	0.00	0.04
FeO	6.74	7.63	7.45	16.44	23.72	7.16	28.97	34.76	26.72
MnO	0.17	0.20	0.22	0.40	0.49	0.25	0.50	0.67	0.62
MgO	19.02	19.53	20.38	13.52	8.54	16.75	2.14	10.32	15.37
CaO	18.73	17.69	16.56	16.74	16.13	19.91	19.54	5.28	5.52
Na2O	0.12	0.07	0.11	0.14	0.11	0.19	0.19	0.08	0.07
K2O	0.05	0.02	0.00	0.00	0.01	0.04	0.01	0.02	0.03
Si	1.94	1.95	1.95	1.95	1.94	1.91	1.97	1.95	1.96
Ti	0.00	0.01	0.00	0.01	0.02	0.01	0.01	0.01	0.01
Al	0.06	0.07	0.05	0.05	0.05	0.12	0.03	0.03	0.04
Cr	0.01	0.01	0.01	0.00	0.00	0.00	0.00	0.00	0.00
Fe2+	0.21	0.23	0.23	0.53	0.79	0.23	0.99	1.16	0.86
Mn	0.01	0.01	0.01	0.01	0.02	0.01	0.02	0.02	0.02
Mg	1.04	1.06	1.12	0.77	0.51	0.94	0.13	0.61	0.88
Ca	0.74	0.69	0.65	0.69	0.69	0.80	0.86	0.23	0.23
Na	0.01	0.00	0.01	0.01	0.01	0.01	0.02	0.01	0.01
K	0.00	0.00	0.00	0.00	0.00	0.00	0.00	0.00	0.00
Cation Total	4.02	4.01	4.02	4.02	4.02	4.03	4.02	4.02	4.01
[O]	6.00	6.00	6.00	6.00	6.00	6.00	6.00	6.00	6.00
Mg Number	83.42	82.03	82.98	59.44	39.08	80.66	11.65	34.61	50.62

Table A7-B: Representative augite compositions from EPMA.

Sample	PS35	PS35	PS35	PS54	PS54	PS54	PS38	PS38	PS38
Type	Qtz Dol	Qtz Dol	Qtz Dol	Fay. Gran.	Fay. Gran.	Fay. Gran.	Gran	Gran	Gran
Oxide Total	100.43	100.44	100.17	100.24	99.85	99.90	99.30	100.39	99.24
SiO2	51.38	51.87	49.87	47.81	47.46	47.94	48.48	49.88	47.05
TiO2	0.40	0.31	0.43	0.66	0.63	0.75	0.15	0.09	0.72
Al2O3	1.36	1.28	1.08	0.61	0.99	1.02	0.25	0.43	0.65
Cr2O3	0.01	0.00	0.00	0.00	0.02	0.00	0.00	0.00	0.00
FeO	15.15	13.20	23.81	29.52	28.05	27.45	26.25	21.24	29.60
MnO	0.27	0.31	0.57	0.56	0.61	0.61	0.39	0.67	0.48
MgO	14.01	14.58	11.73	2.02	4.85	4.89	3.35	5.25	2.00
CaO	17.70	18.74	12.55	18.73	17.08	17.05	20.21	22.46	18.48
Na2O	0.15	0.14	0.11	0.27	0.16	0.19	0.19	0.34	0.21
K2O	0.00	0.00	0.02	0.05	0.02	0.00	0.01	0.01	0.04
Si	1.94	1.95	1.95	1.96	1.93	1.94	1.98	1.98	1.95
Ti	0.01	0.01	0.01	0.02	0.02	0.02	0.00	0.00	0.02
Al	0.06	0.06	0.05	0.03	0.05	0.05	0.01	0.02	0.03
Cr	0.00	0.00	0.00	0.00	0.00	0.00	0.00	0.00	0.00
Fe2+	0.48	0.41	0.78	1.01	0.96	0.93	0.90	0.70	1.03
Mn	0.01	0.01	0.02	0.02	0.02	0.02	0.01	0.02	0.02
Mg	0.79	0.82	0.68	0.12	0.29	0.30	0.20	0.31	0.12
Ca	0.72	0.75	0.52	0.82	0.75	0.74	0.89	0.95	0.82
Na	0.01	0.01	0.01	0.02	0.01	0.01	0.02	0.03	0.02
K	0.00	0.00	0.00	0.00	0.00	0.00	0.00	0.00	0.00
Cation Total	4.02	4.02	4.02	4.01	4.03	4.02	4.02	4.02	4.02
[O]	6.00	6.00	6.00	6.00	6.00	6.00	6.00	6.00	6.00
Mg Number	62.25	66.32	46.76	10.85	23.57	24.09	18.51	30.59	10.77

Table A8: Representative pigeonite compositions from EPMA.

Sample	PS47	PS47	PS47	PS47	PS47	PS35	PS35	PS35	PS63	PS63	PS63
Type	Dol	Dol	Dol	Dol	Dol	Qtz Dol	Qtz Dol	Qtz Dol	Pegm.	Pegm.	Pegm.
Oxide Total	99.36	99.93	100.05	100.50	100.19	100.61	99.90	98.41	99.68	99.64	96.74
SiO2	53.45	52.63	51.15	48.88	48.40	53.10	48.27	48.65	47.41	47.72	46.97
TiO2	0.13	0.19	0.30	0.77	0.49	0.16	0.52	0.18	0.41	0.43	0.35
Al2O3	0.80	0.68	0.71	0.93	0.72	0.75	0.64	0.60	0.68	0.56	0.55
Cr2O3	0.03	0.02	0.00	0.03	0.00	0.02	0.00	0.03	0.02	0.01	0.00

FeO	15.39	19.71	25.23	31.04	34.74	20.78	34.03	31.42	38.41	38.35	35.69
MnO	0.40	0.46	0.51	0.75	0.71	0.45	0.73	0.68	0.79	0.79	0.72
MgO	22.88	21.47	17.23	8.23	8.13	21.23	8.06	12.84	6.51	8.36	9.28
CaO	6.20	4.72	4.86	9.75	6.85	4.07	7.56	3.96	5.35	3.39	3.17
Na2O	0.04	0.04	0.07	0.12	0.13	0.06	0.09	0.04	0.10	0.03	0.02
K2O	0.03	0.01	0.00	0.00	0.03	0.00	0.01	0.00	0.01	0.00	0.00
Si	1.97	1.96	1.96	1.95	1.96	1.97	1.96	1.96	1.96	1.96	1.97
Ti	0.00	0.01	0.01	0.02	0.01	0.00	0.02	0.01	0.01	0.01	0.01
Al	0.03	0.03	0.03	0.04	0.03	0.03	0.03	0.03	0.03	0.03	0.03
Cr	0.00	0.00	0.00	0.00	0.00	0.00	0.00	0.00	0.00	0.00	0.00
Fe2+	0.48	0.62	0.81	1.04	1.18	0.65	1.16	1.06	1.33	1.32	1.25
Mn	0.01	0.01	0.02	0.03	0.02	0.01	0.03	0.02	0.03	0.03	0.03
Mg	1.26	1.19	0.98	0.49	0.49	1.18	0.49	0.77	0.40	0.51	0.58
Ca	0.25	0.19	0.20	0.42	0.30	0.16	0.33	0.17	0.24	0.15	0.14
Na	0.00	0.00	0.00	0.01	0.01	0.00	0.01	0.00	0.01	0.00	0.00
K	0.00	0.00	0.00	0.00	0.00	0.00	0.00	0.00	0.00	0.00	0.00
Cation Total	4.01	4.02	4.02	4.00	4.01	4.01	4.01	4.02	4.01	4.01	4.01
[O]	6.00	6.00	6.00	6.00	6.00	6.00	6.00	6.00	6.00	6.00	6.00
Mg Number	72.60	66.01	54.90	32.09	29.43	64.56	29.68	42.14	23.21	27.97	31.66

Table A9: Representative orthopyroxene compositions from EPMA.

Sample	**KIW5-1**	**KIW5-1**	**KIW5-1**	**PS31**	**PS31**	**PS31**	**PS72**	**PS72**
Type	**KI Basalt**	**KI Basalt**	**KI Basalt**	**CM**	**CM**	**CM**	**Pegm.**	**Pegm.**
Oxide Total	100.10	99.90	100.39	99.68	99.87	100.54	99.07	99.28
SiO2	55.24	55.10	55.09	54.72	55.23	55.40	49.03	51.36
TiO2	0.07	0.08	0.13	0.10	0.10	0.08	0.20	0.22
Al2O3	0.81	0.96	1.17	1.49	1.30	1.24	0.32	0.41
Cr2O3	0.15	0.13	0.17	0.24	0.26	0.19	0.03	0.04
FeO	10.90	11.15	11.23	10.47	10.10	10.63	35.13	26.74
MnO	0.29	0.21	0.25	0.24	0.22	0.22	0.65	0.59
MgO	30.32	29.76	29.69	29.92	30.16	30.18	12.19	18.24
CaO	2.27	2.48	2.63	2.50	2.45	2.58	1.48	1.65
Na2O	0.02	0.03	0.03	0.00	0.04	0.02	0.01	0.00
K2O	0.01	0.00	0.02	0.00	0.02	0.00	0.03	0.02
Si	1.96	1.96	1.95	1.95	1.96	1.95	1.98	1.98
Ti	0.00	0.00	0.00	0.00	0.00	0.00	0.01	0.01
Al	0.03	0.04	0.05	0.06	0.05	0.05	0.02	0.02
Cr	0.00	0.00	0.00	0.01	0.01	0.01	0.00	0.00

Fe2+	0.32	0.33	0.33	0.31	0.30	0.31	1.19	0.86
Mn	0.01	0.01	0.01	0.01	0.01	0.01	0.02	0.02
Mg	1.60	1.58	1.57	1.59	1.59	1.59	0.73	1.05
Ca	0.09	0.09	0.10	0.10	0.09	0.10	0.06	0.07
Na	0.00	0.00	0.00	0.00	0.00	0.00	0.00	0.00
K	0.00	0.00	0.00	0.00	0.00	0.00	0.00	0.00
Cation Total	4.02	4.02	4.02	4.02	4.01	4.02	4.01	4.00
[O]	6.00	6.00	6.00	6.00	6.00	6.00	6.00	6.00
Mg Number	83.21	82.63	82.50	83.59	84.18	83.50	38.22	54.88

Table A10-A: Representative plagioclase compositions from EPMA.

Sample	**KIW5-1**	**KIW5-1**	**KIW5-1**	**PS47**	**PS47**	**PS47**	**PS50**	**PS50**	**PS50**
Type	**KI Basalt**	**KI Basalt**	**KI Basalt**	**Dol**	**Dol**	**Dol**	**Qtz Dol**	**Qtz Dol**	**Qtz Dol**
Oxide Total	99.858	99.177	99.331	98.808	98.347	98.451	100.722	100.836	100.531
SiO2	50.532	47.527	46.701	47.480	53.151	45.978	47.944	54.966	51.883
TiO2	0.035	0.005	0.000	0.016	0.059	0.016	0.015	0.080	0.044
Al2O3	30.057	32.024	32.656	31.872	27.555	32.371	32.966	28.177	30.008
Cr2O3	0.000	0.000	0.000	0.013	0.041	0.000	0.034	0.000	0.004
FeO	0.854	0.491	0.663	0.579	0.862	0.607	0.695	0.830	0.680
MnO	0.028	0.009	0.018	0.007	0.000	0.024	0.000	0.000	0.078
MgO	0.238	0.248	0.299	0.030	0.069	0.054	0.031	0.007	0.023
CaO	14.762	16.698	17.185	16.623	11.746	17.541	16.944	11.272	13.645
Na2O	3.114	2.067	1.638	2.083	4.563	1.789	2.024	5.122	3.930
K2O	0.238	0.109	0.172	0.105	0.302	0.070	0.069	0.381	0.237
Si	2.319	2.205	2.169	2.211	2.455	2.159	2.192	2.472	2.356
Ti	0.001	0.000	0.000	0.001	0.002	0.001	0.001	0.003	0.001
Al	1.626	1.751	1.787	1.749	1.500	1.791	1.776	1.494	1.606
Cr	0.000	0.000	0.000	0.000	0.001	0.000	0.001	0.000	0.000
Fe2+	0.033	0.019	0.026	0.023	0.033	0.024	0.027	0.031	0.026
Mn	0.001	0.000	0.001	0.000	0.000	0.001	0.000	0.000	0.003
Mg	0.016	0.017	0.021	0.002	0.005	0.004	0.002	0.000	0.002
Ca	0.726	0.830	0.855	0.830	0.581	0.882	0.830	0.543	0.664
Na	0.277	0.186	0.148	0.188	0.409	0.163	0.179	0.447	0.346
K	0.014	0.006	0.010	0.006	0.018	0.004	0.004	0.022	0.014
Cation Total	5.013	5.015	5.016	5.010	5.005	5.029	5.011	5.012	5.019
[O]	8.000	8.000	8.000	8.000	8.000	8.000	8.000	8.000	8.000
An	72.377	81.699	85.288	81.519	58.724	84.421	82.226	54.876	65.739

Table A10-B: Representative plagioclase compositions from EPMA.

Sample	**PS26**	**PS26**	**PS26**	**PS54**	**PS54**	**PS54**	**PS38**	**PS38**	**PS13**
Type	**Dol**	**Dol**	**Dol**	**Fay. Gran.**	**Fay. Gran.**	**Fay. Gran.**	**Gran.**	**Gran.**	**Gran.**
Oxide Total	99.59	98.47	98.78	100.53	98.92	99.80	100.082	97.683	102.075
SiO2	58.24	47.76	54.68	57.48	54.75	58.79	67.808	65.942	70.434
TiO2	0.08	0.01	0.06	0.04	0.01	0.02	0.000	0.030	0.000
Al2O3	25.36	31.44	27.02	26.56	27.04	25.28	19.933	19.661	19.455
Cr2O3	0.00	0.01	0.03	0.00	0.06	0.00	0.000	0.000	0.023
FeO	0.39	0.63	0.48	0.60	0.68	0.36	0.214	0.566	0.048
MnO	0.00	0.00	0.03	0.01	0.02	0.02	0.000	0.038	0.000
MgO	0.00	0.04	0.04	0.00	0.01	0.01	0.009	0.039	0.017
CaO	8.27	16.14	10.77	9.11	10.52	7.82	0.590	0.408	0.632
Na2O	6.39	2.31	5.15	6.23	5.43	7.03	11.495	10.937	11.435
K2O	0.85	0.13	0.52	0.51	0.39	0.46	0.032	0.062	0.031
Si	2.63	2.23	2.51	2.57	2.51	2.64	2.967	2.958	3.011
Ti	0.00	0.00	0.00	0.00	0.00	0.00	0.000	0.001	0.000
Al	1.35	1.73	1.46	1.40	1.46	1.34	1.028	1.040	0.980
Cr	0.00	0.00	0.00	0.00	0.00	0.00	0.000	0.000	0.001
Fe2+	0.01	0.02	0.02	0.02	0.03	0.01	0.008	0.021	0.002
Mn	0.00	0.00	0.00	0.00	0.00	0.00	0.000	0.001	0.000
Mg	0.00	0.00	0.00	0.00	0.00	0.00	0.001	0.003	0.001
Ca	0.40	0.81	0.53	0.44	0.52	0.38	0.028	0.020	0.029
Na	0.56	0.21	0.46	0.54	0.48	0.61	0.975	0.951	0.948
K	0.05	0.01	0.03	0.03	0.02	0.03	0.002	0.004	0.002
Cation Total	5.00	5.01	5.01	5.01	5.02	5.01	5.008	4.998	4.973
[O]	8.00	8.00	8.00	8.00	8.00	8.00	8.000	8.000	8.000
An	41.70	79.45	53.59	44.68	51.69	38.07	2.760	2.018	2.964

Table A11: Representative alkali feldspar compositions from EPMA.

Sample	**PS38**	**PS38**	**PS38**	**PS72**	**PS72**	**PS72**	**PS54**	**PS54**	**PS54**	**PS65**
Type	**Gran.**	**Gran.**	**Gran.**	**Pegm.**	**Pegm.**	**Pegm.**	**Fay. Gran.**	**Fay. Gran.**	**Fay. Gran.**	**CM**
Oxide Total	99.44	98.68	100.09	98.49	99.18	98.96	98.80	99.31	99.14	99.25
SiO2	64.18	64.09	65.60	64.46	65.05	64.97	64.88	65.10	64.01	69.75
TiO2	0.02	0.04	0.01	0.07	0.04	0.00	0.00	0.08	0.00	0.05
Al2O3	18.14	18.09	18.48	17.95	18.03	18.22	18.58	18.54	18.05	15.18
Cr2O3	0.00	0.00	0.03	0.02	0.00	0.00	0.00	0.04	0.00	0.05
FeO	0.05	0.24	0.15	0.09	0.12	0.12	0.11	0.17	0.26	0.21

MnO	0.00	0.03	0.02	0.00	0.05	0.00	0.02	0.04	0.00	0.01
MgO	0.00	0.03	0.00	0.01	0.01	0.00	0.00	0.00	0.00	0.00
CaO	0.00	0.13	0.24	0.22	0.21	0.24	0.38	0.48	0.12	0.18
Na2O	0.11	2.12	3.59	2.17	2.20	2.31	4.09	4.55	0.99	1.10
K2O	16.93	13.92	11.97	13.48	13.47	13.09	10.75	10.31	15.71	12.73
Si	3.00	2.99	2.99	3.00	3.01	3.00	2.98	2.98	2.99	3.17
Ti	0.00	0.00	0.00	0.00	0.00	0.00	0.00	0.00	0.00	0.00
Al	1.00	0.99	0.99	0.99	0.98	0.99	1.01	1.00	0.99	0.81
Cr	0.00	0.00	0.00	0.00	0.00	0.00	0.00	0.00	0.00	0.00
Fe2+	0.00	0.01	0.01	0.00	0.00	0.00	0.00	0.01	0.01	0.01
Mn	0.00	0.00	0.00	0.00	0.00	0.00	0.00	0.00	0.00	0.00
Mg	0.00	0.00	0.00	0.00	0.00	0.00	0.00	0.00	0.00	0.00
Ca	0.00	0.01	0.01	0.01	0.01	0.01	0.02	0.02	0.01	0.01
Na	0.01	0.19	0.32	0.20	0.20	0.21	0.36	0.40	0.09	0.10
K	1.01	0.83	0.70	0.80	0.79	0.77	0.63	0.60	0.94	0.74
Cation Total	5.01	5.02	5.02	5.00	5.00	4.99	5.01	5.02	5.03	4.84
[O]	8.00	8.00	8.00	8.00	8.00	8.00	8.00	8.00	8.00	8.00
Or	99.00	81.23	68.68	80.34	80.10	78.82	63.36	59.84	91.28	88.45

Table A12: Representative amphibole compositions from EPMA.

Sample	**PS50**	**PS50**	**PS50**	**PS63**	**PS63**	**PS63**	**PS54**	**PS54**	**PS54**
Type	**Qtz Dol**	**Qtz Dol**	**Qtz Dol**	**Pegm.**	**Pegm.**	**Pegm.**	**Fay. Gran.**	**Fay. Gran.**	**Fay. Gran.**
Oxide Total	97.35	97.53	97.35	97.63	97.51	94.39	97.90	96.60	97.08
SiO2	40.55	40.01	41.59	43.08	45.39	42.02	40.06	39.38	40.19
TiO2	2.16	1.85	1.36	1.55	0.99	1.53	1.99	1.95	1.82
Al2O3	7.40	7.75	6.68	6.34	5.29	6.62	7.65	7.53	7.53
Cr2O3	0.00	0.00	0.00	0.00	0.02	0.01	0.01	0.02	0.02
FeO	29.85	31.28	30.55	26.70	24.59	24.89	31.41	31.10	30.86
MnO	0.32	0.35	0.36	0.28	0.32	0.24	0.28	0.23	0.21
MgO	3.35	2.34	3.57	5.97	8.15	6.06	2.66	2.33	2.50
CaO	10.39	10.39	9.95	10.57	10.03	10.02	10.32	10.73	10.53
Na2O	1.96	2.09	1.99	1.97	1.79	1.89	1.93	2.00	2.00
K2O	1.36	1.46	1.30	1.18	0.94	1.10	1.59	1.33	1.41
Si	6.59	6.55	6.75	6.83	7.07	6.84	6.53	6.52	6.59
Ti	0.26	0.23	0.17	0.18	0.12	0.19	0.24	0.24	0.22
Al	1.42	1.50	1.28	1.18	0.97	1.27	1.47	1.47	1.45
Cr	0.00	0.00	0.00	0.00	0.00	0.00	0.00	0.00	0.00
Fe2+	4.06	4.28	4.15	3.54	3.20	3.39	4.28	4.30	4.23

Mn	0.04	0.05	0.05	0.04	0.04	0.03	0.04	0.03	0.03
Mg	0.81	0.57	0.86	1.41	1.89	1.47	0.65	0.57	0.61
Ca	1.81	1.82	1.73	1.80	1.67	1.75	1.80	1.90	1.85
Na	0.62	0.66	0.63	0.60	0.54	0.60	0.61	0.64	0.64
K	0.28	0.30	0.27	0.24	0.19	0.23	0.33	0.28	0.30
Cation Total	15.89	15.96	15.89	15.82	15.69	15.75	15.96	15.97	15.92
[O]	23.00	23.00	23.00	23.00	23.00	23.00	23.00	23.00	23.00
Mg Number	16.65	11.75	17.22	28.49	37.14	30.27	13.10	11.77	12.60

Table A13: Representative fayalite compositions from EPMA.

Sample	**PS54**	**PS54**	**PS54**
Type	**Fay. Gran.**	**Fay. Gran.**	**Fay. Gran.**
Oxide Total	100.385	99.364	100.424
SiO2	29.883	29.327	29.782
TiO2	0.166	0.057	0.042
Al2O3	0.000	0.002	0.005
Cr2O3	0.000	0.000	0.000
FeO	66.981	66.723	67.015
MnO	1.102	1.081	1.191
MgO	1.961	1.871	1.989
CaO	0.285	0.302	0.381
Na2O	0.007	0.000	0.019
K2O	0.000	0.000	0.000
Si	0.994	0.989	0.992
Ti	0.004	0.001	0.001
Al	0.000	0.000	0.000
Cr	0.000	0.000	0.000
Fe2+	1.864	1.882	1.867
Mn	0.031	0.031	0.034
Mg	0.097	0.094	0.099
Ca	0.010	0.011	0.014
Na	0.000	0.000	0.001
K	0.000	0.000	0.000
Cation Total	3.002	3.009	3.007
[O]	4.000	4.000	4.000
Mg Number	4.959	4.761	5.025

Table A14: Ilmenite and Magnetite pair recalculations for the Red Hill samples.

	PS47 Magnetite	Dol Ilmenite	PS50 Magnetite	Qtz Dol Ilmenite	PS54 Magnetite	Fay. Gran. Ilmenite	PS38 Magnetite	Gran. Ilmenite	PS13 Magnetite	Gran. Ilmenite
SiO2	2.01	0.07	0.46	0.11	0.97	0.07	0.20	0.09	1.43	0.16
TiO2	17.34	50.04	8.94	50.46	3.22	50.17	2.29	49.40	4.28	49.58
Al2O3	0.80	0.00	1.33	0.00	0.56	0.00	0.38	0.00	0.60	0.00
Fe2O3(T)	0.00	0.00	0.00	0.00	0.00				0.00	0.00
FeO(T)	66.97	46.06	80.96	47.30	86.82	46.60	86.70	45.72	82.04	43.70
MnO	1.29	0.51	0.21	0.63	0.12	1.17	0.34	1.77	0.52	3.37
MgO	0.08	0.40	0.04	0.12	0.03	0.15	0.09	0.33	0.04	0.07
CaO	1.11	0.03	0.26	0.03	0.11	0.02	0.06	0.03	0.73	0.09
Na2O	0.02	0.02	0.02	0.01	0.03	0.02	0.07	0.05	0.02	0.00
K2O	0.02	0.01	0.01	0.01	0.01	0.02	0.03	0.02	0.02	0.02
Cr2O3	0.00	0.00	0.00	0.00	0.00	0.00	0.00	0.00	0.00	0.00
BaO	0.00	0.00	0.00	0.00	0.00	0.00	0.00	0.00	0.00	0.00
ZnO	0.00	0.00	0.00	0.00	0.00	0.00	0.00	0.00	0.00	0.00
V2O3	1.43	3.42	1.58	3.45	0.25	3.35	0.14	3.21	0.32	3.50
NiO	0.00	0.00	0.00	0.00	0.00	0.00	0.00	0.00	0.00	0.00
Nb2O3	0.00	0.00	0.00	0.00	0.00	0.00	0.00	0.00	0.00	0.00
Sum:	91.06	100.55	93.81	102.10	92.12	101.56	90.32	100.61	90.00	100.50
Carmichael (1967)	**Recalculated Iron and Total**		**Recalculated Iron and Total**		**Recalculated Iron and Total**		**Recalculated Iron and Total**		**Recalculated Iron and Total**	
Fe2O3 wt. %	24.16	2.48	46.47	2.96	58.18	3.19	61.01	3.99	53.26	2.86
FeO wt. %	45.24	43.83	39.15	44.64	34.47	43.73	31.81	42.13	34.12	41.13
Total:	93.48	100.80	98.47	102.40	97.95	101.88	96.43	101.01	95.33	100.79
cations	**Cation prop. (Carmichael 1967)**		**Cation prop. (Carmichael 1967)**		**Cation prop. (Carmichael 1967)**		**Cation prop. (Carmichael 1967)**		**Cation prop. (Carmichael 1967)**	
SiO2	0.08	0.00	0.02	0.00	0.04	0.00	0.01	0.00	0.06	0.00
TiO2	0.52	0.94	0.26	0.94	0.09	0.94	0.07	0.93	0.13	0.93
Al2O3	0.04	0.00	0.06	0.00	0.03	0.00	0.02	0.00	0.03	0.00
Fe2O3(T)	0.72	0.05	1.34	0.05	1.70	0.06	1.82	0.07	1.59	0.05
FeO(T)	1.50	0.92	1.25	0.92	1.12	0.91	1.06	0.88	1.13	0.86
MnO	0.04	0.01	0.01	0.01	0.00	0.02	0.01	0.04	0.02	0.07
MgO	0.01	0.01	0.00	0.00	0.00	0.01	0.01	0.01	0.00	0.00
CaO	0.05	0.00	0.01	0.00	0.00	0.00	0.00	0.00	0.03	0.00
Na2O	0.00	0.00	0.00	0.00	0.00	0.00	0.01	0.00	0.00	0.00
K2O	0.00	0.00	0.00	0.00	0.00	0.00	0.00	0.00	0.00	0.00
Cr2O3	0.00	0.00	0.00	0.00	0.00	0.00	0.00	0.00	0.00	0.00
BaO	0.00	0.00	0.00	0.00	0.00	0.00	0.00	0.00	0.00	0.00
ZnO	0.00	0.00	0.00	0.00	0.00	0.00	0.00	0.00	0.00	0.00
V2O3	0.05	0.07	0.05	0.07	0.01	0.07	0.00	0.06	0.01	0.07
NiO	0.00	0.00	0.00	0.00	0.00	0.00	0.00	0.00	0.00	0.00
Nb2O3	0.00	0.00	0.00	0.00	0.00	0.00	0.00	0.00	0.00	0.00
	3.00	2.00	3.00	2.00	3.00	2.00	3.00	2.00	3.00	2.00
	Mol % Usp	**Mol % Ilm**	**Mol % Usp**	**Mol % Ilm**	**Mol % Usp**	**Mol % Ilm**	**Mol % Usp**	**Mol % Ilm**	**Mol % Usp**	**Mol % Ilm**
	0.57	0.98	0.27	0.97	0.10	0.97	0.07	0.96	0.13	0.97
	Temp (°C)	**log10 fO2**	**Temp (°C)**	**log10 fO2**	**Temp (°C)**	**log10 fO2**	**Temp (°C)**	**log10 fO2**	**Temp (°C)**	**log10 fO2**
	842.50	-14.22	690.95	-17.22	651.43	-17.83	637.53	-17.65	666.48	-17.62

Table A15: Representative trace element concentrations of Red Hill augites measured by LA-ICP-MS (ppm)

Sample	CPX KIW5-1	CPX KIW5-1	CPX PS38	CPX PS38	CPX PS47	CPX PS47	CPX PS47	CPX PS50	CPX PS50	CPX PS54X	CPX PS54X	CPX PS54X	CPX PS63	CPX PS63
Type	KI Basalt	KI Basalt	Gran.	Gran.	Dol	Dol	Dol	Qtz. Dol	Qtz. Dol	Fay. Gran.	Fay. Gran.	Fay. Gran.	Pegm.	Pegm.
Li	6.36	17.53	30.83	56.07	8.79	7.90	10.00	9.07	14.57	56.13	47.36	46.28	40.70	30.07
Na	1132.46	1092.88	1789.26	1040.52	1145.64	1867.19	1066.48	105.35	91.76	1547.77	1569.47	1012.44	1729.22	1122.16
Mg	137441	265616	17899	17597	129499	116085	120529	56896	45103	40905	34078	49800	71786.	59816.61
Si	256091	428228	228406	225915	249660	263785	260819	23607	23367	260581	229326	249850	262633	217802.83
P	29.61	57.68	21.56	35.70	23.66	24.80	28.24	18.40	17.75	87.65	50.42	51.00	44.75	34.61
K	56.84	46.14	14.56	2.21	111.42	37.35	33.08	4.29	5.87	299.96	528.84	50.21	78.06	40.54
Ca	137455	129147	143654	127931	142940	132219	132219	11435	10220	114352	114352	110778	121499	107919.83
Sc	113.52	155.21	168.04	221.60	86.02	137.09	131.31	189.01	184.77	199.11	188.00	201.57	170.33	170.89
Ti	1510.65	2247.37	1562.09	5354.94	1165.76	2498.86	2274.54	3440.68	3534.97	4655.62	4026.74	4237.74	4089.60	3911.48
V	723.65	935.22	2.32	2.81	568.75	923.78	873.37	1270.39	660.62	215.51	129.50	88.59	997.43	812.04
Cr	1339.58	672.18		0.56	1218.31	53.90	88.47	4.56				0.85	1.06	
Mn	1699.41	4272.24	4029.72	4243.03	1849.43	2920.52	2707.61	3663.67	4383.36	5716.77	4649.92	5074.09	4622.72	3829.22
Fe	27718	76564	113249	124400	30252	49726	52284	61723	77050	144711	118394	130527	61674	77870.22
Co	63.68	160.12	51.20	59.68	57.37	102.60	93.76	138.70	144.91	78.87	67.92	99.26	111.55	91.89
Ni	281.86	507.54	0.36		240.05	174.02	180.29	90.65	34.95	1.85	1.23	3.28	17.82	16.84
Cu	3.48	4.38	8.34	0.64	1.60	0.81	0.77	0.29	0.35	6.00	0.50	0.61	276.40	3.82
Zn	40.48	134.80	378.24	300.06	45.51	94.70	95.74	144.66	190.20	369.19	290.57	272.08	317.39	221.38
Ga	3.62	4.72	10.62	7.96	3.50	4.18	3.90	5.58	6.00	8.03	6.60	5.63	7.91	5.70
Ge	2.44	3.48	9.81	6.44	2.22	3.44	2.48	4.16	3.70	5.52	5.62	4.29	5.68	4.05
As	<0.23	0.52	2.29	0.62	0.88	0.32	0.26			0.62	0.64	0.64	0.43	0.29
Rb	0.23	0.20	0.24		0.56	0.35	0.23		0.07	2.13	3.04	0.14	0.44	0.04
Sr	9.02	6.25	1.90	15.42	9.41	8.99	7.73	4.30	3.37	9.57	9.88	6.77	8.31	6.86
Y	10.71	14.57	188.61	126.15	15.57	17.97	17.10	24.63	31.07	95.12	100.17	42.86	79.40	46.75
Zr	6.60	9.54	161.25	98.18	3.67	8.32	7.30	15.62	17.51	54.33	55.52	25.97	37.50	25.02
Nb	0.06	0.20	0.15	0.21	0.06	0.06	0.04		0.04	0.61	0.41	0.13	0.15	0.11
Mo	<0.25	<0.37	<0.23	<0.21	0.36	<0.26	<0.27			<0.27	<0.26	<0.30	<0.34	<0.26
Sn	1.59	2.21	6.69	1.42	2.10	1.84	1.44	1.31	1.37	1.77	1.51	1.52	1.86	1.33
Ba	0.71	0.99	0.44		2.44	0.84	0.58			11.88	18.19	0.64	0.64	0.16
La	0.59	0.62	66.85	15.54	3.12	1.43	1.46	1.36	2.05	18.04	20.98	4.17	12.89	6.10
Ce	2.51	2.65	189.71	61.41	9.14	5.13	5.01	5.39	7.42	56.73	66.62	14.12	45.92	21.10
Pr	0.45	0.50	23.97	10.83	1.12	0.83	0.77	1.01	1.32	8.46	9.97	2.33	6.66	3.37
Nd	3.06	2.76	95.60	57.43	4.85	4.66	4.44	6.22	8.00	41.30	48.09	12.55	31.78	17.03
Sm	1.04	1.14	24.85	18.66	1.33	1.64	1.54	2.63	3.28	11.87	13.65	4.49	9.63	5.26
Eu	0.28	0.28	0.52	1.27	0.28	0.38	0.28	0.57	0.55	1.11	0.96	0.66	0.74	0.62
Gd	1.60	1.92	26.84	21.49	1.70	2.51	2.38	3.61	3.74	14.59	15.75	6.07	10.81	6.27
Tb	0.26	0.33	4.68	3.69	0.34	0.45	0.39	0.64	0.75	2.54	2.79	1.09	2.01	1.14
Dy	2.01	2.52	34.60	25.50	2.48	3.37	3.05	4.52	5.57	18.68	20.08	8.16	15.08	8.95
Ho	0.42	0.60	7.31	5.28	0.58	0.72	0.66	0.95	1.24	3.93	4.12	1.75	3.30	1.86
Er	1.24	1.68	22.00	15.47	2.08	2.10	2.05	2.81	3.54	11.86	12.17	5.26	9.87	5.67
Tm	0.17	0.25	3.72	2.41	0.33	0.31	0.29	0.43	0.53	1.79	1.90	0.79	1.55	0.86
Yb	1.33	1.86	31.19	18.04	2.67	2.32	2.11	3.13	4.14	12.61	12.92	5.70	11.12	5.94

Lu	0.17	0.30	5.30	3.10	0.37	0.33	0.31	0.47	0.65	1.90	1.98	0.92	1.60	0.94
Hf	0.39	0.51	9.40	4.09	0.17	0.42	0.37	0.73	0.76	1.73	1.73	1.01	1.18	0.86
Ta			0.05	0.02						0.05	0.05			
Pb	0.17	0.21	8.45	0.70	0.99	1.00	0.42	0.20	0.22	3.12	1.81	1.27	1.12	0.80
Th	0.02	0.08	0.53	0.13	<0.0172	<0.0149	0.02	0.02		1.27	0.95	0.38	0.36	0.20
U	0.02	0.05	0.10	0.04	0.02	0.02	0.05		0.02	0.29	0.20	0.30	0.18	0.11

Table A16: Representative trace element concentrations of Red Hill low Ca pyroxenes measured by LA-ICP-MS (ppm).

Sample	**OPX KIW5-1**	**OPX PS65**	**Pig PS47**	**OPX PS47**	**Pig PS74**	**Pig PS47**	**Pig PS74**	**Pig PS63**	**OPX PS50**	**OPX PS50**	**Pig PS50**
Type	**KI Basalt**	**CM**	**Dol**	**Dol**	**Pegm.**	**Dol**	**Pegm.**	**Pegm.**	**Qtz. Dol**	**Qtz. Dol**	**Qtz. Dol**
Li	2.07	13.53	4.78	5.68	1.66	11.02	11.34	12.08	9.07	10.21	15.52
Na	171.17	212.04	280.64	420.92	139.08	461.32	393.94	502.18	37.13	28.40	38.52
Mg	259083	224033	124530	87113	70087	76760	166331	18568	47203	42921	62132
Si	323728	290337	220096	152435	110206	203853	314693	75808	16598	17534	26234
P	33.15	46.1	21.38	17.14	14.11	20.43	131.93	14.19	14.919	16.008	18.643
K		19.34	2.93	264.06	18.35	6.09	10.33	43.84	9.09		0.614
Ca	17845	17868	29517	20726	12436	38094	35735	36450	2602	2787	4503
Sc	36.51	51.42	58.32	37.75	20.39	94.09	68.38	48.20	62.86	80.07	131.61
Ti	523.19	768.37	1184.11	560.02	309.47	2874.10	978.12	1074.81	1206.68	1729.49	2872.65
V	181.05	313.26	343.86	237.10	102.90	459.25	328.36	299.31	408.89	487.76	527.13
Cr	1272.32	1907.89	26.54	58.67	66.52	7.98	206.44	0.29	2.82	1.44	
Mn	2484	2147	3441	1825	1307	4324	4890	1323	3414	3937	6179
Fe	48880	46643	49603	39044	32610	57968	126718	17357	60230	76838	115346
Co	124.28	104.91	128.33	74.17	50.27	119.96	154.90	28.70	124.96	140.20	207.50
Ni	577.26	494.54	197.96	153.21	93.64	76.17	199.32	4.62	61.83	50.73	53.07
Cu	2.23	2.80	0.45	1.06	1.86	0.42	9.48	7.75	0.31	0.24	0.36
Zn	102.85	94.38	166.52	107.83	85.20	230.12	332.31	94.84	194.68	229.10	338.76
Ga	1.50	2.42	1.74	3.96	0.72	2.66	2.14	2.72	2.18	2.70	4.14
Ge	1.95	2.98	2.43	1.06	0.79	2.64	2.44	1.83	2.08	2.62	4.30
As	0.32	<0.27	<0.193	0.59	<0.091	<0.144	0.39	0.29			
Rb		0.14		1.09	0.28	0.04	0.05	0.18	0.10		
Sr	0.09	0.64	0.42	6.13	0.37	1.02	0.88	2.68	0.48	0.35	0.60
Y	1.26	1.91	5.28	5.13	2.50	22.44	17.15	35.00	7.26	9.81	16.18
Zr	0.46	1.50	2.79	3.91	0.93	9.23	7.95	18.64	2.89	4.96	7.49
Nb				0.13	0.04	0.04	0.05	0.04			0.04
Mo	0.38	<0.28	<0.201	<0.143	<0.106	<0.19	0.44	<0.074			
Sn	1.37	1.10	1.08	0.75	0.71	0.95	1.83	0.41	0.91	0.86	1.52
Ba		0.72		1.35	0.13	0.10		0.48			
La	<0.0210	0.05	0.10	1.04	0.62	1.15	0.62	5.39	0.38	0.15	0.29
Ce	<0.0212	0.17	0.44	3.12	1.23	3.62	2.25	20.25	1.29	0.56	1.27
Pr	0.02	0.02	0.06	0.34	0.12	0.59	0.37	3.15	0.18	0.12	0.27
Nd		0.09	0.46	1.33	0.47	3.29	2.14	15.53	1.07	0.90	1.84

Sm	0.13	<0.095	0.22	0.37	0.14	1.27	0.93	4.54	0.42	0.52	0.95
Eu	<0.026	<0.021	0.07	0.04	0.03	0.13	0.11	0.34	0.08	0.10	0.21
Gd	0.12	0.12	0.53	0.52	0.22	1.91	1.28	5.41	0.65	0.70	1.29
Tb	0.02	0.03	0.09	0.09	0.05	0.39	0.30	0.93	0.14	0.17	0.33
Dy	0.18	0.27	0.87	0.78	0.38	3.05	2.72	7.00	1.06	1.51	2.57
Ho	0.06	0.07	0.22	0.20	0.09	0.77	0.62	1.46	0.28	0.37	0.61
Er	0.13	0.24	0.68	0.65	0.32	2.47	2.24	4.28	0.91	1.24	2.05
Tm	<0.0182	0.05	0.13	0.10	0.06	0.45	0.38	0.64	0.14	0.21	0.33
Yb	0.31	0.31	1.00	0.73	0.43	3.05	3.20	4.28	1.25	1.65	2.68
Lu	0.06	0.07	0.16	0.11	0.06	0.53	0.51	0.59	0.18	0.29	0.44
Hf	0.00	0.06	0.08	0.15	0.02	0.29	0.20	0.52	0.16	0.17	0.37
Ta											
Pb	0.05	0.07	0.10	0.17	0.06	0.05	0.37	1.13	0.20	0.04	0.10
Th	<0.0159	0.03	0.04	<0.0070	0.01	0.09	0.07	0.47	0.03	0.02	
U	<0.0136	<0.0119	0.03	0.34	0.02	0.03	0.05	0.08			

Table A17: Representative trace element concentrations of Red Hill plagioclase measured by LA-ICP-MS (ppm).

Sample	**KIW5-1**	**KIW5-1**	**PS47**	**PS54X**	**PS63**	**PS65**	**PS74**	**PS38**
Type	**KI Basalt**	**KI Basalt**	**Dol**	**Fay. Gran.**	**Pegm.**	**CM**	**Pegm.**	**Gran.**
Li	14.28	18.47	8.86	7.97	6.8	18.16	7.28	0.0933
Na	15741.54	14166.33	39275.87	42231.72	38174.12	18864.39	21509.41	6240.68
Mg	2680.18	2277.39	1584.61	352.3	180.55	1754.08	322	1307.6
Si	228764.1	235626.7	320634.2	266795.6	257410.3	265932.4	238618.2	22382.88
P	35.03	41.04	53.79	66.1	57.31	65.83	45.96	3.39
K	1370.31	867.89	2734.64	2441.29	2367.91	1450.93	1405.42	230.03
Ca	111967.2	121499.2	112922.7	69326	79331.8	125072.7	107205.2	2858.8
Sc	2.54	2.53	3.68	2.52	3.8	2.4	2.54	0.1931
Ti	120.37	88.77	391.94	308.15	322.26	121.4	173.96	5.97
V	8.99	5.45	18.4	0.697	7.22	8.59	7.63	0.0725
Cr	7.66	1.89	4.84	1.05		1.67		0.657
Mn	54.69	46.13	69.81	42.68	27.44	54.07	26.92	1.003
Fe	1787.69	1350.62	3131.43	3087.57	1078.96	2043.32	1547.51	33.26
Co	1.92	1.55	2.33	0.675	0.447	1.35	0.557	0.0283
Ni	1.99		1.99	1.61	1.05	0.67	0.5	0.053
Cu	1.68	<0.25	0.33	3.23	0.97	0.49	2.01	0.125
Zn	13.25	7.85	31.33	38.77	41.14	15.42	18.64	0.591
Ga	19.22	17.74	36.63	30.45	29.45	20.01	20	0.674
Ge	0.86	0.76	1.44	0.69	0.68	1	<0.52	<0.034
As	<0.35	<0.32	<0.33	<0.28	<0.27	<0.47	<0.29	0.0193
Rb	1.124	0.309	0.821	9.01	1.212	3.28	3.04	1.11

Sr	187.29	176.61	356.12	277.34	334.67	209.37	263.21	6.89
Y	0.124	0.101	0.356	0.187	0.26	0.127	0.529	0.116
Zr	0.42	0.071	0.217	6.35	0.746		0.163	1.633
Nb								0.0199
Mo	<0.36	<0.37	<0.41	<0.30	<0.33	<0.47	<0.33	<0.0207
Sn	0.82	0.78	0.85	1.46	2.19	1.05	1.29	1.153
Ba	32.52	23.79	130.39	134.68	156.39	38.67	111.41	4.5
La	0.423	0.369	1.575	1.633	1.327	0.481	1.572	0.247
Ce	0.879	0.741	3	3.03	2.57	0.971	3.27	0.355
Pr	0.092	0.0628	0.254	0.276	0.24	0.074	0.308	0.0313
Nd	0.305	0.201	1.036	1.204	0.863	0.485	1.064	0.1109
Sm	<0.124	<0.111	0.186	0.204	<0.123	0.146	0.196	0.0235
Eu	0.3	0.242	1.571	1.547	2.41	0.489	1.095	0.0302
Gd	<0.134	<0.130	<0.164	0.146	<0.124	<0.149	<0.116	0.0154
Tb	0.0239	<0.0196	<0.0192	<0.0158	<0.0161	<0.023	0.0191	0.00246
Dy	<0.080	<0.073	<0.086	0.096	<0.075	<0.095	0.137	0.021
Ho	<0.0190	<0.0171	<0.0209	<0.0168	0.034	<0.023	<0.0185	0.00363
Er	<0.055	<0.048	<0.068	<0.051	<0.055	<0.063	0.071	0.0103
Tm	<0.0171	<0.0169	<0.0217	<0.0160	<0.0162	0.025	<0.0181	0.00192
Yb	<0.082	<0.073	<0.081	<0.067	<0.078	<0.091	<0.082	0.0102
Lu	<0.0211	<0.0192	<0.0222	<0.0183	<0.0193	<0.023	<0.0187	0.00159
Hf	0	0	0	0	0	0	0	0.0437
Ta					0.027			0.00283
Pb	0.898	0.486	2.76	2.273	4.79	4.38	4.32	0.2027
Th	<0.0226	<0.0160	<0.0196	0.141	0.04	0.03	0.0226	0.0567
U	<0.0145	<0.0131	<0.0179	0.114	<0.0143	<0.0161	<0.0147	0.0312

Explanation of the Rayleigh Fractionation Model

The model used here to estimate the evolution of the isotopic composition of iron is based upon a simple Rayleigh fractionation model. Furthermore, it uses XRF data for 59 whole rocks from the Red Hill intrusion to constrain the liquid line of descent, as well as microprobe analyses for mineral phases, whose proportions are approximated through a linear least-squares regression (Stormer and Nicholls, 1978), making for an internally-consistent dataset.

Table A18: Example of the derivation of PS47 (Dolerite) from PS65 (Chilled Dolerite) using Least Squares. Average microprobe analyses were used for the mineral compositions.

	Bulk X Subtracted	**PS65**	**PS47**		**Observed Diff**	**Calculated Diff**	**Residual**
SiO_2	52.65	54.66	55.24	0.574	0.568	0.686	-0.118
TiO_2	0	0.64	0.73	0.084	0.087	0.188	-0.101
Al_2O_3	14.88	14.76	14.74	-0.018	-0.017	-0.031	0.014
Fe_2O_3	0	1.75	2.71	0.961	0.966	0.704	0.262
FeO	8.38	7.46	7.16	-0.304	-0.306	-0.312	0.006

MnO	0	0.17	0.17	-0.001	0.002	0.044	-0.042
MgO	9.96	6.83	5.79	-1.039	-1.039	-1.079	0.040
CaO	12.46	10.89	10.36	-0.527	-0.527	-0.540	0.013
Na_2O	1.67	1.86	2.04	0.178	0.179	0.097	0.082
K_2O	0	0.85	0.94	0.086	0.089	0.243	-0.154
Sum of Squares	0.127						
	Cotectic	Cotectic Prop					
KIW51-OPX	-1.42	5.48					
65Pig	-6.73	25.98					
65CPX	-5.41	20.89					
65Plag	-12.34	47.64					
F Remaining	74.1						
Sum of Squares/(O-P)	0.021						

Modelling Iron Enrichment in the Melt

To model the stable isotope fractionation of iron between crystals and melts necessitates the modelling of the ∑Fe first. Given that the oxidation state of iron is of paramount importance to the evolution of $\delta^{57(56)}$Fe, both Fe^{3+} and Fe^{2+} needed to be estimated as a function of differentiation (*figure A1*). We assumed that all Fe in pyroxenes is Fe^{2+}, and that plagioclase does not contain Fe. Additionally, in order to create a model that is consistent with petrographic observations and electron-probe micro-analysis (EPMA) of the mineral phases, a least-squares regression was used to estimate their proportions (Stormer and Nicholls, 1978) (*Table A18*).

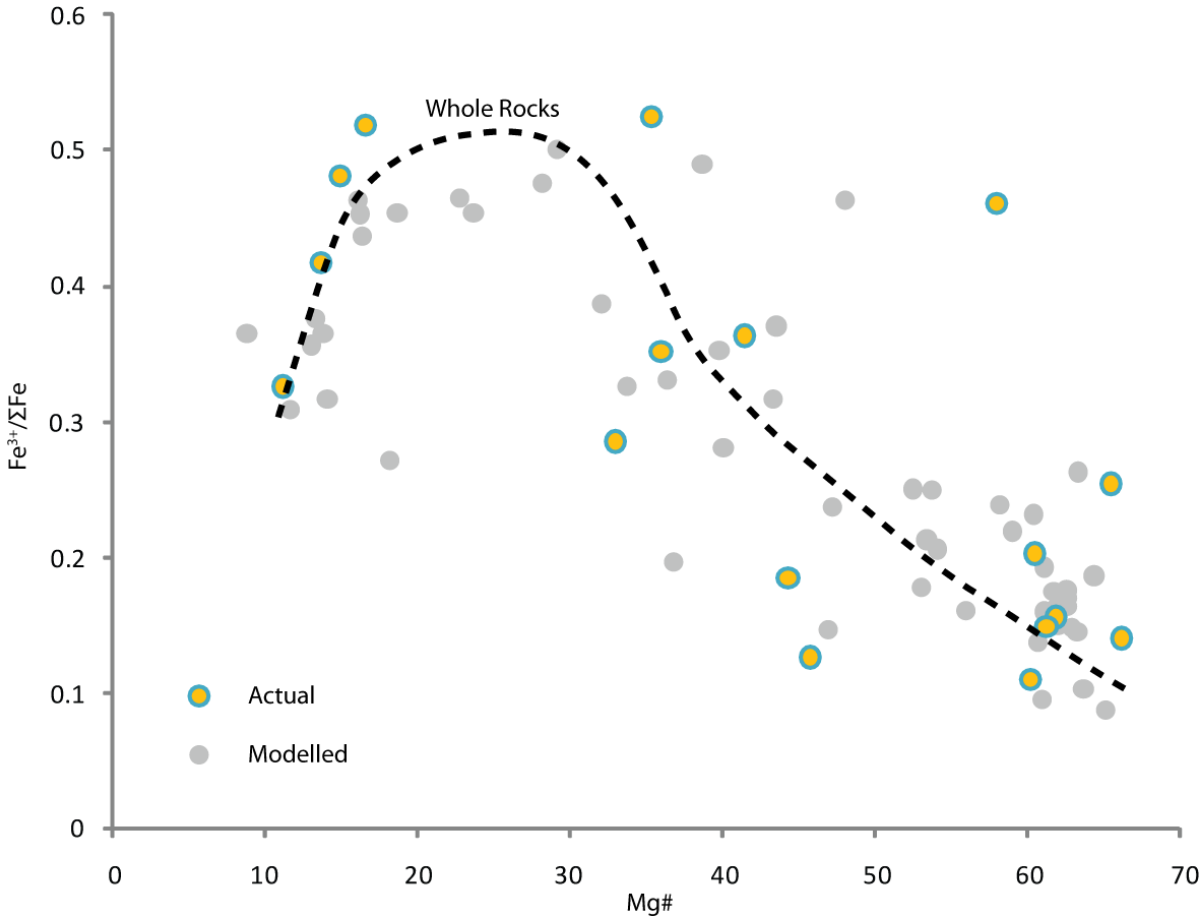

Figure A1: The $Fe^{3+}/\Sigma Fe$ of the whole rock samples (yellow circles) and the modelled $Fe^{3+}/\Sigma Fe$ of the 59 Red Hill samples (grey circles), illustrating its initial increase and inflection at Mg# ≈ 20.

Since electron microprobe analyses are available for only a discrete subset of the rocks, the effective fractionating phase proportions, P^n (and compositions, X^n) were interpolated according to a linear mixing equation (Albaréde, 1996, p.4, eq. 1.1.5):

$$P^n = \frac{\left(P^{initial} - P^{final}\right)}{\left(F^{initial} - F^{final}\right) \times \left(F^{now} - F^{final}\right)} + P^{final} \quad \text{(A-1)}$$

Where F refers to the fraction of melt remaining, and initial and final refer to the states of the system for which EPMA data is available, such that the compositions and phase proportions are known. The only variable is F^{now}, and it requires that the fraction of melt left in the system be estimated separately.

In order to estimate F, the Rayleigh equation was used to solve for F, where the concentration of C is given by the rock, C_0 by the average chilled margin, and D was fitted to the data. The oxide used was MgO due to its monotonic decrease with differentiation.

$$F = e^{\frac{\ln\left(\frac{C_l}{C_0}\right)}{D-1}} \quad \text{(A-2)}$$

Knowing the relative crystallising proportion of a given mineral phase P^n, the concentration of an oxide component in that phase, X_n^A, and the concentration of that oxide component in the melt, X_{Melt}^A, enables the calculation of a partition coefficient for that oxide, in a given phase $(X_n^A/X_{Melt}^A) = K^A$. From there, a bulk partition coefficient may be calculated:

$$D_{Bulk}^A = K^A * P^1 + K^B * P^2 + \ldots + K^n * P^n \quad \text{(A-3)}$$

For magnetite, following Toplis and Carroll (1996), its crystallising proportions were estimated from the concentration of Fe_2O_3 in the melt ($X_{Fe_2O_3}$):

$$P^{Mtn} = \left(\frac{\left(\frac{X_{Fe_2O_3}}{100}\right)}{f} \times \frac{1}{f} \right) \times c \quad \text{(A-4)}$$

This technique enables the projection of a multiphase system into a binary system by estimating a bulk partition coefficient for the constituent phases. The D parameter may then be readily substituted into the Rayleigh equation.

$$C = C_0 F^{D-1} \quad \text{(A-5)}$$

Modelling Stable Isotope Fractionation

In order to model stable isotope fractionation, the Rayleigh equation is modified to incorporate isotope ratios and fractionation factors, in lieu of concentration and bulk partition coefficient, respectively.

$$\left(\frac{^{57}Fe}{^{54}Fe}\right)_{at\ f} = \left(\frac{^{57}Fe}{^{54}Fe}\right)_{original} f^{(\alpha_{prod-reac}-1)} \quad \text{(A-6)}$$

Given that ε is equal to $10^3(\alpha_{prod-reac} - 1)$, effectively casting it into per mille, we can re-write the equation as:

$$\ln\left(\frac{1000 + \delta}{1000 + \delta_0}\right) = \frac{\varepsilon}{1000} \ln f \quad \text{(A-7)}$$

When the δ-values are small (within 10‰) and have a low fractionation factor, the equation can be closely approximated by the following:

$$\delta - \delta_0 \cong 10^3(\alpha - 1) \ln f = \varepsilon \ln f \quad \text{(A-8)}$$

It is clear that not all minerals will partition iron to an equal amount. Therefore, the effect they have on shifting iron isotope composition must be weighted by the fraction of iron they incorporate. Each mineral is assigned a quantitative weighting factor according to their affinity for iron as dictated by their iron content and cotectic proportion.

$$W^n = \frac{P^1 \times X_{Fe}^1}{\Sigma P^n X_{Fe}^n} \quad \text{(A-9)}$$

W^n is the weighting factor for phase n, P^n is the cotectic proportion of phase n and X_{Fe}^n is the weight % FeO or Fe_2O_3 in phase n.
Applying the weighting factor to derive the bulk fractionation factor is straightforward:

$$\varepsilon_{bulk} = \Sigma(\Delta^{57Fe}_{mineral-melt} \times W^n) \quad \text{(A-10)}$$

The fractionation factor for each mineral is given by the expression:

$$\Delta^{57Fe}_{mineral-melt} = \varepsilon \times \frac{10^6}{T^2} \quad \text{(A-11)}$$

Where ε is a constant fractionation factor, and is modified only by the absolute temperature, T, in Kelvin.

A unique temperature was calculated for each sample's bulk composition from the expression in Sisson and Grove, (1993). The temperature can subsequently be substituted into equation (A-11)

$$T°(K) = 969 - 33.1(LOI) + 0.0052(P-1) + 742.7\left(\frac{Al_2O_3}{(Al_2O_3 + SiO_2)}\right) - 138\left(\frac{(K_2O + Na_2O)}{(K_2O + Na_2O + CaO)}\right) + 125\left(\frac{Mg}{(Mg + Fe^{2+})}\right) \quad \text{(A-12)}$$

Returning to the significance of the distinction between Fe^{2+} and Fe^{3+} for this model, because it is cited that the $Fe^{3+}/\sum Fe$ of the fractionating phases and residual melt enact a change in $\delta^{57(56)}Fe$, such a value must be modelled accurately in all phases.

To that end, it is necessary to formulate separate Rayleigh equations that describe the fraction of Fe^{2+} and the fraction of Fe^{3+} remaining in the melt. Consequently, the weighting factors are subject to the X_{FeO}^n or $X_{Fe_2O_3}^n$. In either case, we take $X_{FeO}^{initial}$ and $X_{Fe_2O_3}^{initial}$ to be the concentration of the oxides in the average chilled margin composition, taken to represent the melt parental to any subsequent differentiation products. It is then possible to normalise f at continually lower fractions of melt remaining.

$$f_{eff}^{Fe} = f * \left(\frac{X_{Fe}^{at\,f}}{X_{Fe}^{initial}}\right) \quad \text{(A-13)}$$

f_{eff}^{Fe} is the effective fraction of iron (FeO or Fe_2O_3) remaining in the melt, f is the fraction of melt remaining as obtained from equation (A-2).

Knowing these parameters, they can be substituted into the general form of the Rayleigh equation, recast into delta notation:

$$\delta \cong \delta_0 + \varepsilon_{bulk} \ln f_{eff}^{Fe} \quad \text{(A-14)}$$

This equation allows the $\delta^{57(56)}Fe$ to be calculated considering Fe^{2+} or Fe^{3+}. Since $f_{eff}^{FeO} \neq f_{eff}^{Fe_2O_3}$ at a given f, the equations need to be combined to yield:

$$\delta = \delta_{FeO} - \left(\delta_0 - \delta_{Fe_2O_3}\right) \quad \text{(A-15)}$$

Deriving the Fractionation Factor

The derived fractionation factors are dependent on several factors, as illustrated by the preceding calculations.

a. The modal proportions of pyroxenes and magnetite

Since pyroxenes and magnetite partition largely Fe^{2+} and Fe^{3+}, respectively, their modal abundance affects the degree of total iron enrichment, as well as Fe^{3+} and ^{57}Fe enrichment or depletion. When magnetite and augite co-precipitate (*figure 2.8.*), the isotopic composition of the residual melt depends on their relative abundance. However, because magnetite is the dominant host of iron, it controls the modelled fractionation trend. Changes in the modelled iron isotopic composition are very insensitive to the plagioclase/pyroxene ratio during early crystallisation, although it does control the extent of iron enrichment in the melt. Thus, both pyroxene-melt and magnetite-melt fractionation factors are considered robust.

b. Amount of melt remaining

The amount of melt remaining as estimated by MgO is easily corroborated by modelling through least squares regressions. Values are largely coincident, and deviations are minimal such that they do not noticeably affect the modelled isotopic compositions.

c. Temperature estimates

The temperature formulation from Sisson and Grove (1993) was applied to the Red Hill magmas because it is calibrated in the absence of olivine, and in the presence of augite and plagioclase, the two phases which are present throughout the intrusion. Furthermore, it accounts for the effect of water and pressure on the liquidus temperature. However, the accuracy of the temperature estimate is shown to have little impact on the calculated fractionation factors. A systematic temperature offset of 100°C results in deviations of the modelled $\delta^{57}Fe$ of <0.05‰, even at the lowest temperatures.

d. The initial composition

Owing to the presence of chilled margins that line the Red Hill intrusion, and given that the resulting differentiates are produced from fractional crystallisation of this single parent magma, the iron isotopic composition of the initial melt may be estimated. We approximate that $\delta_0^{57}Fe \approx +0.14‰$, which is the average of the Kangaroo Island basalt and the Red Hill chilled dolerite.

Taking these caveats into account, the sensitivity of the modelled fractionation factor may be investigated by applying $\Delta^{57Fe}_{mineral-melt} = \varepsilon \pm 0.1‰ \times \frac{10^6}{T^2}$, where ε is the ideal fractionation factor (*figure A2a*).

The model employing the lower estimate for $\Delta^{57Fe}_{mineral-melt}$ exhibit very restricted variation of roughly 0.1‰ over the crystallisation history, subsequently failing to explain the observed trend (*figure A2b*). Similarly, upper values for $\Delta^{57Fe}_{mineral-melt}$ ($\Delta^{57Fe}_{px-melt}$ = -0.35‰ × $\frac{10^6}{T^2}$ and $\Delta^{57Fe}_{mtn-melt}$ = +0.30‰ × $\frac{10^6}{T^2}$ result in too drastic changes in the calculated δ^{57}Fe with respect to the data (*figure A2c*).

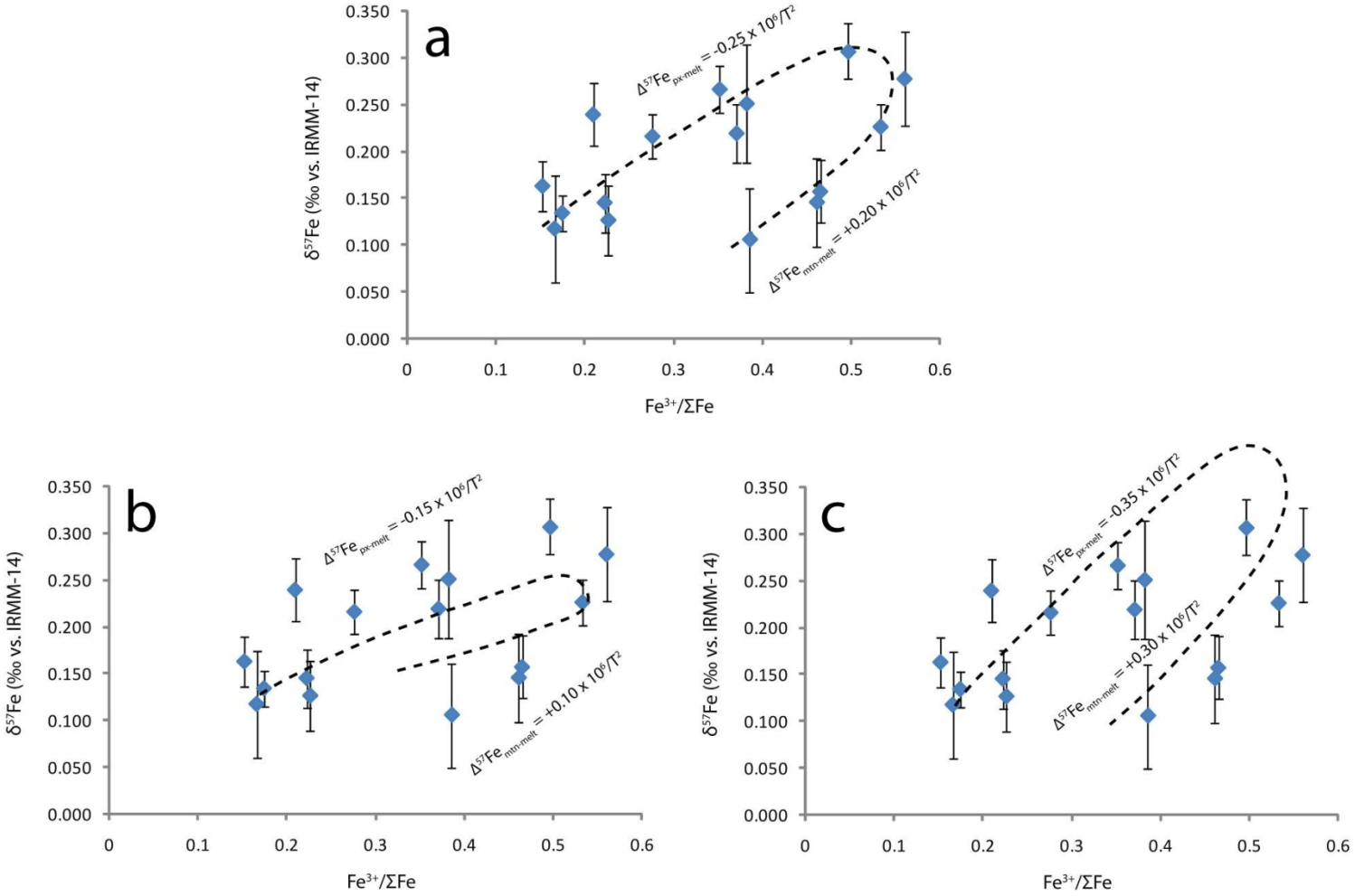

Figure A2: The effect of varying pyroxene-melt and magnetite-melt fractionation factors on the model calculations. a) The ideal fractionation factors; b) The lower estimates for the fractionation factors; c) Their upper estimates.

Table A19: Iron Isotope Data for all samples investigated, and their $Fe^{3+}/\Sigma Fe$

Sample	Type	δ^{57}Fe	δ^{57}Fe (2SE)	δ^{56}Fe	δ^{56}Fe (2SE)	Repetitions	$Fe^{3+}/\Sigma Fe$
KIW5-1	K.I. Basalt	.145	*.031*	.101	*.029*	4	0.20
65	Chilled Margin	.134	*.020*	.082	*.061*	3	0.15
47	Dolerite	.216	*.023*	.153	*.014*	3	0.25
50	Qtz. Dolerite	.267	*.025*	.195	*.011*	4	0.29
35	Dolerite	.163	*.027*	.120	*.035*	4	0.13
54	Fay. Granophyre	.307	*.030*	.196	*.028*	3	0.48

38	Granophyre	.226	*.024*	.147	*.024*	4	0.52
14	Granophyre	.157	*.033*	.101	*.020*	6	0.42
15	Granophyre	.105	*.056*	.070	*.045*	5	0.33
63	Peg. Dolerite	.219	*.031*	.139	*.026*	4	0.35
44	Fay. Gran.	.278	*.050*	.186	*.035*	5	0.53
61	Fay. Gran.	.251	*.063*	.184	*.054*	3	0.36
21	Dolerite	.126	*.037*	.087	*.030*	7	0.20
52	Qtz. Dolerite	.240	*.033*	.161	*.026*	3	0.19
32	Dolerite	.117	*.058*	.084	*.040*	3	0.14
74	Peg. Dolerite	.145	*.048*	.096	*.035*	3	0.46
BHVO-2	Hawaiian Basalt	.159	*.068*	.104	*.043*	4	-
BCR-2	Columbia River Basalt	.139	*.044*	.091	*.034*	4	-
HEM	Haematite (ETH)	.760	*.026*	.513	*.022*	16	-